The Dissertation Committee for Jonathan Allen Bollinger
certifies that this is the approved version of the following dissertation:

From confinement to clustering: decoding the structural and diffusive signatures of microscopic frustration

Committee:

Thomas M. Truskett, Supervisor

Roger T. Bonnecaze

Venkat Ganesan

Nathaniel A. Lynd

Dmitrii E. Makarov

From confinement to clustering: decoding the structural and diffusive signatures of microscopic frustration

by

Jonathan Allen Bollinger, B.S., M.S.

DISSERTATION

Presented to the Faculty of the Graduate School of

The University of Texas at Austin

in Partial Fulfillment

of the Requirements

for the Degree of

DOCTOR OF PHILOSOPHY

THE UNIVERSITY OF TEXAS AT AUSTIN

December 2016

Dedicated to the great teachers

who taught me thus far

Acknowledgments

First, many thanks to Tom for exemplifying intellectual integrity and level-headedness as I gained my scientific footing. I take away from your mentorship: (1) a great appreciation for elegance in physics and (2) a model of open-mindedness and creativity that I hope to emulate during the coming years. Many thanks are also due to my lab-mates: Avni, James, Ryan, Beth, and Kyle. Avni, in particular, deserves special recognition for being steadfast through the squalls of the early years and always providing excellent food for thought (and food in general). And the latter chapters of this manuscript would not have happened without the kind influence and teaching of Ryan, who got us all thinking about clusters in new ways. Much appreciation also goes to Keith Johnston and his students for providing illuminating collaborations and the chance to get an inside view of experiments on complex fluids.

Outside of my scientific niche, Austin has been an incredibly warm place, both literally and–more importantly–figuratively. It is rich with friendships, adventures, potlucks, etc. that have kept me sane and made for a great life here. An extra special thanks goes to Becca Pride, who was one of the first (and certainly most dependable) friends I've made here, and the lovely Ron and Melissa Pride who are Official Texas Parents Forever. In turn, much of my non-UT community is best summarized in the form of houses: here's to the fine folks of Argosy, Hamp-

ton, Sandstone, the Sandlot, Raven, the Abbey, M Station, Harmony, and Ave F. Then there are my UT ChE compatriots, with whom it has been a pleasure to cook, create, and commiserate. Here's to Joseph (and your better half), Greg M. and Mia, Jeff, Dylan, Renee, Alex P., Cara, and Brent (and the book club). And, finally, to A.–you're the best and bravest of us all.

Looking back further, I owe such a deep (and yet light) debt to my beloved community in Baltimore. From Hilltop to Gilmor, from Lombard to Load of Fun, it is you all that I have to thank for opening my mind and instilling profound appetites for justice, humility, and–sorry, Austin–*weirdness.* I swear that I'll get back to y'all sooner or later. Profound thanks are in order for Dr. Leach (go Longhorns), Dr. Bayles, and Dr. Loehe, who all provided such diverse yet complementary examples of great teaching and trustworthiness. And, of course, to Dr. C–whose downright baffling (or at least awe-inspiring) levels of enthusiasm and support got me hooked on research in the first place.

Then there's you, E. Through the highs and the lows of the last five years (and the three-and-a-half before that), you have constantly challenged me to become not just a better brain, but a better human. You are trustworthy, zany, brave, fierce, smart-as-hell, independent, beautiful, and I am constantly impressed by you. I love you very much.

From confinement to clustering: decoding the structural and diffusive signatures of microscopic frustration

Jonathan Allen Bollinger, Ph.D.
The University of Texas at Austin, 2016

Supervisor: Thomas M. Truskett

There are diverse technological contexts where fluids and suspensions are perturbed by applied fields like interfaces or intrinsically governed by complex interparticle potentials. When these interactions act over lengthscales comparable to the fluid particle size and become strong enough to frustrate particle packing or rearrangements, they drive systems to exhibit microscopically inhomogeneous (i.e., position-dependent) structural and relaxation responses. We use computer simulations and statistical-mechanical tools to find connections between such frustrating interactions and inhomogeneous fluid responses, which can profoundly impact macroscopic material properties and processing requirements.

We first consider how to measure and predict the position-dependent and average diffusion coefficients of particles along inhomogeneous free-energy landscapes (i.e., potentials of mean force). Characterizing diffusion in such inhomogeneous fluids is crucial for modeling, e.g., the transit of colloids across microfluidic

devices and of solutes through biological membranes. We validate a practical technique based on the Fokker-Planck diffusion formalism that measures diffusivities based solely on particle trajectory data. We focus on hard-sphere fluids confined to thin channels or subjected to external fields that impose density fluctuations at various wavelengths. We find, for example, that hydrodynamic predictions of tracer diffusion in confinement are surprisingly robust given non-continuum solvents. We also demonstrate that correlations between fluid static structure and diffusivity can qualitatively depend on the lengthscale of density fluctuations or the onset of supercooling.

We next examine fluids governed by competing short-range attractions and long-range repulsions that drive formation of equilibrium cluster phases, which comprise monodisperse aggregates of monomers. The formation of such morphologies greatly impacts, e.g., the manufacturing of therapeutic protein solutions. We first address a major challenge in probing the real-space structure of such suspensions: detecting and characterizing cluster phases based on the static structure factor accessible via scattering experiments. Using computer simulations and liquid-state theory, we validate rules for interpreting low-wavenumber features in the structure factor in terms of cluster emergence, size, spatial distribution, etc. We then validate a thermodynamic model that predicts cluster size based on the strengths of monomer interactions, adapting classical nucleation theory to incorporate new empirical scalings for the surface energies of small stable droplets.

Table of Contents

Chapter 1

Introduction

In this dissertation, we focus on understanding how particles in fluids and suspensions respond–in terms of their microscopic spatial self-organization and diffusive motions–to "frustrating" interactions. Frustrating interactions take many forms, and include the presence of solid interfaces that restrict and slow down proximal fluid rearrangements compared to the bulk fluid or interparticle interactions that inherently drive, e.g., self-association, as in the common case of surfactant molecules that must reconcile their water soluble and insoluble moieties.

Connecting frustrating interactions with their impacts on fluid structure and dynamics is critical for the rational engineering of new materials and manufacturing processes because these *microscopic* responses can ultimately set the *macroscopic* system properties (mechanical, electrochemical, optical, etc.). Given our increasingly precise control over the synthesis of material "building blocks" like functionalized nanoparticles, we have unprecedented opportunities to tune the properties of materials from the ground up provided we have a fundamental grasp on how interactions impact fluid behavior. Developing this type of understanding is especially necessary–and especially *challenging*–in the case of systems affected by applied fields or interactions that induce frustration at lengthscales comparable

to the characteristic particle size, because such frustration often drives materials to exhibit heterogeneous properties in ways that are non-trivial to predict.

We consider two different classes of frustrating interactions, with distinct goals in each case. First, we consider fluids influenced by the presence of confining multiphase interfaces and other external fields, which drive the fluid particles to exhibit inhomogeneous (i.e., position-dependent) structural correlations and/or diffusive dynamics. Here, we focus on validating approaches for measuring and predicting the local and average dynamic responses of these inhomogeneous fluids, which are not well-understood for particles traversing anisotropic free-energy landscapes (i.e., potentials of mean force). Understanding diffusive dynamics in such cases is important for engineering particle transport along, e.g., permeation pathways mediated by biological membranes. We then examine fluids governed by multi-lengthscale competing interactions that drive the formation of equilibrium cluster phases. We focus on improving the interpretation of scattering experiments for systems that can form these microscopic aggregates, and develop a thermodynamic model that predicts cluster size based on the interaction strengths between monomers. These results facilitate improved control of, e.g., the manufacturing of therapeutic protein solutions, where protein-protein interactions can favor quiescent cluster and network formation that compromises quality assurance.

In Sections 1.1-1.2, we briefly survey the previous scientific work in these complementary areas, and present the open lines of inquiry that we aim to investigate. Then, in Section 1.3, we outline the remainder of the dissertation, providing summaries of the goals, methodologies, and major findings of each chapter.

1.1 Diffusion along complex free-energy landscapes

Particles in a fluid or suspension often display position-dependent diffusive dynamics while moving through confined spaces or external fields, and characterizing diffusion is such cases facilitates the engineering of particle transport in a wide array of technological scenarios. For instance, the diffusive dynamics might reflect the inhomogeneous structuring (e.g., particle layering) and frustrated relaxation induced by proximity to multiphase interfaces [75, 90]. Or perhaps local particle motions reflect the influence of anisotropic gravitational [19, 162, 175, 212], depletion [9, 120], electromagnetic [98, 202], and optical [67] forces, etc., which induce phenomena ranging from (but by no means limited to): the sedimentation equilibrium of particle suspensions [95]; reversible solidification in electrorheological fluids [221]; and the spatial entrapment of colloidal particles via optical tweezers [224].

Knowledge of corresponding *position-dependent diffusion coefficients* that describe the motions of a "tracer" particle opens up numerical modeling opportunities. One could model how quickly nanoparticles transit across pores in micro-fluidic devices or geological environments [23, 198]; the kinetics of diffusion-controlled reactions at an interfaces [205]; the dynamics of particles along external fields that drive self-assembly of crystal structures [56, 94]; or how water-soluble compounds like perfumes permeate through the epidermis [115, 158]. In all of these cases, the local diffusion coefficients of these tracer particles can drastically differ from their bulk (i.e., isotropic) diffusivities within the same solvent in the absence of the frustration induced by interfaces, external fields, membranes, etc.

Aside from numerical modeling, of course, possession of diffusivities as a function of (in our cases, *physical*) position can be instructive for identifying, rationalizing, and re-engineering, e.g., undesirable bottlenecks, along the potentially complex free-energy pathways connecting "source" and "target" locations of the tracer(s).

Despite the ubiquity of fluids that exhibit inhomogeneous diffusive dynamics, even the conceptualization of position-dependent–as opposed to spatially-constant–diffusion coefficients remains relatively nascent, with the exceptions of some classic idealized problems in hydrodynamics and some very recent groundwork for simple fluids at interfaces. To wit, in most engineering contexts, one encounters diffusivities in the so-called *drift-diffusion equation*, which models the probability distribution of particle position–or, analogously, a density or concentration profile–with respect to time, and is conventionally written as if the resistance to diffusion (e.g., drag due to collisions with solvent particles) is *spatially-invariant*. However, it has long been appreciated that diffusion coefficients ought to be localized in, e.g., Stokes-flow problems for particles near interfaces. A wide variety of theoretical treatments have been developed over the last several decades to predict how the drag forces acting on a particle (or pair of particles) suspended in a viscous continuum solvent will vary with location due to hydrodynamic coupling with proximal confining walls [18, 58, 75, 82, 123, 199, 203]. Likewise, in the past decade, there has been an increasing recognition in the soft-matter community that when describing the diffusive motions of tracer particles that are *comparable* in size (or identical) to surrounding solvent particles, effects like heterogeneous structuring of the solvent near an interface can non-trivially influence tracer motions and neces-

sitate describing dynamics based on local diffusion coefficients [124, 149, 187, 215]. Simple examples include concentrated thin films of monodisperse colloidal particles, where a given "tracer" diffuses through a structurally inhomogeneous "solvent" composed of comparably-sized neighbors [149, 155, 156], or a small aqueous solute not much larger than a water molecule, which encounters slowly-relaxing layers of solvent near a hydrophilic surface [187].

To describe tracer-particle motions in such systems, it is appropriate to appeal to the more generalized *Fokker-Planck* (*Smoluchowski*) *equation* [55] that accounts for position-dependent diffusive dynamics and inhomogeneous free-energy landscapes (i.e., potentials of mean force). The latter is important because, as in the examples above, external fields that induce local dynamic variations often drive heterogeneous fluid structuring. But if one does not possess *a priori* predictions for local diffusivities (e.g., from hydrodynamic theory), how does one parametrize this master equation? In other words, how can one measure position-dependent diffusion coefficients in real systems? After all, a typical approach for obtaining average diffusion coefficients, like fitting particle mean-squared displacements to the Einstein equation [2], would be inappropriate because it is predicated on an isotropic free-energy landscape. Recent efforts to address this "methods gap" have resulting in several distinct frameworks designed to measure local diffusivities along arbitrary free-energy landscapes based on knowledge of particle trajectories, including approaches based on Bayesian inference [86, 149], "color"-reactions [35], mean-first passage times (MFPTs) [81, 187, 220], and more [124]. However, validation of these techniques–especially via tests on systems where tracer diffusivity

profiles are *known* in certain limits–has been patchy and focused on relatively complicated approaches. Thus, validating an approach that is readily accessible for simulations or experiments (via, e.g., confocal imaging) remains an important goal that could open up investigations of diffusion within inhomogeneous systems.

Given practical means for measuring position-dependent diffusion coefficients, it is important to improve our physical intuition regarding how diffusive dynamics vary with respect to fluid structure, and to test the degree to which they are *predictable*. By way of analogy: we know how simple fluids respond in terms of their local microscopic structure (e.g., density profile) to the imposition of external fields via classical density functional theories (DFT) [172, 174]; can the same be done for diffusive dynamics? If fluid dynamics along inhomogeneous pathways are predictable based on knowledge of certain static quantities in the system, then one can exploit known theories (e.g., DFT) connecting particle interactions and structure to rationally control local (and average) transport from the ground up. This scenario is plausible because dynamics along structurally *isotropic* directions of inhomogeneous fluids are known to be predictable based on semiempirical, quasi-universal scaling laws that relate average transport coefficients of interest (e.g., diffusivities, viscosities) to average static properties (e.g., excess entropy) based on how these quantities relate to one another in the bulk [29, 38, 65, 66, 88, 126, 134, 145, 146]. Recent theories have also adapted frameworks like mode-coupling theory to do the same for supercooled inhomogeneous fluids [105,110–112]. However, such laws and frameworks have yet to be systematically tested on a position-dependent basis. Indeed, the few previous investigations in this vein comprise a patchwork of dis-

parate interparticle interactions, external fields, and protocols for characterizing local diffusive dynamics [51, 111, 149, 155, 157].

Given the relative novelty of characterizing local diffusive dynamics, there remain basic questions regarding what diffusivity profiles that tracer particles should exhibit in response to imposed external fields, even for idealized systems. To wit, as mentioned above, there exist well-established solutions for the local diffusivities of, e.g., a single spherical tracer diffusing in a viscous continuum solvent while confined between two parallel walls, which are separated by a lengthscale on the order of several tracer diameters. But in this simple scenario, the tracer traverses a *flat* free-energy landscape between the walls. What happens when the ratio between the sizes of tracer and solvent is no longer infinite, and is instead small and finite (even order unity)? Like in the systems discussed above, heterogeneous static structuring of the solvent particles near the walls could perturb both the effective free-energy landscape and further complicate the dynamics of the tracer. It would be very instructive to know when and how predictions from hydrodynamic theory break down given increasingly "non-continuum" solvent baths, as this would spur the development of more generalized predictive frameworks for diffusive motions.

More conceptually, this question can be expressed: for dense fluids, what is the interplay between emergent static structure (i.e., perturbations in the tracer free-energy landscape) and local variations in diffusive dynamics? And from a "prediction" standpoint, how does the correlation between local diffusive mobility and, e.g., a local structural property like number density, depend on the character-

istic lengthscale or strength of structural inhomogeneity? Certainly for weak- or gentle-enough variations in fluid structure–e.g., very gradual gradients in number density–one might be able to approximately predict local particle dynamics by referencing the appropriate static-dynamic correlation for the bulk-fluid, but at what point does this type of simple local "mapping" break down?

Meanwhile, in thinking about local diffusive dynamics given various relative lengthscales between the tracer, surrounding solvent bath, and features in the free-energy landscape (as set by, e.g., pore size), it becomes relevant to consider the influence of the microscopic dynamics–whether "molecular" or "colloidal" in nature–that instantaneously govern particle motions. For bulk fluids, computer simulations have shown that the distinction can often be ignored when operating at relatively coarse-grained levels of physics. To wit, average *long-time* diffusion coefficients can be directly mapped between systems governed by either deterministic Newtonian dynamics (i.e., classic molecular dynamics) or by stochastic Brownian dynamics (i.e., overdamped Langevin, ignoring interparticle hydrodynamic coupling) based on master correlations that are robust for diverse interparticle potentials [99, 167]. In other words, for these systems, computationally-efficient Newtonian dynamics simulations are sufficient for characterizing the dynamics of (simplified) colloidal systems, even though the former ignore even the implicit effects of underlying solvent degrees of freedom [17,57,107,150]. But when tracer particles are moving along non-flat free-energy landscapes, how robust are these quasi-universal mappings for tracer diffusivity? Addressing this question can greatly aid in, e.g., the practical selection of a simulation protocol for modeling a

dense colloidal suspension influenced by an external field.

Finally, there are open questions about the diffusive dynamics of fluids that are both structurally inhomogeneous and supercooled. To wit, some of the first studies to characterize position-dependent diffusivity considered simple monodisperse fluids that are confined in thin channels [51, 149, 155]. Coincidentally, these studies respectively focused on sets of states that were *either* all in equilibrium or all decidedly glassy; in comparing the dynamics of the two types of systems, one reaches *opposing* conclusions about how emergent diffusivity profiles should locally correlate with emergent density profiles. Thus, it is pertinent to ask: is the correspondence between local diffusive dynamics and structure *qualitatively* sensitive to the emergence of cooperative rearrangements? And if so, can we still validate any frameworks for interpreting or predicting the diffusive dynamics of inhomogeneous fluids that are universal across equilibrium and glassy conditions?

Given that these lines of inquiry focus on foundational knowledge of the diffusive dynamics of inhomogeneous fluids, computer simulations are especially useful because they allow for precise *a priori* incorporation of interparticle and external interactions, and direct access to particle trajectories. Throughout Chapters 2-5, we choose to investigate hard-sphere fluids because they capture some of the essential shared physics of molecular fluids and colloidal suspensions: microscopic coordination structure, diffusive motions (when the bath is not very dilute), density layering near interfaces, etc. Meanwhile, many static quantities of interest, like the local available space, are unambiguously defined, and established tools like Fundamental Measure Theory [172, 174] can aid in designing external potentials

that impose desired density profiles.

We use these simulations to validate a technique [81, 187, 220] based on the Fokker-Planck formalism that uses MFPTs to measure position-dependent diffusion coefficients. This approach is straightforward to implement based on knowledge of particle trajectories, and our findings support its adoption for scrutinizing dynamics in simulations and experiments on diverse classes of inhomogeneous fluids. Applying this technique to our hard-sphere systems, we untangle how position-dependent and average diffusion coefficients relate to the free-energy landscapes that particles traverse, and examine how diffusive motions depend (or not) on static properties such as density, void space, available volume, etc. In this way, we test physical interpretations of diffusion coefficients and demonstrate the conditions under which diffusivities can be predicted on the basis of, e.g., hydrodynamic theory, static quantities, and thermodynamic properties.

1.2 Cluster phases in fluids with competing interactions

Strong competing interactions that act at different lengthscales generate heterogeneous micro- and mesoscopic morphologies in a wide array of materials [42, 72, 77, 93, 114, 179, 189, 232]. If the frustration (i.e., incompatibility) of the interactions is strong enough, these types of systems can minimize their free energies by transitioning from homogeneous phases with uniform density distribution to equilibrium states exhibiting heterogeneous density fluctuations at the microscopic scale. Such states are characterized as exhibiting "intermediate range order" (IRO), which reflects how corresponding static structure factors $S(k)$ show

pre-peaks positioned at low but non-zero wavenumber, i.e., between the $k = 0$ limit and the primary peak position commensurate with monomer-scale packing [27, 31, 40, 62, 63, 100, 125, 127, 164, 186, 227]. In turn, these microstructural transformations can impact the macroscopic properties of the materials (mechanical, optical, etc.) or have important device implications, such as exploiting block-copolymer self-segregation to facilitate electronic data storage at enhanced areal densities [11].

We focus on colloidal suspensions governed by short-range attractions and long-range repulsions that can be tuned to favor the formation of a class of IRO with significant recent interest: *equilibrium cluster phases*. These cluster phases comprise self-assembled aggregates of several to dozens of particle monomers, where aggregates are ideally dense fluid-like droplets that are highly monodisperse. This type of clustering behavior has been widely studied during the past decade via theoretical and computational treatments of idealized fluids [6, 28, 62, 63, 68, 91, 96, 136, 153, 182, 204, 209, 233]; experiments on archetypal colloids, such as microscopic PMMA spheres in density-matched organic solvents [32, 102, 131, 228, 231]; and–more intriguingly–experiments on nanoscopic monomers with heterogeneous surface chemistry and non-spherical shape, mainly proteins [64, 97, 127, 161, 168, 201, 229, 230],

In turn, the characterization and control of colloidal clustering has applications in–to pick examples from the medical field–non-invasive imaging and drug development. For instance, rationally exploiting environmental cues (such as pH) to reversibly assemble metallic nanoparticles into clusters would open up new

routes for targeted imaging of internal body-tissue [135]. Likewise, developing high-concentration suspensions of therapeutic proteins, such as monoclonal antibodies, are an important manufacturing target for treating autoimmune diseases and cancers via patient-administered injections [36, 192]. However, a major challenge is that protein-protein interactions can generate reversible mesoscale structures (i.e., clusters, networks) in solution that are associated with high viscosities, which compromise quality assurance and patient comfort [64, 117, 118, 229]. Thus, the goal in this context is to understand when and how cluster formation occurs so as to avoid it.

The basic "recipe" for microscopic cluster formation is considered well-established and universal across these different contexts. First, induce short-range attractions by, e.g., (a) either introducing neutral crowder molecules, such as polymers, to induce entropic depletion attractions between monomers, or (b) for monomers like proteins, allowing hydrophobic interactions (or complementary charge association) to similarly induce contact-bonding. Second, set competing repulsions by, e.g., modulating the solvent ionic strength to (un)screen Coulombic interactions between like-charge sites on the monomer surfaces. Altogether, as attractions are made stronger, they drive monomer association, while the longer-ranged repulsions collectively build up across growing aggregates to eventually self-limit growth at a thermodynamically-favored size. Thus, one generates cluster states resembling a microscopic "liquid-gas" separation (because clusters typically coexist with some interstitial monomer) while greatly suppressing or eliminating macroscopic phase separation that otherwise occurs given very dominant attrac-

tions.

However, despite the many previous studies and the general phenomenological recipe for clustering, many basic questions have remained about how to characterize the *in situ* microstructure of experimental systems where clusters might form, and whether the simplified physical recipe above can be turned into a predictive thermodynamic model for real particles.

First, an ongoing challenge has been to interpret structure factors $S(k)$ available from x-ray or neutron scattering experiments–the static information most accessible *in situ* across diverse monomer and aggregate lengthscales–in terms of tangible real-space characteristics of aggregate morphologies. To wit, it has been difficult even to positively identify cluster phases when they emerge because an IRO pre-peak feature in $S(k)$–which must *exist* if monodisperse aggregates have formed–can also point to, e.g., highly-amorphous morphologies, arrested gel phases, etc.; thus, an IRO pre-peak is a rather ambiguous signature absent empirical rules for interpretation. This has spurred attempts to develop practical criteria that pinpoint the onset of clustering, via, e.g., a threshold magnitude of the IRO pre-peak [62, 63, 127]. Likewise, given one is analyzing an $S(k)$ profile corresponding to a cluster phase, there remains considerable confusion in the literature as to what lengthscale(s) (e.g., cluster size, intercluster spacing) are reflected in the wavenumber position of the IRO pre-peak [62, 182, 193, 200, 201]. Developing such rules for $S(k)$ interpretation will allow for stronger experimental connections to be made between equilibrium microstructure, underlying monomer interactions, and, e.g., non-equilibrium properties like low-shear viscosity that are of interest

for applications.

Meanwhile, though clustering is often superficially explained by assuming that monomers interact via pair potentials resembling the the classic Derjaguin-Landau-Verwey-Overbeek (DLVO) model [46, 90, 214]–with its short-range (van der Waals) attractions and long-range electrostatic interactions–there has previously been no free-energy model shown to predict equilibrium cluster size given knowledge of monomer pair interactions, even for such idealized interactions. Certainly, a DLVO-type pair potential should capture the relevant physics for some real archetypal colloidal suspensions (though only accounting two-body interactions may be insufficient to predict phase behavior [159, 160]), but it is probably a very poor model for small nanoparticles and non-globular proteins [195]. To help clarify these issues, it would be very instructive to know how reference systems *exactly* governed by DLVO pair potentials (or similar) behave in terms of clustering. A long-established thermodynamic model for predicting cluster size is due to Groenewold and Kegel [68, 69, 231], which is both elegant and highly-cited; however, this model has not been systematically compared against cluster phases formed over wide ranges of relevant experimental variables, e.g., Debye screening length, monomer surface charge, etc. Of course, with a validated model in-hand, one could ascertain when and how real systems deviate from the reference DLVO-type predictions for clustering, and then incorporate new additional free-energy contributions.

For both of these lines of inquiry, computer simulations and integral equation theory represent *uniquely useful* tools for directly connecting short-range at-

tractive long-range repulsive interactions with microstructural clustering responses and their corresponding thermodynamics. In Chapters 6 and 7, we unambiguously fix idealized DLVO-type pair interactions between monomers. Given these potentials, we can tune interactions to generate cluster phases while simultaneously accessing both pair and multibody static correlations–invaluable for validating connections between k-space pair correlations and real-space dimensions of aggregates that can improve interpretation of scattering experiments. Likewise, we can readily measure characteristic cluster sizes as a function of potential parameters like short-range attraction strength, and analyze aggregate configurations in detail in order to test free-energy size-scaling arguments. In this way, we can validate a predictive model for idealized cluster formation that is suitable for comparison against experiments.

1.3 Chapter summaries

As discussed above, the chapters of this dissertation are informally divided into two groups: Chapters 2-5 are focused on understanding the diffusive dynamics of tracer particles within inhomogeneous fluids, and Chapters 6-7 are focused on investigating cluster phases that are formed by colloidal suspensions exhibiting multi-lengthscale competitive interactions. Below, we briefly summarize the focus and main findings of each chapter in order.

Chapter 2: Impact of solvent granularity and layering on tracer hydrodynamics in confinement

Classic hydrodynamic arguments establish that when a spherical tracer particle is suspended between parallel walls, tracer-wall coupling mediated by the solvent will cause the tracer to exhibit position-dependent diffusivity. We investigate how the diffusivity profiles of confined tracers are impacted by the diameter size-ratio of the tracer to solvent: starting from the classic limit of infinite size-ratio (i.e., continuum solvent), we consider size-ratios of four or less to examine how hydrodynamic predictions are disrupted for systems where the tracer and solvent are of similar scale.

We use computer simulations and a technique based on the Fokker-Planck (FP) formalism to calculate the diffusivity profiles of hard-sphere (HS) tracer particles in HS solvents, focusing on the dynamics perpendicular to the walls. Given wall separations of several tracer diameters, we first consider confinement between hard walls, where anisotropic structuring at the solvent lengthscale generates inhomogeneity in the tracer free-energy landscape and undermines hydrodynamic predictions locally. We then introduce confining planes that analogously restrict tracer and solvent center-accessibility while completely eliminating static anisotropy, revealing underlying position-dependent signatures in tracer diffusivity solely attributable to confinement. Finally, we briefly consider systems where only the one-body density is made uniform, while allowing for anisotropic two-body (and higher) static correlations. With or without suppressing static heterogeneity, we find that tracer diffusivity systematically deviates on a local basis from

hydrodynamic predictions at smaller size-ratios. However, hydrodynamic theory still approximately captures spatially-averaged dynamics across the pores even for very small tracer-solvent size-ratios over a wide range of solvent densities and wall separations.

Chapter 3: Structure, thermodynamics, and position-dependent diffusivity in fluids with sinusoidal density variations

We use molecular dynamics (MD) simulations and the same stochastic method based on the FP equation to explore the consequences of inhomogeneous density profiles on the thermodynamic and dynamic properties of the HS fluid. The impacts of the inhomogeneity lengthscale are systematically considered via the imposition of sinusoidal density profiles of various pre-defined wavelengths, which we fix via external fields derived from Fundamental Measure Theory. For long-wavelength density profiles, bulk-like relationships between local structure, thermodynamics, and diffusivity are observed as expected. However, a crossover in behavior occurs as a function of wavelength, with qualitatively different correlations between the local static and dynamic quantities emerging as density variations approach the scale of a particle diameter. Irrespective of the density variation wavelength, average diffusivities of HS fluids in the inhomogeneous and homogeneous directions are coupled and approximately correlate with the volume available for insertion of another particle.

Chapter 4: How local and average particle diffusivities of inhomogeneous fluids depend on microscopic dynamics

We use computer simulations and the FP framework to build upon the previous chapter and compare the diffusion coefficients of equilibrium HS fluids exhibiting identical inhomogeneous static structure and governed by either Brownian (i.e., overdamped Langevin) or Newtonian microscopic dynamics. As before, the physics of inhomogeneity is explored via the imposition of one-dimensional sinusoidal density profiles of different wavelengths and amplitudes. When imposed density variations are small in magnitude for distances on the scale of a particle diameter, bulk-like average correlations between local structure and mobility are observed. In contrast, when density variations are significant on that lengthscale, qualitatively different structure-mobility correlations emerge that are sensitive to the governing microscopic dynamics. Correspondingly, a previously proposed scaling between long-time diffusivities for bulk isotropic fluids of particles exhibiting Brownian versus Newtonian dynamics cannot be generalized to describe the position-dependent behaviors of strongly inhomogeneous fluids.

While average diffusivities in the inhomogeneous and homogeneous directions are coupled, their qualitative dependencies on inhomogeneity wavelength are sensitive to the details of the microscopic dynamics. Nonetheless, average diffusivities of the inhomogeneous fluids can be approximately predicted for either type of dynamics based on knowledge of bulk isotropic fluid behavior and how inhomogeneity modifies the distribution of available volume. Analogous predictions for average diffusivities of experimental, inhomogeneous colloidal dispersions (based on

known bulk behavior) suggest that they will exhibit qualitatively different trends than those predicted by models governed by overdamped Langevin dynamics that do not account for hydrodynamic interactions.

Chapter 5: Structure-mobility relationships of confined fluids undergoing supercooling

We examine the structural and dynamic properties of confined binary hard-sphere mixtures designed to mimic realizable colloidal thin films. Using simulations, governed by either Newtonian or overdamped Langevin dynamics, together with the FP-based method above, we measure the position-dependent and average diffusivities of particles along structurally isotropic and inhomogeneous dimensions of the fluids. At moderate packing fractions, local single-particle diffusivities normal to the direction of confinement are higher in regions of high total packing fraction; however, these trends are reversed as the film reaches denser average packings corresponding to the onset of supercooling. Auxiliary short-time measurements of particle displacements mirror data obtained for experimental supercooled colloidal systems. We find that average dynamics can be approximately predicted based on the distribution of available space for particle insertion across orders of magnitude in diffusivity regardless of the governing microscopic dynamics.

Chapter 6: Decoding the structure factor to detect and characterize clustering in fluids with competing interactions

We use liquid state theory and computer simulations to gain insights into the shape of the structure factor for fluids of particles interacting via a combination

of short-range attractions and long-range repulsions. Such systems can reversibly morph between homogeneous phases and states comprising compact self-limiting clusters. We first highlight trends with respect to the presence and location of the intermediate-range order (IRO) pre-peak in the structure factor, which is commonly associated with clustering, for wide ranges of the tunable parameters that control interparticle interactions (e.g., Debye screening length). Next, for approximately 100 different cluster phases at various conditions (where aggregates range in size from six to sixty monomers), we quantitatively relate the shape of the structure factor to physical characteristics including intercluster distance and cluster size. We also test two previously postulated criteria for identifying the emergence of clustered phases that are based on IRO peak-height and -width, respectively. We find that the criterion based on peak-width, which encodes the IRO thermal correlation length, is more robust across a wide range of conditions and interaction strengths but nonetheless approximate. Ultimately, we recommend a hybrid heuristic drawing on both pre-peak height and width for positively identifying the emergence of clustered states.

Chapter 7: Validating a free energy model for equilibrium cluster size in fluids with competing interactions

Building on the previous chapter, we validate a simple free energy model that can be analytically solved to predict the equilibrium size of the self-limiting clusters. The model is a semi-empirical adaptation and extension of the canonical free energy-based result due to Groenewold and Kegel [*J. Phys. Chem. B*, 105 (2001)], where we use our computer simulation data to systematically improve the

cluster-size scalings with respect to the strengths of the competing interactions driving aggregation. We find that one can adapt a classical nucleation like theory for small energetically-frustrated aggregates provided one appropriately accounts for a size-dependent, microscopic energy penalty of interface formation, which requires new scaling arguments. This framework is verified in part by considering the extensive scaling of intracluster bonding, where we uncover a superlinear scaling regime distinct from (and located between) the known regimes for small and large aggregates. We validate our model based on comparisons against approximately 100 different simulated systems comprising compact spherical aggregates with characteristic (terminal) sizes between six and sixty monomers, which correspond to wide ranges in experimentally-controllable parameters.

Chapter 2

Impact of solvent granularity and layering on tracer hydrodynamics in confinement

2.1 Introduction

There are diverse fluid contexts where tracer particles exhibit position-dependent diffusive dynamics when navigating confined spaces, and accurately characterizing such tracer motions is critical for engineering transport within inhomogeneous systems. For example, one may be interested in describing the transit of microscopic stabilized droplets or colloids within small device geometries [23, 198], the motions of nanoparticles near multiphase boundaries [152, 225] or water-soluble compounds through membranes [115, 158, 215], or the kinetics of diffusion-controlled reactions [205]–all cases where solvent-mediated interactions with any interfaces can cause tracer dynamics to deviate from those of the same

To be published in revised form as J.A. Bollinger, J. Carmer, A. Jain, T.M. Truskett, "Impact of solvent granularity and layering on tracer hydrodynamics in confinement." *Soft Matter*, 2016. J.A. Bollinger performed computer simulations, analyzed results, created figures, and wrote the manuscript.

tracer-solvent pairing in the bulk. The deviations from bulk dynamics may greatly differ between these cases because–besides disparate surface chemistries–there are vast differences in the *relative lengthscales* of the tracers and their respective solvents. For the micron-sized colloids, the size-ratios between the tracer diameters and that of typical suspending solvents (e.g., water) are effectively infinite–i.e., the solvents are of *continuum* scale. But for the latter examples, the tracer and solvent species are *comparable* in size; thus, effects like heterogeneous interfacial structuring of the solvent could non-trivially influence tracer motions [90]. Validating techniques that can probe particle diffusion [35,81,86,124,149] and physical frameworks that can predict the impacts of confinement [5, 20, 105, 110–112, 145]–especially across such disparate lengthscales–would provide powerful avenues for modelling and manipulating tracer mobility.

One of the best-studied systems where tracer diffusion is position-dependent is that of a single spherical particle moving in a viscous continuum solvent while confined between two parallel walls, which are separated by a lengthscale on the order of several tracer diameters. A number of exact and approximate approaches have been used to predict the local drag forces on the sphere as it moves either parallel or perpendicular to the boundaries, where boundary-constraints on solvent flow generate hydrodynamic coupling between the moving particle and the fixed walls [18,58,75,82,123,199,203]. This hydrodynamic coupling results in local tracer diffusion coefficients that are suppressed compared to the bulk (i.e., unconfined) tracer diffusion coefficient and that monotonically decrease with proximity to either surface. In turn, these hydrodynamic predictions are borne out by experiments on

dilute colloidal suspensions [47, 54, 109, 119, 128].

Our main goal in this chapter is to investigate how these well-established hydrodynamic predictions of local tracer diffusivities–which assume that the tracer-solvent size-ratio is infinite–break down (if at all) for a given wall separation as the tracer-solvent size-ratio becomes small yet finite. For instance, the continuum solvent in the reference case is inherently structureless, with perfectly homogeneous physical properties. Combined with the assumption that the tracer is perfectly isolated, this means that the tracer diffuses along a *flat* equilibrium free-energy landscape (i.e., experiences a uniform potential of mean force) across the center-accessible region of the pore and exhibits no preferential positioning. However, this distinct scenario for the free-energy landscape is inappropriate for common classes of systems. As alluded to in the opening paragraph, for a small aqueous nanoparticle (e.g., diameter $d \approx 10$Å) not much larger than water ($d \approx 3$Å), anisotropic static correlations amongst water molecules near a confining interface would generate an inhomogeneous tracer free-energy landscape and likely impact tracer mobility. Likewise, in highly-concentrated thin-films of monodisperse microscopic colloids, a chosen "tracer" would diffuse through a "solvent" composed of its comparably-sized colloidal neighbors. (In other words, the main obstacle for particle transport would be rearrangement of the suspended particles themselves, while hydrodynamic interactions due to the underlying continuum solvent would be well-screened [141, 142].) that exhibit tracer-scale signatures of inhomogeneous structure and dynamics [149, 155, 156]. And by considering size-ratios less than unity, where the tracer of interest is smaller than surrounding solvent, one

can make connections with binary "host-intruder" mixtures that mimic crowded biological environments [70, 188].

With this goal in mind, we use computer simulations and techniques based on the Fokker-Planck (FP) formalism to rigorously measure position-dependent (and spatially-averaged) diffusion coefficients for confined tracers in dense solvents, where we focus our analysis on the following questions: (1) What distinctive static and dynamic signatures emerge in the free-energy and diffusivity profiles of a confined tracer as the tracer-solvent size-ratio decreases (i.e., as the solvent becomes "non-continuum")? (2) What are the ranges of size-ratios, solvent densities, and wall separations where hydrodynamic theory reasonably predicts local and/or spatially-averaged diffusion coefficients? And (3) more fundamentally, can any local signatures that emerge in the diffusivity profiles at finite size-ratios be predicted based on features in the free-energy landscapes?

To address these questions, we first conduct single-particle simulations that recreate the reference case of slit-pore confinement (i.e., with continuum solvent), and next conduct molecular dynamics (MD) simulations of single hard-sphere (HS) tracers situated in highly-dense HS solvents between hard walls (see Fig. 2.2). In this way, we can capture confinement effects in systems with similar physics as the classic case (i.e., "simple" interactivity) while isolating the impact of finite tracer-solvent size-ratios. Throughout, we focus on the free-energy landscapes and diffusivity profiles of the tracers perpendicular to the confining walls. First, we use the continuum case to briefly review hydrodynamic effects and to verify that the FP framework self-consistently captures local diffusion constants solely from

simulated particle trajectories. Then, for the systems with non-continuum solvent, we show how distinctive local oscillations in the diffusivity (and free-energy) profiles consistently emerge at the solvent lengthscale, where these oscillations increasingly deviate from hydrodynamic predictions with decreasing tracer-solvent size-ratio. Interestingly, we find that local correlations between free-energy and diffusivity can qualitatively change depending on tracer-solvent size-ratio. This suggests that local dynamics are not dependent on local structure in any straightforward way–a line of inquiry that we expand upon in subsequent chapters.

To explore this latter finding, we next examine HS tracer-solvent combinations that are bounded by "transparent" walls (see Fig. 2.2), which are designed to restrict center-accessibility just like hard walls while eliminating anisotropic structural correlations between solvent particles that would otherwise emerge due to confinement. Using this framework, we reveal generic *anisotropic* signatures in the tracer diffusivity profiles that emerge at the solvent-scale–even though solvent structure is *isotropic* and identical to the bulk fluid, and the tracer free-energy landscape is correspondingly flat. In this way, we effectively consider systems with non-continuum solvent that–compared to hard-wall systems–better correspond to the structureless background solvent inherent to the continuum case. This correspondence is confirmed by improved quantitative agreement between local dynamic measurements and hydrodynamic predictions.

Finally, using our measurements of local free-energies and diffusion coefficients, we calculate *spatially-averaged* diffusion constants and corresponding first-passage times across the slit-pores, where we find that hydrodynamic predictions

are reasonably accurate even for small tracer-solvent size-ratios and very strong confinement, especially in the presence of transparent walls. In particular, we examine monodisperse HS systems confined between hard walls at a variety of wall separations and average packing fractions, where we find that the theory is accurate within 20% for average diffusion coefficients even given only moderately dense solvent (e.g., $\phi_{\mathrm{s}} = 0.20$) and channel sizes as small as four tracer-diameters across ($H/\sigma_{\mathrm{t}} = 4$). Given the simulations are governed by Newtonian mechanics, these results suggest that hydrodynamic theories may be useful for modelling the dynamics of tracers comparable in size to small molecular solvents.

2.2 Methods

2.2.1 Diffusion models for particle motions

For fluids, diffusion is a conceptual framework meant to describe the motions of a tracer particle or molecule on timescales much larger than those associated with randomized collisions from other particles (solvent) that serve to dissipate its momentum. Inasmuch as diffusion is a good description of the physics underlying the tracer dynamics, diffusion coefficients are parameters that allow one to quantitatively reconstruct or predict the spatiotemporal probability distribution of its location. In this way, diffusion coefficients are a basis for comparing particle mobilities or, equivalently, relaxation rates between materials governed by diverse interparticle interactions (e.g., shapes of pair potentials), geometries (e.g., presence of interfaces), and thermodynamic conditions (e.g., densities). Given this chapter (and the following chapters) are largely concerned with *position-dependent* diffu-

sion coefficients for confined fluids–relatively non-trivial quantities to consider– we begin by providing some context with respect to the various diffusion models adopted for fluid systems, both isotropic and inhomogeneous, with an emphasis on providing clear concise descriptions of the assumptions underlying different models.

One generally encounters diffusion coefficients in the context of the "standard" drift-diffusion equation, which models the probability distribution $p(z,t)$ of observing the particle at position z and time t as it moves in response to a conservative applied field (drift) and random collisions (diffusion). A key simplifying assumption is that resistance to diffusion is *spatially-invariant*. In the absence of sources or sinks for the particle, this model can be expressed via

$$\frac{\partial p(z,t)}{\partial t} = -\frac{\partial j_{\text{drift}}(z,t)}{\partial z} - \frac{\partial j_{\text{diff}}(z,t)}{\partial z} \tag{2.1}$$

or, alternatively, via

$$\frac{\partial p(z,t)}{\partial t} = -\zeta_{\text{z}}^{-1}\frac{\partial [F(z)p(z,t)]}{\partial z} + D_{\text{z}}\frac{\partial^2 p(z,t)}{\partial z^2} \tag{2.2}$$

where, here and below, it is implied that $p(z,t)$ is subject to an initial probability distribution at $t = 0$, i.e., $p(z,t) \equiv p(z, \Delta t | z_0, 0)$, where Δt is the lag-time and $p(z_0, 0)$ is the initial condition. The first term on the right side in Eqn. 2.2 expresses the probability flux $j_{\text{drift}}(z)$ due to drift (or convection): this is a function of (1) the drag coefficient ζ_{z} that relates the viscous dissipative force $F_{\text{z}}^{\text{drag}}(z) = \zeta_{\text{z}} v_{\text{z}}(z)$ to the particle velocity $v_{\text{z}}(z)$ in the z-direction; and (2) the conservative force $F(z) = -\beta dU(z)/dz$, which is due to an arbitrary free-energy landscape $U(z)$ normalized

by $\beta = (k_{\mathrm{B}}T)^{-1}$ (where k_{B} is Boltzmann's constant and T is temperature). The second term on the right side in Eqn. 2.2 captures the flux due to diffusion, which–because the diffusion rate in the z-direction is assumed homogeneous–corresponds to Fick's law $j_{\mathrm{diff}}(z) = -D_{\mathrm{z}}\partial p(z,t)/\partial z$ as parameterized by the isotropic diffusion coefficient D_{z}.

By considering the steady-state (i.e., $\partial p(z,t)/\partial t = 0$) limit of Eqn. 2.2, where $p(z) \propto \exp\{-\beta U(z)\}$ according to the Boltzmann distribution, one can readily derive the well-known Einstein relation

$$D_{\mathrm{z}} = \zeta_{\mathrm{z}}^{-1} k_{\mathrm{B}} T \tag{2.3}$$

that, subject to the assumptions above, connects particle diffusion and viscous drag effects. In turn, for particles suspended in viscous continuum solvents, Eqn. 2.3 is subsequently combined with the Stokes expression for the drag coefficient ζ_{z} to give the Stokes-Einstein equation

$$D_{\mathrm{z}} = k_{\mathrm{B}} T/(f\pi\eta_{\mathrm{s}} R) \tag{2.4}$$

where f encodes the particle-solvent boundary condition ($f = 4$ for slip, $f = 6$ for stick), η_{s} is the viscosity of the bulk solvent (without tracer), and R is the radius of the particle. (Note that mass does not play a role as viscous forces are assumed to vastly dominate momentum.)

By far, the most popular method for measuring D_{z} is via mean-squared displacements Δz^2 of the particle of interest over sufficiently long lag-times Δt,

which can be fit to what is also called the Einstein relation:

$$D_z = \langle \Delta z^2 \rangle / (2\Delta t) \tag{2.5}$$

Given its familiarity, what might be commonly overlooked is that Eqn. 2.5 is based on a diffusion model that, compared to Eqn. 2.2, is *more restrictive* because it lacks a drift term:

$$\partial p(z,t)/\partial t = D_z \partial^2 p(z,t)/\partial z^2 \tag{2.6}$$

In other words, Eqn. 2.5 is only a valid method for measuring D_z from trajectory data when: (1) there is no position-dependent conservative force acting on the tracer particle (i.e., there is a flat free-energy landscape); and (2) it is reasonable to assume that diffusive resistance is spatially-invariant.

For the confined systems of interest here, the assumptions underlying the very common Eqns. 2.2-2.5 are inappropriate. For instance, the rate of diffusion will generally be position-dependent due to how the strength of hydrodynamic interactions vary with distance to the wall(s). Meanwhile, the free-energy landscape can be arbitrarily non-flat if the solvent particles are comparable in scale to the tracer and exhibit strong inhomogeneous structuring near the walls. Thus, we must begin with a *generalized* drift-diffusion equation, the Fokker-Planck (or Smoluchowski) equation:

$$\frac{\partial p(z,t)}{\partial t} = -\frac{\partial [\zeta_z^{-1}(z) F(z) p(z,t)]}{\partial z} + \frac{\partial^2 [D_z(z) p(z,t)]}{\partial z^2} \tag{2.7}$$

Compared to the framework of Eqn. 2.2, here one allows for the possibility that particle motions may best be described by position-dependent diffusivity and free-energy profiles, though these profiles can ultimately be uniform. Note that Eqn. 2.7 incorporates a flux term of the form $j_{\text{diff}}(z) = -\partial[D_{\text{z}}(z)p(z,t)]/\partial z$, appropriate for many (but not necessarily all) physical scenarios where diffusive resistance is inhomogeneous [55, 180]. In turn, Eqn. 2.7 can be rewritten in the common form

$$\frac{\partial p(z,t)}{\partial t} = \frac{\partial}{\partial z}\left(D_{\text{z}}(z) e^{-\beta U(z)} \frac{\partial}{\partial z}[e^{\beta U(z)} p(z,t)] \right) \tag{2.8}$$

which explicitly casts the temporal evolution of the Markovian propagator $p(z,t)$ solely in terms of the static free-energy landscape $U(z)$ and the local diffusion coefficients $D_{\text{z}}(z)$. Eqn. 2.8 has been shown to self-consistently capture tracer motions in dense inhomogeneous fluids exhibiting position-dependent dynamics [149].

Given the generalized framework of Eqn. 2.8, one can obtain diffusivities $D_{\text{z}}(z)$ via methods analogous to those above: (1) theoretical expressions meant to predict tracer motions and (2) techniques for directly measuring $D_{\text{z}}(z)$ profiles based on trajectory data. For example, in the reference case of an isolated tracer that is suspended in a continuum solvent and proximal to confining walls, it is customary to estimate diffusivities based on a localized version of Eqn. 2.4:

$$D_{\text{z}}(z) = k_{\text{B}}T/(f\pi\eta_{\text{s}}R\lambda_{\text{z}}(z)) \tag{2.9}$$

Here, $\lambda_{\text{z}}(z)$ is a profile of prefactors that correct for how hydrodynamic tracer-wall interactions will modulate the bulk isotropic tracer-solvent diffusion coefficient D_{z}.

As discussed in Section 2.1, a long-standing goal has been to develop and validate expressions that describe this modulation [18,58,75,82,123,199,203], and we make use of such expressions in .

Of course, a main aim of this chapter is to compare these hydrodynamic results with direct measurements of $D_{\mathrm{z}}(z)$, which we accomplish using a mean-first passage times (MFPT) treatment [81, 187, 220] of Eqn. 2.8 where the only inputs are tracer trajectories measured from simulations or experiments (the latter via, e.g., confocal imaging [41,218]). This treatment is one of several recently-developed frameworks that extract equivalent local diffusion coefficients [33,86,124,147,149], which we choose based on its accessibility (especially for confined systems). Briefly, this MFPT method recasts the steady-state (i.e., $\partial p(z,t)/\partial t = 0$) limit of Eqn. 2.8 as

$$D_{\mathrm{z}}(z) = -\frac{e^{\beta U(z)}}{\partial \tau(z, z_a)/\partial z} \int_{z_r}^{z} e^{-\beta U(z')} \mathrm{d}z' \tag{2.10}$$

which is valid provided the tracer motions are confined by a reflective boundary at z_r and an absorbing boundary at z_a. In turn, $\tau(z, z_a)$ is the tracer MFPT from a starting location $z_r \leq z < z_a$ at $t = t_0$ to the absorbing boundary $z = z_a$ at $t = t_0 + \tau(z, z_a)$ (assuming motion in the positive-z direction is of interest). Any absorbing boundary is "virtual" in the sense that particles do not truly need to disappear; rather, it is simply a target location where the tracking is completed. Meanwhile, the equilibrium free-energy landscape is given by

$$\beta U(z) = -\ln\{\rho(z)\} + C \tag{2.11}$$

where $\rho(z)$ is the readily-measured local density and C is an arbitrary constant. This profile encodes the potential of mean force on the tracer due to all other particles, walls, etc.

2.2.2 Single-particle tracer simulations

To validate the MFPT approach, we conduct several single-particle one-dimensional (1D) simulations that are evolved according to pre-defined $U_{\mathrm{t}}(z)$ and $D_{\mathrm{t,z}}(z)$ profiles *for the tracer*, which allow us to directly test whether we can accurately reconstruct the *a priori* free energies and diffusivities given access solely to particle trajectories. In Section 2.3.1, we use this single-particle setup to investigate the reference hydrodynamic problem where a single tracer is suspended in continuum solvent between two walls; in this section, however, we first conduct tests with some complementary systems subject to various combinations of flat and position-dependent $U_{\mathrm{t}}(z)$ and $D_{\mathrm{t,z}}(z)$ profiles.

For these simulations, we advance the tracer position $z_{\mathrm{t}}(t)$ with time-step $\delta t = 0.001$ according to the generalized equation for Brownian diffusive motion that allows us to directly enforce the profiles [2, 52, 86]:

$$z_{\rm t}(t+\delta t) = z_{\rm t}(t) + \left\{ \frac{{\rm d}D_{\rm t,z}[z_{\rm t}(t)]}{{\rm d}z} - D_{\rm t,z}[z_{\rm t}(t)] \frac{\beta {\rm d}U_{\rm t}[z_{\rm t}(t)]}{{\rm d}z} \right\} \delta t + r^{\rm G} \sqrt{2D_{\rm t,z}[z_{\rm t}(t)]\delta t} \tag{2.12}$$

where $r^{\rm G}$ is a Gaussian noise variable with $\langle r^{\rm G} \rangle = 0$ and variance $\sigma^2 = 1$. Subsequently, we can measure the density profile of the tracer to independently calculate $U_{\rm t}(z)$ and, combined with measurements of MFPTs $\tau(z, z_a)$, use Eqn. 2.10 to obtain $D_{\rm t,z}(z)$.

In implementing Eqn. 2.10 for both single-particle systems (and below in MD simulations), we check for crossing events at time increments of $\delta\tau_{\rm MFPT} = 0.05$, where we simultaneously implement several "absorbing" planes with positions z_a relative to a given reflective boundary z_r (leftward or rightward). Thus, we obtain several $\tau(z, z_r)$ profiles that all range from the same reflective (i.e., confining) plane at z_r to each $z_{\rm a}$. These redundant profiles provide checks on the subsequent $\partial\tau(z, z_a)/\partial z$ profiles, which we calculate via linear fits of $\tau(z, z_a)$ about z over small δz ranges. These ranges are $\delta z = (n_{\rm fit})(\Delta z)$, where the spatial-resolution is $\Delta z = 0.02$ and $n_{\rm fit}$ is the number of discrete Δz bins in the fit. We choose $n_{\rm fit} = 11$ as it smooths out statistical noise while retaining relevant particle-scale features in $D_{\rm t,z}(z)$. Note that we discard the derivatives within $\Delta z = 0.30$ of (i.e., closest to) absorbing boundaries because these regions can display non-Markovian artifacts [187, 215].

Common to all of these single-particle simulations is that the tracer particle is confined to some non-periodic range of z-values by two steeply repulsive poten-

tials that define a system of size H. These potentials resemble hard flat walls and are given by a highly-powered Week-Chandler-Andersen (WCA) potential [37]

$$\varphi(z) = \begin{cases} 4\epsilon\left[\left(\dfrac{\sigma_{\mathrm{t}}}{z}\right)^{48} - \left(\dfrac{\sigma_{\mathrm{t}}}{z}\right)^{24}\right] + \epsilon & \text{if } z \leq 2^{1/24}\sigma_{\mathrm{t}} \\ 0 & \text{otherwise} \end{cases} \tag{2.13}$$

where $\epsilon = k_{\mathrm{B}}T$ is the characteristic energy scale; σ_{t} is the characteristic lengthscale of the tracer (in these simulations, taken as unity); and z is the tracer distance from the reference position of the nearest confining boundary. For a system of size H, the reference boundary positions are $\pm(H + \sigma_{\mathrm{t}})/2$, meaning that the center-accessible region for the tracer is $-(H - \sigma_{\mathrm{t}})/2 \leq z_{\mathrm{t}} \leq +(H - \sigma_{\mathrm{t}})/2$. These accessibility limits correspond to the *reflective* boundaries of two separate MFPT analyses–one for each direction of particle motion. Then, *absorbing* boundaries are placed in the respective opposing halves of the center-accessible region to provide redundant coverage around $z \approx 0$.

Ahead of the results in Section 2.3.1, here we apply the MFPT analysis to single-particle trajectories propagated according to combinations of: (1) non-flat symmetric $U_{\mathrm{t}}(z)$ and flat $D_{\mathrm{t,z}}(z)$; (2) and (3) non-flat symmetric $U_{\mathrm{t}}(z)$ and non-flat asymmetric $D_{\mathrm{t,z}}(z)$ for different scales of variations in $D_{\mathrm{t,z}}(z)$. Of course, one could consider myriad functional forms for $U_{\mathrm{t}}(z)$ and $D_{\mathrm{t,z}}(z)$; however, our intent is not to exhaustively test all combinations, but simply demonstrate that the MFPT method is sufficient to analyze several types of systems. The $U_{\mathrm{t}}(z)$ fields are linear superimpositions of the functional forms given in Fig. 2.7 and

wall potentials (Eqn. 2.13) in the z-direction. Note that for the cases governed by asymmetric $D_{\mathrm{t,z}}(z)$ fields, we collect separate MFPT statistics for motions away from each wall. Though this is not strictly necessary, it does demonstrate that the measurements overlap around $z \approx 0$.

As shown in Fig. 2.7, the MFPT analysis nicely reproduces the *a priori* defined fields despite drawing only on knowledge of temporal particle positions. It is worth noting that this method of measuring the $D_{\mathrm{t,z}}(z)$ field is advantageous compared to using Bayesian inference methods [86, 149] that simultaneously optimize for $U_{\mathrm{t}}(z)$ and $D_{\mathrm{t,z}}(z)$ profiles: this is because the MFPT-based analysis leverages the straightforward relation $\beta U_{\mathrm{t}}(z) = -\ln\{\rho_{\mathrm{t}}(z)\} + C$ prior to calculation of $D_{\mathrm{t,z}}(z)$. The MFPT method used here also provides equivalent results compared to a recently-developed "color-diffusion" approach [35].

2.2.3 Simulations with non-continuum solvent

2.2.3.1 Confinement between hard walls

The majority of cases that we analyze are three-dimensional (3D) systems comprising single HS tracers that are confined to slit-pores and are situated in dense baths of HS solvent particles, where the size-ratios between the diameters of the tracers and solvents are small yet finite. As illustrated in Fig. 2.2, these pores are periodic in the x- and y-directions and bounded in the z-direction by either (1) prototypical hard walls that induce inhomogeneous fluid structuring or (2) so-called "transparent" walls (defined below) that restrict center-accessibility while preserving isotropic fluid structure across the pore. The first defining feature of

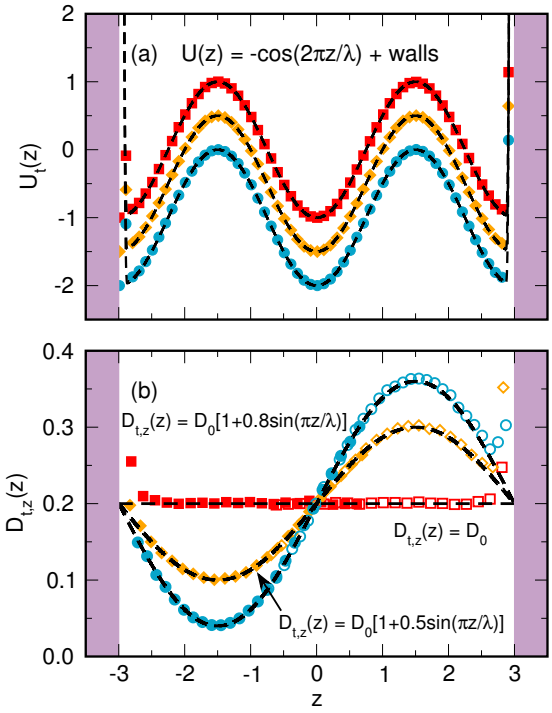

Figure 2.1: (a) Free energy landscapes $U_{\mathrm{t}}(z)$ and (b) diffusivity profiles $D_{\mathrm{t,z}}(z)$ for single-particle simulations (see Section 2.2.2). Solid black lines and corresponding equations are the fields used to encode the simulations, where $\lambda = 3$ and $D_0 = 0.2$ for all cases. Symbols are results obtained by applying the MFPT-based analysis to the trajectory data. In panel (a), note that $U_{\mathrm{t}}(z)$ profiles are vertically shifted for clarity and the bounding walls are as described in Section 2.2.2. In (b), filled and unfilled symbols correspond to measurements referenced against the left and right walls, respectively. The case represented by yellow diamond symbols is comparable to a previous test conducted with Bayesian-inference methods [86].

each system is the size-ratio $\sigma_{\mathrm{t}}/\sigma_{\mathrm{s}}$ between the diameters of the tracer and the many solvent particles, where we note that $\sigma_{\mathrm{t}}/\sigma_{\mathrm{s}} \equiv 1$ corresponds to a *monodisperse* HS fluid. The second defining feature of each system is the pore size H, which we always report relative to the tracer diameter σ_{t}. The last defining feature is the average packing fraction ϕ_{s} of the monodisperse HS solvent, which is associated with the reference bulk viscosity η_{s}.

To generate particle trajectories, we conduct molecular dynamics (MD) simulations using LAMMPS [165], where we integrate the Newtonian equations of motion with a time step of $\delta t = 0.001$ while fixing temperature with a Nose-Hoover thermostat. The tracer-solvent and solvent-solvent HS potentials between two particles of types i and j (either t for tracer or s for solvent) are given by the WCA potential

$$\varphi_{i,j}(r) = \begin{cases} 4\epsilon\left[\left(\dfrac{\sigma_{\mathrm{s}}}{r+\Delta_\sigma}\right)^{48} - \left(\dfrac{\sigma_{\mathrm{s}}}{r+\Delta_\sigma}\right)^{24}\right] + \epsilon & \text{if } r \leq 2^{1/24}\sigma_{\mathrm{s}} - \Delta_\sigma \\ 0 & \text{otherwise} \end{cases} \tag{2.14}$$

where $\epsilon = k_{\mathrm{B}}T$ is the characteristic energy scale (as above); r is the interparticle separation; σ denotes particle diameter; and $\Delta_\sigma = \sigma_{\mathrm{s}} - (1/2)(\sigma_i + \sigma_j)$. Across all systems with finite $\sigma_{\mathrm{t}}/\sigma_{\mathrm{s}}$, the solvent diameter σ_{s} is fixed as the characteristic lengthscale (unity), and we effectively modulate σ_{t} and H to examine different levels of solvent granularity and strengths of confinement. Note that in order to avoid problematic finite-size effects (e.g., solvent counter-flow issues) that become relevant for large $\sigma_{\mathrm{t}}/\sigma_{\mathrm{s}}$ ratios, we follow previous work on unconfined tracer-solvent

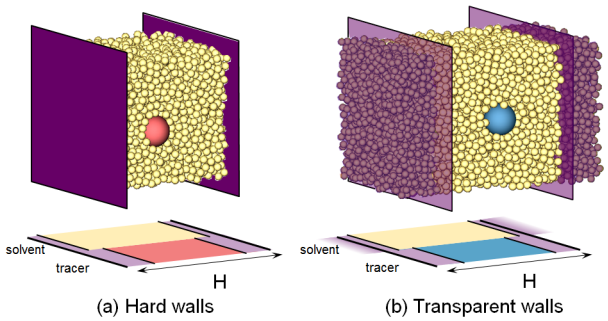

Figure 2.2: (a) Canonical simulation setup for a tracer-solvent system in a slit pore, where a single HS tracer (red) of diameter $\sigma_{\rm t}$ is situated in HS solvent (yellow) of diameter $\sigma_{\rm s}$ confined in the z-direction between two smooth, parallel hard walls. For a channel width of H, the center-accessible widths for tracer and solvent are $H - \sigma_{\rm t}$ and $H - \sigma_{\rm s}$, respectively; these are illustrated in the lower diagram by thin black lines, with center-accessible z-regions shaded red and yellow (for tracer and solvent, respectively) and inaccessible z-regions shaded light purple. (b) Confinement setup with "transparent" walls designed to eliminate anisotropic solvent structural correlations that normally emerge due to confinement. These walls constrain the positions of the tracer (blue) and solvent (yellow) while allowing them to interact via excluded volume with an outer reservoir of reciprocally-constrained solvent (purple). Center-accessible widths for the confined tracer and solvent are still $H - \sigma_{\rm t}$ and $H - \sigma_{\rm s}$, which are illustrated in the lower diagram by thin black lines, with center-accessible z-regions shaded blue and yellow (for tracer and solvent, respectively) and inaccessible z-regions shaded light purple.

systems and universally define the tracer mass as equal to the solvent mass [197].

For hard-wall systems of size H, the wall-particle interactions are identical in shape to the tracer-solvent and solvent-solvent 48-24 WCA interactions above, but defined such that the center-accessible z-region for particle i (either tracer or solvent) is $-(H - \sigma_i)/2 \leq z \leq +(H - \sigma_i)/2$, as illustrated in Fig. 2.2(a). We define the solvent packing fraction $\phi_{\rm s}$ based on the total (surface- rather than

center-accessible) volume of the slit-pore accessible to the solvent, where we correct for the losses (or gains) in solvent-accessible volume associated with growing or shrinking of a single particle to the desired tracer size [197]. For the systems with the densest solvent (e.g., $\phi_s \geq 0.42$) and smallest pore sizes (e.g., $H/\sigma_t \leq 5$), we generally consider systems with $N_{box} = 4800$ particles, with one of these particles being the tracer. However, for monodisperse systems at less dense conditions (e.g., $\phi_s \leq 0.30$), this burden is reduced down to $N_{box} = 2400$.

2.2.3.2 Confinement between transparent walls

The transparent wall systems are designed to restrict tracer and solvent motions while eliminating anisotropic equilibrium static correlations between solvent particles, such as pronounced local density variations, that typically result from conventional hard walls. As shown in Fig. 2.2(b), we accomplish this by introducing flat planes that restrict center-accessible regions for the tracer and solvent like in hard-wall systems, but where "in-pore" particles are allowed to interact with "out-of-pore" reservoirs of solvent particles that act as perfectly fluid walls. In turn, the confined tracer and solvent particles exhibit completely flat free-energy landscapes, and the structure of the solvent within (and outside) the pore region is *isotropic* and *identical* to the bulk fluid at the same ϕ_s because the infinitely-thin transparent walls do not exclude any volume in the system. This setup bears close resemblance to the framework of Scheidler et. al. [177], one of a number of studies probing the glass transition in the absence of structural inhomogeneity–though most work in this area considers *frozen* walls of disordered solvent [103, 178, 217].

As in the hard-wall cases, the transparent-wall potentials for the tracer and the in-pore solvent are defined such that the center of particle i (either tracer or solvent) can access $-(H-\sigma_i)/2 \leq z \leq +(H-\sigma_i)/2$. However, at the center-accessible limits (i.e., $\pm(H-\sigma_{\rm s})/2$) for the inner solvent, we introduce oppositely-facing potentials that reciprocally restrict the center-accessibility of the outer solvent while allowing excluded-volume contact between particles on either side of the dividing plane.[2] Practically-speaking, the systems are periodic in the z-direction such that the same outer reservoir of solvent makes contact with both transparent walls, which reduces the computational burden. We set the center-accessible width of the outer reservoir of solvent as $\Delta z_{\rm outer} = 12\sigma_{\rm s}$, which even at the highest solvent densities is sufficient for dynamic effects near either of the confining planes to decay, especially given the lack of anisotropic structuring.

Altogether, the total length of a given simulation box in the z-direction is the solvent center-accessible width of the inner pore of interest plus this outer reservoir region, i.e., $L_{\rm z} = [(H/\sigma_{\rm t})(\sigma_{\rm t}/\sigma_{\rm s})-1]\sigma_{\rm s}+12\sigma_{\rm s}$. We set the complementary dimensions $L_{\rm xy}$ based on $N_{\rm box}$ and $\phi_{\rm s}$, accounting for the growing (or shrinking) of a single particle to the desired tracer size. For the systems with the densest solvent (e.g., $\phi_{\rm s} \geq 0.42$) and smallest pore sizes (e.g., $H/\sigma_{\rm t} \leq 5$), we generally consider systems with $N_{\rm box} = 9000$ particles (one being the tracer). To prepare systems, we first equilibrate tracer-solvent mixtures where only the tracer is confined and

[2]Thus, for an inner-solvent limit located at $+(H-\sigma_{\rm s})/2$, there is one leftward-facing WCA potential (with $\Delta_\sigma = 0$) with the reference position $+(H+\sigma_{\rm s})/2$ to confine the inner solvent, and an analogous rightward-facing potential with the reference position $+(H-\sigma_{\rm s}-\delta_{\rm w})/2$, where $\delta_{\rm w} \approx 0.02$ is a minor adjustment parameter that we empirically found best suppresses fluid-structuring given the continuous nature of the particle and boundary potentials.

measure the *de facto* populations of inner and outer solvent particles (relative to the future locations of the transparent walls) over short production runs. We then introduce the solvent boundaries into frames exhibiting these average populations, which are used as initial configurations for full-scale production runs.

For both hard- and transparent-wall systems, the MFPTs that are used to calculate the tracer diffusion coefficients $D_{\mathrm{t,z}}(z)$ are averaged from dozens of independently initialized trajectories. For the monodisperse ($\sigma_{\mathrm{t}}/\sigma_{\mathrm{s}} = 1$) cases, we treat all particles in the pores as tracers and average their dynamics. Across all tracer-solvent systems, we check for crossing events every $\delta t_{\mathrm{MFPT}} = 0.05$ and calculate $U_{\mathrm{t}}(z)$ and $D_{\mathrm{t,z}}(z)$ with a resolution of $\Delta z = 0.02\sigma_{\mathrm{s}}$, which is crucial as we find diffusivity profiles generally show features at the solvent scale. Finally, note that in Section 2.3.2.3, we also consider select systems confined by prototypical hard walls that are supplemented by auxiliary z-dependent potentials inversely-designed to eliminate emergent one-body density fluctuations *only*, as opposed to one- and higher-order correlations.

2.3 Results & Discussion

2.3.1 Confined tracer hydrodynamics in continuum solvent

We begin our discussion by considering the classic hydrodynamic problem of particle confinement described in Section 2.1: a single isolated tracer particle sit-

uated in a viscous continuum solvent and diffusing between two parallel walls. By focusing on this physical setup, we can orient ourselves with respect to how strong confinement impacts the free energy landscape $U_{\mathrm{t}}(z)$ and the position-dependent diffusion coefficients $D_{\mathrm{t,z}}(z)$ of the tracer particle perpendicular to the boundaries in the limit where the tracer diameter is so large compared to solvent diameter that the size-ratio $\sigma_{\mathrm{t}}/\sigma_{\mathrm{s}}$ is infinite. As discussed above, this scenario has been of interest for quite some time, but is worth reviewing here to provide a point of reference before considering tracer dynamics in non-continuum solvents, and to validate that the MFPT-based approach for measuring $D_{\mathrm{t,z}}(z)$ from tracer trajectories accurately captures known results.

As shown in Fig. 2.3, the basic features of the reference case are: (1) a flat free-energy profile, which reflects the lack of tracer-wall interactions and heterogeneous solvent structuring that could enthalpically or entropically bias tracer positioning; and (2) a diffusivity profile that captures how hydrodynamic interactions slow down tracer motion near the walls and suppress dynamics on average relative to the same tracer-solvent pairing in the absence of confinement. Specifically, we plot $U_{\mathrm{t}}(z)$ and $D_{\mathrm{t,z}}(z)$ profiles for a tracer of unity diameter $\sigma_{\mathrm{t}} = 2R = 1$ (as there is no finite solvent scale) suspended in a *very dense* HS solvent that is idealized as a true continuum. To this end, we set the non-dimensionalized viscosity as $\eta_{\mathrm{s}} = 2.09$, which is the zero-shear viscosity of the HS fluid at $\phi_{\mathrm{s}} = 0.42$, [71] and choose slip boundary conditions $f = 4$ between the tracer and solvent, known to be appropriate for HS interactions [197]. The corresponding bulk diffusion coefficient of the tracer is $D_{\mathrm{t}}^{\mathrm{blk}} = 0.076$ via Eqn. 2.3, which in this context returns the self-

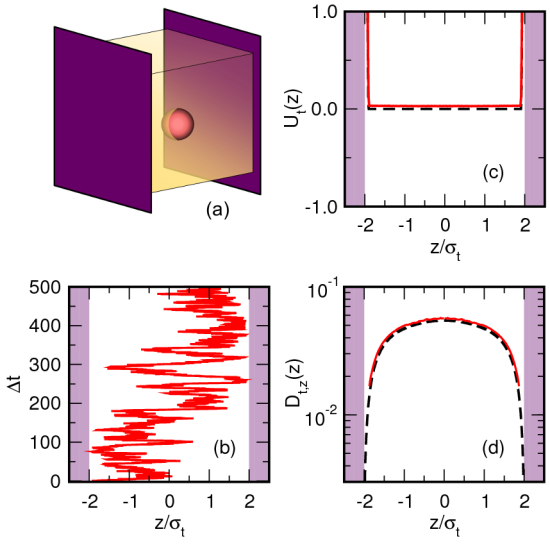

Figure 2.3: (a) Illustration of the reference confined suspension: a single tracer diffusing in a viscous continuum solvent between hard walls. (b-d) Static and dynamic quantities measured from single-particle Brownian trajectories governed by free energy and diffusivity profiles from hydrodynamic theory (see text), which were calculated based on a tracer diameter $\sigma_t = 1$, solvent viscosity $\eta_s = 2.09$, and channel width $H/\sigma_t = 5$. (b) One portion of a particle trajectory comprising tracer position z/σ_t versus lag-time Δt as recorded from one of many realizations. (c) Position-dependent free-energy landscapes $U_t(z)$ input (dashed black) into the simulation and measured (solid red) via $U_t(z) = -k_B T \ln \rho_t(z) + C$ where $\rho_t(z)$ is local tracer number density and C is an arbitrary constant. (d) Position-dependent diffusion coefficients $D_{t,z}(z)$ for motions in the z-direction input (dashed black) into the simulation and measured (solid red) via the MFPT treatment of the FP equation. Purple shading indicates regions inaccessible to the tracer center.

diffusivity of the bulk monodisperse HS fluid [107]. We account for the influence of the walls via Eqn. 2.9 using previous $\lambda_z(z)$ correction factors from hydrodynamic theory [58] for a spherical particle moving perpendicular to flat surfaces separated by distance H/σ_t. [3]

These *a priori* profiles for the tracer free-energy and diffusivity are complemented in Fig. 2.3 by measurements from single-particle Brownian simulations, where the simulations let us directly examine tracer trajectories and confirm that trajectory data alone can be used to reconstruct underlying $U_t(z)$ and $D_{t,z}(z)$ profiles. Fig. 2.3(b) shows a representative portion of a single-particle trajectory, which in itself gives the impression that the particle does indeed traverse regions near the walls more slowly than near the center of the pore, though the particle ultimately visits all regions of the pore *equally often* given sufficient time. In Figs. 2.3(c-d), we show $U_t(z)$ profiles derived from measuring the equilibrium tracer density profile and show $D_{t,z}(z)$ profiles subsequently obtained from MFPTs via Eqn. 2.10. We observe excellent agreement between the *a priori* and *posteriori* functions.

More broadly, an important takeaway from this reference setup is that $U_t(z)$ and $D_{t,z}(z)$ profiles in fluid tracer-solvent systems need not exhibit similar z-dependence or display (anti-)correlated local extrema. This is perhaps not surprising given the diversity of functional forms that ought to be compatible with the generic FP equation, though one could ostensibly construct profiles incompati-

[3]The predicted diffusivity profile for $H/\sigma_t = 5$ and unity tracer diameter is most easily expressed about the pore center as the polynomial $D_{t,z}(z) = D_t^{blk}/\lambda_z(z) = -6.35 \times 10^{-4} z^6 + 1.16 \times 10^{-3} z^4 - 7.83 \times 10^{-3} z^2 + 5.45 \times 10^{-2}$.

ble with conservative positive $p(z,t)$ surfaces. However, the idea that there should be *direct* correspondence between the free energy and diffusivity landscapes of diffusive tracer particles has been tacitly assumed in previous work focused on predicting local diffusion coefficients [157]. It is crucial to bear these points in mind as we consider the results for the systems below with non-continuum solvent.

2.3.2 Local confined tracer dynamics in non-continuum solvent

2.3.2.1 Comparing emergent structural and diffusivity signatures between hard walls

We now move on to examine how tracer diffusive dynamics are impacted by confinement when the tracer-solvent size-ratio is finite, which lets us test the accuracy of hydrodynamic theory when the solvent is non-continuum (i.e., granular). Fig. 2.4 shows $U_{\mathrm{t}}(z)$ and $D_{\mathrm{t,z}}(z)$ profiles measured for various small tracer-solvent size-ratios $\sigma_{\mathrm{t}}/\sigma_{\mathrm{s}} \leq 3$, and shows two-body tracer-solvent pair correlations $g^{\parallel}_{\mathrm{t,s}}(y|z)$ for one of these cases. Here and below, these measurements are compared directly against hydrodynamic predictions, which we calculate via Eqn. 2.9 by inputting the tracer radius, solvent viscosity [71], tracer-solvent slip boundary conditions [197], and known [58] correction factors $\lambda_{\mathrm{z}}(z)$ from the reference continuum case. Note that the correction factors $\lambda_{\mathrm{z}}(z)$ are based on no-slip boundary conditions between the HS solvent and confining surfaces. This is somewhat at odds with the slip boundary conditions between the tracer and solvent; however, previous work shows that hydrodynamic correction factors perpendicular to boundaries are not very sensitive to the solvent-boundary slip conditions [216]. With this in mind, we appeal to the the no-slip results as they are the most established and unambiguous.

Finally, note that $\sigma_t/\sigma_s = 3$ was the largest tractable limit in MD simulations with hard walls given the amount of trajectory data required to converge MFPT values at high spatial resolution.

For all cases in Fig. 2.4, we observe oscillations in $U_t(z)$ and $D_{t,z}(z)$ commensurate in lengthscale with the *diameter of the solvent particles*, where the shape of $U_t(z)$ reflects the two-body tracer-solvent static correlations (Fig. 2.4(a)) that emerge due to solvent static correlations near the walls. These oscillations at finite σ_t/σ_s are not predicted by the hydrodynamic theory as it does not account for solvent structuring. However, it is reasonable that if σ_t/σ_s were increased, the $D_{t,z}(z)$ profiles would smoothly approach the theoretical predictions as solvent inhomogeneity occurs at vanishing lengthscales. Nonetheless, hydrodynamic theory does roughly track the *average* slowdown in tracer dynamics with growing σ_t/σ_s, though the measured $D_{t,z}(z)$ profiles are slightly depressed near the pore-center for the larger σ_t/σ_s values. This depression is presumably due to non-ideal frustrations in the solvent flow (i.e., rearrangements) between the tracer and wall(s) relative to the continuum case.

The $U_t(z)$ and $D_{t,z}(z)$ profiles in Figs. 2.4(b-c) respectively exhibit consistent shapes across the various σ_t/σ_s values; however, by comparing these two types of profiles *against each other*, we observe that there may be no universal connection between local free energy and diffusivity. To wit, at different σ_t/σ_s values, we observe either mostly positive *or* mostly negative local correlations between $U_t(z)$ and $D_{t,z}(z)$. In the $\sigma_t/\sigma_s = 1$ case, we observe a mostly *negative* correlation between $D_{t,z}(z)$ and $U_t(z)$, which corresponds to a *positive* correlation between

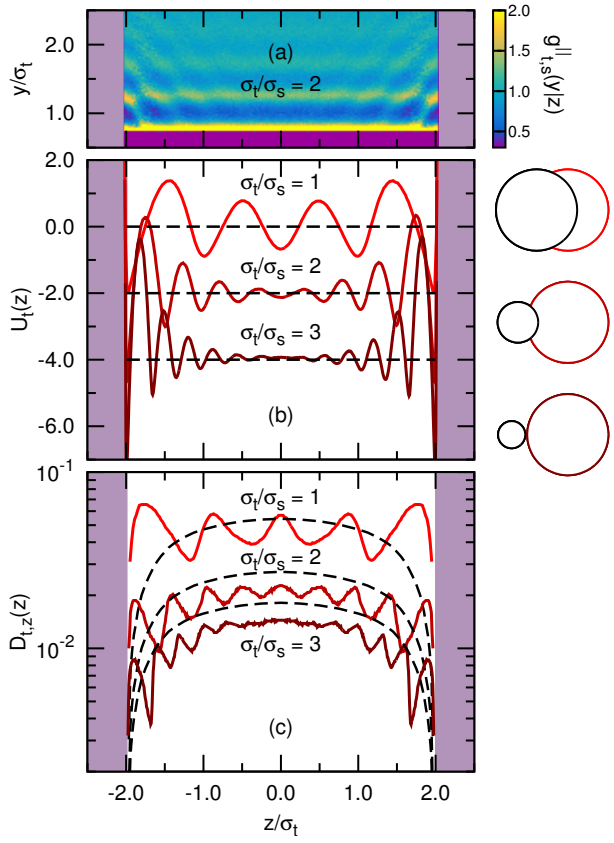

Figure 2.4: Structural and dynamic measurements for single tracers suspended in solvents ($\phi_s = 0.42$) in pores of width $H/\sigma_t = 5$ with hard walls. (a) Tracer-solvent pair correlations $g^{\parallel}_{t,s}(y|z)$ for relative diameter ratio $\sigma_t/\sigma_s = 2$, where correlations are measured as a function of position z and radial distance y along the pores. Position-dependent (b) free energy landscapes $U_t(z)$ and (c) diffusivity profiles $D_{t,z}(z)$ for the tracers (red lines) given various size ratios σ_t/σ_s, along with results from hydrodynamic theory (black lines). Circles on the right illustrate solvent (left, black) and tracer (right, red) sizes, drawn to scale with respect to other panels.

diffusivity and density (as the tracer and solvent particles are interchangeable). This positive correlation is the opposite of the density-diffusivity relationship of the bulk HS fluid, and was observed in a previous study of confined HS fluids: there, it was suggested that this non-intuitive behavior emerges because the dense layers possess more void space for particle insertion [149]. Here, of course, by only modestly increasing $\sigma_{\rm t}/\sigma_{\rm s} > 1$, correlations between $U_{\rm t}(z)$ and $D_{\rm t,z}(z)$ mostly reverse and become negative.

That this reversal occurs so readily is in line with results in upcoming chapters (other studies [24–26]) on monodisperse and lightly-polydisperse inhomogeneous HS fluids, which alternatively found that local correlations between diffusivity and other microscopic static quantities (like void space) can *qualitatively* depend on context, e.g., the characteristic lengthscale of static inhomogeneity. Altogether, in contrast to the idea that structural correlations drive the emergence of specific dynamic signatures, it appears equally fair to say that there is a generic oscillatory signature in $D_{\rm t,z}(z)$ that emerges near confining surfaces. In turn, this signature propagates away from boundaries without strong regard for the effective free-energy landscape $U_{\rm t}(z)$, although details of the former are no doubt moderately affected by those of the latter.

2.3.2.2 Transparent walls: anisotropic diffusivity signatures despite isotropic structure

In Fig. 2.5, we test the notion that these "signatures of confinement" in

$D_{\mathrm{t,z}}(z)$ exhibit little to no dependence on local structural correlations or the effective free-energy landscape $U_{\mathrm{t}}(z)$. We begin by comparing static and dynamic measurements for monodisperse HS fluids confined between either (1) between hard walls or (2) between transparent walls that bound tracer and solvent motions while completely eliminating inhomogeneous static correlations (see Fig. 2.2). In other words, the latter transparent-wall framework allows us to examine tracer dynamics in confinement given *isotropic* in-pore structure and a flat $U_{\mathrm{t}}(z)$ profile, both features of the continuum hydrodynamic scenario normally unrealizable given a finite tracer-solvent size-ratio. To establish that this is the case, we can consider Figs. 2.5(d) and (f), which show how two-body correlations $g^{\parallel}_{\mathrm{t,s}}(y|z)$ between particles (note that tracer and solvent are identical) and the corresponding $U_{\mathrm{t}}(z)$ are not z-dependent in the presence of the transparent walls–a complete erasure of the static correlations due to hard walls shown in Figs. 2.5(c) and (e). In fact, the pair correlations in Fig. 2.5(d) along the y-direction are identical to the radial distribution function (RDF) the bulk HS fluid at the same ϕ_{s}. This is consistent with the introduction of planes that restrict the center-accessibility of the inner and outer solvent particles without reducing the total accessible volume. Thus, from a *static* perspective, the particles do not "feel" the transparent walls at all.

Looking at the transparent-wall results in Fig. 2.5, we observe that despite the lack of position-dependent static correlations, there are nonetheless particle-scale variations in the tracer $D_{\mathrm{t,z}}(z)$ profile that emerge due solely in response to confinement: this underlines that local variations in diffusive dynamics cannot be straightforwardly based on typical measures of local structure. In other words,

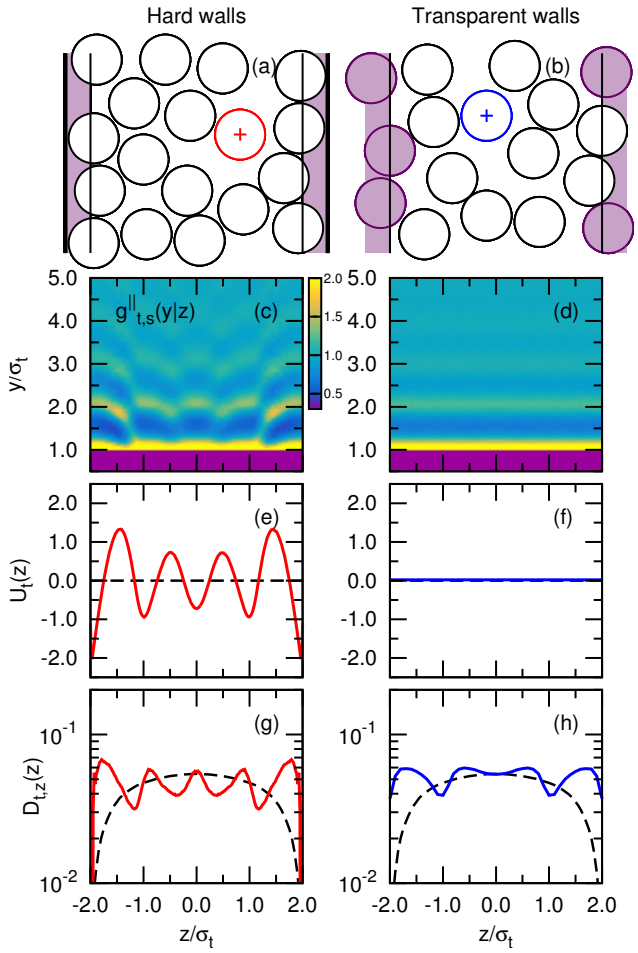

Figure 2.5: Structural and dynamic measurements for single tracers suspended in solvents ($\phi_s = 0.42$) of size ratio $\sigma_t/\sigma_s = 1$ (i.e., monodisperse HS fluids) in pores of width $H/\sigma_t = 5$ with hard and transparent walls. (a,b) Illustrations of pores drawn to scale with respect to other panels, where tracers are marked with crosses and center-inaccessible regions are shaded purple. (c,d) Tracer-solvent pair correlations $g^{\parallel}_{t,s}(y|z)$ measured as a function of position z and radial distance y along the pores. (e,f) Measured tracer free energy landscapes $U_t(z)$ (color) and results from hydrodynamic theory (black). (g,h) Diffusivity profiles $D_{t,z}(z)$ for the tracers (color) and results from hydrodynamic theory (black).

nothing about the static structure itself–including one- or two-body correlations, local void space for particle insertion (not shown) [73, 149, 222], etc.–points to anisotropic diffusive dynamics absent *a priori* knowledge that there are confining planes. This leaves it an open question how one might predict the (hopefully generic) mechanisms of non-continuum solvent rearrangement near the confining surfaces. One the other hand, it is apparent from Figs. 2.5(g-h) that the tracer dynamics are comparable in magnitude for the two types of confinement on a *spatially-averaged basis*. Thus, the average diffusive resistance across the pore may be more dominated by the lengthscale of confinement and the solvent viscosity than by the precise fluid structuring–an idea that we test further in Section 2.2.2.

In Fig. 2.6, we plot the static and dynamic signatures of transparent-wall systems at various finite tracer-solvent size ratios, which reveal that measured $D_{\mathrm{t,z}}(z)$ profiles converge upon predictions from hydrodynamic theory as $\sigma_{\mathrm{t}}/\sigma_{\mathrm{s}}$ grows. First, this suggests that the anisotropic solvent-scale variations in diffusivity seen in Fig. 2.5(h) emerge gradually at small size ratios. To wit, note how similar the oscillations in $D_{\mathrm{t,z}}(z)$ are across the different $\sigma_{\mathrm{t}}/\sigma_{\mathrm{s}}$ values: this points to *generic* frustrated patterns of non-continuum solvent rearrangement (i.e., flow) that generate *generic* motifs in the diffusive dynamics. More broadly, this behavior–which emerges naturally away from the continuum limit–reaffirms that the MFPT framework for calculating $D_{\mathrm{t,z}}(z)$ is capturing reliable information in simulations with non-continuum solvent. In other words, if the MFPT analysis is indeed appropriate for investigating dynamics in this class of tracer-solvent systems, then as the solvent increasingly resembles a structureless continuum, $D_{\mathrm{t,z}}(z)$ measurements must di-

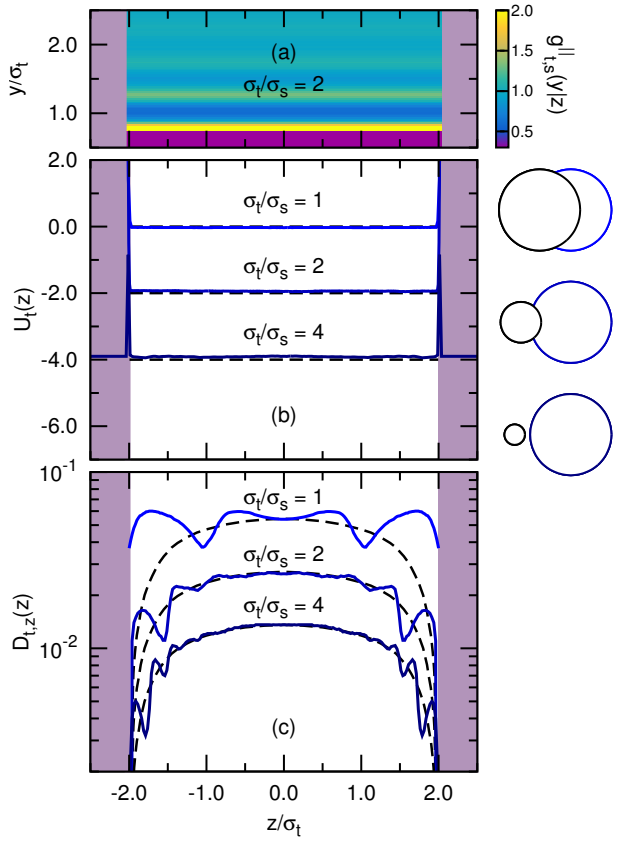

Figure 2.6: Structural and dynamic measurements for single tracers suspended in solvents ($\phi_s = 0.42$) in pores of width $H/\sigma_t = 5$ with transparent walls. (a) Tracer-solvent pair correlations $g^{\parallel}_{t,s}(y|z)$ for relative diameter ratio $\sigma_t/\sigma_s = 2$, where correlations are measured as a function of position z and radial distance y along the pores. Position-dependent (b) free energy landscapes $U_t(z)$ and (c) diffusivity profiles $D_{t,z}(z)$ for the tracers (blue lines) given various size ratios σ_t/σ_s, along with results from hydrodynamic theory (black lines). Circles on the right illustrate solvent (left, black) and tracer (right, blue) sizes, drawn to scale with respect to other panels.

rectly reflect known hydrodynamic predictions–particularly because we have eliminated anisotropic structuring that might otherwise complicate the comparison. Indeed, our results for $\sigma_t/\sigma_s = 4$ (the largest computationally-tractable system) are clear evidence that the FP-based analysis can return known hydrodynamic results for simulations that roughly mimic the physics of the reference problem.

2.3.2.3 Diffusivity signatures in response to density-flattening external fields

The plots from transparent-wall systems in this previous section demonstrate that anisotropic solvent-scale signatures in $D_{t,z}(z)$ can emerge given the presence of confining planes even when inhomogeneous static correlations between solvent particles are completely absent. In this section, we round out our discussion of local diffusivity signatures by investigating whether similar motifs in $D_{t,z}(z)$ emerge for less "exotic" confined systems with only *partially* suppressed static inhomogeneity–i.e., possessing flattened free-energy profiles $U_t(z)$–that are arguably more easily realized in experiments than transparent-wall systems. By focusing on monodisperse HS fluids ($\sigma_t/\sigma_s = 1$), we can make connections with previous work [34, 65] focused on the interplay of density profiles (i.e., free-energy landscapes) and tracer diffusion in confinement. More broadly, the following results underline that free-energy profiles $U_t(z)$ are seemingly insufficient for predicting local variations in diffusive dynamics.

In Fig. 2.7, we show static and dynamic tracer measurements for (1) hard-

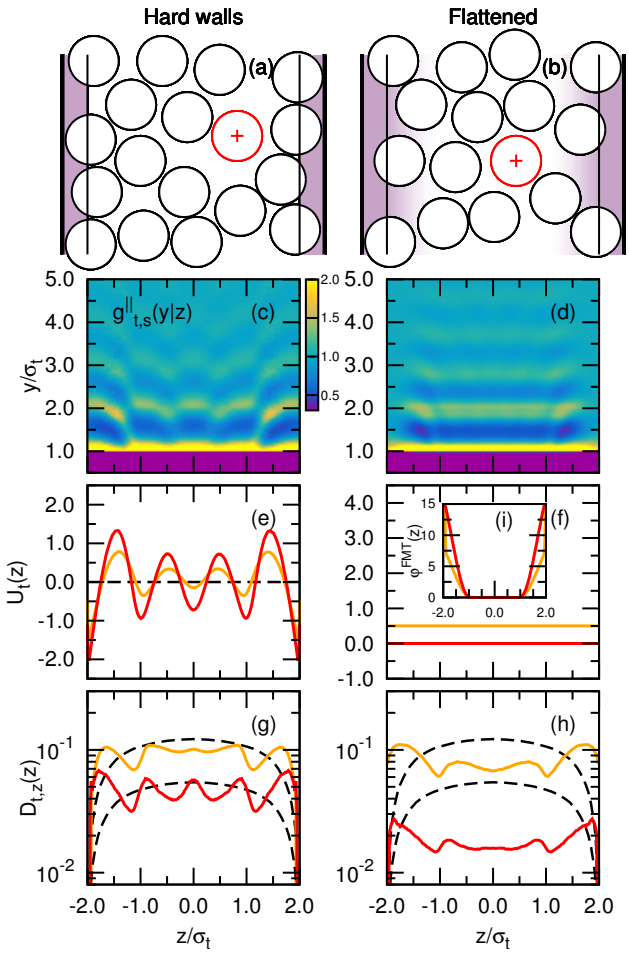

Figure 2.7: Structural and dynamic measurements for tracer-solvent mixtures of size-ratio $\sigma_t/\sigma_s = 1$ (i.e., monodisperse HS fluids) in pores of width $H/\sigma_t = 5$ with hard walls in the absence and presence of additional external fields that flatten density fluctuations. Throughout, gold and red lines correspond to $\phi_s = 0.336$ and 0.42, respectively. (a,b) Illustrations of pores drawn to scale with respect to other panels, where tracers are marked with crosses and center-inaccessible regions are shaded purple. (c,d) Tracer-solvent pair correlations $g^{\parallel}_{t,s}(y|z)$ measured as a function of position z and radial distance y along the pores for $\phi_s = 0.42$. (e,f) Measured tracer free energy landscapes $U_t(z)$ (color) and hydrodynamic theory (black), where results are shifted vertically by arbitrary constants for clarity. (g,h) Diffusivity profiles $D_{t,z}(z)$ for the tracers (color) and hydrodynamic theory (black). (i) External fields $\varphi^{FMT}(z)$ derived from FMT to flatten $U_t(z)$ profiles.

wall systems (one of which is identical to that in Fig. 2.5) and (2) systems that are confined by hard walls superimposed with auxiliary potentials $\phi^{\mathrm{FMT}}(z)$ that are calculated from Fundamental Measure Theory (FMT) [172, 173] to eliminate local density variations across the pores. As seen in other studies focused on flattening HS density variations [33, 34, 65], the $\phi^{\mathrm{FMT}}(z)$ profiles in Fig. 2.7(i) have simple ramp-like shapes that decay over lengthscales on the order of the solvent diameter. Here, the $\phi^{\mathrm{FMT}}(z)$ potentials successfully flatten the solvent density profiles $\rho_{\mathrm{s}}(z)$–here, equivalent to the tracer profiles $\rho_{\mathrm{t}}(z)$–and correspondingly flatten the tracer free-energy profiles $U_{\mathrm{t}}(z)$. However, in contrast to the transparent-wall systems in Section 2.3.2.2, we note that this flattening transformation does not completely eliminate inhomogeneity in *higher-order* static correlations, as evidenced by the modestly anisotropic pair correlations $g^{\parallel}_{\mathrm{t,s}}(y|z)$ shown in Fig. 2.7(d).

For the flattened systems in Fig. 2.7(h), we observe $D_{\mathrm{t,z}}(z)$ with local signatures reminiscent of those in the transparent-wall cases, supporting the notion that the *simultaneous* observation of flat $U_{\mathrm{t}}(z)$ profiles and oscillatory $D_{\mathrm{t,z}}(z)$ profiles (with particle-scale variations) is not unique to the transparent-wall framework. In other words, these results–like the transparent-wall measurements in Fig. 2.5–show that features (e.g., extrema) in $U_{\mathrm{t}}(z)$ or lack thereof need not be mirrored in corresponding $D_{\mathrm{t,z}}(z)$ profiles for confined systems with non-continuum solvent. We also observe that the dynamics in these flattened systems are suppressed on average compared to hard- and transparent-wall systems at the same ϕ_{s}. As discussed by Goel et. al. for similar confined fluids [65], this is because the ramp-like potentials suppress one-body density variations at the expense of reducing the

number of accessible static (thermodynamic) configurations for the confined particles, ultimately frustrating rearrangements and slowing diffusion (similar impacts are observed for the dynamics parallel to the confining walls). In a rough sense, we have "densified" the systems because the $\phi^{\mathrm{FMT}}(z)$ potentials partition particles toward the centers of the pores, which is why the hydrodynamic predictions provide over-estimates of diffusivity away from the walls, especially at high ϕ_{s}.

2.3.3 Average confined tracer dynamics in non-continuum solvent

While all of the systems in the previous section exhibit local solvent-scale signatures in $D_{\mathrm{t,z}}(z)$ that are not predicted by hydrodynamic theory (given its structureless solvent), we next demonstrate that theory is nonetheless reasonably accurate on a *spatially-averaged basis* for tracer-solvent size-ratios as small as $\sigma_{\mathrm{t}}/\sigma_{\mathrm{s}} \approx 1$. Fig. 2.8(a) shows measured and predicted tracer diffusion coefficients averaged across the pores that are calculated via

$$\langle D_{\mathrm{t,z}}(z)\rangle = \frac{\int_{z_r}^{0} D_{\mathrm{t,z}}(z)\rho_{\mathrm{t}}(z)\mathrm{d}z}{\int_{z_r}^{0} \rho_{\mathrm{t}}(z)\mathrm{d}z} \tag{2.15}$$

for tracer-solvent size ratios between $0.6 \leq \sigma_{\mathrm{t}}/\sigma_{\mathrm{s}} \leq 4.0$, along with bulk tracer diffusivities $D_{\mathrm{t}}^{\mathrm{blk}}$ predicted via Eqn. 2.4. Fig. 2.8(b) shows the corresponding measured and predicted MFPTs from one wall to the other calculated via

$$\tau_{\mathrm{MFPT}} = 2\frac{\int_{z_r}^{0} \mathrm{d}z'[e^{\beta U_{\mathrm{t}}(z')}/D_{\mathrm{t,z}}(z')]}{\int_{z_r}^{z'} \mathrm{d}z'' e^{-\beta U_{\mathrm{t}}(z'')}} \tag{2.16}$$

for the same confined tracer-solvent systems. For both calculations, $z_r = -(H - \sigma_t)/2$ is the leftward limit of center-accessibility and we exploit the symmetry of the systems.

On the whole, we observe agreement within 20% between measurements and predictions for most tracer sizes, though the best quantitative agreement occurs for *transparent-wall* systems with $\sigma_t/\sigma_s \geq 2.0$, which are evidently good "granular" extensions of the classic continuum-solvent case. In particular, we point out the high accuracy of the hydrodynamic theory even for the monodisperse HS cases–though, interestingly, the hard-wall case adheres to the predictions more closely than transparent-wall case at this and smaller σ_t/σ_s values. We postulate that this occurs because the isotropic structuring in the transparent-wall case indeed *minimizes* solvent frustration (and thus diffusive resistance) for given choices of ϕ_s and H/σ_t; this correspondingly *maximizes* the difference between the instantaneously "patchy" drag induced by non-continuum solvent collisions and the uniform viscous drag assumed in the continuum limit. However, the inhomogeneous structuring in the hard-wall case–and the added frustration of solvent rearrangements–effectively (re-)suppresses tracer mobility, which is reflected by the consistent differential between transparent- and hard-wall results at all σ_t/σ_s. In turn, it is not surprising that the predictive capability of the theory falters as the tracer becomes *smaller* than the solvent (e.g., $\sigma_t/\sigma_s = 0.6$), where one can envision a growing prevalence of instantaneous cavities in the solvent that facilitate rapid tracer transit.

Regarding Fig. 2.8, we also note that the measured hard-wall $\langle D_{t,z}(z) \rangle$ values are suppressed relative to theory even at the *largest* practically-accessible

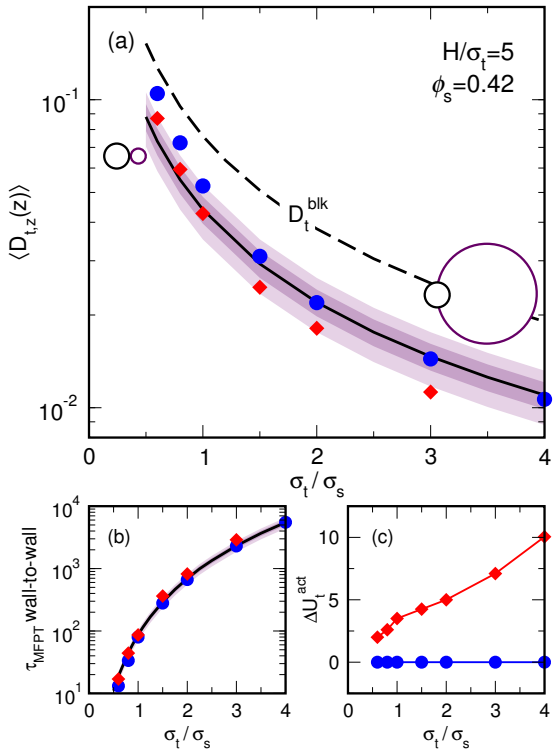

Figure 2.8: (a) Average tracer diffusivities $\langle D_{\mathrm{t,z}}(z)\rangle$ and (b) mean first-passage times τ_{MFPT} across pores (wall-to-wall) versus tracer-solvent diameter ratio $\sigma_{\mathrm{t}}/\sigma_{\mathrm{s}}$ measured from simulations with hard walls (red diamonds) and transparent walls (blue circles). Solid black lines show results from hydrodynamic theory, with dark and light purple shading denoting ± 10 and 20% bounds, respectively. Dashed black line in (a) shows slip-result for tracer diffusivity $D_{\mathrm{t}}^{\mathrm{blk}}$ in bulk solvent. Pairs of circles illustrate relative solvent (left) and tracer (right) sizes for $\sigma_{\mathrm{t}}/\sigma_{\mathrm{s}} = 0.6$ and 4.0. (c) Free energy barriers $\Delta U_{\mathrm{t}}^{\mathrm{act}}$ for tracer particles moving from positions at walls to the nearest local minima away from the walls.

size-ratios σ_t/σ_s, meaning that we cannot directly speak to convergence with the continuum limit (as seen for the transparent-wall systems). In essence, while the hard-wall results must converge with the continuum results for sufficiently large σ_t/σ_s, it is difficult to observe this because at intermediate tracer-solvent size ratios (e.g., $\sigma_t/\sigma_s = 4$), the tracer is entropically driven to partition at the wall to free up configurational space for the solvent. As plotted in Fig. 2.8(c), this generates free-energy barriers ΔU_t^{act} for the tracer moving from wall-contact past the first solvent layer that rapidly approach $10k_BT$ or more, making it difficult to observe sufficient numbers of tracer transit events and biasing MFPT measurements. (We measure ΔU_t^{act} based on the height difference between $U_t(z)$ at the (leftward) limit of center-accessibility, $z = -(H - \sigma_t)/2$, and the adjacent local maximum at $z \approx -(H - \sigma_t - \sigma_s)/2$.) Of course, as the tracer becomes very large, these problematic edge-regions of the channel constitute vanishingly small fractions of the system, and would not greatly impact average dynamics.

Given the agreement between measured and predicted average diffusivities in Fig. 2.8, we close our discussion in Fig. 2.9 by showing that hydrodynamic predictions of $\langle D_{t,z}(z)\rangle$ are highly accurate for monodisperse HS systems at a variety of H/σ_t and ϕ_s values, where we focus on hard-wall systems as these are more physically-intuitive and realizable in experiments. Fig. 2.9(a) shows strong overlap between theory and most measurements down to $\phi_s = 0.20$, a moderate density in the middle of the ϕ_s-range for the equilibrium bulk HS fluid. Indeed, Fig. 2.9(b) demonstrates that it is only under *extreme* confinement (e.g., $H/\sigma_t \leq 3$) that measured values for $\langle D_{t,z}(z)\rangle$ are more than 20% removed from the predictions,

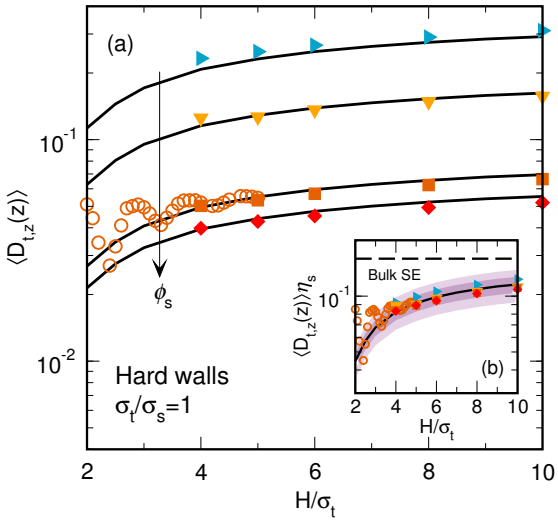

Figure 2.9: (a) Average tracer diffusivities $\langle D_{\mathrm{t,z}}(z)\rangle$ for the monodisperse HS fluid (i.e., $\sigma_{\mathrm{t}}/\sigma_{\mathrm{s}} = 1$) versus pore size H/σ_{t} measured for hard-wall systems at packing fractions $\phi_{\mathrm{s}} = 0.20$, 0.30, 0.40, and 0.42 (top to bottom). Filled symbols show results from this study; unfilled circles at $\phi_{\mathrm{s}} = 0.40$ reproduced from previous study [149]. Solid black lines show results from hydrodynamic theory. (b) Stokes-Einstein (SE) values $\langle D_{\mathrm{t,z}}(z)\rangle\eta_{\mathrm{s}}$ for all state points in (a), where η_{s} is HS solvent viscosity at ϕ_{s}. Solid black line shows results from hydrodynamic theory, with dark and light purple shading denoting ± 10 and 20% bounds, respectively. Dashed black line shows the expected SE value in the slip limit for monodisperse HS in the bulk, $D_{\mathrm{t}}^{\mathrm{blk}}\eta_{\mathrm{s}} = (2\pi)^{-1}$.

which are generally suppressed by factors of two to four relative to bulk Stokes-Einstein predictions. That average dynamics at these levels of extreme confinement would depart from theory is not necessarily surprising: while it was previously established that the FP equation self-consistently describes local tracer motions for, e.g., systems with $\sigma_t/\sigma_s = 1$ and $H/\sigma_t = 3$, the very strong inhomogeneous layering at this confinement lengthscale (and the relative dearth of collisions given the short wall-to-wall distance) is vastly different than the structureless viscous solvent of the continuum scenario [149].

Finally, in considering these results, it is important to recall that we are measuring diffusivities from simulations where tracer and solvent particles are governed by *Newtonian* dynamics: given the good prediction quality even down to moderate densities (e.g., $\phi_s = 0.20$), this supports the idea that hydrodynamic theories are useful for describing systems comprised of small-molecule solvents and comparably-sized tracers. Of course, we have focused on $\sigma_t/\sigma_s = 1$ partly because of the strong quantitative agreement at $H/\sigma_t = 5$ and $\phi_s = 0.42$ shown in Fig. 2.8 (which is arguably coincidental; see above). However, even acknowledging that the continuum predictions would slightly overestimate $\langle D_{t,z}(z)\rangle$ for hard-wall systems at larger σ_t/σ_s, it stands to reason that the good agreement between hydrodynamic theory and direct measurements would hold for diverse choices of H/σ_t and ϕ_s.

2.4 Conclusions

By analyzing MD simulations of confined HS tracer particles suspended in viscous continuum or non-continuum HS solvents, we have investigated how the

static and dynamic consequences of strong confinement evolve as solvent particles become comparable in size to the tracer. Our measurements of position-dependent diffusion coefficients $D_{\mathrm{t,z}}(z)$ are based on a recently-developed MFPT-based treatment of the FP equation, and we reaffirm previous studies [24–26, 187, 215] in finding that this straightforward technique accurately extracts local diffusivities $D_{\mathrm{t,z}}(z)$ from particle trajectories. Based on our findings here and elsewhere, we recommend this technique for probing the dynamics of inhomogeneous fluids in simulations or experiments as it is simpler to implement than alternatives requiring, e.g., Bayesian inference [86, 149].

Notably, we considered tracer-solvent systems bounded by either classic hard walls or by so-called transparent walls, the latter designed to restrict tracer and solvent center-accessibilities while preserving isotropic solvent structure (and flat tracer free-energy landscapes). We find that for a tracer diffusing between hard walls in non-continuum solvent, oscillatory signatures emerge in the static free-energy landscape $U_{\mathrm{t}}(z)$ and position-dependent diffusivity profile $D_{\mathrm{t,z}}(z)$ that are commensurate with the solvent lengthscale. These oscillatory motifs are not predicted by hydrodynamic theory as the latter assumes a structureless continuum-scale solvent. However, it is apparent that these local signatures would systematically "smear" as the tracer-solvent size-ratio grows, ultimately converging upon the theoretical results. When we examine analogous tracer-solvent systems confined by transparent walls, we observe anisotropic signatures in $D_{\mathrm{t,z}}(z)$ that are generic in shape (i.e., consistent across tracer sizes) and emerge solely due to the influence of the confining planes. These results support the idea that local diffu-

sion coefficients in inhomogeneous fluids cannot be uniquely predicted based on the knowledge of the free-energy landscape $U_{\mathrm{t}}(z)$ or local static quantities such as solvent density, available space, etc.

While the local oscillatory motifs in $D_{\mathrm{t,z}}(z)$ that emerge at the solvent lengthscale are not anticipated by hydrodynamic theory, we find that knowledge of the theoretical correction factor profile $\lambda_{\mathrm{z}}(z)$ is sufficient to approximately predict *average* diffusivities $\langle D_{\mathrm{t,z}}(z)\rangle$ for a variety of systems with non-continuum solvent. Of course, one caveat is that we have considered simulations without strong or specific interactions between tracer, solvent, and/or confining surfaces–consistent with the simple physics of the classic hydrodynamic scenario. Nonetheless, given this good agreement holds even for tracer-solvent size ratios of unity and only moderately dense solvent–along with the choice of Newtonian mechanics for propagating trajectories–we posit that hydrodynamic corrections for tracer dynamics near confining interfaces may be reasonable for decidedly non-continuum solvents.

Chapter 3

Structure, thermodynamics, and position-dependent diffusivity in fluids with sinusoidal density variations

3.1 Introduction

When a fluid is subjected to an external field $\varphi(\mathbf{r})$, it becomes inhomogeneous; i.e., its structural properties such as the one-particle density $\rho(\mathbf{r})$ and its dynamic properties (e.g., relaxation times, diffusivity tensor, etc.) exhibit dependencies on position $\mathbf{r}$. Such inhomogeneities are ubiquitous, with examples ranging from the slowly varying properties of particulate suspensions in gravitational, magnetic, or centrifugal fields to the stronger spatial variations characteristic of liquid molecules near an interface with another phase. As a result, there is interest in developing an understanding of how to accurately model and predict these position dependencies across a wide range of lengthscales, which in turn could enable the

Reproduced in part with permission from J.A. Bollinger, A. Jain, T.M. Truskett, "Structure, thermodynamics, and position-dependent diffusivity in fluids with sinusoidal density variations." *Langmuir*, 2014, 30 (28), pp. 8247–8252 (DOI: 10.1021/la5017005z). J.A. Bollinger performed computer simulations, analyzed results, created figures, and wrote the manuscript.

design of new material systems with novel properties. Unfortunately, despite the recent progress in developing theories that predict the static properties of inhomogeneous fluids [172], very little is known about how to estimate the corresponding position-dependent dynamics [149].

If density variations in an inhomogeneous fluid are sufficiently weak, then the local dynamic properties can be estimated by simply inputting $\rho(\mathbf{r})$ into known relationships that describe how the bulk isotropic fluid's dynamic properties depend on density. However, this local density approximation will break down for fluids displaying stronger density inhomogeneity (e.g., structuring near an interface with a solid) and will necessarily fail for systems where $\rho(\mathbf{r})$ takes on values larger than can be realized in the isotropic fluid. A natural question is whether there are other position-dependent models or structural metrics that more reliably anticipate, and perhaps provide mechanistic insights into, the local dynamic properties in such systems.

In this chapter, we use molecular dynamics (MD) simulations together with a stochastic method based on the Fokker-Planck equation to provide detailed information about the relationships between position-dependent static and dynamic quantities for inhomogeneous fluids. We consider the hard-sphere (HS) fluid, a canonical reference model for the structure and dynamics of dense simple liquids that exhibits negative correlations between density and diffusivity [44]. Because inhomogeneities can emerge on a variety of lengthscales, we examine fluids exhibiting periodic, one-dimensional (1D) sinusoidal density profiles of various wavelengths. By construction, these model systems are simpler to assess than those of other

commonly studied inhomogeneous liquids such as confined fluids (which exhibit specific interfacial and finite-size effects due to the presence of solid boundaries) or sheared fluids (which display non-equilibrium effects), but still capture the essential physics of inhomogeneity in a general way.

We examine the relationships between the position-dependent diffusivity $D_{\mathrm{z}}(z)$ in the inhomogeneous direction and various position-dependent static quantities for these models, including density $\rho(z)$, the one-body direct correlation function $c^{(1)}(z)$, and the two-body contribution to the excess entropy (relative to ideal gas) $s^{(2)}(z)$. For HS fluids, $c^{(1)}(z)$ and $s^{(2)}(z)$ characterize local contributions to "available space" and "available states" in the system [66], and the corresponding global versions have been shown, under confinement, to strongly correlate with the oscillatory pore width dependence of diffusivity parallel to confining boundaries [66, 145, 146]. More broadly, excess entropy has been found empirically to correlate with appropriately nondimensionalized transport coefficients for a variety of fluids in the bulk [50,61,170,181] as well as those describing average dynamics in the homogeneous directions under confinement [65, 66, 88]. We also investigate the predictions of a heuristic local average density model (LADM) for diffusivity motivated by analogous treatments of the free energy density in classical density functional theory [21].

As we report below, our simulation results demonstrate the emergence of nontrivial relationships between local static quantities and position-dependent diffusivity in fluids with different scales of structural inhomogeneity. Despite their ability to successfully predict dynamic trends in certain limits, we show that neither

the LADM approximation nor the known static-dynamic correlations of isotropic fluids (with inhomogeneous structure as an input) can provide reliable predictions of local and average diffusivity across a wide variety of density profiles, highlighting that a "mechanistic" understanding of such processes is still lacking.

3.2 Methods

3.2.1 Model interactions

To model the HS fluid with a continuous representation, we adopt the following steeply repulsive Weeks-Chandler-Andersen (WCA) pair potential [37]: $\varphi(r) = 4\epsilon([\sigma/r]^{48} - [\sigma/r]^{24}) + \epsilon$ for $r \leq 2^{1/24}\sigma$ and $\varphi(r) = 0$ for $r > 2^{1/24}\sigma$, where r is the interparticle separation. Unless otherwise indicated, we report quantities for this system that are implicitly non-dimensionalized by appropriate combinations of the characteristic lengthscale, σ, and energy scale, ϵ ($\epsilon = k_{\mathrm{B}}T$, where k_{B} is Boltzmann's constant and T is temperature).

3.2.2 Generating fluids with controlled inhomogeneous structure

To explore the effects of inhomogeneity lengthscale and magnitude, we consider three-dimensional (3D) equilibrium HS fluids exhibiting sinusoidal density profiles along the z-dimension, schematically illustrated in Fig. 3.1. Local density $\rho(z)$ is defined by

$$\rho(z) = \rho_{\mathrm{avg}} - (1/2)A\cos(2\pi z/\lambda) \tag{3.1}$$

where the average density is $\rho_{\mathrm{avg}} = (2/\lambda)\int_0^{\lambda/2}\rho(z)\mathrm{d}z$, A is the oscillation ampli-

tude, and λ is the wavelength (similar to previous studies [43, 83]). At any given z-position, the fluids are structurally isotropic in the x- and y-dimensions.

To impose the desired $\rho(z)$ profiles, we subject particles to one-body external potentials $\varphi^{\text{osc}}(z)$ that are analytically calculated via Fundamental Measure Theory (FMT), which has been shown to accurately describe the structural and thermodynamic properties of inhomogeneous HS fluids for the densities considered here [66, 172]. To generate $\varphi^{\text{osc}}(z)$, we input $\rho(z)$ profiles with total lengths L of at least 24 particle diameters in the z-direction, where $L = n\lambda$ and n is an integer number of periods. We then calculate the local one-body direct correlation function $c^{(1)}(z)$ within the FMT formalism and solve for $\beta\varphi^{\text{osc}}(z) = c^{(1)}(z) + \beta\mu - \ln\{\rho(z)\}$, where, μ is the chemical potential of the system [73]. Note that in the absence of the external fields, the fluids under consideration would simply exhibit bulk properties corresponding to ρ_{avg}.

3.2.3 Quantifying available space and excess entropy

We calculate several static properties of these inhomogeneous HS fluids that previous studies indicate might correlate well with their dynamics [66, 145, 149], including the one-body direct correlation function $c^{(1)}(z)$ (same as above), the excess entropy per particle s^{ex}, and the local two-body contribution to the excess entropy per particle $s^{(2)}(z)$. Note that $c^{(1)}(z) = \ln p_0(z)$, where $p_0(z)$ is the average areal fraction of the plane located at z that can accommodate an identical hard sphere "added" to the system without overlapping existing particles [73]. In other words, $c^{(1)}(z)$ provides quantitative information about the local available

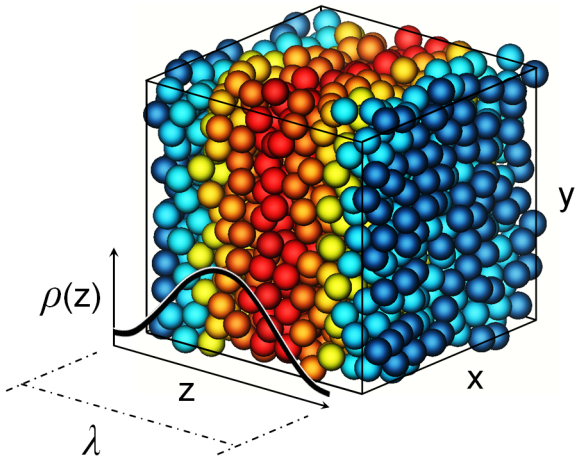

Figure 3.1: Schematic of the inhomogeneous fluids under consideration. Systems consist of equilibrium HS fluids exhibiting 1D sinusoidal density profiles $\rho(z)$ of wavelength λ (see Eqn. 1) due to the imposition of z-dependent external fields. Particles are shaded based on their instantaneous location within low-density (blue) versus high-density (red) regions.

space in the system. On the other hand, s^{ex} characterizes the global reduction of fluid entropy due to static interparticle correlations (i.e., relative to an ideal gas exhibiting an equivalent $\rho(z)$ profile), and $s^{(2)}(z)$ quantifies the local excess entropy contribution due to pair correlations. In 3D, the local two-body excess entropy $s^{(2)}(z)$ along coordinate z is calculated via:

$$\frac{s^{(2)}(z)}{k_{\text{B}}} = -\frac{1}{2}\int_{z-z^{\text{cut}}}^{z+z^{\text{cut}}} \rho(z')\mathrm{d}z' \int_{0}^{r_{xy}^{\text{cut}}} r_{xy}\{g(r_{xy}|z,z')[\ln g(r_{xy}|z,z') - 1] + 1\}\mathrm{d}r_{xy} \tag{3.2}$$

where r_{xy} is the distance between the particles in the x- and y-dimensions only (i.e., $r_{xy}^2 = r^2 - (z - z')^2$ and r is the total distance between two particles); and $g(r_{xy}|z,z') = \rho^{(2)}(r_{xy}|z,z')/[\rho(z)\rho(z')]$ is the pair correlation function in the xy-dimensions between particles positioned at z and z'. For the systems in this study, we used $z^{\text{cut}} = r_{xy}^{\text{cut}} = 5$, which was sufficient for pair correlations in this framework to decay. For isotropic bulk systems, Eqn. 3.2 reduces to

$$\frac{s^{(2)}}{k_{\text{B}}} = -\frac{1}{2}\rho\int\{g(\mathbf{r})[\ln g(\mathbf{r}) - 1] + 1\}\mathrm{d}\mathbf{r} \tag{3.3}$$

as established previously [10]. The quantities $c^{(1)}(z)$ and s^{ex} are calculated from FMT, which is known to accurately describe the structure and thermodynamics of inhomogeneous HS fluids for the densities considered here [66,172], while $s^{(2)}(z)$ is calculated using configurations from MD particle trajectories.

3.2.4 Characterizing diffusive dynamics

As in the previous chapter, we are especially interesting in measuring position-dependent diffusion coefficients $D_{\mathrm{z}}(z)$ in the inhomogeneous z-dimension, which appear in the context of the 1D Smoluchowski (or Fokker-Planck) diffusion equation:

$$\frac{\partial G}{\partial t} = \frac{\partial}{\partial z}\left(D_{\mathrm{z}}(z) e^{-\beta F(z)} \frac{\partial}{\partial z}[e^{\beta F(z)} G] \right) \tag{3.4}$$

where $G(z, t_0 + \Delta t | z', t_0)$ is the Markovian propagator describing temporal particle displacements between two positions z and z' in a conservative mean field $F(z)$, which is self-consistently given by $F(z) = -k_{\mathrm{B}} T \ln\{\rho(z)\}$ within an arbitrary constant for dense fluids [149].

To obtain $D_{\mathrm{z}}(z)$, we use a mean-first passage times (MFPT) analysis [81, 187, 220] that rewrites the steady-state Eqn. 3.4 as:

$$D_{\mathrm{z}}(z) = -\frac{\exp\{\beta F(z)\}}{\partial \tau(z, z_t)/\partial z} \int_{z_{\mathrm{refl}}}^{z} \exp\{-\beta F(z')\} \mathrm{d}z' \tag{3.5}$$

which is applicable given a "reflective" boundary at z_{refl} and an "absorbing" boundary at z_t, where $\tau(z, z_t)$ is the MFPT for tagged particles translating between a starting location $z_{\mathrm{refl}} < z < z_t$ at $t = t_0$ and crossing $z = z_t$ at $t = t_0 + \tau(z, z_t)$. This method requires non-periodic boundary conditions in the z-dimension, so to generate simulation trajectories compatible with the MFPT analysis, we must confine particle movements in the z-dimension while still imposing the desired density

profile $\rho(z)$ over the vast majority of the simulation box to obtain diffusivities unbiased by the "wall" effects. Thus, for a given density variation wavelength λ, we apply an external potential $\varphi^{\mathrm{tot}}(z)$ that stitches together wall potentials $\varphi^{\mathrm{wall}}(z)$ with the FMT-derived $\varphi^{\mathrm{osc}}(z)$. The former, given by $\varphi^{\mathrm{wall}}(z) = 4\epsilon[(\sigma/2)/z]^9$, is applied at opposing ends of the simulation box and smoothly interpolated with $\varphi^{\mathrm{osc}}(z)$ using a $\tanh(z)$ switching function. The confining walls are separated by distances large enough to ensure that they do not affect static or dynamic properties in the "core" system of interest, a criterion straightforward to verify in this system.

In turn, by examining particle configurations recorded every Δt, we obtain $\tau(z, z_t)$ for several distances z_t from the confining walls, which is possible because the absorbing boundaries are virtual. We calculate $\tau(z, z_t)$ profiles using discrete spatial resolutions of $\Delta z \ll \lambda$. Given MFPTs $\tau(z, z_t)$ for various z_t, we calculate the derivatives $\partial\tau(z, z_t)/\partial z$ via linear fits to small regions δz about z, where $\delta z = (n_{\mathrm{fit}})(\Delta z)$ and n_{fit} is the number of discrete Δz bins used. We constrain $\delta z < 0.15\lambda$, which smooths out statistical noise while retaining relevant $D_{\mathrm{z}}(z)$ features even for small λ. The resulting $D_{\mathrm{z}}(z)$ profiles range from a common z_{refl} to their respective z_t positions, which we average together along segments from $z_t - 3.0 \leq z \leq z_t - 0.5$, discarding the other portions of the $D_{\mathrm{z}}(z)$ profiles. Note that we discard the derivatives within $\Delta z = 0.30$ of (i.e., closest to) absorbing boundaries because these regions can display non-Markovian artifacts [187, 215].

Calculating $D_{\mathrm{z}}(z)$ profiles requires extensive trajectory data. To facilitate MD parallelization, we perform canonical ensemble (NVE) simulations of $N = 2400$

particles using GROMACS 4.5.5 [79] with a time step of 0.001, fixing $T = 1.0$ with a Nose-Hoover thermostat. For each wavelength, we execute a number of independently-initialized trajectories that we analyze to obtain $\tau(z, z_t)$ profiles, which are then averaged between the runs. In tracking particles for the MFPTs, we treat all particles as equivalent candidate tracers.

Average diffusion coefficients in the homogeneous dimensions D_{xy} are measured from separate MD simulations of 3D systems with periodic boundary conditions in all dimensions, making it unnecessary to account for particle proximity to walls. We conduct these MD simulations with a custom program in the microcanonical (NVE) ensemble using $N = 2400$ particles and integrate the equations of motion using the velocity-Verlet algorithm [2] with a time-step of 0.0002. To obtain the desired density profiles in these systems, the $\varphi^{\mathrm{osc}}(z)$ potentials are applied without modification for systems at $\rho_{\mathrm{avg}} = 0.573$. The ratios of box lengths in the inhomogeneous (z) and homogeneous (x, y) dimensions are kept approximately the same as in the confined simulations above: $L_{\mathrm{z}}/L_{\mathrm{xy}} \approx 2$. We extract D_{xy} from particle trajectories by fitting the long lag-time ($\Delta t \gg 1$) behavior of the average mean-squared displacements $\Delta\mathbf{r}^2$ of all the particles to the Einstein relation $\langle \Delta\mathbf{r}^2 \rangle = 4D\Delta t$.

3.3 Results & Discussion

3.3.1 Local correlations between diffusivity and density

We begin our discussion by examining Fig. 3.2, which compares local density $\rho(z)$ and diffusivity $D_{\mathrm{z}}(z)$ for various wavelengths λ to explore how differ-

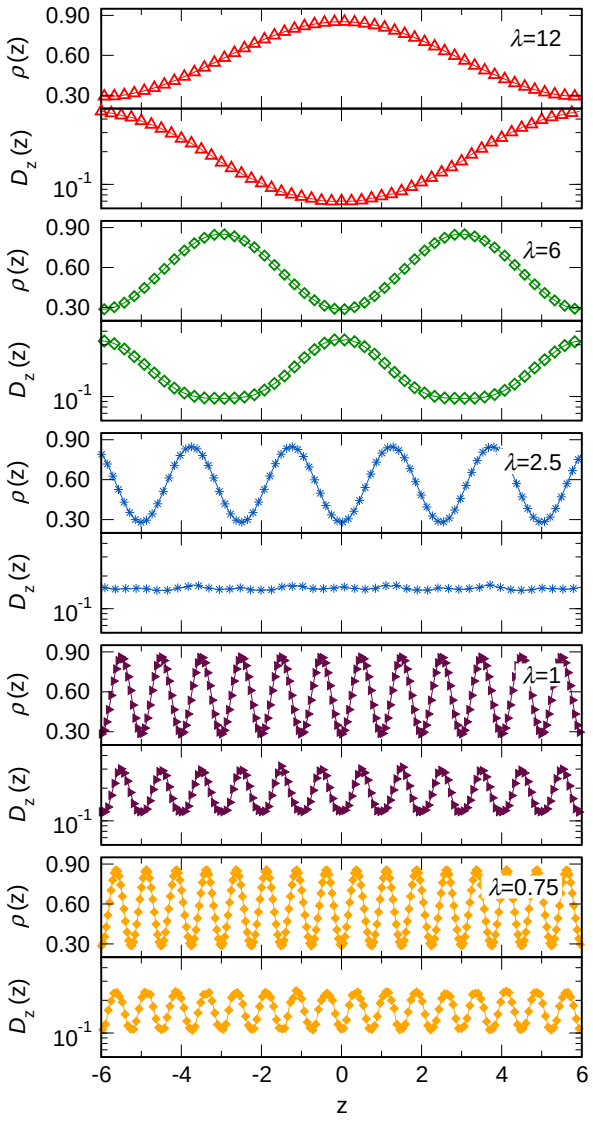

Figure 3.2: Position-dependent density, $\rho(z)$, and diffusivity in the inhomogeneous z direction, $D_{\mathrm{z}}(z)$, for 3D HS fluids exhibiting sinusoidal density profiles with $\rho_{\mathrm{avg}} = 0.573$, $\rho(z) = [0.287, 0.860]$, and wavelengths $\lambda = 12$, 6, 2.5, 1, and 0.75.

ent lengthscales of density variations impact correlations between equilibrium HS structure and mobility. The average density ρ_{avg} and the range of $\rho(z)$ are kept constant across systems to isolate the influence of λ. We choose ρ_{avg} to correspond to a bulk packing fraction $\phi = (\pi/6)\rho = 0.30$. At long wavelengths (e.g. $\lambda \geq 6$), local diffusivity simply decreases with increasing density (and vice versa), as expected based on the physics of the bulk HS fluid. However, for density variations on the scale of a particle diameter (e.g. $\lambda \approx 1$), $D_{\text{z}}(z)$ is clearly positively correlated with $\rho(z)$, as previously observed in confined systems exhibiting similar inhomogeneities [149, 157]. Remarkably, this qualitative crossover in behavior passes through wavelengths (e.g. $\lambda = 2.5$) for which $D_{\text{z}}(z)$ is spatially homogeneous (i.e. flat profile) despite substantial oscillations in $\rho(z)$. To understand why this result is striking, consider that mean collision frequencies in the bulk HS fluid at densities corresponding to the $\rho(z)$ extrema differ by approximately an order of magnitude.

3.3.2 Predicting local dynamics using weighted-density approximations

The crossover in the correlation between $D_{\text{z}}(z)$ and $\rho(z)$ is presented directly in Fig. 3.3, where it is shown to be a *smooth transition* as a function of λ. The inset shows that the crossover is qualitatively captured by an existing LADM approximation [21, 22] (recently modified by [83, 84]), which calculates $D_{\text{z}}(z)$ as a weighted sum of the bulk diffusion coefficients corresponding to the surrounding local density values. This LADM expression is given by

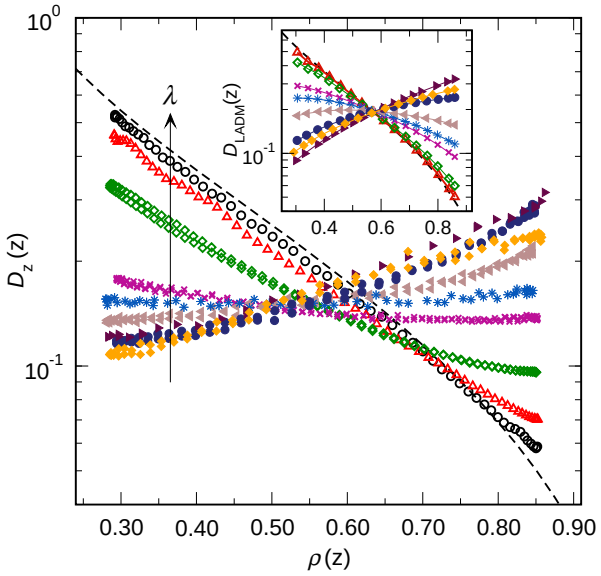

Figure 3.3: Position-dependent diffusivity in the inhomogeneous z direction, $D_z(z)$, plotted versus density, $\rho(z)$, for 3D HS systems at $\rho_{\rm avg} = 0.573$, $\rho(z) = [0.287, 0.860]$, and $\lambda = 24$, 12, 6, 3, 2.5, 2, 1.5, 1, and 0.75 (black circles to gold diamonds, consistent with Fig. 3.2). Heuristic predictions $D_{\rm LADM}(z)$ (see text) are shown in the inset (same symbols). Data for the bulk 3D HS fluid are shown as dashed lines.

$$D_{\mathrm{LADM}}(z) = \frac{\bar{\rho}^{\sigma}(z)}{\bar{\rho}^{\tau}(z)} D_{\rho}^{\mathrm{bulk}}[\bar{\rho}^{\tau}(z)] \tag{3.6}$$

which assumes that transport quantities can be estimated by analogy to free-energy densities Φ within the weighted density approximation (WDA) of density functional theory [73]:

$$\Phi_{\mathrm{WDA}}\{\rho(\mathbf{r}), \mathbf{r}\} = \frac{\bar{\rho}^{\sigma}(\mathbf{r})}{\bar{\rho}^{\tau}(\mathbf{r})} \Phi_{\rho}^{\mathrm{bulk}}[\bar{\rho}^{\tau}(\mathbf{r})] \tag{3.7}$$

Here, we calculate the weighted densities $\bar{\rho}^{\sigma}(z)$ and $\bar{\rho}^{\tau}(z)$ in Eqn. 3.6 using models previously applied to transport properties in the LADM formalism [21, 22, 83, 84], including the Tarazona, generalized van der Waals (GVDW), and generalized hard-rod (GHR) models [44]. The inset shows results from the Tarazona model, which approximately predicts the transition between the long- and short-wavelength correlations. (Although not shown here, we find that predictions based on the GVDW model also qualitatively capture the transition; those based on the more simplistic GHR model do not). Crucially, however, while using the LADM approach grossly captures the local trends in local diffusivity for the range of wavelengths shown in Fig. 3.3, it fails to converge to the correct local and average diffusivities as $\lambda \to 0$ (see Fig. 3.6 discussion).

3.3.3 Local correlations between diffusivity, available space, and excess entropy

In Fig. 3.4, we examine how $D_{\mathrm{z}}(z)$ correlates with $\exp\{c^{(1)}(z)\}$ (main panel) and $s^{(2)}(z)$ (inset), which quantify the local fractional available volume and two-

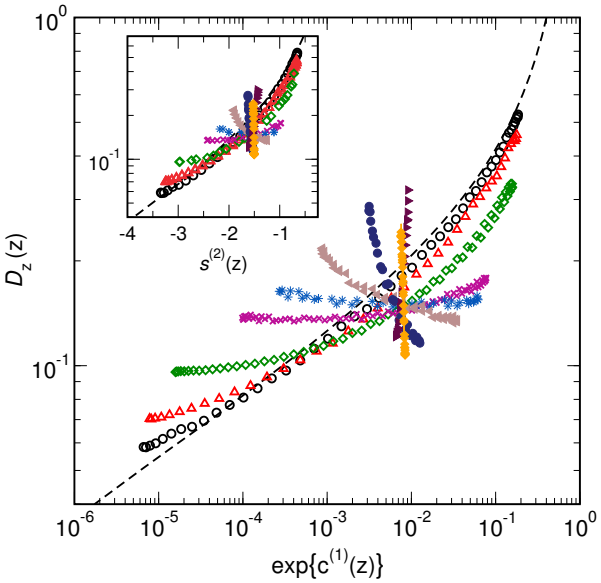

Figure 3.4: Position-dependent diffusivity in the inhomogeneous z direction, $D_z(z)$, plotted versus fractional available volume, $\exp\{c^{(1)}(z)\}$, and (inset) two-body excess entropy, $s^{(2)}(z)$, for 3D inhomogeneous HS fluids at $\rho_{\rm avg} = 0.573$, $\rho(z) = [0.287, 0.860]$, and $\lambda = 24$, 12, 6, 3, 2.5, 2, 1.5, 1, and 0.75 (black circles to gold diamonds; consistent with Fig. 3.3). Data for the bulk 3D HS fluid are shown as dashed lines.

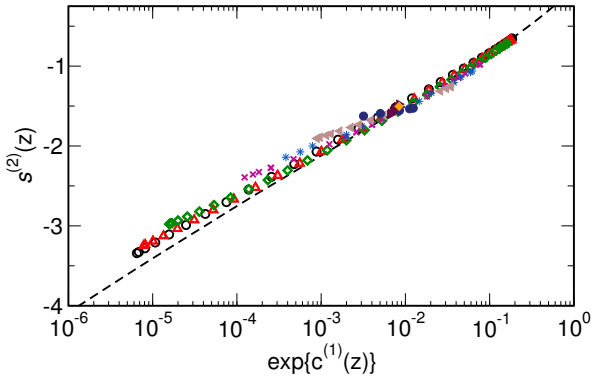

Figure 3.5: Local two-body excess entropy (Eqn. 3.2) versus fractional available volume $\exp\{c^{(1)}(z)\}$ for 3D inhomogeneous HS fluids at $\rho_{\text{avg}} = 0.573$, $\rho(z) = [0.287, 0.860]$, and $\lambda = 24$, 12, 6, 3, 2.5, 2, 1.5, 1, and 0.75 (black circles to gold diamonds; consistent with Fig. 3.3). Data for the bulk 3D HS fluid are shown as dashed lines.

body excess entropy, respectively. This is an important comparison because for HS diffusion along *isotropic* dimensions of systems–whether in the bulk, or in the structurally-homogeneous directions of confined fluids–average available volume and excess entropy positively correlate with each other and with average fluid diffusivity [66, 145, 149].

Significantly, we observe in Fig. 3.4 that $D_z(z)$ exhibits highly nontrivial λ-dependent correlations with $\exp\{c^{(1)}(z)\}$ and $s^{(2)}(z)$, where $D_z(z)$ can display positive correlations with $\exp\{c^{(1)}(z)\}$ and $s^{(2)}(z)$ (e.g., $\lambda = 12$); $D_z(z)$ can remain constant while $\exp\{c^{(1)}(z)\}$ and $s^{(2)}(z)$ vary considerably (e.g., $\lambda = 2.5$); and $D_z(z)$ can vary considerably while $\exp\{c^{(1)}(z)\}$ and $s^{(2)}(z)$ converge on the values associated with the bulk fluid at ρ_{avg} (e.g., $\lambda \leq 1$). To our knowledge, such a diversity of local static-dynamic correlations has not been previously observed, and demonstrates that correlations for isotropic fluids do not generalize in a straightforward

way to describe inhomogeneous particle motions.

Based on Fig. 3.4, it is evident that comparing $D_z(z)$ against both local available space and two-body excess entropy is somewhat redundant. As shown in Fig. 3.5, this is because $s^{(2)}(z)$ and $\exp\{c^{(1)}(z)\}$ measurements for all wavelengths collapse onto a common line exhibiting strong positive correlation. To our knowledge, such a comparison has not been previously shown. In terms of assessing the packing frustration as a function of position, this correspondence is interesting as $c^{(1)}(z)$ can be rapidly calculated from analytical approaches (e.g., like FMT for HS), while $s^{(2)}(z)$ is perhaps more suited to a wide range of systems because it only requires knowledge of particle positions. Of course, investigating whether the "interchangeability" of $c^{(1)}(z)$ and $s^{(2)}(z)$ is universal–e.g., for diverse interparticle potentials and different types of structurally-inhomogeneous systems–is beyond the scope of the current work.

3.3.4 Dependence of average diffusivity on lengthscale of density variations

In Fig. 3.6, we examine the λ-dependence of average diffusivities along the inhomogeneous dimension, given by

$$D_z^{\text{avg}} = \langle D_z(z) \rangle_\rho = \frac{\int_0^{\lambda/2} D_z(z)\rho(z)\mathrm{d}z}{\int_0^{\lambda/2} \rho(z)\mathrm{d}z} \tag{3.8}$$

and the homogeneous dimensions, given by D_{xy}, both of which characterize global aspects of particle single-particle mobility. As is evident, D_z^{avg} and D_{xy} are roughly *coupled* and depend *non-monotonically* on wavelength λ, though diffusivity in the

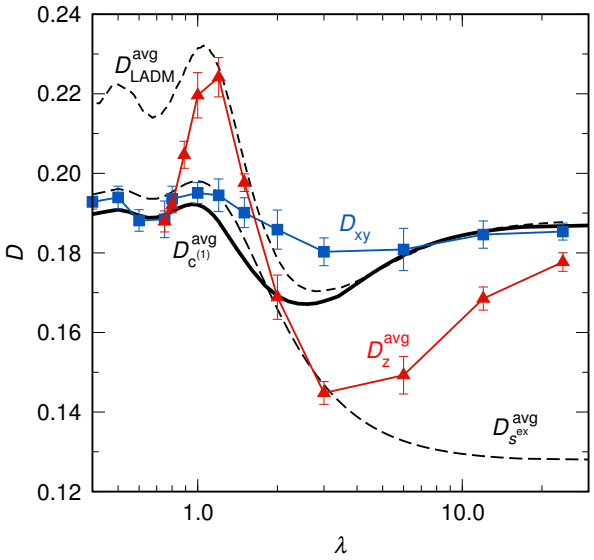

Figure 3.6: Average diffusivities $D_{\mathrm{z}}^{\mathrm{avg}}$ (red triangles) and D_{xy} (blue squares) versus wavelength λ for 3D HS fluids at $\rho_{\mathrm{avg}} = 0.573$, $\rho(z) = [0.287, 0.860]$. Model predictions $D_{\mathrm{LADM}}^{\mathrm{avg}}$ (short-dashed line), $D_{c^{(1)}}^{\mathrm{avg}}$ (solid line), $D_{s^{\mathrm{ex}}}^{\mathrm{avg}}$ (long-dashed line) are calculated using knowledge of various structural quantities (see text). Note that as $\lambda \to 0$, we recover a bulk isotropic fluid with a density of ρ_{avg}. $D_{\mathrm{z}}^{\mathrm{avg}}$ was only calculated down to $\lambda = 3/4$ due to the increasing computational burden of converging local dynamic data at vanishing but finite wavelengths.

inhomogeneous direction is evidently more sensitive to structural changes. Both $D_{\mathrm{z}}^{\mathrm{avg}}$ and D_{xy} exhibit relative maxima at $\lambda \approx 1$, which approximately corresponds to stacked "sheets" of particles and recalls previous work that optimized particle mobility along slit-pores by imposing strongly layered $\rho(z)$ [65]. In contrast, the diffusivities exhibit minima at $\lambda \approx 3$, which suggests that crossover wavelengths inherently frustrate single-particle motions.

3.3.5 Predicting average dynamics based on static structure

Fig. 3.6 also shows three "model" predictions for average diffusivity D^{avg}, the first using the $D_{\mathrm{LADM}}(z)$ profiles in Fig. 3.3, and the latter two using available volumes and excess entropies calculated with FMT, respectively. The first prediction is simply given by

$$D_{\mathrm{LADM}}^{\mathrm{avg}} = \langle D_{\mathrm{LADM}}(z) \rangle_{\rho} \tag{3.9}$$

which qualitatively captures the oscillatory dependence on λ at smaller wavelengths, but fails to converge upon the known zero-wavelength limit: the diffusivity $D_{\rho}^{\mathrm{bulk}}(\rho_{\mathrm{avg}})$ of the bulk HS fluid at ρ_{avg}. This latter idea is physically-intuitive when one considers that as λ becomes infinitesimal, the variations in local density will be blurred (i.e., much smaller than the particle lengthscale); thus, the structure and dynamics of the fluid become effectively–and, eventually, perfectly–uniform.

Here, Eqn. 3.9 does not converge to the correct limit because of the behavior of the $\bar{\rho}^{\sigma}(z)/\bar{\rho}^{\tau}(z)$ prefactor in Eqn. 3.6. The Tarazona and GVDW models, which capture the crossover in local static-dynamic correlations in Fig. 3.3, set $\bar{\rho}^{\sigma}(z) =$

$\rho(z)$ at all wavelengths and, as the wavelength goes to zero, show rapid convergence of $\bar{\rho}^{\tau}(z) \to \rho_{\text{avg}}$ below $\lambda \leq 0.5$. Thus, the limiting prediction of average diffusivity at small wavelengths is:

$$\lim_{\lambda \to 0} D_{\text{LADM}}^{\text{avg}} = D_{\rho}^{\text{bulk}}[\rho_{\text{avg}}]\left(1 + \frac{A^2}{8\rho_{\text{avg}}^2}\right) \tag{3.10}$$

where the biasing coefficient on the right persists because $\rho(z)$ will *always* exhibit the same functional form in Eqn. 4.1 regardless of wavelength, and this gets integrated (to the square) during the averaging. (This fixed behavior is different from more "microscopic" quantities like available space that are wavelength-dependent; see below). The dimensionless $\bar{\rho}^{\sigma}(z)/\bar{\rho}^{\tau}(z)$ factor in Eqn. 3.6 can be removed to resolve this problem, but then $D_{\text{LADM}}^{\text{avg}}$ no longer captures the *local* diffusivity crossover observed in Fig. 3.3.

The most successful approach shown in Fig. 3.6 exploits knowledge of the local available space, and is generated via

$$D_{c^{(1)}}^{\text{avg}} = \langle D_{c^{(1)}}^{\text{bulk}}[c^{(1)}(z,\lambda)]\rangle_{\rho} \tag{3.11}$$

which is based on averaging local diffusivity profiles generated by substituting the wavelength-dependent $c^{(1)}(z)$ profiles into the bulk HS relationship between diffusivity and fractional available volume. This approach qualitatively captures all extremes while converging to the correct limits, and builds on an intuitive physical connection–namely that diffusion might be conceptualized as particles probing unoccupied space [66, 149]. Based on Figs. 3.4-3.5, it is obvious that predictions

of similar quality would result from knowledge of $s^{(2)}(z)$. We note, however, that the success of these local measures–with regard to describing spatially-averaged dynamics–should be considered cautiously in terms of mechanistic interpretation given their failure to *directly* and *uniquely* predict local diffusivities (see Fig. 3.4).

The final prediction is based on the global excess entropy–which as discussed above has been highly useful for predicting relative trends in diffusive mobility for many types of systems. This prediction is given by

$$D_{s^{\mathrm{ex}}}^{\mathrm{avg}} = D_{s^{\mathrm{ex}}}^{\mathrm{bulk}}[s^{\mathrm{ex}}(\lambda)] \tag{3.12}$$

which is based on substituting wavelength-dependent molar excess entropy, s^{ex}, values into the bulk HS relationship between diffusivity and excess entropy. This approach qualitatively captures the short-wavelength oscillations in the Fig. 3.6 data, but converges to an incorrect long-wavelength prediction. This is not surprising because s^{ex} is a global–rather than local–quantity and thus, for long wavelengths, does not necessarily weight position-dependent static correlations in a way that is predictive of averaged local diffusivities. At very large λ, "organizing" the fluid into high- and low density regions makes s^{ex} more negative relative to the bulk fluid with the same ρ_{avg}. But because the $D_{s^{\mathrm{ex}}}^{\mathrm{avg}}$ prediction is based on the (positive) bulk correlation between diffusivity and excess entropy, this leads to a spurious underestimate of particle mobility for the inhomogeneous fluid at long wavelengths, where it exhibits *bulk-equivalent* dynamics as a function of location and, thus, on average.

3.4 Conclusions

The results in this chapter highlight–despite considerable recent progress–the lack of a physically intuitive model that quantitatively relates equilibrium inhomogeneous fluid structure and position-dependent particle mobility. While transport coefficients in isotropic fluids and along homogeneous coordinates of confined fluids correlate with thermodynamic quantities for a diverse array of scenarios, we find that–even for simple fluids with precisely imposed density variations–static quantities cannot be used to reliably predict local and average diffusivity.

We look forward to addressing whether alternative theoretical or empirical models (e.g., other WDAs for LADM) can provide insight into the connections between externally induced structural variations and local and average dynamic responses reported here. It tentatively appears that any models which capture the qualitative crossover in diffusive motions as a function of λ might be applicable to both simple and complex fluids, including those that exhibit anomalous bulk fluid relationships between diffusivity and compression. More investigations must be conducted to ascertain if such crossovers extend to other equilibrium fluid models such as those with significant attractions or penetrable cores, and to non-equilibrium systems including, e.g., carefully manipulated shear conditions.

Chapter 4

How local and average particle diffusivities of inhomogeneous fluids depend on microscopic dynamics

4.1 Introduction

Inhomogeneous fluids, which exhibit position-dependent structural (e.g., one-body density) and relaxation (e.g., diffusivity tensor) properties, are ubiquitous within natural and technological contexts due to the presence of external fields acting on their constituent particles or molecules. These external fields can originate from gravitational [19, 162, 175, 212], depletion [9, 120], electromagnetic [98,202], and optical [67] forces, etc., which underlie phenomena including the sedimentation equilibrium of particle suspensions [95], the strong positional ordering of fluids in contact with substrates [90], and the precise entrapment of colloidal particles via optical tweezers [224], as well as many other examples. While it is

Reproduced in part with permission from J.A. Bollinger, A. Jain, T.M. Truskett, "How local and average particle diffusivities of inhomogeneous fluids depend on microscopic dynamics." *J. Phys. Chem. B*, 2015, 119 (29), pp. 9103–9113 (DOI: 10.1021/jp508887r). J.A. Bollinger performed computer simulations, analyzed results, created figures, and wrote the manuscript.

relatively well-understood how to predict the static structure of simple atomistic and colloidal fluids subjected to external fields [172, 226], fundamental microscopic theories that can anticipate corresponding dynamic responses within inhomogeneous fluids have only recently begun to emerge [5, 12, 20, 105, 106, 110–112]. Since the interactions or external fields that induce fluid inhomogeneity can often be controlled experimentally, progress in relating inhomogeneous structure to dynamics is critical for the "inverse" design of new material systems with targeted transport properties [94].

From a practical perspective, some of the most useful links between static and dynamic quantities are phenomenological structure-property correlations motivated by exact results for idealized systems [49, 61, 170, 171]. Such correlations, which provide approximate connections between transport properties (e.g., shear viscosity and diffusivity) and static quantities (e.g., excess entropy), have aided in rationalizing and predicting the relaxation properties not only of dense bulk fluids with diverse interparticle potentials across a range of thermodynamic state points [39, 49, 50, 53, 61, 85, 89, 108, 116, 143, 144, 151, 166, 170, 171, 190], but also the dynamics associated with particle motions along *isotropic* directions of inhomogeneous fluids confined in various geometries (e.g., thin films, rectangular channels, or cylindrical pores) [**?**, 38, 65, 66, 88, 126, 134, 145, 146, 148]. Several recent investigations have also examined the *position-dependent* single-particle diffusive dynamics that emerge within inhomogeneous fluids [25, 35, 124, 147, 149, 157, 187, 215]. But because the calculation and interpretation of these position-dependent transport quantities are relatively new endeavors, little is known about the extent to which

existing static-dynamic correlations for bulk fluids can be straightforwardly generalized to local particle motions in these systems.

In this chapter, we address a related question that, to our knowledge, has yet to be systematically explored: whether the local diffusive dynamics of inhomogeneous fluids are sensitive to the type of microscopic dynamical rules governing the particle motions. Specifically, to what extent are qualitative trends in molecular transport dependent upon whether particles are governed by Brownian (i.e., stochastic) versus Newtonian (i.e., deterministic) physics? Addressing this question can provide new insights into which dynamic features, if any, can be expected to be universal across inhomogeneous fluids, thereby aiding in the development of theories for describing local relaxation processes *and* in the selection of appropriate simulation strategies for modeling their various behaviors. Regarding the latter point, pragmatic considerations often influence the selection of microscopic dynamics adopted in computer simulations of dense fluids; to wit, "coarse-grained" colloid trajectories are commonly generated with classical Newtonian dynamics, ignoring even the implicit effects of fast solvent degrees of freedom to improve computational efficiency [17, 57, 107, 150].

For bulk isotropic systems, it has been shown that these kinds of choices are justified: while short-time particle motions are sensitive to the type of microscopic dynamics, the long-time diffusion coefficients of equilibrium Brownian and Newtonian fluids are straightforwardly related for diverse interparticle potentials [61, 99, 113, 129, 130, 167, 170, 171]. Likewise, the average relaxation properties of model glassformers are insensitive to the choice of microscopic dynamics (includ-

ing Monte Carlo) [14–16, 60, 132, 206]. However, these findings deserve more careful scrutiny for other physical scenarios. For example, it remains unclear whether position-dependent diffusion coefficients of structurally identical *inhomogeneous* fluids computed independently from Brownian and Newtonian trajectories will relate to one another via the same semi-empirical scaling laws observed in bulk isotropic fluids [99, 167], or whether they will even display the same qualitative trends for different strengths of density inhomogeneity.

To address whether the choice of microscopic dynamics qualitatively impacts mobility within inhomogeneous fluids, we build upon a previous study [25] in which we measured the single-particle long-time diffusivity coefficients of equilibrium hard-sphere fluids exhibiting periodic, one-dimensional (1D) sinusoidal density profiles from particle trajectories in the context of the 1D Fokker-Planck diffusion equation. Given that inhomogeneities can emerge at a variety of strengths and lengthscales depending on the nature the external field and the liquid constituents under consideration, we consider density profiles characterized by a variety of wavelengths and amplitudes. Though these periodically-structured equilibrium fluids ought to be differentiated from more complex or non-equilibrium systems (e.g., specific multiphase interfaces, sheared fluids), they nonetheless capture some of the essential physics of inhomogeneity while remaining as simple as possible. Despite this simplicity, analogous correlations between local density and diffusivity have been observed in, e.g., confined fluids and periodically-structured fluids designed to imitate the structural characteristics of fluid interfaces [25, 149].

For pairs of inhomogeneous HS systems exhibiting identical static struc-

tures, which are simulated with Newtonian molecular dynamics (MD) and Brownian (*i.e.*, overdamped Langevin) dynamics (BD), respectively, we compare position-dependent diffusivities $D_z(z)$ in the inhomogeneous direction and average diffusivities in all directions. For the former, we draw upon (and augment) data from the previous chapter, which considered only MD simulations [25]. We also examine local correlations between $D_z(z)$ and static quantities of interest for inhomogeneous HS fluids, including density $\rho(z)$, packing fraction $\phi(z)$, and the one-body direct correlation function $c^{(1)}(z)$, which characterizes local available volume [73]. We compare the accuracy of a simple phenomenological model [25] for predicting average diffusivities of BD and MD systems that draws upon knowledge of $c^{(1)}(z)$ and bulk fluid properties. We also assess the degree to which existing quantitative scalings between BD and MD long-time diffusivities in isotropic fluids [99, 167] apply to local particle motions in inhomogeneous fluids.

As discussed below, we find that local and average diffusivity coefficients of strongly inhomogeneous fluids governed by BD and MD exhibit *qualitative* differences in terms of their correlations with static structure. Correspondingly, quantitative scalings between transport coefficients previously derived for bulk systems do not generally apply to local particle mobilities in these systems. However, we also show that average diffusion coefficients for inhomogeneous fluids subject to both types of microscopic dynamics can be approximately predicted via knowledge of the corresponding bulk isotropic fluid behaviors and the available volume distribution within the inhomogeneous fluids. Analogous predictions for average diffusivities of experimental colloidal dispersions with sinusoidal density profiles suggest, perhaps

counterintuitively, that their qualitative behavior will more closely mimic the results of MD simulations than the BD simulations without hydrodynamics. This latter observation calls into question the utility of overdamped Langevin dynamics for capturing the physics of colloidal suspensions in strongly inhomogeneous states (e.g., under confinement).

4.2 Methods

4.2.1 Model interactions

We examine systems of monodisperse hard-sphere (HS) particles modeled with the following continuous, steeply repulsive Weeks-Chandler-Andersen (WCA) pair potential [37]: $\varphi(r) = 4\epsilon([\sigma/r]^{48} - [\sigma/r]^{24}) + \epsilon$ for $r \leq 2^{1/24}\sigma$ and $\varphi(r) = 0$ for $r > 2^{1/24}\sigma$, where r is the interparticle separation. To simplify notation, we implicitly non-dimensionalize quantities by appropriate combinations of the characteristic lengthscale σ and energy scale ϵ ($\epsilon = k_{\mathrm{B}}T$, where k_{B} is Boltzmann's constant and T is temperature).

4.2.2 Generating and characterizing inhomogeneous fluid structure

As in the previous chapter, particles are subjected to one-body external potentials, $\varphi^{\mathrm{osc}}(z)$, derived via Fundamental Measure Theory (FMT) [172] to produce 1D sinusoidal density profiles

$$\rho(z) = \rho_{\mathrm{avg}} - (1/2)A\cos(2\pi z/\lambda) \tag{4.1}$$

where the average density is $\rho_{\mathrm{avg}} = (2/\lambda)\int_0^{\lambda/2}\rho(z)\mathrm{d}z$, A is the oscillation ampli-

tude, and λ is the wavelength (similar to previous studies [43, 83]). Beyond local density $\rho(z)$, we also consider two structural properties that are well-defined for the HS fluid and encode greater information about particle packing: the local packing fraction $\phi(z)$ and the one-body direct correlation function $c^{(1)}(z)$. Local packing fraction $\phi(z)$ is straightforwardly obtained from $\rho(z)$ via

$$\phi(z) = \pi \int_{z-1/2}^{z+1/2} \rho(z') \left(\frac{1}{4} - (z' - z)^2 \right) \mathrm{d}z' \tag{4.2}$$

and quantifies the average areal fraction of the plane located at z that is occupied by particle cores. The quantity $c^{(1)}(z)$ is obtained from FMT, where $c^{(1)}(z) = \ln p_0(z)$ and $p_0(z)$ is the average areal fraction of the plane located at z that can accommodate insertion of an additional hard-sphere center *without overlap* with existing particles [73]. In essence, $c^{(1)}(z)$ quantifies the distribution of local "available space" in the system. In the bulk isotropic fluid, $p_0 = \exp\{c^{(1)}\} = \exp\{-\mu^{\mathrm{ex}}\}$ and quantifies the particle insertion probability, where μ^{ex} is the excess chemical potential (relative to an ideal gas at the same density).

4.2.3 Characterizing diffusive dynamics

In terms of particle dynamics, diffusion provides an excellent description of motions over times t much greater than the intervals between particle collisions. For isotropic systems of dimensionality d where particles experience zero net force, the Einstein equation, $\langle \Delta \mathbf{r}^2 \rangle = 2dDt$, relates the diffusion coefficient D to the mean-squared displacement $\Delta \mathbf{r}^2$. However, to describe particle displacements

along inhomogeneous dimensions, e.g., through regions of varying density, the Einstein relation is no longer appropriate because diffusion coefficients are spatially-varying and particles experience *non-zero* average net forces [124]. For fluids exhibiting 1D inhomogeneity along a coordinate z, it has instead been shown [149] that particle displacements follow the 1D Fokker-Planck (FP) equation

$$\frac{\partial G}{\partial t} = \frac{\partial}{\partial z}\left(D_{\mathrm{z}}(z) e^{-F(z)} \frac{\partial}{\partial z}[e^{F(z)} G] \right) \tag{4.3}$$

with position-dependent diffusion coefficients $D_{\mathrm{z}}(z)$. Here, $G(z, t_0 + \Delta t | z', t_0)$ is the Markovian propagator describing temporal single-particle displacements given a non-uniform potential of mean force $F(z) = -\ln\{\rho(z)\} + C$, where C is an arbitrary constant.

In this study, we specifically consider the steady-state (i.e., $\partial G/\partial t = 0$) limit of the FP equation, and use a previously published mean-first passage times (MFPT) method [81, 220] to derive $D_{\mathrm{z}}(z)$ coefficients via:

$$D_{\mathrm{z}}(z) = -\frac{\exp\{F(z)\}}{\partial \tau(z, z_t)/\partial z} \int_{z_{\mathrm{refl}}}^{z} \exp\{-F(z')\} \mathrm{d}z' \tag{4.4}$$

This expression assumes a reflective (i.e., non-periodic) boundary at z_{refl} and an absorbing boundary at $z_t > z_{\mathrm{refl}}$, where $\tau(z, z_t)$ is the ensemble-averaged MFPT of particles starting from $z_{\mathrm{refl}} < z < z_t$ at $t = t_0$ and crossing $z = z_t$ at $t = t_0 + \tau(z, z_t)$. We filter the MFPT information to exclude short-time non-Markovian displacements, which are straightforward to identify [81, 187], and subsequently obtain

quantitative coefficients of diffusive (as opposed to ballistic) motion through different regions of the fluid. We have tested to ensure that the MFPT method agrees with $D_z(z)$ coefficients obtained from a Bayesian analysis of the FP equation [149] using z displacement data from simulations. We have also tested that it yields results in agreement with a color counterdiffusion steady-state solution of the FP equation [35].

The MFPT analysis requires non-periodic boundary conditions in the z-dimension, so we generate suitable trajectories from simulations subject to external potentials that stitch together the FMT-derived $\varphi^{\text{osc}}(z)$ fields and purely repulsive confining potentials. The confining walls are separated by distances large enough (i.e., there is enough buffer volume) to ensure that the static and dynamic properties in the "core" regions of interest with oscillatory profiles are unaffected by the external confinement, which is straightforward to verify in these systems. Because calculating $D_z(z)$ coefficients requires extensive trajectory data, we perform these MD and BD simulations using GROMACS 4.5.5 [79] to facilitate parallelization.

We note one important modification to the MFPT approach as originally presented [81, 187]: when analyzing the MD trajectories, we do not track all particles located at $z < z_t$ at time t_0, but instead track only a fraction of them with probability p. We employ this change based on previous studies using the MFPT method and related approaches for ballistic HS [25, 35], where it was found that by tracking all particles (i.e., $p = 1.0$), the velocity distributions of "tagged" particles near the reflective boundaries are incorrectly biased toward faster particles relative to the appropriate Maxwell-Boltzmann distribution. This, in turn, results in

artificially elevated diffusivities near the reflective boundaries (particularly if extended low-density regions are situated nearby), because an insufficient number of collisions have occurred to redistribute particles' momenta. We find that $p \leq 0.01$ is sufficient to eliminate bias in all of our systems, and as $\lambda \to 1$, we find the bias can be corrected by less selective probabilities $p \leq 0.2$. Thus, we choose $p = 0.01$ for wavelengths $\lambda \geq 12$ and $p = 0.05$ for $1 \leq \lambda \leq 6$, since increasing p lessens that amount of trajectory information required to obtain smooth diffusivity profiles. For the BD trajectories, however, this selectivity is unnecessary because inertia is ignored; thus, $D_z^{\mathrm{BD}}(z)$ profiles are unaffected by the choice of p.

Diffusion coefficients in the homogeneous direction, D_{xy}, are obtained from separate simulations performed with a custom program in which periodic boundary conditions are applied in all three dimensions, with box lengths in the z-direction being multiples of λ. D_{xy} values are extracted by fitting the long-time ($t \gg 1$) behavior of the average mean-squared displacement to the Einstein relation $\langle \Delta \mathbf{r}^2 \rangle = 4 D_{\mathrm{xy}} t$, where $\Delta \mathbf{r}^2$ represents the mean-squared displacement of each particle in the x and y directions.

4.2.4 Simulation protocols

BD trajectories are generated by solving the overdamped Langevin equation in the absence of hydrodynamic interactions for systems of $N = 2400$ particles. The position $\mathbf{r}_i$ of each particle $i \in [1, N]$ at time t is updated with time-step $\Delta t = 0.02$ according to the expression [2, 52]:

$$\mathbf{r}_i(t+\Delta t) = \mathbf{r}_i(t) + D_0 \Delta t \mathbf{F}_i(\mathbf{r}_i(t)) + \boldsymbol{\xi}_i(t) \tag{4.5}$$

where $D_0 = 0.001$ is the infinite dilution ($\rho \to 0$) diffusivity, $\mathbf{F}_i(t)$ is the force on each particle due to interparticle and external potential interactions, and $\boldsymbol{\xi}_i(t)$ is the stochastic contribution to motion. In each dimension, $\xi_i(t) = r_i^{\mathrm{G}}(t)\sqrt{2D_0\Delta t}$ where $r_i^{\mathrm{G}}(t)$ is a Gaussian distributed white noise with $\langle r_i^{\mathrm{G}}(t)\rangle = 0$ and standard deviation $\sigma = 1$. MD simulations are identical to the BD simulations with respect to population ($N = 2400$), structure, and thermodynamics, and our protocols are identical to those in the previous chapter.

4.3 Results & Discussion

4.3.1 Local correlations between diffusivity and varying density or packing fraction

We begin by discussing Fig. 4.1, which shows how local density $\rho(z)$ relates to local diffusivity in the inhomogeneous z-direction $D_{\mathrm{z}}(z)$. The latter is calculated from BD [$D_{\mathrm{z}}^{\mathrm{BD}}(z)$, normalized by D_0] and MD [$D_{\mathrm{z}}^{\mathrm{MD}}(z)$] simulations for several wavelengths λ. The BD and MD systems at each λ are identical in terms of their inhomogeneous static structures, which isolates the effect of microscopic dynamics on local single-particle mobility. Note that BD data and MD data are plotted on linear and logarithmic axes, respectively. This is done because of the much larger diffusivity range in MD (up to an order of magnitude) and to facilitate comparisons with past studies [25,167]. This treatment is applied through the remainder of this section.

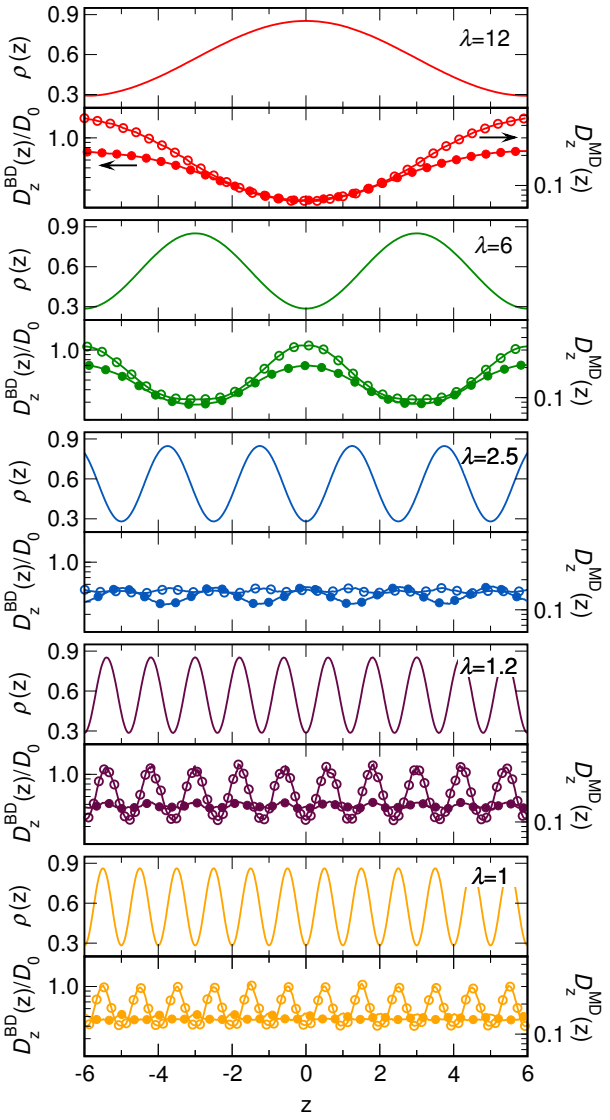

Figure 4.1: Position-dependent density $\rho(z)$ and diffusivities in the inhomogeneous z-direction $D_z^{BD}(z)$ (filled symbols, left y-axis) and $D_z^{MD}(z)$ (unfilled symbols, right y-axis), calculated from BD and MD simulations, respectively, of HS fluids exhibiting sinusoidal density profiles with $\rho_{avg} = 0.573$, $\rho(z) = [0.287, 0.860]$, and wavelengths $\lambda = 12$, 6, 2.5, 1.2, and 1.0. Note that the y-axes have different absolute scales, but both span an order-of-magnitude as shown.

To further simplify the analysis, we fix the average density ρ_{avg} and the amplitude A defining $\rho(z)$ such that we consider only structural variations with respect to inhomogeneity wavelength λ. We choose $\rho_{\text{avg}} = 0.573$, which corresponds to a moderately dense bulk HS fluid (the freezing density of the isotropic fluid occurs at $\rho_{\text{f}}^{\text{bulk}} = 0.943$). The density range $\rho(z) = [0.287, 0.860]$ encompasses nearly two-thirds of the bulk HS fluid regime, across which mean bulk collision frequencies vary by approximately an order of magnitude. For these density ranges, the potential depths of $\varphi^{\text{osc}}(z)$ range from $|\varphi_{\text{max}}^{\text{osc}}(z) - \varphi_{\text{min}}^{\text{osc}}(z)| < 1$ for $\lambda = 1.0$ up to $|\varphi_{\text{max}}^{\text{osc}}(z) - \varphi_{\text{min}}^{\text{osc}}(z)| \approx 12$ when $\lambda = 24$.

For the longer wavelengths in Fig. 4.1 (e.g., $\lambda \geq 6$), both $D_{\text{z}}^{\text{BD}}(z)$ and $D_{\text{z}}^{\text{MD}}(z)$ are negatively correlated with local density, meaning that mobility is slowed through more highly packed regions. This is intuitively expected based on the physics of the bulk HS fluid, which exhibits a negative correlation between self-diffusivity and density. However, as the inhomogeneity wavelength decreases to $\lambda \leq 3$, correlations between local density and diffusivity exhibit intriguing sensitivities to both wavelength λ and the type of microscopic dynamics. First consider $\lambda = 2.5$, where $D_{\text{z}}^{\text{BD}}(z)$ exhibits negative correlations with $\rho(z)$ (not unlike those at larger λ), while $D_{\text{z}}^{\text{MD}}(z)$ becomes virtually insensitive to the strong variations in local density, the latter a remarkable behavior we noted previously [25]. Even more interesting and distinct behaviors emerge between $2.5 \geq \lambda \geq 1.0$. Here, the BD systems exhibit *two* sequential crossovers in terms of the correlations between $D_{\text{z}}^{\text{BD}}(z)$ and $\rho(z)$, from negative at $\lambda = 2.5$ to positive at $\lambda = 1.2$ and back to negative at $\lambda = 1.0$. Meanwhile, in the MD systems, there emerges a growing positive

correlation between $D_{\mathrm{z}}^{\mathrm{MD}}(z)$ and $\rho(z)$ that is most prominent around $\lambda = 1.2$ to 1.0, an observation made in other MD studies [149, 157] of highly confined fluids exhibiting density profiles of $\lambda \simeq 1$.

Altogether, local diffusivities from both BD and MD are qualitatively similar for sufficiently long λ, where they display behaviors that appear to be simple extensions of bulk-fluid like physics. But non-trivial static-dynamic correlations specific to BD or MD emerge as λ decreases below several particle diameters, not only highlighting that intuitions about local behaviors should not be naïvely extrapolated from bulk fluids, but also offering evidence that the expected qualitative connections between position-dependent mobilities of systems governed by different microscopic dynamics do not hold in strongly inhomogeneous states.

The comparisons in Fig. 4.1 are recast and augmented in the left panels of Fig. 4.2, which directly compare local diffusivities versus densities for BD (top) and MD (bottom) over expanded collections of λ values. Here, the transition from negative correlations at large λ to the breakdown of bulk-like behaviors at small λ is evident, demonstrating that $\rho(z)$ does not exhibit any "universal" relationship with local particle mobility in strongly inhomogeneous fluids. For $\lambda \geq 12$, the curves for BD and MD are virtually indistinguishable from the respective D_{ρ}^{bulk} versus ρ curves, indicating that for sufficiently gradual density variations, particles experience a continuum of bulk-like regions with respect to local mobility. Of course, this must be true as $\lambda \to \infty$ for the finite A considered here, but it is notable that even for such large amplitudes of $\rho(z)$, the characteristic inhomogeneity lengthscale must only reach several particle diameters to effectively reach this

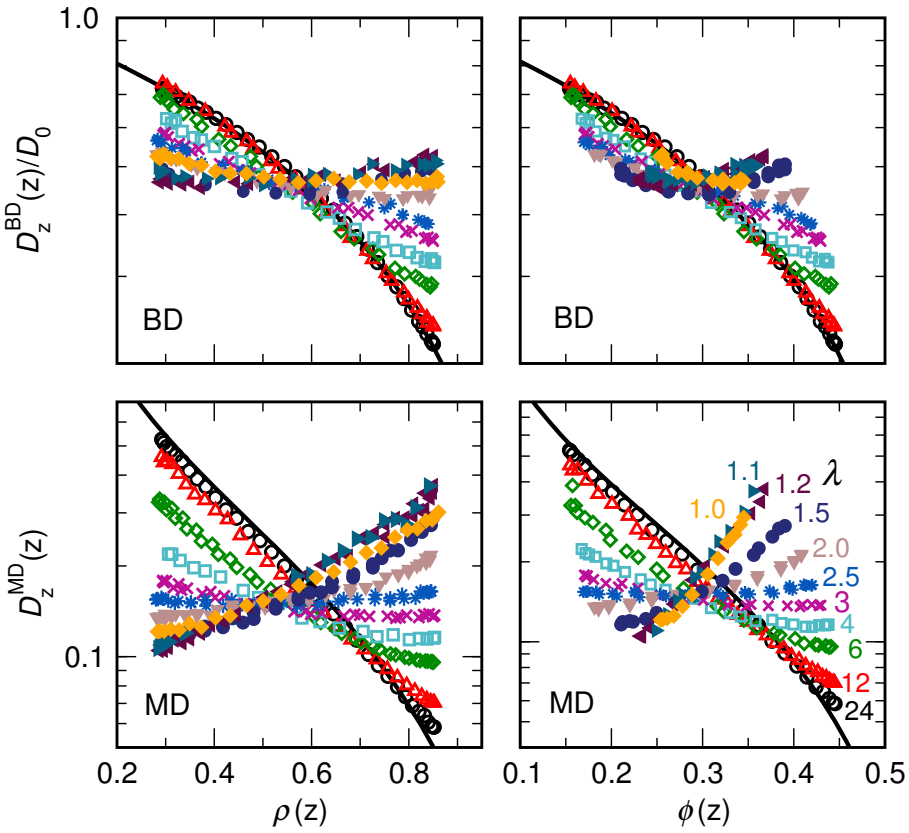

Figure 4.2: Position-dependent diffusivities in the inhomogeneous z-direction $D_z^{BD}(z)$ (top panels) and $D_z^{MD}(z)$ (bottom panels) plotted versus local density $\rho(z)$ (left panels) and local packing fraction $\phi(z)$ (right panels) for HS systems at $\rho_{avg} = 0.573$, $\rho(z) = [0.287, 0.860]$, and $\lambda = 24$ (black), 12, 6, 4, 3, 2.5, 2.0, 1.5, 1.2, 1.1 and 1.0 (gold). Data for the bulk HS fluid are shown as solid black lines.

limit regardless of microscopic dynamics. For $\lambda \leq 3$, however, the MD and BD do not generally exhibit qualitatively similar curvature: for $\lambda = 3.0$ and 2.5, the BD curves show appreciable variation in diffusivity while the MD curves are virtually flat; and for $\lambda = 2.0$ and 1.0, the BD and MD curves have opposite slopes (negative and positive, respectively). At even smaller wavelengths, we observe that the BD curves become increasingly flat while, as shown in the previous chapter, the MD curves exhibit strong positive correlations between $\rho(z)$ and $D_z^{\mathrm{MD}}(z)$ (especially around $\lambda \approx 1$.

Perhaps this lack of consistent correlation between local structure and dynamics arises because $\rho(z)$ is "too local" to be an adequate measure of the particles' structural environments. We address this in the right panels of Fig. 4.2, where we plot the same diffusivity data against local packing fraction $\phi(z)$, which for HS contains a greater amount of information about the nature of particle packing than $\rho(z)$. While the data for both MD and BD do modestly collapse around their respective D_ϕ^{bulk} versus ϕ curves, $\phi(z)$ is clearly not a qualitatively strong predictor of local mobility for these systems. In fact, this transformation arises rather trivially because $\phi(z)$ itself collapses as a function of $\rho(z)$ as λ decreases. Given such a straightforward relationship between $\phi(z)$ and $\rho(z)$, it is unsurprising that packing fraction does not reconcile MD and BD behaviors with respect to λ.

4.3.2 Local correlations between diffusivity and available space

In Fig. 4.3, we consider correlations between local diffusivity and a more microscopic static property: the local available space $\exp\{c^{(1)}(z)\}$, which quan-

tifies the fractional volume at z into which an additional HS particle can be *inserted without overlap*. Average available volume positively correlates with average diffusivity in the isotropic directions of bulk and inhomogeneous HS fluids more strongly than density or packing fraction [66], making it a natural quantity to examine on a position-dependent basis. Additionally, it is known that average and local measures of available volume provide very similar information compared to excess entropy [25, 66], a thermodynamic property that is more generalizable (i.e., applicable to non-HS fluids) and well-known to semi-quantitatively predict appropriately non-dimensionalized transport coefficients for a wide array of fluid systems [**?**, 38, 39, 49, 50, 53, 61, 65, 66, 85, 88, 89, 108, 116, 126, 134, 143–146, 148, 151, 166, 170, 171, 190]. Before moving forward, note that $\exp\{c^{(1)}(z)\}$ is *not* simply equivalent to the void space defined by $\phi_{\text{void}}(z) = 1 - \phi(z)$ as it accounts for the space excluded to particle centers.

Significantly, we observe that the $D_{\text{z}}^{\text{BD}}(z)$ curves at various λ roughly collapse (within 20%) onto a single curve as a function of $\exp\{c^{(1)}(z)\}$, at least relative to the $D_{\text{z}}^{\text{MD}}(z)$ curves, which exhibit highly non-trivial λ-dependent behaviors, including broadly positive (e.g., $\lambda = 12$), negative (e.g., $\lambda = 2$), and completely decoupled (e.g., $\lambda = 2.5, 1.0$) correlations with $\exp\{c^{(1)}(z)\}$. For example, consider the wavelength $\lambda \leq 1.5$: $D_{\text{z}}^{\text{BD}}(z)$ values show some curvature relative to $\exp\{c^{(1)}(z)\}$ (particularly at $\lambda = 1.5$), but overall do not significantly deviate from the bulk reference curve. In contrast, the corresponding MD curves collapse very poorly, with $D_{\text{z}}^{\text{MD}}(z)$ varying by factors of about 3 when $\lambda = 1$, despite the fact that $\exp\{c^{(1)}(z)\}$ is virtually homogeneous at these wavelengths. This dichotomy

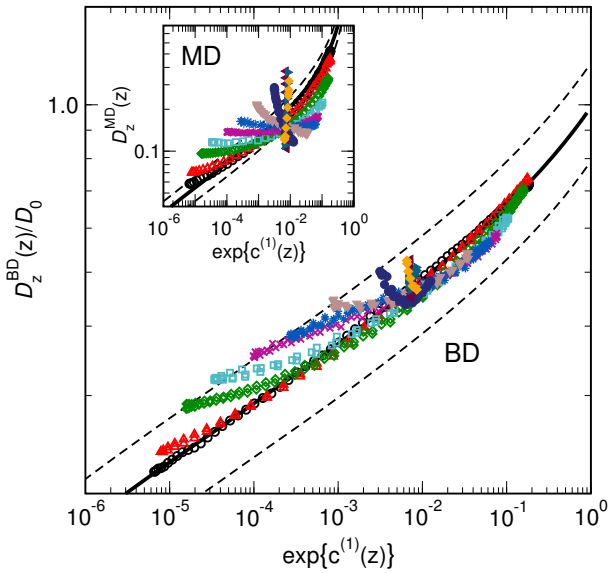

Figure 4.3: Position-dependent diffusivities in the inhomogeneous z-direction $D_z^{BD}(z)$ and $D_z^{MD}(z)$ (inset) plotted versus fractional available space $\exp\{c^{(1)}(z)\}$ for HS at $\rho_{avg} = 0.573$, $\rho(z) = [0.287, 0.860]$, and $\lambda = 24$, 12, 6, 4, 3, 2.5, 2.0, 1.5, 1.2, 1.1 and 1.0 (symbols consistent with Fig. 4.2). Data for the bulk HS fluid are shown as solid lines and $\pm 20\%$ bounds on the bulk curves are plotted as black dashed lines.

in data collapse reinforces the idea that static-dynamics correlations for isotropic fluids do not necessarily generalize to describe particle mobility in inhomogeneous fluids, and furthermore that the quality of mapping between bulk and local behaviors is sensitive to the governing microscopic dynamics.

4.3.3 Do local correlations change based on alternative scalings of diffusivity?

We conclude our discussion of local dynamics by examining whether the poor qualitatively mapping between $D_{\mathrm{z}}^{\mathrm{BD}}(z)$ and $D_{\mathrm{z}}^{\mathrm{MD}}(z)$ might be corrected by using alternative diffusivity scalings already known to relate bulk transport coefficients from BD and MD simulations. The scalings we consider derive from fluids interacting via inverse power law (IPL) pair potentials, i.e., $\varphi(r) = \epsilon(\sigma/r)^{\mu}$, which are a reference model for dense fluids dominated by interparticle repulsions. For IPL fluids, it has been shown that there exists a one-to-one mapping between appropriately reduced (i.e., non-dimensionalized) long-time bulk diffusivities from MD and BD [61, 113, 170, 171]. These diffusivities are

$$\widetilde{D}_{\rho}^{\mathrm{MD}} = D_{\rho}^{\mathrm{MD}} \rho^{1/3} \sqrt{m/k_B T} \tag{4.6}$$

where $\rho^{1/3}$ corresponds to the mean interparticle spacing, and $D_{\rho}^{\mathrm{BD}}/D_0$, respectively. Additionally, a heuristic function [167] based on the leading order dependencies of D_{ρ}^{BD} and D_{ρ}^{MD} upon density has been shown to quantitatively relate these quantities, given by

$$1 - D_\rho^{\mathrm{BD}}/D_0 = \{1 + c_1 \widetilde{D}_\rho^{\mathrm{MD}} + c_2 (\widetilde{D}_\rho^{\mathrm{MD}})^{3/2}\}^{-1} \tag{4.7}$$

where c_1 and c_2 are constants. Eqn. 4.7 acts as a universal curve correlating $\widetilde{D}_\rho^{\mathrm{MD}}$ and D_ρ^{BD}/D_0 over a wide range of bulk state points not only for "hard" IPL fluids but also for diverse "soft" model fluids that exhibit complex diffusivity trends [99, 167]. For our purposes, these non-dimensional scalings represent an important test because IPL fluids with sufficient sharpness (i.e., $\mu \geq 48$) behave quite similarly to the HS system with respect to structure and long-time relaxation for the density range considered here [80, 113].

Does this one-to-one mapping between BD and MD transport coefficients generally apply to the local diffusivities of inhomogeneous fluids? To address this question, one necessary task is to identify an appropriate mean interparticle spacing to use when non-dimensionalizing $\widetilde{D}_{\mathrm{z}}^{\mathrm{MD}}(z)$. Using ρ_{avg} (as in the bulk case), would only trivially shift all of the $\widetilde{D}_{\mathrm{z}}^{\mathrm{MD}}(z)$ values considered thus far regardless of λ, since we have kept ρ_{avg} constant. However, it is evident from Figs. 4.1-4.3 that λ affects the qualitative correspondence between BD and MD. Instead, a straightforward way to capture the influence of λ is to use local density $\rho(z)$ or the weighted densities from the previous chapter.

In Fig. 4.4, we plot $D_{\mathrm{z}}^{\mathrm{MD}}(z)$ scaled by $\rho(z)$ versus the appropriately reduced $D_{\mathrm{z}}^{\mathrm{BD}}(z)$ values. Of course, for large wavelengths where $D_{\mathrm{z}}^{\mathrm{BD}}(z)$ and $D_{\mathrm{z}}^{\mathrm{MD}}(z)$ converge to locally "bulk-like" values (e.g., $\lambda \geq 12$), and the $\widetilde{D}_{\mathrm{z}}^{\mathrm{MD}}(z)$ versus $1 - D^{\mathrm{BD}}/D_0$ curves follow the form of eqn. 4.7; however, at smaller wavelengths

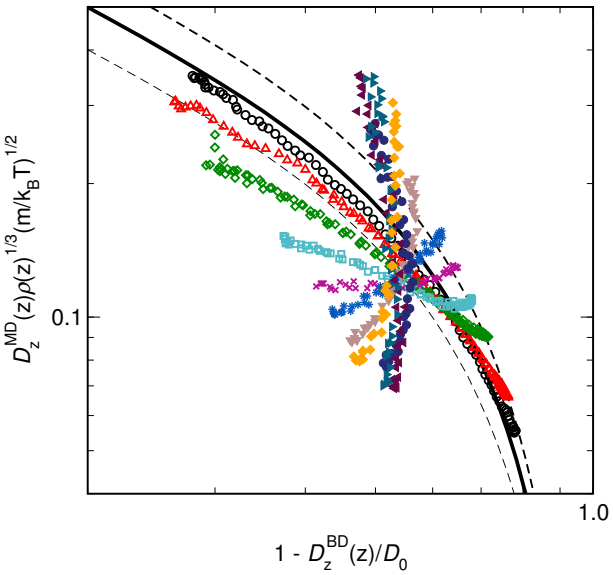

Figure 4.4: Non-dimensionalized position-dependent diffusivity in the inhomogeneous z-direction in MD simulations $\widetilde{D}^{\mathrm{MD}}$ *versus* the fractional slowdown in BD diffusivity relative to the dilute limit, $1 - D_z^{\mathrm{BD}}(z)/D_0$. The density used to scale $\widetilde{D}^{\mathrm{MD}}$ is local density $\rho(z)$. Curves are for HS systems at $\rho_{\mathrm{avg}} = 0.573$, $\rho(z) = [0.287, 0.860]$, and $\lambda = 24$, 12, 6, 4, 3, 2.5, 2, 1.5, 1.2, 1.1 and 1.0 (symbols consistent with Fig. 4.2). The bulk relationship is shown as a solid black line and $\pm 20\%$ bounds on the bulk curve are plotted as black dashed lines.

(e.g., $\lambda \leq 6$), the bulk relationship between MD and BD diffusivities clearly breaks down. Given that the mapping between $\widetilde{D}^{\mathrm{MD}}$ and D^{BD}/D_0 is rigorous for repulsive model fluids [61, 170], this breakdown confirms, perhaps even more so than the previous plots, that bulk-derived connections between BD and MD transport coefficients demand scrutiny in the context of inhomogeneous particle mobility. Finally, note that we also tested the more coarse-grained Van der Waals and Tarazona weighted densities $\bar{\rho}^{\tau}(z)$ that arise in density functional theory (DFT) for inhomogeneous fluids [44, 73], but these result in very similar curves.

4.3.4 Average diffusivity dependence on structure is sensitive to choice of microscopic dynamics

In the upper panels of Fig. 4.5, we examine the λ-dependence of measured average diffusivities $D_{\mathrm{z}}^{\mathrm{avg}}$ and D_{xy}, which characterize some aspects of global single-particle mobility, and compare them with analytically derived "model" predictions of diffusivity for both BD and MD systems. Average diffusivity in the inhomogeneous direction is defined as [21]:

$$D_{\mathrm{z}}^{\mathrm{avg}} = \int_0^{\lambda/2} D_{\mathrm{z}}(z)\rho(z)\mathrm{d}z \; / \int_0^{\lambda/2} \rho(z)\mathrm{d}z \tag{4.8}$$

which results from the fact that $D_{\mathrm{z}}^{\mathrm{avg}}$ is the average of the diffusivities of individual particles that are distributed according to $\rho(z)$.

For a given choice of microscopic dynamics, the measured $D_{\mathrm{z}}^{\mathrm{avg}}$ and D_{xy} curves are roughly coupled as a function of λ, but the pairs of curves exhibit qualitatively distinct λ-dependencies for BD versus MD. Namely, the average BD

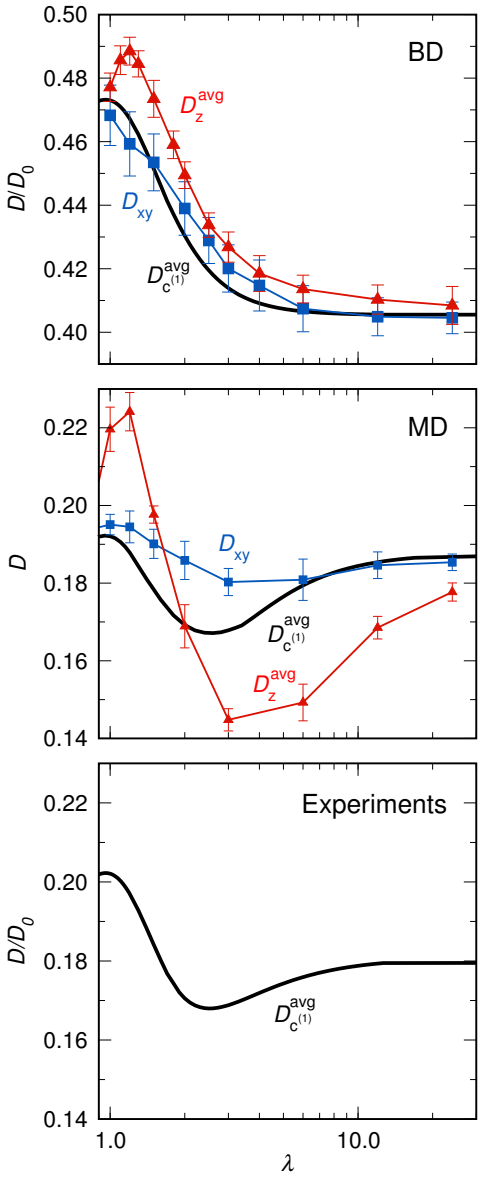

Figure 4.5: Average diffusivities D_z^{avg} (red triangles) and D_{xy} (blue squares) versus wavelength λ for HS fluids at $\rho_{avg} = 0.573$ and $\rho(z) = [0.287, 0.860]$. Solid black lines are model predictions $D_{c^{(1)}}^{avg}$ via Eqn. 4.9 (see discussion in text). The top and middle panels corresponds to results obtained for BD and MD systems, respectively. The model prediction in the bottom panel draws upon experimental data collected for a variety of pseudo-HS colloids [122].

diffusivities overall decrease upon transitioning from short λ, where they converge to the D_{ρ}^{bulk} associated with ρ_{avg} as $\lambda \to 0$, to long λ, where they converge to a noticeably-shifted analytical limit of Eqn. 4.8 as $\lambda \to \infty$. In contrast, the MD curves exhibit global minima around $\lambda \simeq 3$ and the long-λ limit is only subtly shifted from the bulk limit. The magnitudes of $D_{\text{z}}^{\text{avg}}$ are also less sensitive to λ for BD relative to MD, with diffusivity increasing by ≈15% versus ≈60% between $3.0 \geq \lambda \geq 1.0$, respectively. Interestingly, both the BD and MD curves both exhibit relative maxima at $\lambda \simeq 1$, which approximately corresponds to stacked "sheets" of particles, and recalls previous studies showing that strongly layered density profiles maximize HS particle mobility along slit-pores [65]. Taken altogether, however, the measured curves demonstrate that despite the imposition of identical inhomogeneous static structures, different global diffusive trends emerge depending on the choice of microscopic dynamics.

The predicted curves in Fig. 4.5 are calculated using the expression

$$D_{c^{(1)}}^{\text{avg}} = \int_0^{\lambda/2} D_{c^{(1)}}^{\text{bulk}}[c^{(1)}(z)]\rho(z)\mathrm{d}z \Big/ \int_0^{\lambda/2} \rho(z)\mathrm{d}z \tag{4.9}$$

which involves averaging over local diffusivity predictions derived by substituting the λ-dependent $c^{(1)}(z)$ profiles into the *bulk* HS relationship between diffusivity and fractional available volume. This approach is based on the idea that diffusion can be conceptualized as particles probing unoccupied space in their vicinity [66, 149], and we showed in the previous chapter that Eqn. 4.9 was an approximate predictor of diffusivities for inhomogeneous MD systems [25]. Here, we find it is

equally successful for BD, despite the qualitatively different behaviors of BD and MD with respect to λ: the model lines in both cases approximately capture all extremes and converge to the correct short- and long-λ limits.

This suggests that the underlying physics connecting structure and diffusivity in the bulk fluid, while not necessarily directly applicable to *local* particle motions (see Fig. 4.3), nonetheless play a more subtle role in governing *average* diffusion along inhomogeneous paths–regardless of the type of governing microscopic dynamics. With this in mind, the differences between the predicted (and measured) diffusivity curves for BD and MD must emerge due to the different correlations between dynamics and available volume in the respective bulk fluids. For example, these correlations between static environment and dynamics in MD subsequently give rise to the prominent minimum in diffusivity at $\lambda \simeq 3$, which apparently presents an inefficient (dynamically frustrating) distribution of available volume. In contrast, the uniform "frictional effects" in the BD system wash out this effect and hence eliminate the minimum.

4.3.5 Comparisons against experiments on colloidal suspensions

Given that the BD and MD systems exhibit qualitatively different average diffusivities (via both measurement and prediction), a natural issue to consider is what these curves might look like for similar *experimental* systems, i.e., pseudo-HS Brownian suspensions that are intrinsically subject to interparticle hydrodynamic interactions. We address this issue in the bottom panel of Fig. 4.5, where we plot $D^{\text{avg}}_{c^{(1)}}$ predicted with Eqn. 4.9 using a $D^{\text{bulk}}_{c^{(1)}}$ curve fit to self-diffusivity data collected

for a variety of pseudo-HS colloids [122]. Interestingly, the predicted curve for the experimental systems has a different qualitative shape than the corresponding overdamped BD curves, and is instead more similar to the MD curves, exhibiting a prominent minima at $\lambda \simeq 3$. This is surprising given that BD might intuitively be considered a better approximation of experiments due to its incorporation of the stochastic movements characteristic of real colloids.

While it is beyond the scope of this study whether the model prediction for experiments is borne out by experiments on suspensions exhibiting sinusoidal density variations, comparisons between all three of the $D^{\text{avg}}_{c^{(1)}}$ curves demonstrate that one should be wary of assuming that even the *average* transport coefficients of inhomogeneous fluids straightforwardly map between systems governed by different microscopic dynamics. Furthermore, these findings suggest that in order to approximate real colloidal physics, one might simply choose MD (rather than BD) if chiefly interested in efficiency–or alternatively use techniques, e.g., Stokesian dynamics, that better capture the physics of colloidal suspensions [30, 48, 194].

4.3.6 A generalized test of correlations between average diffusivity and available space

Drawing upon the predictive capability of Eqn. 4.9, we can also rapidly survey a larger variety of $\rho(z)$ profiles, with not only diverse wavelengths λ, but also average densities ρ_{avg} and amplitudes A (recall Eqn. 4.1). In the top panel of Fig. 4.6, we examine the λ-dependence of $D^{\text{avg}}_{c^{(1)}}$ predictions for BD at several amplitudes A given an average density $\rho_{\text{avg}} = 0.6$ (comparable to $\rho_{\text{avg}} = 0.573$ in

Figs. 4.1-4.5). It is evident that the qualitative λ-dependence of the $D^{\text{avg}}_{c^{(1)}}$ curves is invariant with respect to A, where extrema in the functional form of $D^{\text{avg}}_{c^{(1)}}(\lambda|A)$ simply become more exaggerated as A increases. In other words, average particle mobility becomes increasingly sensitive to wavelength as the density variations increase in scale. The form of $D^{\text{avg}}_{c^{(1)}}(\lambda)$ also remains the same for fluids with $0.2 \leq \rho_{\text{avg}} \leq 0.8$ and appropriate ranges of A. (Note that any choice of A must necessarily avoid accessing $\rho(z) \leq 0$ or any $\rho(z)$ large enough that the functional relationship between $D^{\text{bulk}}_{c^{(1)}}$ and $c^{(1)}$ would break down.) Similar findings apply for the analogous families of curves as calculated for MD and experimental systems, though naturally the respective functional forms of $D^{\text{avg}}_{c^{(1)}}(\lambda)$ resemble those in Fig. 4.5.

As a closing consideration, we compare the top and bottom panels in Fig. 4.6 to demonstrate a subtle but important point regarding the connection between available space and particle mobility: while $\exp\{c^{(1)}(z)\}$ profiles can be used via Eqn. 4.9 to approximately predict diffusivity, simply perturbing fluid structure to generate relatively more available space on average does not *universally* result in relatively faster relaxation processes, though this approach will certainly work in many common cases (see, e.g., the following chapter). The bottom panel of Fig. 4.6 shows the average fraction of available space as defined by

$$\langle \exp\{c^{(1)}(z)\} \rangle = (2/\lambda) \int_0^{\lambda/2} \exp\{c^{(1)}(z)\} \mathrm{d}z \tag{4.10}$$

for the λ, A, and ρ_{avg} values presented in the top panel. It is evident that the most available space on average emerges upon imposition of long-wavelength density

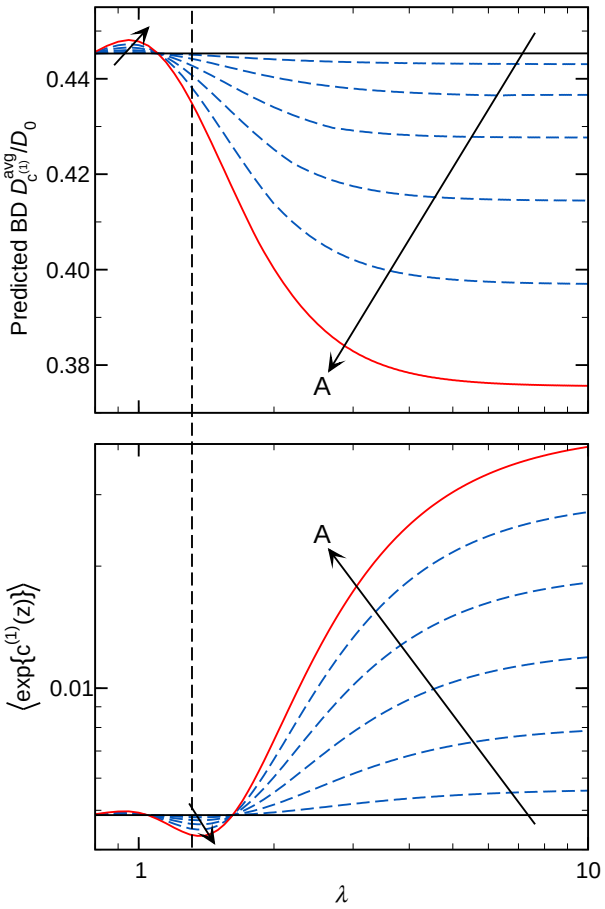

Figure 4.6: $D_{c^{(1)}}^{\text{avg}}$ (top) and average available space $\langle \exp\{c^{(1)}(z)\}\rangle$ (bottom) versus λ for BD HS systems with $\rho(z)$ profiles defined by $\rho_{\text{avg}} = 0.6$ and amplitudes $A = 0.0$, 0.1, 0.2, 0.3, 0.4, 0.5, and 0.6 (see Eqn. 4.1). The solid black line ($A = 0.0$) corresponds to the bulk fluid and the red line ($A = 0.6$) represents the series of systems most similar to those analyzed in Figs. 4.1-4.5 (i.e., $\rho_{\text{avg}} = 0.573$, $A = 0.573$). See text for discussion of the vertical dashed line.

variations. This is due to the imposition of wide regions of relatively low density, combined with the bulk-like negative logarithmic correlation between $\exp\{c^{(1)}(z)\}$ and $\rho(z)$ at long λ. However, as seen in the top panel of Fig. 4.6, this same limit coincides with global minima in average diffusivity because particles must also traverse equally wide regions of high density where diffusivity slows down (regions that are more important from a "mass flux" perspective; see Eqn. 4.8).

While this means there is not a universal positive correlation between diffusivity and available space across all lengthscales of inhomogeneity, we do note that these quantities are roughly positively correlated below $\lambda \leq 1.2$, marked in Fig. 4.6 by a vertical dashed line. Most studies examining static-dynamic correlations for inhomogeneous fluids have focused on this regime (i.e., $\lambda \simeq 1$), hence the previous success in using available volume (or, equivalently, excess entropy) to predict average transport coefficients [66]. But for $\exp\{c^{(1)}(z)\}$ profiles to be useful as general predictors of diffusivity for inhomogeneous fluids, we find they should be used in the context of Eqn. 4.9, which requires an accurate functional relationship between bulk diffusivity and available volume.

4.4 Conclusions

Unlike the simple scalable relationships that link the transport coefficients of bulk isotropic fluids treated governed by Brownian versus Newtonian mechanics, the results presented here demonstrate that local and global single-particle mobilities of inhomogeneous fluids *are qualitatively sensitive* to the type of governing microscopic dynamics. As we show, when available volume and particle density

exhibit strong inhomogeneities in a fluid, differences between how mobility correlates to density due to the microscopic dynamics (reflected even in the bulk fluid) should be expected to produce a nontrivial relationship between average transport properties of inhomogeneous fluids treated by MD and BD that depends on the details of the density profile.

For even the simple systems considered here, correlations between local diffusivity and static structure non-trivially depend upon inhomogeneity wavelength, and for wavelengths below several particle diameters, these correlations are distinct for BD and MD. Accordingly, it is problematic to identify a physically-intuitive local static quantity (i.e., a "mechanistic" description) that universally predicts both isotropic (e.g., bulk) and position-dependent mobility for these systems, and existing functional one-to-one relationships between BD and MD transport coefficients–valid for bulk systems with diverse interaction potentials–do not apply to position-dependent particle motions in strongly inhomogeneous fluids.

An overarching goal of this study was to compare two types of physics normally associated with "colloidal" and "atomic" fluid regimes–as exemplified by BD and MD, respectively–but our findings suggest that these designations might be problematic. This originates from our discovery of a simple expression (Eqn. 4.9) that predicts the dependence of *average* particle mobility upon static structure via information about available space and bulk diffusivity. A highlight here is that the expression is successful for both BD and MD, capturing the qualitative dichotomies that emerge between their respective diffusivities as a function of inhomogeneity wavelength. More crucially, similar predictions for experimental pseudo-HS col-

loids qualitatively differ with BD (i.e., overdamped Langevin) simulations, with MD results instead better reflecting the behaviors expected from the experimental systems. Thus, if one is interested in studying the dynamics of strongly inhomogeneous colloidal suspensions via computer simulations, these results not only recommend MD *over* BD treated at the simplest level, but also emphasize the need for further comparisons with more sophisticated techniques incorporating effects due to inertia and hydrodynamic interactions [30, 48, 194].

Chapter 5

Structure-mobility relationships of confined fluids undergoing supercooling

5.1 Introduction

Confined fluids exhibit inhomogeneous structural and relaxation properties, which are general features of materials subjected to position-dependent external fields. Because confined fluids emerge in a diverse array of natural and technological contexts (e.g., water in biological media, polymer thin films, etc.), considerable attention has been directed at understanding how their static and dynamic properties relate to bulk fluid physics observed under similar conditions. As a result, the static properties of confined fluids, such as local one-body density $\rho(z)$, are now well-understood in terms of physical intuition (e.g., emergence of particle layering near boundaries to relieve packing frustration [90, 101]) and can be predicted using microscopic approaches like density functional theory [172, 226].

Reproduced in part with permission from J.A. Bollinger, A. Jain, J. Carmer, and T.M. Truskett, "Local structure-mobility relationships of confined fluids reverse upon supercooling." *J. Chem. Phys.*, 2015, 142 (16), p. 161102 (DOI: 10.1063/1.4919688). Copyright 2015 American Institute of Physics. J.A. Bollinger performed computer simulations, analyzed results, created figures, and wrote the manuscript.

However, much less is understood about what controls the dynamics of inhomogeneous fluids, and only recently have efforts broadened to include developing theories [5, 20, 105, 110–112, 157] and other tools [35, 81, 86, 149, 155] for characterizing particle dynamics both on a spatially-averaged basis and as a function of position.

Given the difficulty of applying first principles to understand the dynamics of such systems, progress has been made by virtue of use pragmatic approaches, e.g., application and testing of semiempirical, quasi-universal scaling laws that relate transport coefficients of interest to static properties [49, 61, 85, 108, 143, 144, 151, 166, 170, 171, 190]. To wit, it has been shown that single-particle diffusivities, relaxation times, and viscosities along structurally-invariant (i.e., isotropic) dimensions of simple confined fluids can be predicted based on knowledge of how dynamic properties of the bulk fluid relate to static quantities including excess entropy s^{ex} (relative to the ideal gas) and fractional available space $\exp\{c^{(1)}\}$ (or insertion probability p_0), which characterize short-range static correlations and particle packings, respectively [**?**, 38, 65, 66, 88, 126, 134, 145, 146, 148].

In this spirit, one might expect that local particle mobility in an inhomogeneous fluid should similarly correlate with position-dependent static properties; in other words, the way particles navigate through the inhomogeneous environment might be encoded in the physics of motion observed in a bulk, homogeneous fluid. However, the validity of such a connection has yet to be carefully and systematically evaluated. Despite providing other important insights, previous investigations directly measuring inhomogeneous dynamics have studied a variety of fluids governed by disparate interactions, external fields, and conditions, and they have also

used different protocols to characterize the dynamics [25, 26, 51, 111, 149, 155, 157]. As a result, even fundamental questions related to confined (and more generally inhomogeneous) fluids remain open: Do local and average correlations between particle mobility and structure universally reflect bulk behaviors? Do new structure-mobility relations emerge as inhomogeneous fluids are supercooled toward glass transitions? And does the choice of microscopic dynamics affect these qualitative trends?

To address these questions, we analyze computer simulations of binary hard-sphere (HS) mixtures confined in slit-pores using techniques based on the Fokker-Planck diffusion equation to systematically characterize how position-dependent and spatially-averaged particle mobilities–as quantified by single-particle diffusion coefficients–relate to local and average static properties in fluids that are approaching the glass transition with increasing packing fraction. In particular, we focus on diffusion coefficients *in the direction perpendicular to the walls*, along which particles traverse inhomogeneous free-energy landscapes and can be expected to display strong variations in diffusive mobility. (These are complemented by average diffusion coefficients in the directions parallel to the walls, where particles encounter isotropic structure.) Notably, these thin film systems are designed to mimic real colloidal thin films previously realized in experiments [51, 155].

First, based on comparisons between local structure and dynamics, we demonstrate that signatures in diffusivity profiles near confining planes are insensitive to considerable structural transformations that occur with increasing packing frustration, even if those transformations coincide with the onset of cooperative

motion (i.e., supercooling). This lends further support to the notion–introduced in previous chapters–that there is no "master" correlation between dynamic and static properties on a position-dependent basis. We also discuss how the findings from above and below the emergence of supercooling nicely tie together seemingly incompatible observations from previous simulations and experiments on similar thin film systems. We then demonstrate that while local dynamics are not readily predictable based on structural measurements, spatially-averaged diffusion coefficients either perpendicular or parallel to the walls are predictable based on knowledge of the available (void) space for (i.e., probability of) particle insertion, even under increasingly glassy conditions. Notably, we consider results from simulations propagated with either classic (Newtonian) molecular dynamics or Brownian dynamics protocols, demonstrating that–at least for highly-packed confined scenarios–there is little effective difference in local and average dynamic results.

5.2 Methods

5.2.1 Model interactions

We examine bulk and confined binary mixtures of small (sm) and large (lg) hard spheres (HS) approximated by a steeply-repulsive Weeks-Chandler-Andersen (WCA) pair potential [37] between particles i and j, adapted for multiple particle diameters: $\varphi_{i,j}(r) = 4\epsilon([\sigma_{\rm sm}/(r+\Delta)]^{48} - [\sigma_{\rm sm}/(r+\Delta)]^{24}) + \epsilon$ for $r \leq (2^{1/24}\sigma_{\rm sm} - \Delta)$ and $\varphi_{i,j}(r) = 0$ for $r > (2^{1/24}\sigma_{\rm sm} - \Delta)$, where ϵ is the characteristic energy scale; r is the interparticle separation; σ denotes particle diameter;

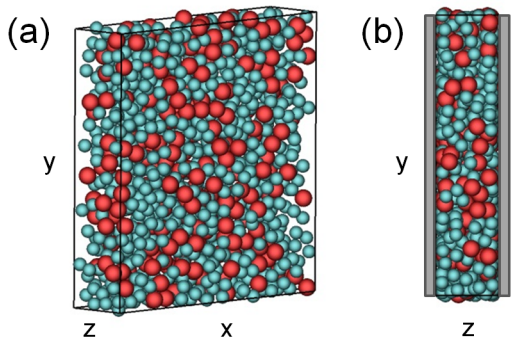

Figure 5.1: Illustration of confined binary mixture comprising small (blue) and large (red) particles.

and $\Delta = \sigma_{\rm sm} - (1/2)(\sigma_i + \sigma_j)$. The binary mixtures are composed of spheres with size ratio $\sigma_{\rm lg}/\sigma_{\rm sm} = 1.3$, volume-proportional masses $m_{\rm lg}/m_{\rm sm} = (\sigma_{\rm lg}/\sigma_{\rm sm})^3$, and composition defined by the fraction of small particles $x_{\rm sm} = 0.75$. These parameters mimic colloidal mixtures investigated in recent experiments [51, 155]. Below, we implicitly non-dimensionalize quantities via appropriate combinations of the characteristic lengthscale $\sigma_{\rm sm}$ and energy scale $\epsilon = k_{\rm B}T$, where $k_{\rm B}$ is Boltzmann's constant, and T is temperature.

5.2.2 Simulation protocols

Periodic boundary conditions are applied in all directions for the bulk systems, while for the confined systems (see Fig. 5.1), particles are situated in slit-pores of size $H = 5$ between two reflective walls placed at $z = \pm H/2$, with periodic boundary conditions applied in the x- and y-directions. The wall-particle inter-

actions are analogous to the hard-sphere-like interactions between particles, but defined such that the center of particle i can access $-(H-\sigma_i)/2 \lesssim z \lesssim (H-\sigma_i)/2$. Spatially averaged packing fractions are given by $\phi^{\text{avg}} = (\pi/6)\rho[x_{\text{sm}} + \sigma_{\text{lg}}^3(1-x_{\text{sm}})]$, where $\rho = (N_{\text{sm}} + N_{\text{lg}})/V$ is the combined number density of both species and V is volume. Here, the ϕ^{avg} values for the confined fluids are defined by the total (surface- rather than center-accessible) slit pore volume.

We propagate particle trajectories governed by either conventional molecular dynamics (MD) or Brownian dynamics (BD) (i.e., overdamped Langevin ignoring hydrodynamic interactions), where we simulate systems of $N_{\text{sm}} + N_{\text{lg}} = 2400$ particles using GROMACS 4.5.5 [79]. MD trajectories are generated by integrating the Newtonian equations of motion with a time step of 0.001 while fixing temperature with a Nose-Hoover thermostat. BD trajectories are generated via the overdamped Langevin equation (ignoring hydrodynamic interactions), where the position $\mathbf{r}_i$ of particle i is propagated with a time-step of 0.01 according to [2, 52]: $\mathbf{r}_i(t+\Delta t) = \mathbf{r}_i(t) + D_{\sigma_i}^{\infty}\Delta t \mathbf{F}_i(\mathbf{r}_i(t)) + \boldsymbol{\xi}_i(t)$. Here, $D_{\sigma_i}^{\infty}$ is the infinite dilution diffusivity, $\mathbf{F}_i(t)$ is the net force due to interparticle and wall interactions, and $\boldsymbol{\xi}_i(t)$ is the stochastic contribution. We set $D_{\sigma_{\text{sm}}}^{\infty} = 0.001$ and $D_{\sigma_{\text{lg}}}^{\infty}/D_{\sigma_{\text{sm}}}^{\infty} = \sigma_{\text{sm}}/\sigma_{\text{lg}}$, and in each direction, $\xi_i(t) = r^{\text{G}}(t)\sqrt{2D_{\sigma_i}^{\infty}\Delta t}$, where $r^{\text{G}}(t)$ is a Gaussian noise with $\langle r^{\text{G}}(t)\rangle = 0$ and variance $\sigma^2 = 1$.

To generate bulk and confined packings at high ϕ^{avg}, we initialize systems of near-"point" particles in simulation boxes with xy-lengths $L_{\text{xy}} = \{(\pi/6)(N_{\text{sm}} + N_{\text{lg}})[x_{\text{sm}} + \sigma_{\text{lg}}^3(1-x_{\text{sm}})]/(\phi^{\text{avg}}H)\}^{1/2}$ and z-length H, which effectively have low $\phi_{\text{init}}^{\text{avg}} \ll \phi^{\text{avg}}$. We then follow the method of Lubachevsky and Stillinger [133],

in which particle diameters are grown linearly with time during a simulation according to the dimensionless growth rate Γ until they reach their full sizes and the system is at ϕ^{avg}. We execute these "compressions" via MD simulations with effective $\Gamma < 1\text{x}10^{-6}$, which allows us to avoid generating partially jammed (i.e., non-equilibrated) structures for all presented ϕ^{avg}. Further equilibration and production runs (MD and BD) are then initialized with the final structures.

5.2.3 Characterizing diffusive dynamics

To characterize particle motions, we calculate mean-squared displacements (MSDs) and diffusivities in the structurally isotropic *and* inhomogeneous directions of the bulk and confined systems. Average diffusivities D^{avg} in the bulk systems and *parallel* to the walls in the confined systems characterize motions in isotropic directions, and are derived by fitting the long-time behavior of the MSD of all the particles to the Einstein relation $\langle \Delta \mathbf{r}^2 \rangle = 2dD\Delta t$. In the bulk (confined) case, $\langle \Delta \mathbf{r}^2 \rangle$ is the MSD in the x-, y-, and z-directions (x- and y-directions) over lag-time Δt and dimensionality $d = 3$ ($d = 2$).

In line with the work in previous chapters, diffusivities in the inhomogeneous z-direction of the confined fluids are generally position-dependent and cannot be calculated via the Einstein relation because particles are subjected to locally non-cancelling potentials of mean force [86, 124]. Particle motions along the z-coordinate are instead accurately described [149] by the 1D Fokker-Planck (or Smoluchowski) equation

$$\frac{\partial G}{\partial t} = \frac{\partial}{\partial z}\left(D_{\mathrm{z}}(z) e^{-\beta F(z)} \frac{\partial}{\partial z}[e^{\beta F(z)} G] \right) \tag{5.1}$$

where the position-dependent diffusion coefficients $D_{\mathrm{z}}(z)$ quantify the dynamics of a body (here, a "tracer" particle) as it traverses an *arbitrary* equilibrium free-energy landscape $\beta F(z)$; in turn, both $D_{\mathrm{z}}(z)$ and $\beta F(z)$ govern the Markovian propagator $G(z, t_0+\Delta t|z', t_0)$ that characterizes its temporal displacements [81,86]. Eqn. 5.1 is known to self-consistently model single-particle dynamics in dense inhomogeneous fluids given the potential of mean force (PMF) $\beta F(z) = -\ln\{\rho(z)\}+C$ (where $\rho(z)$ is local density and C is an arbitrary constant), which encodes the influence of all other particles, walls, etc., on the free energy landscape of the tracer [149]. To calculate $D_{\mathrm{z}}(z)$ profiles for each species from simulation data, we use a mean-first passage times (MFPT) method [81, 187, 220] applicable for the steady-state (i.e., $\partial G/\partial t = 0$) limit of Eqn. 5.1, a method shown to provide equivalent information compared to alternative approaches [35, 149]. Practically, we treat all the particles as tracers and average together their dynamics on a *per-species* basis to improve statistics, i.e., we apply the MFPT analysis to each species separately, drawing on their individual PMFs.

5.3 Results & Discussion

5.3.1 Local structure-mobility relationships can qualitatively reverse in confinement

The first portion of our discussion is focused on Figs. 5.2-5.3 (supplemented by Fig. 5.4), where we compare local total packing fraction $\phi(z)$ and local particle

diffusivities in the z-direction $D_z(z)$ for confined systems over a wide range of ϕ^{avg} and governed by either Newtonian or Brownian microscopic dynamics. First, note that we plot $\phi(z)$ because it more "economically" quantifies the local aggregate packing frustration compared to component density profiles $\rho(z)$. Additionally, in Fig. 5.2, we plot $D_z(z)$ profiles only for the small particles in the binary mixtures obtained from both MD and BD simulations, where the strong similarities in the profile shapes demonstrate that–for these generally highly-frustrated systems–the following analysis in not sensitive to the choice of microscopic dynamics. Likewise, Fig. 5.3 shows that $D_z(z)$ profiles for small *and* large particles in the binary mixtures are also exhibit similar motifs, demonstrating that the dynamic properties are not sensitive to the choice of species at this size-ratio. (Of course, obtaining dynamic results for the small particles is considerably less burdensome given their greater numbers and mobility).

In turn, Fig. 5.4 plots fluid structure from the perspective of the component density profiles $\rho(z)$, which underlines the importance of simultaneously characterizing the packing effects of *both* particle species via $\phi(z)$ in order to gain a consistent picture of local structure. First, for select conditions (e.g., $\phi^{avg} = 0.40$), a given individual component $\rho(z)$ profile can be *out of phase* with $\phi(z)$. This does not happen frequently, and given the characteristics of the mixture (e.g., composition $x_{sm} = 0.75$, size ratio $\sigma_{lg}/\sigma_{sm} = 1.3$) studied here, this behavior is only observed for small particle profiles. However, if one considered these profiles alone, it could lead to *qualitatively* incorrect conclusions about which regions of a fluid are densely packed. For the size ratio studied here, qualitative variations in $\phi(z)$

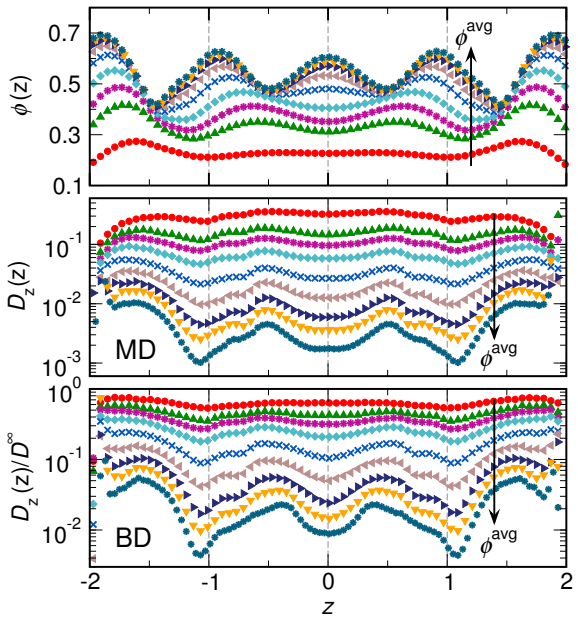

Figure 5.2: Local total packing fractions $\phi(z)$ (top) and local diffusivities in the z-direction $D_z(z)$ of small particles calculated from MD simulations (middle) and BD simulations (bottom) of pore size $H = 5$ and average total packing fractions $\phi^{avg} = 0.20$, 0.30, 0.35, 0.40, 0.45, 0.48, 0.50, 0.51, and 0.52. The BD profiles are normalized by the infinite dilution diffusivity $D^{\infty}_{\sigma_{sm}}$.

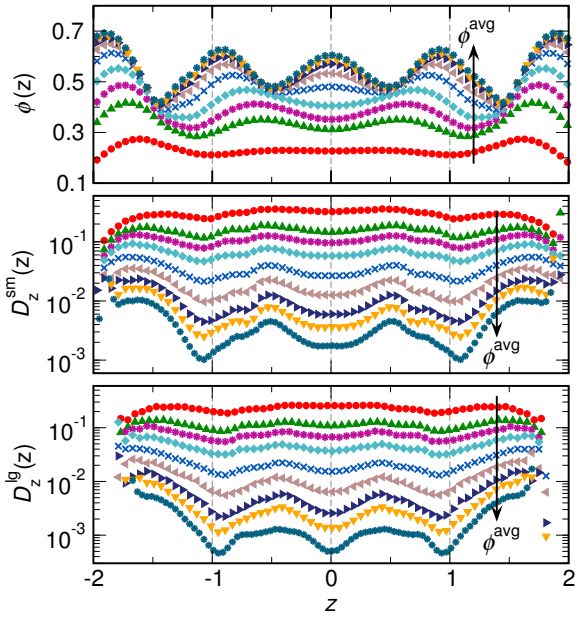

Figure 5.3: Local total packing fractions $\phi(z)$ (top) and local diffusivities in the z-direction $D_z(z)$ of small (middle) and large (bottom) particles calculated from MD simulations of pore size $H = 5$ and average total packing fractions $\phi^{avg} = 0.20$, 0.30, 0.35, 0.40, 0.45, 0.48, 0.50, 0.51, and 0.52.

can mostly be derived from knowledge only of the *large* particle $\rho(z)$ profiles (as would likely be possible for all $x_{\rm sm} \leq 0.75$).

Moving on to the main analysis of Figs. 5.2-5.3, we observe that while the packing structure in the confined pores undergoes an apparent shift from four to five dense particle layers upon increasing $\phi^{\rm avg}$, the shapes of the $D_{\rm z}(z)$ profiles–remarkably–are qualitatively insensitive to this considerable structural rearrangement. Thus, for $\phi^{\rm avg} \leq 0.40$, particles transit *more quickly* though densely-packed regions (except very close to the walls, where particles slow down due to impenetrability), but for $\phi^{\rm avg} \geq 0.45$, particles instead move *more slowly* through densely-packed regions. This gradual reversal from positive to negative local correlations between packing fraction and mobility bridges previous observations based on measurements of particle dynamics in confined fluids–measurements that seemingly pointed to inconsistent local trends, but where comparisons were also complicated by different protocols and dynamic regimes. Mittal et al. [149] measured local diffusivities in Newtonian HS simulations at *equilibrium* conditions ($\phi^{\rm avg} \leq 0.40$) and observed positive correlations between local density $\rho(z)$ (or $\phi(z)$) and $D_{\rm z}(z)$. In contrast, Nugent and co-workers [51, 155] experimentally measured short-time MSDs along the z-coordinate as a function of position for *supercooled* thin films of pseudo-HS colloids, results which pointed to negative correlations between local density and mobility. While the latter results more intuitively correlate to expectations based on bulk HS density trends, Mittal et. al. provide a plausible physical basis for the observed positive correlations. Specifically, they correctly note that higher-density regions in such inhomogeneous HS systems also exhibit the greater

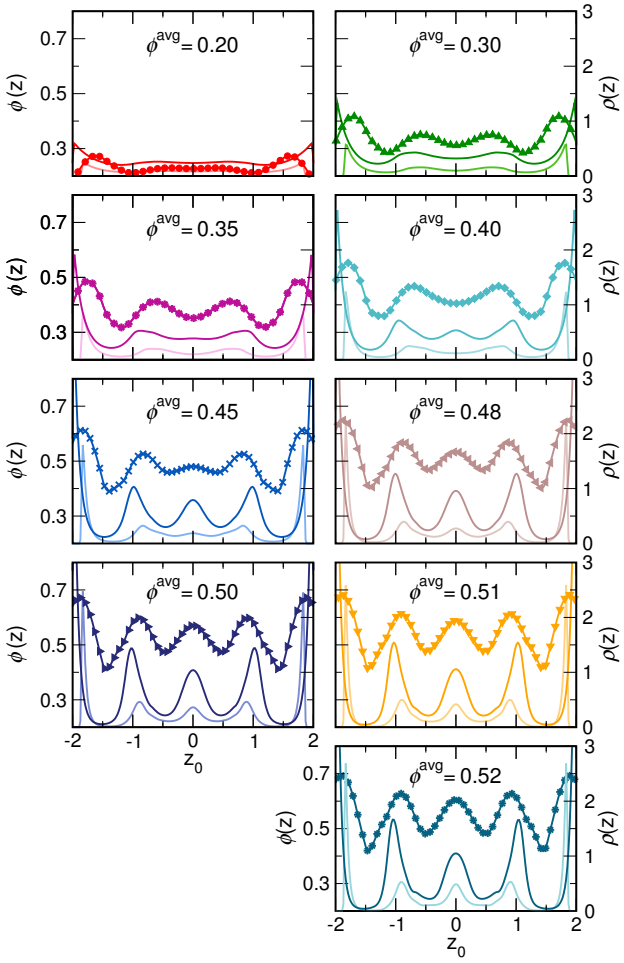

Figure 5.4: Local total packing fractions $\phi(z)$ (line-symbols) and individual component densities $\rho(z)$ (lines) from simulations of pore size $H = 5$ at various average total packing fractions ϕ^{avg}, where results for small and large particles are plotted with darker and lighter curves, respectively.

fraction of locally available space for inserting additional particle centers, i.e., more locally free volume, which might correlate with dynamics [101, 176, 222].

These results clearly demonstrate within a single framework for measuring dynamics that *either* positive or negative correlations between density and diffusivity can be observed in these systems depending on the degree of packing frustration, where we now demonstrate that the reversal coincides with the onset of supercooling–a finding that demonstrates the "conflicting" observations above are indeed compatible and consistent with a unified set of simulations. To wit, by considering Fig. 5.2 in conjunction with Fig. 5.5, where the latter shows particles MSDs parallel to the confining walls as a function of lag-time Δt and ϕ^{avg}, we observe that the reversal in local structure-mobility correlations occurs as we observe the emergence of plateaus in the MSDs at $\phi^{\text{avg}} \gtrsim 0.45$, a classic signature of sub-diffusive "particle caging" characteristic of supercooled glassy states [155, 219].

Taken altogether, the above results imply that *local* packing structure as measured by $\phi(z)$ does not generally correlate in a nontrivial way to position-dependent diffusive mobility, but this turns out to also be true of more "microscopic" static quantities. To wit, the local available (void) space–the static quantity that Mittal et. al. [149] appeal to in mechanistically-explaining their findings for equilibrium states–is proportional to the local insertion probability, which is given by $p_0(z) = \rho(z)/\xi$, where ξ is the spatially-invariant component activity [222] (this is discussed more below in Section 5.3.3); however, as can be seen by considering Figs. 5.2-5.4, it is evident that there is no consistent coupling between $D_{\text{z}}(z)$ and $\rho(z)$ profiles. Of course, this implies that other position-dependent measures of

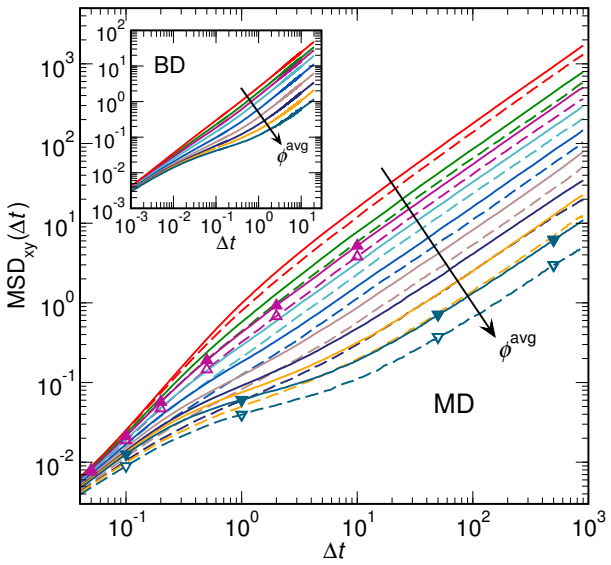

Figure 5.5: (color online). Mean-squared displacements (MSD) per particle in the x- and y-directions versus lag-times Δt for small (solid lines) and large (dashed lines) particles from MD (main) and BD (inset) simulations of pore size $H = 5$ and average total packing fractions $\phi^{\text{avg}} = 0.20$, 0.30, 0.35, 0.40, 0.45, 0.48, 0.50, 0.51, and 0.52. In the inset, only small-particle curves are shown for clarity and lag-times have been normalized by $D^{\infty}_{\sigma_{\text{sm}}}/\sigma^2_{\text{sm}}$. Symbols in the main panel denote times corresponding to the profiles in Fig. 5.6.

structural correlations that are positively correlated with $p_0(z)$, such as the local two-body excess entropy $s^{(2)}(z)$, would likewise exhibit no consistent correlation with local diffusive mobility [25].

In turn, given that bulk HS fluids exhibit simple negative correlations between packing fraction and mobility (and positive correlations between available space and mobility), it is apparent that local static-dynamic correlations in confined fluids cannot be naïvely extrapolated (or predicted) from the bulk physics, in agreement with findings for more idealized density-varying HS systems [25]. Interestingly, for the systems examined here, the choice of microscopic dynamics had no qualitative impact on the shapes of the $D_z(z)$ profiles, though recent results [26] indicate this is not generally true of inhomogeneous fluids.

5.3.2 Connecting dynamic measurements with previous experiments on colloidal thin films

We next provide data reinforcing the idea that the opposing correlations in Fig. 5.2 between packing fraction and diffusivity at equilibrium versus supercooled conditions may also emerge in real colloidal thin films: in Fig. 5.6, we compare position- and time-dependent particles MSDs of the confined fluids against $\phi(z)$ and component $\rho(z)$, results that mirror experimental measurements by Nugent and co-workers (see, e.g., Figs. 7-8 from [51]) for supercooled thin films of pseudo-HS. In particular, we show results calculated from MD simulations for $\phi^{\text{avg}} = 0.35$ and 0.52, which correspond to equilibrium and supercooled conditions, respectively.

Mirroring the experimental findings, for the supercooled conditions in Fig. 5.6,

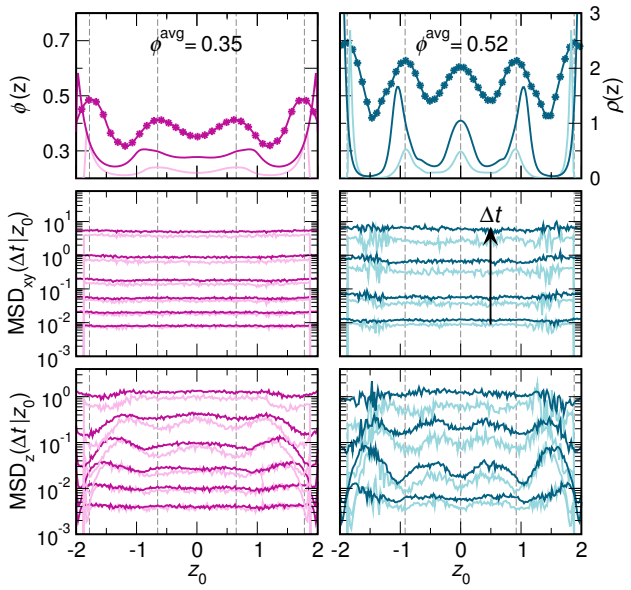

Figure 5.6: Local total packing fractions $\phi(z)$ and individual component densities $\rho(z)$ (top) and MSDs per particle in the x- and y-directions (middle) and z-direction (bottom) for various lag-times Δt plotted as a function of particle position z_0 at $\Delta t = 0$. Except for $\phi(z)$ profiles, which are plotted with line-symbols, results for small and large particles are plotted with darker and lighter lines, respectively. Results are calculated from MD simulations for pore size $H = 5$, where left panels show results for $\phi^{\text{avg}} = 0.35$ and $\Delta t = 0.05$, 0.1, 0.2, 0.5, 2.0, and 10.0 and right panels for $\phi^{\text{avg}} = 0.52$ and $\Delta t = 0.1$, 1.0, 50.0, and 500.0. Lag-times are also plotted in Fig. 5.5 as symbols.

MSDs in the xy-plane are insensitive with respect to originating position z_0 (i.e., position at lag-time $\Delta t = 0$) for all Δt, while MSDs in the inhomogeneous z-direction are negatively correlated with respect to $\phi(z)$ ($\rho(z)$) for sufficiently short Δt. At longer Δt, the MSD dependence on z_0 disappears as particles are no longer generally situated near z_0. At $\phi^{\text{avg}} = 0.35$, MSDs in the xy-plane also do not vary with z_0, but MSDs in the z-direction instead exhibit a weak positive correlation with respect to $\phi(z)$ ($\rho(z)$) at $\Delta t = 0.2$, though the correlations appear to reverse at longer $\Delta t \geq 0.50$ before washing out at long lag-times. To our knowledge, no analogous MSD profiles for real non-supercooled thin films for have yet been published.

Surprisingly, the MSDs in the z-direction at many Δt approximately reflect the $D_{\text{z}}(z)$ profiles in Fig. 5.2 even though the quantified motions are by necessity sub-diffusive and accrued when a particle is no longer at z_0. In turn, only profiles at the *very shortest times* provide information about motions precisely at z_0, but these are also furthest from the diffusive regime. Nonetheless, given that the results for the supercooled system in Fig. 5.5 are consistent with the available experimental data, it is plausible that the results for local diffusive motions–including the positive correlations between $\phi(z)$ and $D_{\text{z}}(z)$ and their reversal at high ϕ^{avg}–can be observed in real confined colloids.

5.3.3 Predicting average dynamics via available space

Given that the previous results undermine any notion of a universal con-

nection between local structure and local mobility, it is natural to wonder whether *average* diffusivities in directions parallel and perpendicular to the confining walls reflect bulk fluid physics and can be predicted based on average static properties. In Fig. 5.7, we address this by comparing average diffusivities $D_{\mathrm{xy}}^{\mathrm{avg}}$ and $D_{\mathrm{z}}^{\mathrm{avg}} = \int_0^{H/2} D_{\mathrm{z}}(z)\rho(z)\mathrm{d}z \,/\, \int_0^{H/2} \rho(z)\mathrm{d}z$ for the small and large particles from the confined systems against curves for bulk mixtures. Here, we plot these dynamic quantities against component-specific average insertion probabilities p_0^{avg} (analogous to plotting against available volumes for particle insertion, considered in the previous chapter [73]), which have been shown to provide the most quantitatively robust connection (i.e., mapping) between bulk diffusivity and D_{xy} in slit pores of HS governed by Newtonian dynamics [66].

To calculate p_0^{avg} for each component, we note that if there is no external field at position z (i.e., $\varphi^{\mathrm{ext}}(z) = 0$), the *local* insertion probability [73] for bulk or inhomogeneous HS is a ratio [222] $p_0(z) = \rho(z)/\xi$ of the local component density $\rho(z)$ and the spatially-invariant component activity $\xi = \exp(\beta\mu)/\lambda^3$, where the latter is defined by the component chemical potential μ and the de Broglie wavelength λ. Given that we have component $\rho(z)$ profiles measured from the MD and BD simulations, all that is required to obtain $p_0(z)$ profiles are activities ξ for the bulk and confined mixtures at the various ϕ^{avg} values. These ξ values are obtained via grand canonical transition matrix Monte Carlo (GC-TMMC) simulations [191], with implementation details presented elsewhere [66]. It is then straightforward to calculate $p_0^{\mathrm{avg}} = H^{-1} \int_0^{H/2} p_0(z)\mathrm{d}z$, which for bulk mixtures is simply $p_0^{\mathrm{avg}} = \rho/\xi$.

As is evident in Fig. 5.7, the average diffusivities D_{xy} and $D_{\mathrm{z}}^{\mathrm{avg}}$ of the con-

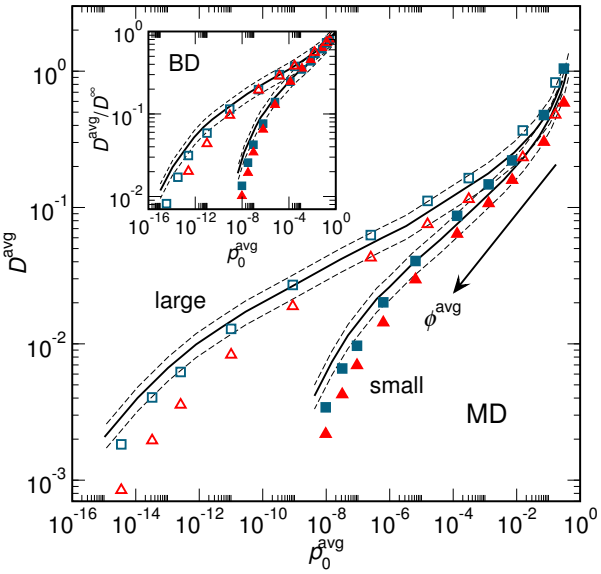

Figure 5.7: Average component diffusivities D^{avg} in the xy-plane (squares) and z-direction (triangles) versus average component insertion probabilities p_0^{avg} for small and large particles (filled and unfilled symbols, respectively) calculated from MD simulations (main) and BD simulations (inset) of pore size $H = 5$ and average total packing fractions $\phi^{\text{avg}} = 0.10$, 0.20, 0.30, 0.35, 0.40, 0.45, 0.48, 0.50, 0.51, and 0.52. Average diffusivities for bulk mixtures shown as solid black lines with $\pm 20\%$ bounds shown as dashed lines.

fined fluids approximately collapse onto the relevant bulk curves over many orders of magnitude in p_0^{avg} for systems governed by either Newtonian and Brownian dynamics. Notably, even at high ϕ^{avg} associated with supercooling, $D_{\text{z}}^{\text{avg}}$ values only differ from the bulk by factors of 2-3 based on component p_0^{avg}; if one instead plots diffusivities against a less "microscopic" static property, e.g., component ρ^{avg}, confined and bulk diffusivities differ by up to an order of magnitude. Overall, the data support the idea that, despite the difficulty of rationalizing position-dependent diffusivity behaviors based on bulk physics, the average dynamics of inhomogeneous fluids are nonetheless strongly encoded with bulk correlations between mobility and available space.

5.4 Conclusions

In closing, by characterizing the particle dynamics of highly confined binary HS mixtures in both inhomogeneous and isotropic dimensions, we find that *local* diffusive mobility is not universally predicated upon packing structure according to bulk HS behaviors, as exemplified by the reversal from positive to negative correlations between local total packing fraction $\phi(z)$ and single-particle diffusivity $D_{\text{z}}(z)$ coinciding with the onset of supercooling. In contrast, *average* diffusive mobility is strongly encoded by the bulk physics, and can be approximately predicted via knowledge of the distribution of available space. For the confined fluids studied here, results are insensitive to whether Newtonian or Brownian (i.e., overdamped Langevin) microscopic dynamics govern particle trajectories, though it is an open question as to whether similar classes of behavior will emerge in real colloidal thin

films treated within the Fokker-Planck formalism.

Given that colloidal hard-sphere systems can be considered canonical reference systems for more complex fluids, a similarly rich array of local correlations between structure and mobility likely emerges in confined molecular fluids and polymer films (indeed, recent work [25] for more idealized inhomogeneous fluids bears this out). Furthermore, while we consider a binary hard-sphere mixture with a size ratio near unity, chosen because it was previously known to remain amorphous at high ϕ^{avg} under confinement [51, 66, 155], it would be valuable to systematically explore the dynamical interplay between species for more exotic (i.e., less uniform) mixtures. More broadly, the shapes of the $D_{\mathrm{z}}(z)$ profiles (and their qualitative insensitivity to ϕ^{avg}) further bolster our claims that there may simply be a "universal" oscillatory signature of local diffusivity that emerges for non-continuum fluids proximal to confining potential–regardless of microscopic dynamics or the specific nature of any emergent structural inhomogeneity.

Chapter 6

Decoding the structure factor to detect and characterize clustering in fluids with competing interactions

6.1 Introduction

Competing interactions between particles or molecules that manifest at distinct lengthscales can generate hierarchical structure in soft matter systems [189]. For contexts as diverse as microemulsions [114], block-copolymers [72,77], graphene oxides [232], and confined fluid mixtures [42,93,179], this type of constituent frustration drives (often abrupt) transformations between homogeneous states and morphologies exhibiting micro- to mesoscopic density fluctuations. Such modulated density fluctuations are typically classified as "intermediate-range order" (IRO) because, for this class of morphologies, the structure factor $S(k)$ displays a characteristic pre-peak at a low but nonzero wavenumber [27, 31, 40, 62, 63, 100,

Reproduced in part with permission from J.A. Bollinger and T.M. Truskett, "Fluids with competing interactions. I. Decoding the structure factor to detect and characterize self-limited clustering." J. Chem. Phys., 2016, 145 (6), p. 064902 (DOI: 10.1063/1.4960338). Copyright 2016 American Institute of Physics. J.A. Bollinger performed computer simulations, executed liquid-state theory calculations, analyzed results, created figures, and wrote the manuscript.

125, 127, 164, 186, 227]. In turn, the emergence of IRO can greatly impact the mechanical, optical, electronic, etc. properties of such systems, and the ability to detect, characterize, and ultimately *engineer* the emergence of IRO structure can facilitate new material processing methods [11, 78, 97].

This chapter concentrates on an IRO morphology of increasing fundamental and technological interest: the *equilibrium cluster phase*. Such a phase comprises self-terminating, finite-sized clusters composed of solute monomers (i.e., primary particles); the clusters themselves are ideally dense, amorphous, and relatively monodisperse in terms of their size. Here, clusters are differentiated from aggregates such as micelles because the characteristic size of the former need not be set by the monomer size. They coexist with a continuous (interstitial) low-density population of monomers; thus, reversible transformations between homogeneous phases (where monomers are well-dispersed) and cluster phases can be viewed as microscopic analogues of macroscopic liquid-gas separation.

Self-limiting cluster phases have been studied via theory, computer simulations, and experiments of various idealized [6, 28, 62, 63, 68, 91, 96, 136, 153, 182, 204, 209, 233] or archetypal colloidal suspensions (e.g., polystyrene spheres) [32, 102, 228, 231] and more complex constituent monomers like proteins [64, 97, 97, 127, 168, 201, 229, 230], organic-inorganic complexes [161], etc. The generic clustering behavior is attributed to a common physical paradigm: aggregates form due to a competition between short-range attractions that drive monomer association and long-range repulsions that collectively build up to attenuate growth. The former can be realized in colloidal suspensions via, e.g., the introduction of crowder molecules (e.g.,

non-interacting polymers) that induce depletion attractions, while the latter are attributable to (typically weakly-screened) electrostatic interactions between the ionic double-layers of nearby monomers due to their surface charges [90, 102, 182].

Despite the attention directed at colloidal suspensions that form cluster phases, there remain basic knowledge gaps regarding their behavior and characterization, particularly in terms of how the shape of the structure factor $S(k)$ relates to real-space morphology. To wit, while characteristic clusters *must* be reflected by the existence of an IRO pre-peak in $S(k)$, it has also been recognized that suspensions can exhibit IRO pre-peaks *without* having formed monodisperse multi-particle aggregates [62, 63, 127]. In other words, it is difficult even to positively detect cluster phases versus either effectively homogeneous phases (exhibiting some other form of IRO) or, alternatively, percolated gel phases. Meanwhile, it remains unclear which morphological lengthscale(s) (e.g., cluster size, intercluster spacing) the wavenumber (position) of the IRO pre-peak captures, or whether it is sensitive to conditions like bulk monomer density [62, 182, 193, 200, 201].

Being able to describe cluster morphologies by decoding $S(k)$ is conceptually powerful because it allows one to obtain knowledge about multi-body structure based on pair correlations alone; it is also of practical interest because *in situ* measurements of pair correlations are feasible for a wide range of soft matter systems and lengthscales, including nanoscopic primary particles and aggregates. In this vein, our goal here is to use integral equation theory and computer simulations to *unambiguously* and *simultaneously* characterize $S(k)$ profiles and corresponding suspension morphologies for a canonical pairwise interaction model that generates

clusters, with a particular emphasis on surveying wide ranges of conditions that might be accessed through experimentally tunable parameters, including monomer packing fraction ϕ, monomer surface charge Z, suspension (Debye) screening length κ^{-1}/d, and short-range attraction strength $\beta\varepsilon$.

Based on our analysis of these model fluids, we first systematically expand upon previous findings [62, 63, 127] to demonstrate the poor correlation between the emergence of the IRO pre-peak in $S(k)$ and the onset (or even energetic favorability) of self-limited clustering. We next demonstrate that the pre-peak position is dependent upon both cluster size in terms of number of monomers and average monomer density, and that it directly quantifies the average real-space intercluster separation. We then test two criteria based on $S(k)$ that have been postulated to pinpoint the onset of clustering (and thus positively detect cluster morphologies), which are based on the IRO pre-peak height [62, 63] and width [91], respectively. We find that the criterion based on the pre-peak width, which encodes the IRO thermal correlation length, is a more robust (albeit still only approximate) predictor of the onset of clustering.

6.2 Methods

6.2.1 Model interactions

We focus on one of the simplest colloidal models [182] known to generate equilibrium cluster phases: a pair potential that combines a short-range attraction (SA) with a long-range repulsion (LR). The so-called SALR potential can be

expressed

$$\beta u_{i,j}^{\mathrm{SALR}}(x_{i,j}) = \beta u_{i,j}^{\mathrm{SA}}(x_{i,j}) + \beta u_{i,j}^{\mathrm{LR}}(x_{i,j}) \tag{6.1}$$

where $\beta = (k_{\mathrm{B}}T)^{-1}$ (k_{B} is Boltzmann's constant and T is temperature); $x = r/d$ is the non-dimensionalized interparticle separation; d is the characteristic particle diameter. Note that we generalize the pair potential to account for *multicomponent* (here, size-polydisperse) suspensions where two interacting particles are of types i and j, respectively.

When conducting simulations (see Section 6.2.3), we follow previous work and simulate three-component mixtures that approximate suspensions with 10% size polydispersity; this favors the formation of amorphous fluid clusters, rather than the microcrystalline (often elongated) aggregates that result from monodisperse monomers [91, 92]. In this context, the generalized interparticle distance in Eqn. 6.1 is defined $x_{i,j} \equiv x - (1/2)(i+j)(\Delta_d/d)$, where i (or j) $= -1, 0, 1$ corresponds to small, medium, and large particles, respectively, and Δ_d/d is a perturbation to particle diameter. Specifically, we study mixtures comprised of 20% small, 60% medium (characteristic size d), and 20% large particles with $\Delta_d = 0.158d$.

Short-range attractions can be realized in colloidal suspensions via the introduction of depletant molecules with exclusion volumes smaller than that of the primary particles. These depletion attractions are represented via a generalized (100-50) Lennard-Jones interaction

$$\beta u_{i,j}^{\mathrm{SA}}(x_{i,j}) = 4[\beta\varepsilon + (1-2\delta_{i,j})\beta\Delta_{\varepsilon}](x_{i,j}^{-100} - x_{i,j}^{-50}) \tag{6.2}$$

where the lengthscale of the attractive well is approximately $0.10d$. Here, $\beta\varepsilon$ is the baseline attraction strength between monomers and $\Delta_{\varepsilon} = 0.25k_{\mathrm{B}}T$ is an energetic perturbation that biases against demixing.

Long-ranged repulsions can be attributed to screened electrostatic interactions between the charge sites located on the surfaces of monomer particles. Ignoring long-range multi-body interactions [159, 160] and microscopic mechanisms of ion dissociation [1,59,138,169], one can approximate this effect via the electrostatic portion of the Derjaguin-Landau-Verwey-Overbeek (DLVO) potential [46, 90, 214]

$$\beta u_{i,j}^{\mathrm{LR}}(x_{i,j}) = \beta A_{\mathrm{MAX}} \frac{\exp\{-(x_{i,j}-1)/(\kappa^{-1}/d)\}}{x_{i,j}} \tag{6.3}$$

with

$$\beta A_{\mathrm{MAX}} = \frac{Z^2(\lambda_{\mathrm{B}}/d)}{[1+0.5/(\kappa^{-1}/d)]^2} \tag{6.4}$$

where βA_{MAX} is the maximum electrostatic barrier between particles at contact, κ^{-1}/d is the Debye-Hückel screening length, Z is the total surface charge per monomer (assumed evenly distributed), and λ_{B}/d is the Bjerrum length of the solvent.

With respect to experimental realization, recall that not all of these quantities are independent, as the screening length is given by

$$\kappa^{-1}/d = \sqrt{\epsilon_0 \epsilon_{\mathrm{R}} k_{\mathrm{B}} T/(2d^2 N_{\mathrm{A}} e^2 I)} \tag{6.5}$$

and the Bjerrum length is given by

$$\lambda_{\mathrm{B}}/d = e^2/(4d\pi\epsilon_0\epsilon_{\mathrm{R}} k_{\mathrm{B}} T) \tag{6.6}$$

where ϵ_0 is the vacuum permittivity, ϵ_{R} is the relative permittivity, N_{A} is Avogadro's number, e is the elementary charge, and I is the ionic strength of the suspending solvent. Parameters tunable in experiments are essentially Z, ϵ_{R}, and I (and, practically, even some of these may be interdependent). In our analysis, we choose to fix the relative Bjerrum length at $\lambda_{\mathrm{B}}/d = 0.014$ (corresponding to, e.g., $d = 50$ nm monomers suspended in room temperature water with $\lambda_{\mathrm{B}} = 0.7$ nm), which means electrostatic effects are set via Z and κ^{-1}/d. Choosing a different reference λ_{B}/d renormalizes the Z values under consideration, which we expound upon in Chapter 7.

To examine model behavior at a given monomer packing fraction $\phi = (\pi/6)\rho d^3$ (where ρd^3 is number density), we set various combinations of Z and κ^{-1}/d and then independently vary the depletion attraction strength $\beta\varepsilon$. This treatment mimics how short- and long-range aspects of constituent interactions are approximately orthogonal for colloidal suspensions, and is worth noting as it is in contrast to some studies where attractions and repulsions are simultaneously scaled via changing T [63, 182, 209]. Finally, note that throughout the remainder

of the chapter, we notate $\beta u_{i,j}^{\mathrm{SALR}}(x_{i,j})$ as $\beta u(r)$ for aesthetic simplicity (unless otherwise indicated).

6.2.2 Integral equation theory

We execute integral equation theory (IET) calculations to efficiently predict $S(k)$ across wide ranges of the parameter space ($\beta\varepsilon$, Z, κ^{-1}/d) underlying the pair interactions $\beta u(r)$. In brief, IET partitions the total correlation function $h(r) = g(r) - 1$ (where $g(r)$ is the radial distribution function) into pair and multibody contributions by introducing the direct correlation function $c(r)$ in the context of the Ornstein-Zernike (OZ) relation:

$$h(r) = c(r) + \rho \int c(r')h(|\mathbf{r} - \mathbf{r}'|)d\mathbf{r} \tag{6.7}$$

In order to use Eqn. 6.7, we require an accompanying closure expression that relates $\beta u(r)$, $g(r)$ and $c(r)$. Because our systems have potentials resembling Coulombic interactions, we follow our previous work [91] and employ the optimized random phase approximation (ORPA) [3,73]. The ORPA formulation we use treats the direct correlation function as $c(r) \approx \exp\{-\beta u(r)\} - 1 + c_0(r)$, where the first two terms constitute a large-r perturbation to the $c_0(r)$ of an underlying reference system. We use the Mayer function to capture effects outside the core because it provides improved results when deep and narrow attraction wells are included in the pair potential [73]. Meanwhile, $c_0(r) = 0$ for $r > d$, while at short-range it is optimized to enforce $h(r) = -1$ for $r \leq d$ (i.e., to exactly incorporate effects of a

reference hard-sphere fluid). Note that in performing these calculations, we do not explicitly enforce thermodynamic self-consistency, which has been shown to provide very strong quantitative agreement between analytical and simulation results for complex fluids [13, 27, 100]. As discussed in Section 6.3.1, we are mainly interested in using IET to capture general trends in pair structural behavior over wide ranges in model parameter space; for these purposes, our approximate approach is practical and reasonably reflects simulation results [91].

In practice, we conduct our IET calculations using the *single-component monodisperse* pair potential (i.e., $\Delta_d/d = \beta\Delta_\varepsilon = 0$), where we fix Z and κ^{-1}/d and then systematically increase $\beta\varepsilon$ after beginning at vanishing attraction strength. Upon numerical solution at a given $\beta\varepsilon$, $S(k)$ is obtained via the relation $S(k) = 1 + (\rho d^3)\hat{h}(k)$, where $\hat{h}(k) = \mathrm{FT}[h(r)]$ and FT is a Fourier transform.

6.2.3 Molecular dynamics simulations

We perform three-dimensional (3D) molecular dynamics (MD) simulations of the ternary SALR mixtures in the NVT ensemble with periodic boundary conditions using LAMMPS [165]. We propagate trajectories with an integration time-step of $dt = 0.001\sqrt{d^2 m/(k_\mathrm{B}T)}$ (taking the mass $m = 1$), and fix temperature via a Nosé-Hoover thermostat with time-constant $\tau = 2000dt$. The pair potential for a given Z and κ^{-1}/d is cut-off such the that interaction strength at distance $x^\mathrm{c}_{i,j}$ (note explicit use of the mixture notation) is $\beta u_{i,j}(x^\mathrm{c}_{i,j}) \leq 2\mathrm{e}^{-3}$ and the force is simultaneously $-\mathrm{d}[\beta u_{i,j}(x^\mathrm{c}_{i,j})]/\mathrm{d}x_{i,j} \leq 1\mathrm{e}^{-3}$.

We examine bulk monomer packing fractions $\phi = 0.015$, 0.030, 0.060, and 0.120 using systems of $N_{\text{box}} = 1920$, 2960, 6800, and 6800 particles, respectively. Starting from randomized initial configurations, we allow systems at $\phi = 0.015$, 0.030, 0.060, and 0.120 to equilibrate for $3\text{x}10^7$, $1\text{x}10^7$, $3\text{x}10^6$, and $2\text{x}10^6$ steps, respectively. (Lower packing fractions require relatively more equilibration time given less frequent monomer-monomer collisions.) We have confirmed that these equilibration times are sufficient by (1) checking that energies have converged and (2) by visualizing the trajectories to check that clusters undergo frequent intracluster rearrangements and intercluster exchanges (i.e., that individual particles ergodically sample the simulation space). Regarding the latter, we indeed find that by employing the lightly polydisperse mixture that we developed and used previously [91, 92], we avoid the formation of highly-arrested microcrystalline phases typical of monodisperse models.

To characterize pair correlations, we calculate the structure factor $S(k)$ via numerical Fourier Transform inversion of the radial distribution function $g(r)$. To characterize multibody structure, we calculate cluster-size distributions (CSDs), which quantify the probability $p(N)$ of observing aggregates comprising N particles. Following previous studies [63, 91, 136, 182], two monomers are considered part of the same aggregate if they are located within the range of the attractive well (i.e., are direct neighbors) and/or they are both direct neighbors with at least one common particle (i.e., are connected via some percolating pathway).

For consistency across many packing fractions and cluster sizes, we consider a phase clustered with characteristic aggregate size N^* based on the following cri-

	κ^{-1}/d	Z = 3 ■	4 ◆	6 ✳	8 ○	10 △	12 ●	15 □
$\phi = 0.015$ ■	0.7	-	-	-	-	-	-	6.55
	0.8	-	-	-	-	-	-	6.80
	1.0	-	-	-	5.55	6.00	6.40	7.10
	1.2	-	-	-	5.65	6.10	-	-
	1.5	-	-	5.35	5.80	6.30	6.80	-
	2.0	-	5.05	5.50	5.95	6.45	7.00	7.90
	2.5	-	-	5.55	6.00	6.60	-	-
	3.0	-	5.10	5.55	6.05	6.60	-	-
	4.0	4.95	5.10	5.60	6.10	6.65	-	-
$\phi = 0.030$ ■	0.7	-	-	-	-	-	-	6.30
	0.8	-	-	-	-	-	-	-
	1.0	-	-	-	5.30	5.70	6.15	6.75
	1.2	-	-	-	5.45	5.80	-	-
	1.5	-	-	5.15	5.55	5.95	6.45	-
	2.0	-	4.80	5.20	5.65	6.10	6.55	7.25
	2.5	-	-	5.20	5.70	6.20	-	-
	3.0	-	4.90	5.25	5.70	6.20	-	-
	4.0	4.70	4.90	5.30	5.70	6.20	-	-
$\phi = 0.060$ ■	0.7	-	-	-	-	-	-	6.00
	0.8	-	-	-	-	-	-	-
	1.0	-	-	-	5.00	5.40	5.65	6.25
	1.2	-	-	4.75	5.10	5.45	-	-
	1.5	-	-	4.80	5.15	5.50	5.80	-
	2.0	-	4.55	4.85	5.20	5.55	5.80	6.40
	2.5	-	-	4.90	5.20	5.60	-	-
	3.0	-	4.60	4.85	-	5.60	-	-
	4.0	4.40	4.60	4.85	5.20	5.60	-	-
$\phi = 0.120$ ■	0.7	-	-	-	-	-	-	5.20
	0.8	-	-	-	-	-	-	5.20
	1.0	-	-	-	-	-	4.95	5.20
	1.2	-	-	-	-	-	-	-
	1.5	-	-	-	-	4.75	4.95	5.20
	2.0	-	-	-	4.60	4.75	4.95	-
	2.5	-	-	-	4.60	-	-	-

Table 6.1: Critical attraction strengths $\beta\varepsilon^*$ determined from simulations at combinations of ϕ, Z, κ^{-1}/d. Symbol types (across top) and colors (left) denote Z and ϕ, respectively, in Figs. 6.2-6.7 (symbols constant for various κ^{-1}/d).

teria: (1) the $p(N)$ distribution exhibits a visibly-apparent local maximum (mode) at some $1 < N^* \ll N_{\rm box}$, where the corresponding local minimum between $N = 1$ and N^* is notated as $N_{\rm min}$; and (2) that at least 80% of the particles in the system participate in aggregates of size $N \geq N_{\rm min}$. Thus, in this framework, the onset of clustering occurs when $0.80 = \sum_{n=N_{\rm min}}^{N_{\rm box}} p(N)$, where $p(N)$ is appropriately normalized. In turn, we identify the *critical* attraction strengths $\beta\varepsilon^*$ best meeting this condition by examining CSDs of simulations performed in increments of $\Delta\varepsilon = 0.05 k_{\rm B}T$. All of the combinations of Z, κ^{-1}/d, and ϕ analyzed via simulations (where cluster phases could be found) are listed in Table 6.1 by their respective $\beta\varepsilon^*$ values.

To characterize the lengthscales and shapes of the N^*-sized clusters, we calculate the radius of gyration $R_{\rm G}/d$ and the relative shape anisotropy κ^2. We first calculate the gyration tensor $\mathbf{S}$, where the elements are $\mathbf{S}_{mn} \equiv N^{*-2} \sum_{i<j} (r_m^i - r_m^j)(r_n^i - r_n^j)$ and r_m^i is the the position of the i-th particle participating in the cluster in the m-th Cartesian coordinate (x, y, or z). The radius of gyration is then given by $R_{\rm G}/d = (\text{Tr } \mathbf{S})^{1/2} = (\lambda_1 + \lambda_2 + \lambda_3)^{1/2}$, where λ_1, λ_2, and λ_3 are the eigenvalues of $\mathbf{S}$ in order of magnitude $\lambda_1 \geq \lambda_2 \geq \lambda_3$. The well-established relative shape anisotropy [208] is calculated via $\kappa^2 = 1 - 3(\lambda_1\lambda_2 + \lambda_2\lambda_3 + \lambda_3\lambda_1)/(R_{\rm G}/d)^4$, which is bounded between 0 and 1: $\kappa^2 = 0$ corresponds to points (particle centers) that are symmetrically distributed and $\kappa^2 = 1$ corresponds to points arranged linearly. To slightly smooth over instantaneous cluster distortions (e.g., when the outer edge is distended due to an imminent particle exchange), measurements of $R_{\rm G}/d$ and κ^2 are derived from $\mathbf{S}$ tensors collected over blocks of 10 individual clusters (where

particle positions are renormalized relative to the respective centers of mass of the clusters); in turn, average and error values are based on 500 of these measurements.

6.3 Results & Discussion

6.3.1 Pre-peak formation, clustering, and macroscopic phase separation

We begin our discussion by considering the existence of a low-wavenumber pre-peak in the structure factor $S(k)$, which emerges at a position $k_{\rm pre}d$ lower than that of the primary peak associated with monomer-monomer packing effects located at $k_{\rm prim}d \simeq 2\pi$ (i.e., a real-space lengthscale of d). A pre-peak position of $k_{\rm pre}d = 0$ is associated with suspensions dominated by short-range attractions, where such a pre-peak corresponds to (infinitely) long-ranged, densified regions and diverges in magnitude at the onset of *macroscopic* liquid-gas phase separation [73]. On the other hand, phases composed of self-terminating *microscopic* clusters must exhibit an intermediate-range order (IRO) peak at some wavenumber $0 < k_{\rm IRO}d < k_{\rm prim}d$ due to their modulated structure; however, as discussed above, it is tentatively understood that not every state exhibiting an IRO peak is actually comprised of characteristically-sized clusters [62, 63, 127].

In Fig. 6.1, we build upon these basic guidelines by examining an SALR system where we fix charge Z and packing fraction ϕ while varying attraction strength $\beta\varepsilon$ and screening length κ^{-1}/d over wide ranges. This allows us to: (1) systematically map out how the *existence* of the $S(k)$ pre-peak and its *position* relate to some

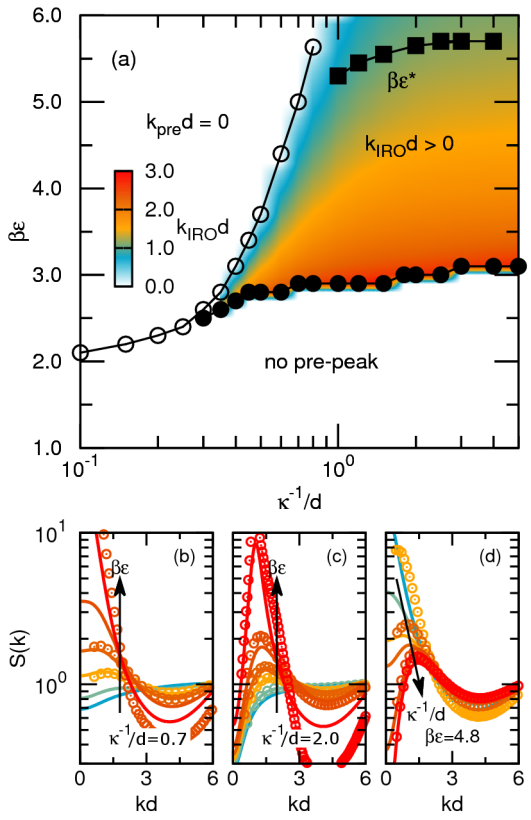

Figure 6.1: (color online) (a) Pre-peak position $k_{\rm pre}d$ in the structure factor $S(k)$ as a function of attraction strength $\beta\varepsilon$ and screening length κ^{-1}/d for packing fraction $\phi = 0.03$ and charge $Z = 8.0$, obtained from integral equation theory (IET). Color portions show conditions for which there is an IRO pre-peak at small but finite $k_{\rm IRO}d > 0$. Filled and unfilled circles delineate transitions between different peak behaviors in IET results. Squares denote critical attraction strengths $\beta\varepsilon^*$ at the onset of clustering obtained from MD simulations. (b,c,d) Structure factors obtained from IET (lines) and simulations (circles) for $\phi = 0.030$ and $Z = 8.0$, where in (b) and (c) the results are for constant κ^{-1}/d values and $\beta\varepsilon = 1.5$, 3.0, 4.0, 4.5, 5.0, and 6.0 (bottom to top). In (d), $\beta\varepsilon$ is constant with $\kappa^{-1}/d = 0.1$, 0.5, 0.8, 1.0, 2.0, 5.0 (top to bottom). Note that simulation results are not shown for every combination of $\beta\varepsilon$ and κ^{-1}/d. In all panels, IET results are based on monodisperse systems while simulation results are based on lightly polydisperse mixtures (see text).

of the tunable parameters controlling interparticle interactions and phase behavior; and (2) consider how the parameter space where IRO pre-peaks exist compares to the parameter space where clusters emerge. In Fig. 6.1(a), we make the mapping tractable by using IET calculations with the approximate ORPA closure (see Methods) that can efficiently survey parameter space; to address the latter comparison, we plot the line of critical attraction strength $\beta\varepsilon^*$ observed in MD simulations (where we can directly characterize multi-body structure), which corresponds to the onset of clustering at a given κ^{-1}/d. Meanwhile, in Figs. 6.1(b-d), we show selected series of $S(k)$ profiles obtained from IET and simulations to illustrate the pre-peak shapes that correspond to the positions in Fig. 6.1(a). Note that here we are using an approximate closure and making comparisons between monodisperse IET calculations and lightly polydisperse MD simulations; thus, while we cannot expect perfect agreement between the methods, we do observe *qualitative* agreement in terms of the evolution of $S(k)$ even in regions where $S(k)$ is changing rapidly (as exemplified in Figs. 6.1(b-d) and elsewhere [91]). Nonetheless, we restrict our comments below to general trends that should not be sensitive to these types of methodological choices.

Focusing on Fig. 6.1(a), it is apparent that for any given repulsive interaction, it is only above a sufficiently strong attraction $\beta\epsilon$ that a pre-peak of any position forms. As might be anticipated, a $k_{\mathrm{pre}}d = 0$ pre-peak forms in the limit of small screening lengths, while at sufficiently large screening lengths ($\kappa^{-1}/d \geq 1.0$), one observes an IRO pre-peak at $k_{\mathrm{IRO}}d > 0$ that grows in from higher to lower k-values with increasing attractions. Moving left-to-right in the direction of in-

creasing screening length, the transition between $k_{\mathrm{pre}}d = 0$ and $k_{\mathrm{IRO}}d > 0$ (where the zero-wavenumber convexity switches from negative to positive) is termed a Lifshitz point, which is a common feature of fluids with generic SALR interactions [40, 164, 186]. Generally-speaking, to reach this transition, repulsions must not only exist but must also be sufficiently *competitive* relative to attractions to favor modulated phases (minimum threshold repulsion strengths are known analytically for some temperature-controlled systems [164]). In the parameter space here, this condition means that given a surface charge Z, one requires a minimum κ^{-1}/d to generate repulsions that can collectively stabilize aggregates once attractions start to pull monomers together.

From Fig. 6.1(a), one can also readily appreciate that the presence of an IRO pre-peak is a poor indicator of: (1) whether a particular state is composed of clusters; and (2) whether the charge-charge repulsions are even strong enough to favor persistent modulated structure. The first point has been postulated previously [62, 63, 127], and here is bolstered by the considerable discrepancy between the region of parameter space where an IRO pre-peak is observed and the region where formation of clusters occurs (i.e., at and above locus of $\beta\epsilon^*$). To wit, there is a energy differential of $\Delta\epsilon \geq 2k_{\mathrm{B}}T$ between the emergence of the IRO pre-peak and the emergence of clusters over many screening lengths.

Meanwhile, one can also observe a second transition in the peak behavior of Fig. 6.1(a) within the screening length range $0.3 \leq \kappa^{-1}/d \leq 1.0$: moving in the direction of increasing attraction strength, an IRO pre-peak initially develops, but subsequently shifts to $k_{\mathrm{pre}}d = 0$ while the system *bypasses the formation of a cluster*

phase. Crossing this type of (reverse) Lifshitz boundary is readily attributable to the physical setup we consider, where attraction strength is "decoupled" from repulsions; after all, one should arguably be able to ramp up attractions to such high strengths that macrophase separation is favorable given even relatively strong repulsions. (Alternatively, our previous work illustrates this switch for one case of extremely weak repulsions [91].) This shift from $k_{\mathrm{IRO}}d > 0$ to $k_{\mathrm{pre}}d = 0$ is exemplified in Fig. 6.1(b), which can be contrasted with Fig. 6.1(c), which shows an $S(k)$ series at larger κ^{-1}/d where the IRO pre-peak persists and grows once it emerges. (These behaviors are rounded out by panel Fig. 6.1(d), which gives a representative series of a system shifting from a $k_{\mathrm{pre}}d = 0$ to $k_{\mathrm{IRO}}d > 0$ pre-peak.) Taking these two observations together, one must keep in mind that IRO pre-peak existence can not only considerably precede cluster formation, but can be very misleading at intermediate screening lengths where existence does not even *universally* signal that increasing attraction strength will result in formation of stable clusters.

To demonstrate that the qualitative trends of pre-peak existence and position shown in Fig. 6.1 are relatively generic, we show in Fig. 6.2 a representative series of pre-peak landscapes for various charges Z (at fixed ϕ), and a comparison between landscapes for different ϕ (at fixed Z). Despite the varying conditions, we generally find: (1) that given sufficient integrated repulsions, the formation of an IRO pre-peak precedes cluster formation by a differential in attraction strength upwards of $\Delta\epsilon = 2$ to $3k_{\mathrm{B}}T$; (2) that there exist intermediate ranges of κ^{-1}/d where IRO pre-peaks shift to $k_{\mathrm{pre}}d = 0$ prior to clustering; and (3) that forma-

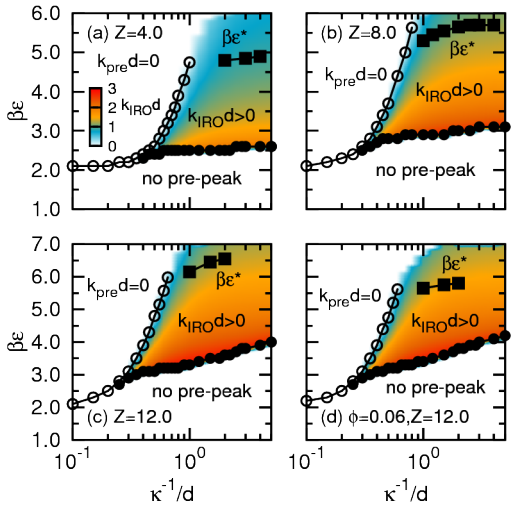

Figure 6.2: Pre-peak position $k_{\mathrm{pre}}d$ in the structure factor $S(k)$ as a function of attraction strength $\beta\varepsilon$ and screening length κ^{-1}/d obtained from IET for (a) packing fraction $\phi = 0.03$, charge $Z = 4.0$; (b) $\phi = 0.03$, $Z = 8.0$; (c) $\phi = 0.03$, $Z = 12.0$; and (d) $\phi = 0.06$, $Z = 12.0$. Filled and unfilled circles delineate transitions between different pre-peak behaviors in IET results. Squares denote critical attraction strengths $\beta\varepsilon^*$ at the onset of clustering obtained from MD simulations. Note that the loci of IRO pre-peak emergence in simulations (not shown) overlap with the filled circles from IET. In all panels, IET results are based on monodisperse systems while simulation results are based on lightly polydisperse mixtures (see text).

tion of finite-sized aggregates is very unlikely for screening lengths $\kappa^{-1}/d \leq 0.60$, though we cannot definitively rule out the possibility.

Indeed, the primary differences across these various conditions are systematic shifts in the critical attraction strength $\beta\varepsilon^*$ to form clusters. The locus of $\beta\varepsilon^*$ shifts to higher values as surface charge Z increases due to the need to overcome greater charge-charge repulsions. In contrast, for fixed Z and κ^{-1}/d, the critical attraction strength $\beta\varepsilon^*$ decreases by between approximately 0.3 and $1.0k_{\mathrm{B}}T$ when ϕ is doubled (trend applies from $0.015 \leq \phi \leq 0.12$) because this reduces the effective energetic barrier for bringing particles from the reference pair distance $L/d \approx (\rho_{\mathrm{M}} d^3)^{-1/3}$ of the homogeneous dispersion to the contact distance $L/d \approx 1$ in aggregates.

As a final point, we note that for a given charge Z, the range in κ^{-1}/d over which the dense phase moves between an infinite scale (i.e., macroscopic liquid-gas separation) at small κ^{-1}/d to an asymptotic modulated structure (given sufficient charge Z) at large κ^{-1}/d is quite narrow. Moving horizontally at, e.g., $\beta\varepsilon^*$, across any of the landscapes of Figs. 6.1-6.2, the pre-peak moves from $k_{\mathrm{pre}}d = 0$ at $\kappa^{-1}/d \leq 0.5$ to an approximately constant $k_{\mathrm{IRO}}d > 0$ for $\kappa^{-1}/d \geq 3.0$. Thus, one effectively reaches the Coulombic limit in terms of the repulsion influence for screening lengths κ^{-1}/d approaching only a few monomer diameters.

6.3.2 Cluster morphologies in simulations

To forge connections between the IRO pre-peak in $S(k)$ and the real-space morphologies observed in SALR systems, we analyze 3D configurations of approxi-

mately 100 different clustered phases generated via MD simulations, where we can obtain $S(k)$ while simultaneously measuring the number-size N^* and real-space lengthscales associated with the aggregates. We consider cluster phases formed for wide ranges of ϕ, Z, κ^{-1}/d, where, for the sake of consistency, we specifically concern ourselves with states *at the onset of clustering* where aggregates of a preferred size have emerged. These states are defined by critical attraction strengths $\beta\varepsilon^*$, where all of the state points that are analyzed in the following sections are listed in Table 6.1 by their respective $\beta\varepsilon^*$ values.)

As demonstrated in Figs. 6.3-6.4, we examine phases comprising clusters in the size range $6 \leq N^* \leq 60$ that are compact and spherically symmetric on average, making these states promising for $S(k)$ interpretation because they are relatively simple (idealized) in terms of their morphologies. We first consider Figs. 6.3(a-b), where we show that plotting the radius of gyration $R_{\rm G}/d$ versus cluster size N^* follows the relation

$$R_{\rm G}/d = \alpha(\phi) N^{*(1/d_{\rm f})} \text{ with } d_{\rm f} = 3 \tag{6.8}$$

where $\alpha(\phi)$ is a ϕ-dependent prefactor on the order of 1/2 (hereafter notated α) and $d_{\rm f}$ is the fractal dimension of the aggregates. The fractal dimension $d_{\rm f} = 3$ signifies that the clusters are compact objects, in contrast with aggregates that are more highly-branched and/or elongated, which would tend to exhibit $d_{\rm f} < 3$. Likewise, the magnitudes of the α prefactors underline that these aggregates have high internal packing fractions, though we do see a modest positive correlation

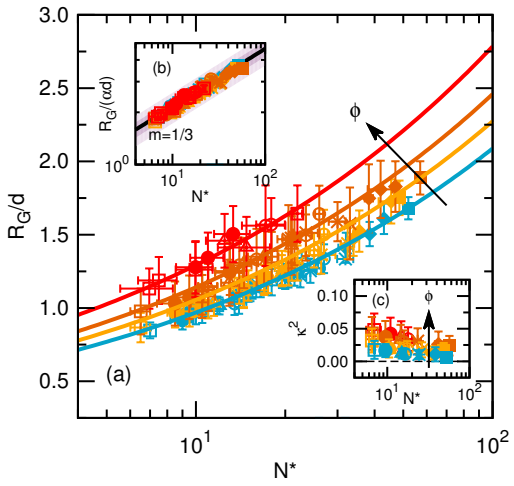

Figure 6.3: (a) Cluster radius of gyration R_G/d versus characteristic cluster size N^*, both measured from MD simulations at the onset of clustering (i.e., at critical attraction strengths $\beta\varepsilon^*$). Blue, yellow, orange, and red symbols correspond to data from simulations at packing fractions $\phi = 0.015$, 0.030, 0.060, and 0.120, respectively. Symbol types correspond to constant charge Z as listed in Table 6.1 (note that we test various screening lengths κ^{-1}/d at each Z). Lines are empirical fits of the form $R_G/d = \alpha N^{*1/3}$, where α is a dimensionless prefactor corresponding to $\alpha = 0.45$, 0.49, 0.53, and 0.60 for $\phi = 0.015$, 0.030, 0.060, and 0.120, respectively. (b) Same data from (a), but rescaled to highlight the characteristic exponent m in the expression $R_G/d = \alpha N^{*m}$, which corresponds to $m = 1/d_f$ with d_f being the fractal dimension of the aggregates. Black line corresponds to $R_G/(\alpha d) = N^{*1/3}$, with dark (light) purple regions denoting 10% (20%) deviation from this relation. (c) Relative shape anisotropy κ^2 of clusters measured from simulations at selected state points from (a), where state points were chosen to roughly span the range of observed equilibrium cluster sizes N^*.

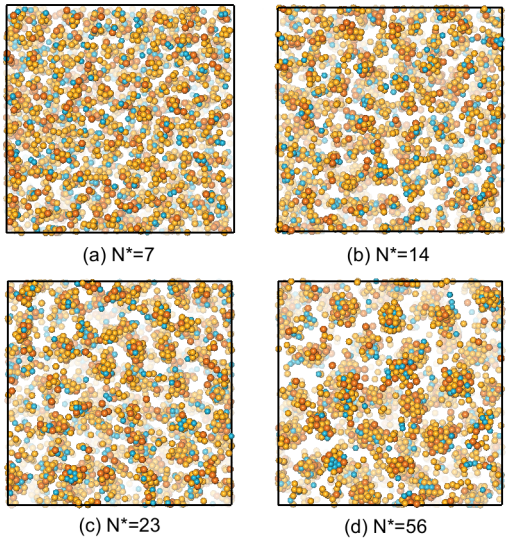

Figure 6.4: Configuration snapshots from simulations of phases at the onset of clustering (i.e., at critical attraction strengths $\beta\varepsilon^*$). The snapshots are at packing fraction $\phi = 0.060$ and chosen to roughly span the range of observed equilibrium cluster sizes N^*. Repulsions are defined by (a) charge $Z = 15.0$ and screening length $\kappa^{-1}/d = 2.0$; (b) $Z = 10.0$ and $\kappa^{-1}/d = 1.5$; (c) $Z = 6.0$ and $\kappa^{-1}/d = 2.0$; and (d) $Z = 4.0$ and $\kappa^{-1}/d = 3.0$. Blue, yellow, and orange shadings correspond to small, medium, and large particles in the polydisperse mixtures (see Methods). Visualizations were produced using VMD [87].

between R_G/d and ϕ given fixed N^*. This indicates that clusters are slightly less dense given closer intercluster proximity, which can be attributed to more frequent monomer exchanges that tend to instantaneously (but, on average, isotropically) enlarge the clusters compared to their "isolated" structure at very low packing fractions, e.g., $\phi = 0.015$.

Meanwhile, measurements of the relative shape anisotropy κ^2, which are shown in Fig. 6.3(c), demonstrate that these cluster objects are highly symmetric even down to small sizes N^*. Here, we calculate the long-established parameter κ^2, where $\kappa^2 = 0$ corresponds to points (particles) that are symmetrically distributed and $\kappa^2 = 1$ corresponds to points arranged linearly [208]. Calculated based on the monomer positions within the clusters, we find $\kappa^2 \leq 0.05$ for all cluster sizes and packing fractions, which indicates symmetric arrangements of particles and complements the R_G/d-based findings above that mainly imply compactness. Specifically, we observe $\kappa^2 \approx 0.01$ (very high symmetry) for the most isolated clusters at $\phi = 0.015$, and a slight positive correlation between κ^2 and ϕ that implies aggregate symmetry is somewhat sensitive to the increasing frequency of (near-)collisions and monomer-exchanges, which tend to generate outlying particles and instantaneously distorted states that positively contribute to κ^2.

As illustrated in Fig. 6.4, visualizations of the cluster phases complement the findings above: the aggregates formed in these systems are highly-compact and roughly spherical on average; furthermore, based on these attributes and the size-scaling of the aggregates, we estimate the typical internal packing fraction of the clusters is $\phi_{\text{int}} \approx 0.40$. To wit, we observe good mixing of the polydisperse

monomers, which frustrates intracluster crystallization and promotes intra- and intercluster diffusion. One can also appreciate the preferred sphericity of the clusters, though this can be instantaneously violated as clusters collide, merge, or exchange monomers. Given the clusters are spherical, we can estimate the internal packing fraction using the expression $\phi_{\text{int}} = N^* V_{\text{mon}}/V_{\text{cl}}(N^*)$ where $V_{\text{mon}} = (4/3)\pi(d/2)^3$ and $V_{\text{cl}} = (4/3)\pi(R_{\text{cl}})^3$ are the volumes of the monomer and cluster, respectively (here we assume monodisperse monomer). We then estimate the N^*-dependent cluster radius as $R_{\text{cl}}/d = R_{\text{G}}/d + 0.5$ where the latter coefficient is added because R_{G}/d is based on particle centers. Using the relation $R_{\text{G}}/d \approx 0.5N^{*1/3}$ gives $0.30 \leq \phi_{\text{int}} \leq 0.50$ over the range $6 \leq N^* \leq 60$, with the majority of sizes $\phi_{\text{int}} \geq 0.35$. This is comparable with dense simple fluids.

Finally, in line with the observations of Godfrin et. al. [63], we find that the emergent aggregates universally exhibit average intracluster coordination numbers (i.e., numbers of nearest-neighbors) of $z_{\text{c}} \geq 2.4$, which is the well-established minimum coordination number corresponding to rigid percolation [76]. Predictably, z_{c} grows with respect to cluster size, where the scaling relationship between these two quantities is important for understanding the thermodynamics of cluster formation. We discuss this more extensively in Chapter 7.

6.3.3 Interpreting the pre-peak position

Based on our collection of simulated cluster morphologies, we first address what physical characteristic(s) of these morphologies that the IRO *pre-peak position* in $S(k)$ captures. This is important because while the *real-space* lengthscale

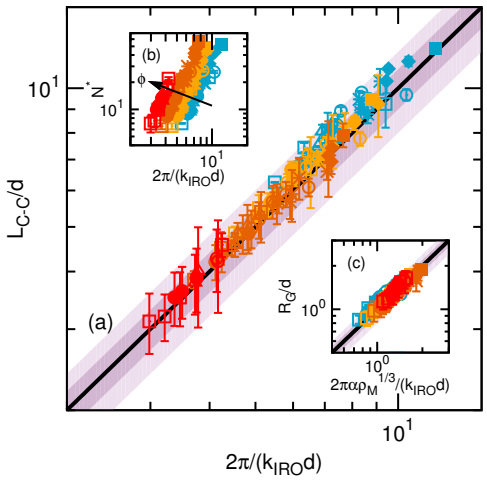

Figure 6.5: (a) Average intercluster center-to-center distance $L_{\text{C-C}}/d \equiv [N^*/(\rho d^3)]^{1/3}$ (see text), where ρd^3 is the bulk monomer density, versus inverse IRO pre-peak wavenumber (i.e., real-space distance) $2\pi/(k_{\text{IRO}}d)$, both measured in MD simulations. (b) Cluster size N^* versus IRO pre-peak lengthscale $2\pi/(k_{\text{IRO}}d)$. (c) Cluster radius of gyration R_{G}/d versus inverse IRO pre-peak wavenumber shifted by α and ρd^3 (combining Eqns. 6.8 and Eqn. 6.9). In (a) and (c), thick lines denote 1:1 correspondence between x- and y-axes, with dark (light) purple regions denoting 10% (20%) deviation from this relation. In all panels, symbol types correspond to constant charge Z as listed in Table 6.1 (note that we test various screening lengths κ^{-1}/d at each Z).

$2\pi/(k_{\mathrm{IRO}}d)$ captured by the inverse pre-peak position is generally thought to encode the real-space cluster diameter (or perhaps intercluster center of mass separation), there has been limited information available allowing for an unambiguous determination of what lengthscale(s) $k_{\mathrm{IRO}}d$ truly captures. As such, there is not yet consensus about whether the pre-peak position should exhibit a systematic dependence upon bulk monomer density [27, 62, 182, 193, 200, 201]. In other words, if similarly sized clusters are found at two densities, should pre-peak position be the same?

Focusing on Fig. 6.5, we find that the real-space lengthscale $2\pi/(k_{\mathrm{IRO}}d)$ is equivalent to the average *center-to-center intercluster distance* $L_{\mathrm{C\text{-}C}}/d$. A direct comparison between the two quantities is presented in Fig. 6.5(a), which demonstrates excellent quantitative agreement, and Fig. 6.5(b) makes it clear that the pre-peak lengthscale is correspondingly a function of both cluster size N^* *and* bulk monomer density ρd^3. To understand why this is so, let us consider the number density of clusters $\rho_{\mathrm{C}}d^3 = n_{\mathrm{C}}/(L_{\mathrm{box}}/d)^3$, where $n_{\mathrm{C}} = N_{\mathrm{box}}/N^*$ is the number of clusters in the simulation assuming perfect size-uniformity and L_{box} is the simulation box length. We can then write $\rho_{\mathrm{C}}d^3 = N_{\mathrm{box}}/[N^*(L_{\mathrm{box}}/d)^3] = (\rho d^3)/N^*$, where the second equality is simply due to the definition of the bulk monomer density $\rho d^3 = N_{\mathrm{box}}/(L_{\mathrm{box}}/d)^3$. Since, in the crudest sense, the average intercluster distance $L_{\mathrm{C\text{-}C}}/d \approx (\rho_{\mathrm{C}}d^3)^{-1/3}$, we thus have:

$$2\pi/(k_{\mathrm{IRO}}d) = L_{\mathrm{C\text{-}C}}/d \equiv \left(\frac{N^*}{\rho d^3}\right)^{1/3} \tag{6.9}$$

As is evident from Fig. 6.5(a), there is excellent collapse in the data along Eqn. 6.9 for all of the cluster phases tested.

This analysis assumes nothing about the shape and/or compactness of the clusters (only that they are distinguishable and of number-size N^*), which has two implications: one can readily obtain cluster size N^* given knowledge of $k_{\mathrm{IRO}}d$ and ρd^3; however, to obtain a real-space cluster diameter, one must *independently* possess an empirical relation between N^* and cluster diameter (or, e.g., R_{G}/d). Of course, given our systems exhibit the size-scaling of Eqn. 6.8, we demonstrate in Fig. 6.5(c) that this type of conversion from pre-peak position to cluster radius is quantitative. Finally, though this model for pre-peak position assumes little about the nature of the aggregates, we cannot rule out that the strength of the quantitative match between $2\pi/(k_{\mathrm{IRO}}d)$ and $L_{\mathrm{C\text{-}C}}/d$ may diminish for less-idealized morphologies that are not primarily composed of highly-packed spherical clusters.

6.3.4 Detecting the onset of clustering based on the structure factor

As already discussed, the existence of an IRO pre-peak is necessary but not sufficient evidence for positively identifying a clustered phase. In this section, we draw on our results from simulations to directly test two criteria postulated to detect the transformation between homogeneous and clustered phases: one based on the IRO pre-peak *height* (i.e., magnitude) and one based on the IRO pre-peak *width*.

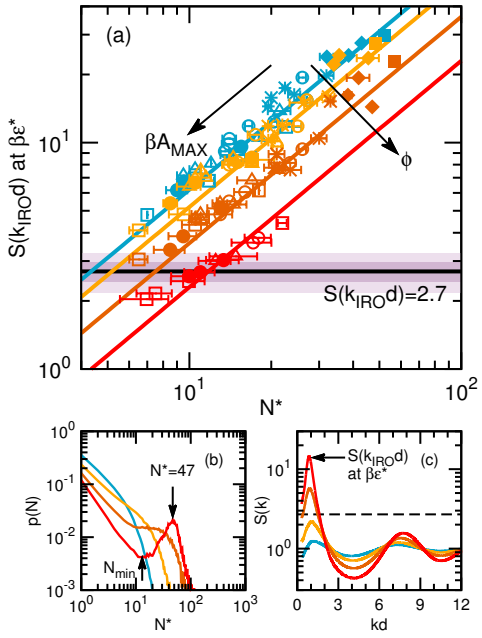

Figure 6.6: (a) IRO pre-peak height $S(k_{\mathrm{IRO}}d)$ at onset of clustering (at $\beta\varepsilon^*$) versus cluster size N^*, both measured in MD simulations. Thick line denotes previously-proposed criterion [62, 63] postulating that the emergence of clusters occurs as $S(k_{\mathrm{IRO}}d) \approx 2.7$. Dark (light) purple regions denote 10% (20%) deviation from this relation. Color lines are guides to the eye for results from (top to bottom) $\phi = 0.015$, 0.030, 0.060, and 0.120. Symbol types correspond to constant charge Z as listed in Table 6.1 (note that we test various screening lengths κ^{-1}/d at each Z). (b) Cluster size distributions $p(N)$ and (c) structure factors calculated from MD simulations for packing fraction $\phi = 0.060$, charge $Z = 4.0$, screening length $\kappa^{-1}/d = 2.0$, and attraction strengths $\beta\varepsilon = 3.50$, 4.00, 4.30 and 4.55 (top to bottom in (b); bottom to top in (c)). The critical attraction strength is $\beta\varepsilon^* = 4.55$. In (b), we note the local minimum N_{min} and maximum N^* in $p(N)$ that characterize the onset of clustering (see Methods). The dashed line in (c) marks $S(k_{\mathrm{IRO}}d) = 2.7$.

6.3.4.1 Pre-peak height

We begin by revisiting previous reports [62, 63] that the onset of clustering occurs as the pre-peak height (magnitude) reaches the threshold value $S(k_{\mathrm{IRO}}d) \approx 2.7$. In brief, this is an adaptation of the empirical Hansen-Verlet freezing rule developed for simple fluids [74], which states that the height of the first pre-peak in the structure factor approaches $S(k) \approx 2.85$ at the fluid-solid transition (i.e., along the melting line). In this way, the $S(k_{\mathrm{IRO}}d) \approx 2.7$ clustering criterion is conceptually like considering cluster formation as a *microcrystallization* event, i.e., a frustrated analog of the bulk freezing transition. However, this criterion for identifying clustering has only been tested for a limited scope of repulsions strengths and lengthscales, generally in schemes (unlike the protocol here) where attraction and repulsions strengths have been simultaneously rescaled by modulating T.

In Fig. 6.6, we plot the magnitudes of the IRO pre-peaks in $S(k)$ measured from simulations at the onset of clustering for our ≈ 100 different systems, where we observe that for the majority of cases tested, the peak-height considerably exceeds (by up to an order of magnitude) the $S(k_{\mathrm{IRO}}d) \approx 2.7$ threshold. In essence, the criterion does not generally pinpoint the *emergence* of aggregates with a characteristic size because many dispersed states (and/or states exhibiting generic amorphous IRO) at a given Z and κ^{-1}/d exhibit IRO pre-peaks with heights of $S(k_{\mathrm{IRO}}d) \geq 2.7$ well before attractions are actually strong enough to stabilize clusters. Thus, one might instead posit that the condition $S(k_{\mathrm{IRO}}d) \geq 2.7$ is a *necessary but not sufficient* criterion for positively identifying clustered phases.

Broadly speaking, the criterion acts only as a minimum threshold because pre-peak height is highly-coupled to the $kd \to 0$ limit of $S(k)$, which is proportional to system compressibility χ_{T} [73]. To wit, the states where the $S(k_{\mathrm{IRO}}d)$ values most exceed the $S(k_{\mathrm{IRO}}d) \approx 2.7$ limit at $\beta\varepsilon^*$ are those governed by relatively weak repulsions (correlated with larger N^* in Fig. 6.6) and lower ϕ, both of which contribute to high χ_{T}. Thus, an IRO pre-peak height can reach large values even as the pre-peak signature itself may be rather weak (i.e., flat, especially away from the clustering locus), simply due to the leading influence of the high-magnitude low-k limit. This type of coupling between the pre-peak and zero-wavenumber limit is evident even at "moderate" packing fractions like $\phi = 0.060$, as shown in Figs. 6.6(b-c): relatively low-strength repulsions combined with the increasing attractions generating heterogeneity drive compressibility to high values (e.g., greater than 1), with the pre-peak emerging and sharpening at correspondingly large magnitudes.

More conceptually, it should perhaps be unsurprising that the Hansen-Verlet freezing rule is a poor fit for these systems. In essence, the rule was developed based on suspensions undergoing solidification due to *packing effects*; however, clustering in an SALR system is driven not by a competition between configurational free volumes, but by a competition between attractions and repulsions. In turn, while describing the cluster formation as "microcrystallization" seems fitting–especially for highly monodisperse monomers that form clusters with crystal motifs–it is a transformation more akin to a frustrated liquid-gas separation.

6.3.4.2 Pre-peak width

We now move on to test a recently proposed framework [91] for identifying the onset of clustering based the IRO pre-peak width, which encodes the *thermal correlation length* ξ_{T}/d. Conceptually, the thermal correlation length quantifies the real-space persistence of structural correlations and is most frequently considered in the context of fluids undergoing *macrophase* liquid-gas separation (i.e., unstable droplet formation). In this context, ξ_{T}/d constitutes a prefactor in the well-established [73] second-order inverse expansion of $S(k)$ about the corresponding pre-peak at $k_{\mathrm{pre}}d = 0$:

$$S(kd)\Big|_{k_{\mathrm{pre}}d=0} \approx \frac{S(0)}{1 + (\xi_{\mathrm{T}}/d)^2(kd)^2} \tag{6.10}$$

and one can identify the liquid-gas transition based on the divergence of $\xi_{\mathrm{T}}/d \to \infty$, which signifies formation of "infinitely" persistent dense regions.

For clustering systems dominated by frustrated interactions, one can analogously consider the ξ_{T}/d encoded in the IRO pre-peak, which quantifies the persistence of the *modulated* dense structure in the fluid characterized by the finite lengthscale $2\pi/(k_{\mathrm{IRO}}d)$. Here, the inverse expansion about the pre-peak can be written:

$$S(kd)\Big|_{k_{\mathrm{IRO}}d>0} \approx \frac{S(k_{\mathrm{IRO}}d)}{1 + (\xi_{\mathrm{T}}/d)^2(k - k_{\mathrm{IRO}})^2d^2} \tag{6.11}$$

which can be readily rearranged to give:

$$\left.\frac{1}{S(kd)}\right|_{k_{\mathrm{IRO}}d>0} \approx \frac{1}{S(k_{\mathrm{IRO}}d)} + \frac{(\xi_{\mathrm{T}}/d)^2}{S(k_{\mathrm{IRO}}d)}(k-k_{\mathrm{IRO}})^2 d^2 \tag{6.12}$$

This expression makes it clear that the combined prefactor $(\xi_{\mathrm{T}}/d)^2/S(k_{\mathrm{IRO}}d)$ is equivalent to the second-order coefficient in a Taylor series expansion of $S^{-1}(kd)$. This equivalence provides a highly practical expression for calculating the IRO thermal correlation length

$$\xi_{\mathrm{T}}/d = \left[\frac{1}{2}S(k_{\mathrm{IRO}}d)\left.\frac{\mathrm{d}^2 S(kd)}{\mathrm{d}k^2}\right|_{k_{\mathrm{IRO}}d>0}\right]^{1/2} \tag{6.13}$$

where one must simply (1) record the pre-peak magnitude and (2) perform a polynomial fit about the pre-peak position $k_{\mathrm{IRO}}d$) to obtain the second-derivative.

In line with other systems that undergo frustrated microstructural transformations [179], the peak-width clustering criterion posits that cluster formation should be characterized not by a true divergence in the IRO ξ_{T}/d, but instead when the IRO ξ_{T}/d first exceeds the only competing (characteristic) lengthscale in the system: the screening length of the repulsions κ^{-1}/d. In other words, the onset of clustering should occur when the IRO thermal correlation length reaches the Debye screening length, i.e.,

$$\xi_{\mathrm{T}}/d \approx \kappa^{-1}/d \tag{6.14}$$

The remainder of this section aims to provide greater physical intuition for this criterion and to demonstrate how it performs versus simulations.

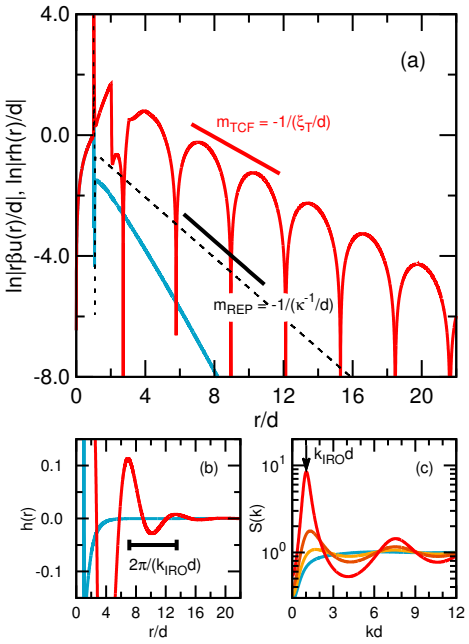

Figure 6.7: (a) Log-positive transforms of the total correlation function (TCF) $h(r) = g(r) - 1$ and pair potential $\beta u(r)$ for $\phi = 0.030$, $Z = 8.0$, and $\kappa^{-1}/d = 2.0$, where solid lines correspond to TCF transform of $h(r)$ at $\beta\varepsilon = 1.5$ (blue, lower) and 6.0 (red, upper), and the dashed line corresponds to $\beta u(r)$ (note: $h(r)$ profiles are obtained from IET). The two types of profiles are plotted to highlight their asymptotic decays at large r/d, with characteristic slopes $m_{\rm TCF}$ and $m_{\rm REP}$, respectively. Note that the thermal correlation length $\xi_{\rm T}/d \simeq 3.1$ for $\beta\varepsilon = 6.0$, which exhibits strong IRO. (b) Untransformed $h(r)$ profiles for same states as in (a), scaled to highlight long-range oscillations at $\beta\varepsilon = 6.0$. (c) Structure factors obtained from IET at $\phi = 0.030$, $Z = 8.0$, and $\kappa^{-1}/d = 2.0$, where $\beta\varepsilon = 1.5$, 4.0, 5.0, and 6.0 from bottom to top. Here, the highlighted IRO wavenumber at $\beta\varepsilon = 6.0$ is $k_{\rm IRO}d = 1.02$.

To get a better physical sense for this comparison between thermal correlation length and Debye length, consider Fig. 6.7(a), where we plot selected transforms of the total correlation function $h(r)$ and the interparticle potential $\beta u(r)$ that highlight how the constants ξ_{T}/d, and κ^{-1}/d reflect the characteristic exponential decays (negative slopes) of the pair structural correlations and repulsive barrier, respectively. Here, while repulsions are obviously defined by the exponential decay in Eqn. 6.3, it is also worth recalling that pair correlations have the form [73]

$$\lim_{r/d\to\infty} h(r) \propto (r/d)^{-1} \exp[-r/\xi_{\mathrm{T}}] \cos[rk_{\mathrm{IRO}} - \theta] \tag{6.15}$$

where the cosine term captures the modulated nature of the IRO structure (it is not normally included for, e.g., simple fluids).

By examining the profiles in Fig. 6.7 calculated for conditions ($\beta\varepsilon = 6.0$) exceeding the Eqn. 6.14 condition, we can readily glean the features of $h(r)$ that characterize cluster phases in the IRO ξ_{T}/d framework: oscillations (humps) in transformed $h(r)$ that asymptotically decay *more slowly* than the potential $\beta u(r)$ (Fig. 6.7(a)), where these tell-tale oscillations mirror long-range oscillatory structure in $h(r)$ that occurs on the lengthscale $2\pi/(k_{\mathrm{IRO}}d)$ (Fig. 6.7(b)) and sets the pre-peak in $S(k)$ (Fig. 6.7(c)). In contrast, for a dispersed phase (here, $\beta\varepsilon = 1.5$), one observes $h(r)$ (transformed or not) decay quickly to zero and display no characteristic oscillations at any intercluster lengthscale. Comparing these cases, it is clear that by searching for sufficiently strong IRO thermal correlation lengths

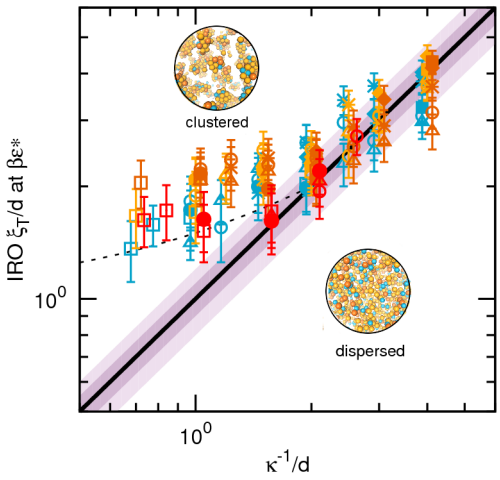

Figure 6.8: IRO thermal correlation lengths ξ_T/d extracted from $S(k)$ profiles at onset of clustering (at $\beta\varepsilon^*$) in MD simulations versus screening length κ^{-1}/d. Thick line denotes previously postulated criterion [91] for identifying onset of clustering ($\xi_T/d \approx \kappa^{-1}/d$), where dark (light) purple regions denote 10% (20%) deviation from this relation. Dotted line at shorter κ^{-1}/d corresponds to an empirical guideline with form $\xi_T/d = 1.0 + 0.5(\kappa^{-1}/d)$. Note that at a given κ^{-1}/d, symbols corresponding to different ϕ are slightly shifted horizontally to improve aesthetic clarity. Symbol types correspond to constant charge Z as listed in Table 6.1 (note that we test various screening lengths κ^{-1}/d at each Z).

ξ_T/d, we are looking for states that exhibit persistent *coordination shell* structure in $h(r)$ at a "cluster-sized" scale. This is intuitive given a clustered phase ideally comprises intermediate-scale densified regions exhibiting disordered fluid structure in themselves.

Finally, we consider Fig. 6.8, where we directly test the $\xi_T/d \approx \kappa^{-1}/d$ criterion by examining the $S(k)$ profiles from our ≈ 100 simulated systems at the

onset of clustering (i.e., at $\beta\varepsilon^*$) and plotting the ξ_T/d values extracted from the IRO pre-peaks versus the κ^{-1}/d values defining the respective repulsive interactions. We obtain the ξ_T/d values via Eqn. 6.13, where we measure the pre-peak position and magnitude and then calculate the second derivative of $S(k)$ based on a third-order polynomial curve centered at $k_{IRO}d$ and fitted over a $\Delta(kd) \approx 0.20$ range. To give a sense for the uncertainty in ξ_T/d, note that we plot error bars corresponding to the standard deviation in ξ_T/d values across the $S(k)$ pre-peaks exhibited at attraction strengths $\beta\varepsilon = \beta\varepsilon^*$ and $\beta\varepsilon = \beta\varepsilon^* \pm 0.05$.

So how does the pre-peak width criterion perform? Fig. 6.8 demonstrates that the emergence of clusters occurs when the IRO $\xi_T/d \approx \kappa^{-1}/d$ for a wide variety of ϕ, Z, and κ^{-1}/d conditions, provided the interactions are governed by sufficiently large screening lengths ($\kappa^{-1}/d \geq 2.0$). At smaller screening lengths, we clearly observe a systematic breakdown of the criterion shown by the empirical dashed line. In retrospect, this is somewhat unsurprising given that IRO pre-peaks manifesting equally diminutive correlation lengths would be very weak (flat), i.e., would not reflect persistent intercluster coordination shells. In turn, thinking about larger screening lengths beyond those tested ($\kappa^{-1}/d > 4.0$), we would note that the critical IRO ξ_T/d likely exhibits weak dependence on κ^{-1}/d because these systems effectively approach the Coulombic limit for $\kappa^{-1}/d \geq 3.0$ (see Figs. 6.1-6.2 and Chapter 7). Indeed, given the spread in the data, there is already little discernible difference between the critical IRO ξ_T/d values recorded from the simulation sweeps at $\kappa^{-1}/d = 3.0$ and 4.0.

Taken altogether, we propose as a general guideline that to detect the onset

of clustering, one search for the conditions at which the IRO thermal correlation length is within the range $2.0 \leq \xi_{\mathrm{T}}/d \leq 3.0$ and where (given the discussion above) the pre-peak height simultaneously exceeds $S(k_{\mathrm{IRO}}d) \geq 2.7$. This two-fold criterion is advantageous because it does not depend on screening length κ^{-1}/d and, while this rule is necessarily inexact, it is nonetheless more empirically robust with respect to conditions (ϕ, Z, κ^{-1}/d), particularly over the intermediate screening lengths (one to three monomer diameters) common to clustering studies. We would also point out that this hybrid rule should serve as a *lower bound* with respect to $\beta\varepsilon$ for the appearance of clusters: above the critical $\beta\varepsilon^{*}$, we have generally observed a bandwidth in attraction strength of $\Delta\varepsilon \simeq 1.5k_{\mathrm{B}}T$ before clusters start to form arrested percolated networks that are tentatively classified as thermoreversible gels [91].

In closing this discussion, we do note that the original pre-peak width criterion, which requires knowledge of κ^{-1}/d, can be used based *solely* on knowledge of $S(k)$ because one can not only extract the IRO ξ_{T}/d, but also an estimate for κ^{-1}/d. (This is an alternative approach to estimating κ^{-1}/d based on Z, ϵ_{R}, I, etc.) Here, one can recall [73] that the direct correlation function $c(r)$ is generally understood to scale at long-range as $\lim_{r/d\to\infty} c(r) \approx -\beta u(r)$. Given that $\hat{c}(k) = (\rho d^3)^{-1} - [(\rho d^3)S(k)]^{-1}$ and $c(r) = \mathrm{FT}^{-1}[\hat{c}(k)]$, one can: (1) measure $S(k)$; (2) convert it $\hat{c}(k)$; (3) and readily obtain $c(r)$. This provides an approximate $\beta u(r)$ profile, which can be plotted (as in Fig. 6.7) to deduce κ^{-1}/d from its slope at long distance. Thus, in principle, one can quantify the characteristic lengthscale of monomer-monomer repulsions *in situ* at arbitrary density.

6.4 Conclusions

We have tested how the existence, position, and shape of the IRO pre-peak in the structure factor $S(k)$ can be interpreted for colloidal fluids that reversibly form self-limiting aggregate clusters due to isotropic competing SALR interactions between monomers. A major goal was to survey a wide array of parameter space spanning both monomer packing fraction ($0.015 \leq \phi \leq 0.120$) and the variables controlling monomer-monomer interactions (including attraction strength $\beta\varepsilon$, surface charge Z, and screening length κ^{-1}/d). The bulk of our findings draw upon results from MD simulations of approximately 100 different phases located along the locus of cluster formation, which exhibited relatively idealized morphologies comprising compact spherical clusters.

First, both IET calculations and MD simulations systematically corroborate the previous observations [62,63,127] that the *existence* of an IRO pre-peak in $S(k)$ is a poor predictor of whether a phase is clustered. Notably, we observe that for many intermediate screening lengths (e.g., $0.3 < \kappa^{-1}/d < 1.0$), IRO pre-peaks can form at wavenumbers $k_{\mathrm{IRO}}d > 0$ as $\beta\varepsilon$ increases, but subsequently shift to $k_{\mathrm{pre}}d = 0$, which corresponds to macroscopic lengthscales, before any microscopic cluster phases can form. Thus, IRO pre-peak formation does not even guarantee that a particular set of conditions (ϕ, Z, κ^{-1}/d) favors self-limited aggregation at any $\beta\varepsilon$.

Provided a phase is clustered, we find that the *position* (wavenumber) of the IRO pre-peak $k_{\mathrm{IRO}}d$ directly encodes the average real-space intercluster distance, where $2\pi/(k_{\mathrm{IRO}}d) = [N^*/(\rho d^3)]^{1/3}$. This dependence on ρd^3 means that for fixed

cluster size N^*, $k_{\mathrm{IRO}}d$ will show a systematic rightward shift with increasing ϕ. We add a note of caution that one cannot directly derive a real-space cluster diameter from $S(k)$; to obtain a cluster diameter, one one must possess an independent relation that can convert between N^* and real-space lengthscale.

We next tested a previously-proposed criterion for detecting the onset of clustering based on the *height* (magnitude) of the IRO pre-peak, which states that the onset of clustering occurs when $S(k_{\mathrm{IRO}}d) \approx 2.7$. Over our wide survey of states, we instead find that the pre-peak height at the onset of clustering frequently exceeds (by up to an order of magnitude) the $S(k_{\mathrm{IRO}}d) \approx 2.7$ threshold because of the coupling between the shape of the IRO pre-peak and the $kd \to 0$ limit of $S(k)$, which equals the system compressibility and is highly sensitive to both ϕ and the strength and lengthscale of interparticle repulsions. Thus, the condition $S(k_{\mathrm{IRO}}d) \geq 2.7$ appears to be a minimum threshold for clustering, i.e., it is a necessary but not sufficient test for positively identifying clustered phases.

We then revisited an alternative criterion for detecting cluster formation based on IRO pre-peak *width*, which encodes the thermal correlation length ξ_{T}/d, where the criterion states that the onset of clustering occurs when $\xi_{\mathrm{T}}/d \approx \kappa^{-1}/d$. We observe that this rule performs well for many different combinations of ϕ and Z provided that the screening length is in the range $2.0 \leq \kappa^{-1}/d \leq 4.0$. However, the criterion breaks down at smaller κ^{-1}/d because clustered phases, which are characterized intermediate-range coordination shells of aggregates, must correspondingly exhibit relatively large "threshold" IRO ξ_{T}/d values.

Because both the pre-peak height and width criteria are only approximate

across wide ranges of monomer interactions and packing fractions, we propose a *hybrid heuristic* for detecting the emergence of cluster phases based on $S(k)$: search for the conditions where (1) the pre-peak height exceeds $S(k_{\mathrm{IRO}}d) \geq 2.7$ and (2) the IRO thermal correlation length encoded in the pre-peak width simultaneously reaches the range $2.0 \leq \xi_{\mathrm{T}}/d \leq 3.0$. The combination of these attributes should ensure that there is both a very strong signature of IRO but also slowly-decaying modulated pair correlations corresponding to well-developed coordination-shell pair structure between clusters. And though inexact, this rule does not require knowledge of κ^{-1}/d and should be reasonably robust to varying conditions and interparticle interactions.

In closing, we remark that beyond the connections considered here between pair correlations and clustering, there remain deep questions about whether one can alternatively identify conditions that favor clustering in SALR fluids based simply on the phase behavior of fluids with equivalent attractions but no repulsions, which exhibit macrophase separation. Indeed, previous work [63] has pointed to strong (predictive) overlap between the onset of clustering and underlying purely-attractive binodal boundaries in systems where temperature is the controlling parameter; meanwhile, our related work on systems where attraction strength is the controlling parameter points to correspondence at least in the limit of very weak repulsions [91]. A fruitful area of inquiry here would be to understand how closely one can map between the temperature- and attraction-strength-based frameworks, which would lend fundamental insights into when and how repulsions drive otherwise macrophase-separating systems to form equilibrium microphase morphologies.

Chapter 7

Validating a free energy model for equilibrium cluster size in fluids with competing interactions

7.1 Introduction

Over the past century, colloidal aggregation has been observed and described in a wide range of contexts via progressively more powerful experimental techniques, phenomenological frameworks, and quantitative models [4, 46, 90, 121, 196, 214]. Spanning processes from droplet nucleation and growth, gel and glass formation, various self-assembly processes, etc., an overarching goal has been to use statistical mechanical or molecular thermodynamic approaches adopted from atomic systems and, if necessary, empirical rules to relate the *strength* and *length-scale* of particle interactions to resulting equilibrium (or non-equilibrium) structures and the thermodynamics (and kinetics) of their formation. These types of relations, especially when based on physically-intuitive thermodynamic arguments,

Reproduced in part with permission from J.A. Bollinger and T.M. Truskett, "Fluids with competing interactions. II. Validating a free energy model for equilibrium cluster size." J. Chem. Phys., 2016, 145 (6), p. 064903 (DOI: 10.1063/1.4960339). Copyright 2016 American Institute of Physics. J.A. Bollinger performed computer simulations, analyzed results, created figures, and wrote the manuscript.

are not only of fundamental importance, but also highlight pathways for engineering materials at the nano- to microscopic level.

As discussed in Chapter 6, we focus on fluids where interactions between primary particles (monomers) are characterized by attractions acting at small lengthscales close to contact that *compete* with repulsions acting at larger lengthscales. This class of interactions can drive the reversible formation of *equilibrium cluster phases* composed of self-terminating aggregates (droplets) of monomers. Such cluster phases have been the focus of much recent work, ranging from theoretical and computational studies of idealized colloidal or nanoparticle suspensions [6, 28, 62, 63, 68, 91, 96, 136, 153, 182, 204, 209, 233] to experimental demonstrations for both archetypal colloidal particles [32, 102, 228, 231] and heterogeneous monomers with anisotropic interactions like proteins [64, 97, 127, 161, 168, 201, 229, 230]. Despite the range of materials and lengthscales, the broad underlying formulation principles appear universal: induce (or allow) depletion (dispersion) attractions between monomers to drive aggregation while simultaneously controlling electrostatic repulsions between the ionic double-layers of monomers such that they collectively build up to attenuate growth.

While this basic paradigm of frustrating interactions is well-accepted, it is not yet established how to best describe observed cluster phases in terms of their thermodynamics and phenomenology. For example, is it possible to develop a simple and physically-motivated free-energy model which can generate accurate predictions of characteristic terminal cluster size N^* based on experimentally-tunable variables governing monomer interactions? We address this question here

by directly comparing free energy-based predictions of such a phenomenological approach against computer simulations for one of the most approachable and idealized cluster-forming models: the short-range attractive, long-range repulsive (SALR) pair potential [182]. Once the behavior for this simple system that coarse-grains over many microscopic details of the short-range interactions, electrostatic double-layers, solvent, etc. is better understood, the goal is then to expand the framework to include more complex free energy contributions relevant for specific realizable colloidal suspensions.

First, we first review the canonical *a priori* free-energy treatment for clustering colloidal suspensions due to Groenewold and Kegel [68, 69, 231], where we compare its predictions for cluster size N^* against a computational survey of phases comprising compact spherical aggregates. We take great care to clarify how this elegant and frequently-cited model adapts the classical nucleation theory of non-terminating droplets (or crystals) [8, 45, 185] for the SALR systems of interest by treating the latter as purely-attractive reference fluids superimposed with perturbative effects due to charges on the monomers and in the suspending solvent. However, while frequently cited (and adapted for related systems, e.g., driven colloids [137]), this model has not been systematically scrutinized against a large "test set" of cluster phases generated by gradually varying relevant independent variables, e.g., monomer surface charge Z. By conducting tests that align with the phenomenological assumptions underlying the model (e.g., apolar solvents, low cluster density), we readily find that the analytical predictive formula derived from their model exhibits a spurious scaling for the range of stable cluster sizes

observable in systems governed by SALR pair potentials.

With this knowledge in-hand, we describe and validate an alternative free energy model that *quantitatively* predicts the characteristic cluster size N^* for approximately 100 different simulated SALR systems, which comprise compact spherical aggregates in the size range $6 \leq N^* \leq 60$ for wide ranges in monomer packing fraction ϕ, attraction strength $\beta\varepsilon$, monomer surface Z, and solvent screening length κ^{-1}/d (notably, even finite values outside the apolar limit). In essence, we find that a framework built on classical nucleation theory can indeed describe the thermodynamics of frustrated, finite-sized clusters provided one introduces a *size-dependent* enthalpic penalty of interface formation that accounts for the missing coordination bonds of "surface" particles in clusters. In justifying this approach, we also examine how the number of intracluster short-range bonds scales with size; interestingly, we find a *superlinear* crossover at our cluster sizes that bridges the previously-established scaling regimes for very small sizes [7,140] (e.g., $N^* \leq 9$) and larger, bulk-like droplets. Surprisingly, we also demonstrate that intercluster effects need not be considered to obtain correct predictions even for rather non-dilute conditions.

7.2 Methods

7.2.1 Model interactions

To systematically test the performance of free energy models for predicting equilibrium cluster formation, it is invaluable to be able to (1) rapidly generate aggregate configurations that can be analyzed in depth and (2) unambiguously

identify relevant free energy contributions. Thus, we consider one of the simplest and most frequently-used models known to form self-limiting aggregates: the short-range attractive (SA), long-range repulsive (LR) pair potential [182]. The combined SALR potential can be expressed

$$\beta u_{i,j}^{\mathrm{SALR}}(x_{i,j}) = \beta u_{i,j}^{\mathrm{SA}}(x_{i,j}) + \beta u_{i,j}^{\mathrm{LR}}(x_{i,j}) \tag{7.1}$$

where $\beta = (k_{\mathrm{B}}T)^{-1}$ (k_{B} is Boltzmann's constant and T is temperature); $x = r/d$ is the non-dimensionalized interparticle separation; d is the characteristic particle diameter. We include the subscripts i and j to account for multiple particle types because we follow previous protocols [91, 92] and examine size-polydisperse three-component mixtures that approximate colloids with 10% size polydispersity. (This favors the formation of amorphous fluid clusters over crystalline dynamically-arrested clusters. [91]) In this context, $x_{i,j} \equiv x - (1/2)(i + j)(\Delta_d/d)$, where i (or j) $= -1, 0, 1$ corresponds to small, medium, and large particles, respectively, and Δ_d/d is a perturbation to particle diameter. Specifically, we study mixtures comprised of 20% small, 60% medium (characteristic size d), and 20% large particles with $\Delta_d = 0.158d$.

The short-range attractions are expressed via a generalized (100-50) Lennard-Jones model

$$\beta u_{i,j}^{\mathrm{SA}}(x_{i,j}) = 4[\beta\varepsilon + (1 - 2\delta_{i,j})\beta\Delta_\varepsilon](x_{i,j}^{-100} - x_{i,j}^{-50}) \tag{7.2}$$

where $\beta\varepsilon$ is the reference monomer-monomer attraction strength and $\Delta_\varepsilon = 0.25k_{\mathrm{B}}T$

is an energetic perturbation to promote mixing of the polydisperse particles. Given its simplicity, the contribution of Eqn. 7.2 (similar to the contact attractions in the free energy model of Groenewold and Kegel [68]) does not specify the microscopic or chemical details; i.e., whether the attractions arise from depletion or other short-range interactions. Generally, the range of the attraction well is approximately $0.10d$.

Long-range repulsions are calculated on the basis of the repulsive portion of the DLVO potential [46, 214], which approximately captures the interactions of electrostatic double-layers formed around each monomer due to (homogeneously distributed) surface charge Z. This is expressed [90]

$$\beta u_{i,j}^{\mathrm{LR}}(x_{i,j}) = \beta A_{\mathrm{MAX}} \frac{\exp\left\{-(x_{i,j}-1)/(\kappa^{-1}/d)\right\}}{x_{i,j}} \tag{7.3}$$

with

$$\beta A_{\mathrm{MAX}} = \frac{Z^2(\lambda_{\mathrm{B}}/d)}{[1+0.5/(\kappa^{-1}/d)]^2} \tag{7.4}$$

where βA_{MAX} is the maximum electrostatic barrier between particles at contact, κ^{-1}/d is the Debye-Hückel screening length, Z is the total surface charge per monomer, and λ_{B}/d is the Bjerrum length of the solvent. Crucially, this formulation neglects any long-range multi-body interactions [159, 160], and any charge renormalization due to counterion condensation [1, 59, 138, 169] or close monomer association [153, 161]. As our goal here is to test how even the *simplest* clustering

systems might be described from a free energy perspective, we reserve incorporation of these phenomena for future studies.

In using this model, we set the average monomer packing fraction $\phi = (\pi/6)\rho d^3$ (where ρd^3 is number density), charge Z, and screening length κ^{-1}/d, and then *independently* tune the attraction strength $\beta\varepsilon$ to drive aggregation as if varying the amount of non-interacting depletant. In terms of experimental control one can exert over repulsive contributions, this picture is somewhat idealized: to wit, tunable repulsion-controlling parameters are more realistically (though still ignoring some possible interdependence) charge Z, solvent relative permittivity ϵ_{R}, and solvent ionic strength I. This is because, even approximately, the screening length $\kappa^{-1}/d = \sqrt{\epsilon_0\epsilon_{\mathrm{R}}k_{\mathrm{B}}T/(2d^2N_{\mathrm{A}}e^2I)}$ and $\lambda_{\mathrm{B}}/d = e^2/(4d\pi\epsilon_0\epsilon_{\mathrm{R}}k_{\mathrm{B}}T)$, where ϵ_0 is the vacuum permittivity, N_{A} is Avogadro's number, and e is the elementary charge. For simplicity, however, we universally *fix* the relative Bjerrum length λ_{B}/d, which means electrostatic effects are set via combinations of Z and κ^{-1}/d. With this experimental picture in mind, we also note that the repulsive strength in Eqn. 6.4 can equivalently be written $\beta A_{\mathrm{MAX}} = \pi d\epsilon_0\epsilon_{\mathrm{R}}\Psi_0^2/(k_{\mathrm{B}}T)$, where Ψ_0 is the surface potential on the monomer (often assumed to approximately equal the ζ-potential measured via electrophoresis).

As illustrated in Fig. 7.1, we conduct a wide survey of Z-κ^{-1}/d combinations designed to span the the weakest repulsions that produce self-limiting aggregates (i.e., near the boundary of macrophase separation) to repulsions with strengths up to $A_{\mathrm{MAX}} \approx 2.0k_{\mathrm{B}}T$. Here, note that to examine this range of repulsion strengths referenced against any plausible relative Bjerrum length λ_{B}/d (e.g., $\lambda_{\mathrm{B}}/d = 0.014$,

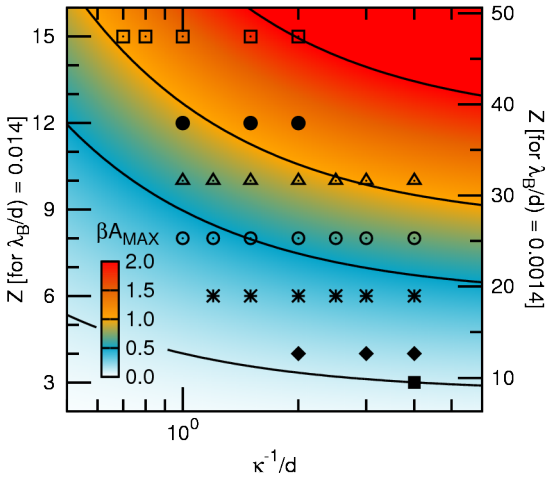

Figure 7.1: Maximum repulsion strength $\beta A_{\mathrm{MAX}} = Z^2(\lambda_{\mathrm{B}}/d)/[1.0 + 0.5/(\kappa^{-1}/d)]^2$ plotted as a function of surface charge Z and screening length κ^{-1}/d, where the left and right y-axes show Z-values referenced against two different reference Bjerrum lengths λ_{B}/d. The two reference Bjerrum lengths are $\lambda_{\mathrm{B}}/d = 0.014$, which corresponds in real units to, e.g., $d = 50$ nm monomers in a solvent with dielectric constant $\epsilon_{\mathrm{R}} = 80$ (equivalently, $d = 100$ nm and $\epsilon_{\mathrm{R}} = 40$, or $d = 200$ nm and $\epsilon_{\mathrm{R}} = 20$); and $\lambda_{\mathrm{B}}/d = 0.0014$, which corresponds to $d = 500$ nm and $\epsilon_{\mathrm{R}} = 80$ (equivalently, $d = 1$ μm and $\epsilon_{\mathrm{R}} = 40$, or $d = 2$ μm and $\epsilon_{\mathrm{R}} = 20$). Symbols mark Z-(κ^{-1}/d) combinations tested via simulations, where Table 6.1 lists the specific combinations tested at each packing fraction ϕ. Throughout the manuscript, simulations are referenced by the Z-values on the left y-axis, i.e., $Z = 3$, 4, 6, 8, 10, 12, and 15. Contours mark $\beta A_{\mathrm{MAX}} = 0.10$, 0.50, 1.0, and 2.0 from bottom to top.

corresponding to $d = 50$ nm monomers suspended in room temperature water with $\lambda_B = 0.7$ nm), one must consider monomers with *very low* effective charge density. Throughout this chapter, we reference Z-values based on the choice of $\lambda_B/d = 0.014$, though choosing a different reference λ_B/d simply renormalizes the range of Z under consideration, with an example of this rescaling given in Fig. 7.1. All of the parameter combinations (ϕ, Z, κ^{-1}/d) we examine are listed in Table 6.1 by their respective critical attraction strengths (discussed below). Finally, note that throughout the remainder of the chapter, we notate $\beta u_{i,j}^{\mathrm{SALR}}(x_{i,j})$ as $\beta u(r)$ for aesthetic simplicity unless otherwise indicated.

7.2.2 Molecular dynamics simulations

We generate configurations of cluster phases via three-dimensional MD simulations of the ternary SALR mixtures described above, where we generate trajectories using LAMMPS [165]. We perform simulations in the NVT ensemble with periodic boundary conditions using an integration time-step of $dt = 0.001\sqrt{d^2m/(k_BT)}$ (taking the mass $m = 1$) and fix temperature via a Nosé-Hoover thermostat with time-constant $\tau = 2000dt$. As outlined in Table 6.1, we consider many combinations of charge Z and screening length κ^{-1}/d at four different packing fractions: $\phi = 0.015$, 0.030, 0.060, and 0.120 (where we simulate $N_{\mathrm{box}} = 1920$, 2960, 6800, and 6800 particles, respectively). Beginning with randomized initial configurations, we equilibrate systems at $\phi = 0.015$, 0.030, 0.060, and 0.120 for 3x10^7, 1x10^7, 3x10^6, and 2x10^6 steps, respectively, and confirm that

they are equilibrated on the basis of energy convergence and visualization, where the latter shows that the systems are ergodic (aggregates undergo frequent intra- and intercluster rearrangements and exchanges). We cut-off the pair potential for a given Z and κ^{-1}/d such that the interaction strength at distance $x_{i,j}^{\mathrm{c}}$ (note explicit use of the mixture notation) is $\beta u_{i,j}(x_{i,j}^{\mathrm{c}}) \leq 2\mathrm{e}^{-3}$ and the force is simultaneously $-\mathrm{d}[\beta u_{i,j}(x_{i,j}^{\mathrm{c}})]/\mathrm{d}x_{i,j} \leq 1\mathrm{e}^{-3}$.

To make our analysis tractable, we focus on states corresponding with the *onset of clustering* (i.e., at the cluster transition locus), where the phases are composed of fluid aggregates with characteristic size N^*, but the systems have not yet begun to form percolated phases or become dynamically arrested. To characterize the size of equilibrium aggregates, we calculate cluster-size distributions (CSDs), which quantify the probability $p(N)$ of observing clusters comprising N particles. Here, we follow the established convention [63,91,136,182] of considering two monomers part of the same cluster if they are directly bonded to one another (i.e., within the range of the attractive well) or each directly bonded to a shared neighbor (i.e., are connected via some percolating pathway).

In turn, to locate the cluster transition locus, we make sweeps in attraction strength $\beta\varepsilon$ (at increments of $\Delta\varepsilon = 0.05k_{\mathrm{B}}T$) and identify states at the onset of clustering based on the following criteria: (1) the $p(N)$ distribution exhibits a visibly-apparent local maximum (mode) at some $1 < N^* \ll N_{\mathrm{box}}$, where the corresponding local minimum between $N = 1$ and N^* is notated as N_{min}; and (2) that 80% of the particles in the system participate in aggregates of size $N \geq N_{\mathrm{min}}$, i.e., $0.80 = \sum_{n=N_{\mathrm{min}}}^{N_{\mathrm{box}}} p(N)$ where $p(N)$ is appropriately normalized. Taken

together, these conditions correspond to the emergence of meaningful bimodality (coexistence) in $p(N)$ between $N = 1$ and the cluster mode N^*. In this way, we obtain the characteristic cluster size N^* associated with a particular combination of ϕ, Z, and κ^{-1}/d and the corresponding *critical* attraction strength $\beta\varepsilon^*$. All of the parameter combinations we consider in our analysis are listed by their respective $\beta\varepsilon^*$ values in Table 6.1, and in the figures below we use the same symbology as in Chapter 6.

7.3 Results & Discussion

7.3.1 Observed cluster sizes and shapes in simulations

Before discussing free energy models for characteristic cluster size N^*, we begin by briefly describing the cluster morphologies under examination: for the approximately 100 different combinations of packing fraction ϕ, surface charge Z, and screening length κ^{-1}/d that we consider (listed in Table 6.1), we observe phases at the corresponding critical attraction strengths $\beta\varepsilon^*$ that comprise compact spherical clusters with characteristic sizes in the range $6 \leq N^* \leq 60$, as plotted in Fig. 7.2. In terms of cluster shape, we find that by measuring the radius of gyration R_G/d and plotting it versus cluster size N^*, our results obey the relation

$$R_\mathrm{G}/d = \alpha(\phi)N^{*(1/d_\mathrm{f})} \text{ with } d_\mathrm{f} = 3 \tag{7.5}$$

where $\alpha(\phi)$ is a ϕ-dependent prefactor of magnitude approximately 1/2 (hereafter

notated α). Together with the fractal dimension $d_f = 3$, this signifies that the aggregates are compact objects, and visual inspection of the MD trajectories confirms the clusters are indeed highly-packed amorphous droplets that are spherical on average and undergo frequent intracluster rearrangement and intercluster exchange (seen previously [91, 92]). As shown in the inset of Fig. 7.2, the clusters do become slightly less packed with increasing ϕ, which is attributable to an increasing frequency of intercluster exchange. (These transfer events tend to instantaneously but, on average, isotropically distort the clusters, effectively expanding them.) We discuss trends in cluster size and shape from a different perspective (and in more detail) in the accompanying publication.

In terms of cluster number size N^*, there are two important observations from Fig. 7.2: (1) characteristic cluster size depends only weakly on packing fraction for the range of $0.015 \leq \phi \leq 0.120$; and (2) the morphologies associated with *unscreened* electrostatic repulsions (i.e., $\kappa^{-1}/d \to \infty$) are effectively generated when the screening length approaches $\kappa^{-1}/d \approx 4.0$. As shown by considering Figs. 7.2(a-b) simultaneously, increasing packing fraction ϕ (given fixed Z and κ^{-1}/d) does not systematically shift N^*, but does slightly inflate the cluster radius R_G/d. (We do note that the CSD peaks at N^* also become wider with increasing ϕ due to more frequent intercluster contacts.) The second point is apparent based on Fig. 7.2(a), which demonstrates that for the larger screening lengths κ^{-1}/d tested, cluster sizes N^* at fixed ϕ and Z have already nearly reached *asymptotic* values, i.e.,

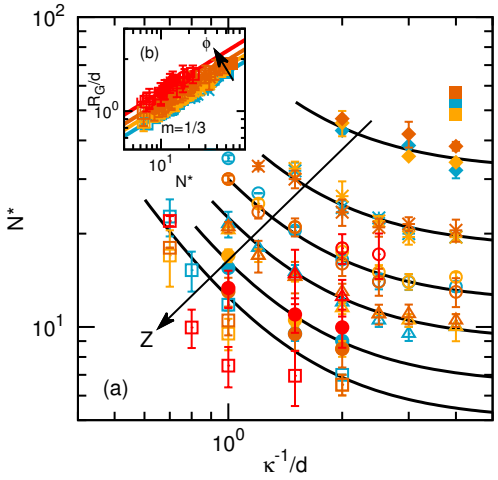

Figure 7.2: (a) Measured cluster size N^* versus screening length κ^{-1}/d for all ϕ, Z, and κ^{-1}/d combinations tested. Blue, yellow, orange, and red symbols correspond to measurements from simulations at $\phi = 0.015$, 0.030, 0.060, and 0.120, respectively. Contours are guides to the eye for constant Z: from top to bottom, $Z = 3.0$ (no line), 4.0, 6.0, 8.0, 10.0, 12.0, and 15.0. These contours are plotted according to the formula $N^*/N_\infty^{\text{est}} = 1.0 + 1.5/(\kappa^{-1}/d)^2$, where N_∞^{est} is the estimated cluster size in the Coulombic limit (i.e., $\kappa^{-1}/d \to \infty$). (b) Cluster radius of gyration R_G/d versus characteristic cluster size N^*, both measured from MD simulations. Lines are empirical fits of the form $R_G/d = \alpha N^{*1/3}$, where α is a dimensionless prefactor corresponding to $\alpha = 0.45$, 0.49, 0.53, and 0.60 for $\phi = 0.015$, 0.030, 0.060, and 0.120, respectively. Symbol types in (a) and (b) correspond to constant charge Z as listed in Table 6.1 (note that we test various screening lengths κ^{-1}/d at each Z).

$$\lim_{\kappa^{-1}/d \to \infty} N^*_\infty \approx N^* \text{ at } \kappa^{-1}/d = 4.0 \tag{7.6}$$

This ability to access the Coulombic limit at finite κ^{-1}/d is important for the following sections.

7.3.2 Existing free energy model for cluster size

We now begin our discussion of the canonical framework for cluster formation due to Groenewold and Kegel [68] (with subsequent follow-ups [69, 231]), with an emphasis on making clear important concepts and assumptions underpinning the model. The model aims to predict characteristic cluster size N^*_∞ for large and perfectly monodisperse aggregates governed by short-range attractions (SA) and long-range (LR) unscreened Coulombic interactions between monomers (the subscript alludes to the $\kappa^{-1}/d \to \infty$ limit). This prediction necessarily begins with an expression for the extensive free energy $\beta\Delta F$ of cluster formation as a function of N (agnostic to N^*_∞):

$$\beta\Delta F = \beta F_N - N\beta F_1 \tag{7.7}$$

where βF_N and βF_1 are the free energies of the N-sized clusters and monomers, respectively.

The free energy change $\beta\Delta F$ is broken into *reference* and *perturbative* contributions: the reference portion is taken to be the free energy of aggregate forma-

tion for a SA (i.e., purely attractive) fluid, which can be described via the classical nucleation theory (CNT) for large droplets (or crystals) [8, 45, 185]. Meanwhile, the perturbations are any contributions to the free energy due to the electrostatic effects. This is simply expressed:

$$\beta\Delta F = \beta\Delta F^{\mathrm{SA}} + \beta\Delta F^{\mathrm{LR}} \tag{7.8}$$

where we detail these (reference) attractive and (perturbative) repulsive free energy differentials in order below.

The CNT-based free energy contributions of the reference SA system comprise two terms, which capture competing effects that scale with aggregate volume and surface area, respectively. The first term accounts for the transfer of monomers from the low-density dispersed phase to the dense (bulk) fluid or crystal phase corresponding to the cluster interior. This transfer is characterized by a favorable change in chemical potential per particle with the magnitude $\beta\Delta\mu_0^{\mathrm{SA}}$. The second term is an enthalpic penalty [183,184] characterized by surface tension $\beta\gamma^{\mathrm{SA}}d^2$, which accounts for the relative number of "missing" intracluster coordination bonds $z_{\mathrm{c,m}}$ of the particles at the droplet surface relative to, e.g., the bulk-like coordination number $z_{\mathrm{c},0}$ of the cluster interior. In principle, the free-energy penalty also includes an *entropic* contribution due to the increased mobility particles might have at the droplet surface compared to the droplet interior; however, this contribution is often negligible [184]. Groenewold and co-workers do not address this issue [68, 69, 231], but for our systems, where clusters possess fluid-like

structures with frequent rearrangement between interior to exterior–nevermind frequent intercluster exchange–we also expect this entropic differential to be small. Thus, the free-energy contributions from the SA bonds can be written

$$\beta\Delta F^{\mathrm{SA}} = -N\beta\Delta\mu_0^{\mathrm{SA}} + 4\pi(R_{\mathrm{c}}/d)^2(\beta\gamma^{\mathrm{SA}}d^2) \tag{7.9}$$

where, reflecting our observed morphologies, we incorporate the expression for cluster surface area assuming *spherical* droplets with radius R_{c}/d. Going forward, this radius is considered interchangeable with the radius of gyration within some $O(1)$ prefactor, i.e., $R_{\mathrm{c}} \approx R_{\mathrm{G}}$.

In turn, the perturbative electrostatic contributions are treated as arising from unscreened repulsions acting between all intracluster pairs of particles (i.e., $N(N-1)/2 \approx N^2/2$ interactions), which can be written:

$$\beta\Delta F^{\mathrm{LR}} \approx \frac{\langle\beta u^{\mathrm{LR}}\rangle N^2}{2} \approx \frac{Z^2(\lambda_{\mathrm{B}}/d)N^2}{2(R_{\mathrm{c}}/d)} \tag{7.10}$$

where $\langle\beta u^{\mathrm{LR}}\rangle \approx Z^2(\lambda_{\mathrm{B}}/d)/(R_{\mathrm{c}}/d)$ is the Coulombic limit ($\kappa^{-1}/d \to \infty$) of the DLVO-type potential of Eqns. 6.3 and 6.4 evaluated at $r = R_{\mathrm{c}}/d$, which assumes that the characteristic (average) intracluster pair distance is simply the cluster radius. (Note that Zhang and co-workers [231] report the wrong exponent with respect to N for this term.) The form of Eqn. 7.10 implies that the repulsive free-energy contribution of each monomer in the dispersed phase is truly negligible compared to the intracluster contribution, which is consistent with the choice of Groenewold and Kegel to *ignore intercluster interactions*, i.e., consider the limit

of very low ϕ. Note that Groenewold and Kegel also originally include a term (see Eqn. 18 in Ref. 68) that roughly accounts for counterion condensation [1, 59, 138, 169], which could occur for strong bare surface charges. However, we neglect this contribution because their approximation naturally drops out of the subsequent analysis and the coarse-grained SALR potential considered here only captures a constant net-effective charge.

Given these expressions for the free energy contributions, one can proceed to the crux of the analysis: identifying the characteristic cluster size N_∞^* at which the driving force to associate per monomer is at its largest magnitude (or energetic minimum), i.e., $\beta\Delta f(N^*) \equiv \min_N[\beta\Delta f(N)]$ where $\beta\Delta f(N) \equiv \beta\Delta F(N)/N$. Of course, here one requires a $\beta\Delta f(N)$ function where the sole dependent variable is N. By combining Eqns. 7.9 and 7.10 with the known relation between cluster radius and number size $R_\mathrm{G}/d = \alpha N^{1/3}$ for compact spherical aggregates, one can readily write:

$$\beta\Delta f(N) = -\beta\Delta\mu_0^{\mathrm{SA}} + \frac{4\pi\alpha^2(\beta\gamma^{\mathrm{SA}}d^2)}{N^{1/3}} + \frac{Z^2(\lambda_\mathrm{B}/d)N^{2/3}}{2\alpha} \tag{7.11}$$

and evaluate its derivative to find the global minimum

$$\left.\frac{\mathrm{d}(\beta\Delta f)}{\mathrm{d}N}\right|_{N_\infty^*} = 0 = -\frac{4\pi\alpha^2(\beta\gamma^{\mathrm{SA}}d^2)}{3{N_\infty^*}^{4/3}} + \frac{Z^2(\lambda_\mathrm{B}/d)}{3\alpha{N_\infty^*}^{1/3}} \tag{7.12}$$

which, dropping prefactors, gives the scaling relation:

$$N_\infty^* \propto \frac{\beta\gamma^{\mathrm{SA}}d^2}{Z^2(\lambda_\mathrm{B}/d)} \tag{7.13}$$

This states that cluster size is simply governed by the strength of the surface energy relative to the characteristic strength of electrostatic repulsion.

To write Eqn. 7.13 completely in terms of experimentally tunable parameters, one then approximates [183, 184, 231] the surface tension of the SA reference fluid $\beta\gamma^{\mathrm{SA}}d^2$ as scaling like the attraction strength $\beta\varepsilon$ multiplied by the aforementioned number of missing bonds per surface particle $z_{\mathrm{c,m}}$ (divided by a "surface area" per monomer A_{m}), i.e.,

$$\beta\gamma^{\mathrm{SA}}d^2 \approx \frac{z_{\mathrm{c,m}}\beta\varepsilon}{(A_{\mathrm{m}}/d^2)} \tag{7.14}$$

Because $z_{\mathrm{c,m}}$ is considered constant with respect to N for large, low-curvature droplets, combining Eqns. 7.13 and 7.14 leads to the master *a priori* scaling relation

$$N_{\infty}^{*} \propto \frac{\beta\varepsilon}{Z^2(\lambda_{\mathrm{B}}/d)} \tag{7.15}$$

Reintroducing prefactors, Eqn. 7.15 is written $N_{\infty}^{*} = \alpha\nu_0\beta\varepsilon/[Z^2(\lambda_{\mathrm{B}}/d)]$, where α remains from the repulsive term in Eqn. 7.11, and ν_0 is a prefactor that is the product of $z_{\mathrm{c,m}}$ and some conversion factor to arrive at a surface energy per area.

7.3.3 Observed size-scaling in the weak-screening limit

Given our wide survey of compact spherical cluster morphologies, we can perform the first *systematic* test of the master scaling law given by Eqn. 7.15

for SALR pair potentials by plotting measured cluster sizes N^* for systems with sufficiently large screening lengths κ^{-1}/d at various ϕ, Z, and $\beta\varepsilon$. Specifically, in Fig. 7.3, we plot N^* values observed at critical attraction strengths $\beta\varepsilon^*$ and screening length $\kappa^{-1}/d = 4.0$, where the latter corresponds to effectively unscreened systems (see Section 7.3.1) as assumed in writing Eqn. 7.15. Here, we note that we use the version of Eqn. 7.15 that incorporates prefactors α and ν_0, which shift predicted sizes approximately in line with the measured N^* values (of course, including or excluding these prefactors does not affect scaling itself).

In Fig. 7.3, we do indeed observe a master ϕ-independent relation between the N^* values measured in simulations and the relative strength of attractions and repulsions between monomers, i.e., the ratio $\beta\varepsilon/[Z^2(\lambda_B/d)]$; however, the observed scaling *does not reflect the exponent of 1* that is expected based on the free energy model underlying Eqn. 7.15. Instead, we clearly observe the empirical relation

$$N^*_\infty \propto \left[\frac{\beta\varepsilon}{Z^2(\lambda_B/d)}\right]^{3/4} \tag{7.16}$$

for various cluster sizes and packing fractions. This immediately begs the questions: what *alternative* (and, ideally, comparatively simple) free energy model for SALR systems results in this softer master scaling? and furthermore, can this alternative model readily predict N^* for *finite* screening lengths κ^{-1}/d?

To ascertain what new model can capture the empirically-observed scaling in Fig. 7.3 (and be extended for generic κ^{-1}/d), we first ought to identify which of the current free energy terms in Eqns. 7.9 and 7.10 correctly (or incorrectly)

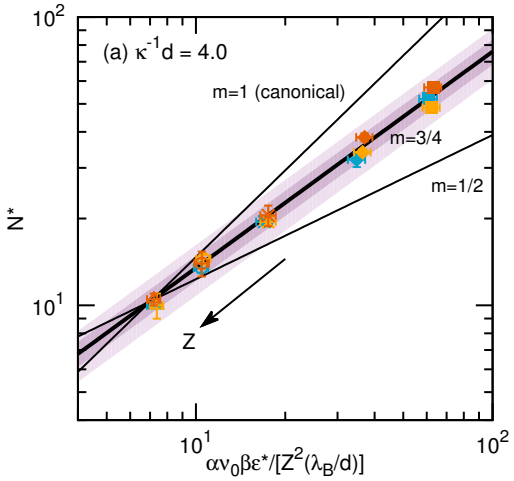

Figure 7.3: (a) Measured cluster size N^*_∞ in the Coulombic limit (approximated by systems with $\kappa^{-1}/d = 4.0$) versus the master scaling ratio of Eqn. 7.15 plotted using measured critical attraction strengths $\beta\varepsilon^*$ and corresponding characteristic repulsion strengths $Z^2(\lambda_B/d)$. Blue, yellow, and orange symbols correspond to measurements from simulations at $\phi = 0.015$, 0.030, and 0.060, respectively, for charges $Z = 3.0$, 4.0, 6.0, 8.0, and 10.0 (top to bottom). Thick black line corresponds to the empirical scaling of Eqn. 7.16 with exponent of $m = 3/4$ (i.e., $N^*_\infty \propto \{\beta\varepsilon^*/[Z^2(\lambda_B/d)]\}^{3/4}$) and dark (light) purple shadings correspond to 10% (20%) deviation from this scaling. Thin black lines show scalings for alternate exponents, where the $m = 1$ scaling (see Eqn. 7.15) derives from the canonical free energy model of Groenewold and Kegel [68, 69, 231]. Note that in this figure, we plot predicted cluster sizes (x-axis) based on including the ϕ-dependent prefactor α for the radius of gyration (see Fig. 7.2) and the (here, arbitrary) constant prefactor $\nu_0 \approx 3.40$ (see text). Symbol types correspond to constant charge Z as listed in Table 6.1 (note that we test various screening lengths κ^{-1}/d at each Z).

describe the energetics of cluster formation in the MD simulations. Given its simplicity, the most straightforward candidate to consider is the *repulsive* free energy contribution of Eqn. 7.10, which we can test against MD configurations by adding up the total repulsive energies (between all intracluster pairs of monomers) of simulated clusters as a function of characteristic size N^*.

As shown in Fig. 7.4, we observe that the repulsive free energy contribution of Eqn. 7.10 quantitatively describes MD results in the unscreened limit and, with a simple extension, also works for finite screening lengths κ^{-1}/d; in other words, the current perturbative free energy term capturing electrostatics is *self-consistent* and should be retained. In Fig. 7.4(a), we see that $\beta\Delta F^{\mathrm{LR}}$ measured in simulations, when normalized by the maximum repulsion barrier $\beta A_{\mathrm{MAX}} = Z^2(\lambda_{\mathrm{B}}/d)$ (corresponding to the $\kappa^{-1}/d \to \infty$ limit of Eqn. 6.4), scales as $N^{5/3}$. Of course, this $N^{5/3}$ scaling is expected given N^2 intracluster pair interactions occurring on the lengthscale of the cluster radius, which scales as $N^{1/3}$ (see Eqn. 7.10. Meanwhile, Fig. 7.2(b) demonstrates that the same scaling holds for finite κ^{-1}/d away from the Coulombic limit provided one appeals to the more generalized form of Eqn. 6.4 for the maximum repulsive barrier energy, i.e., $\beta A_{\mathrm{MAX}} = Z^2(\lambda_{\mathrm{B}}/d)/[1.0 + 0.5/(\kappa^{-1}/d)]^2$.

7.3.4 Accounting for size-dependent surface effects

Given that intracluster repulsions scale as expected (with $N^{5/3}$), the simplest extensive free energy expression (resembling that of Groenewold and Kegel)

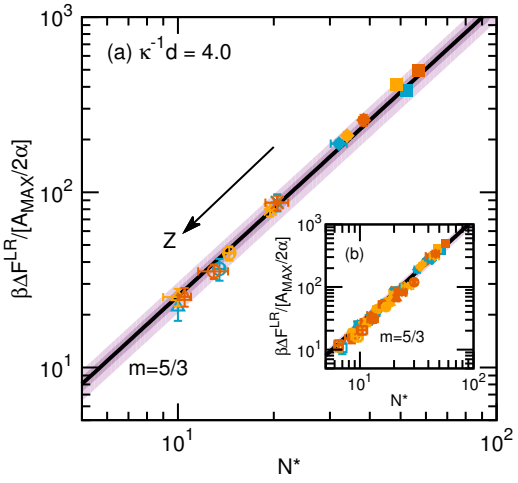

Figure 7.4: (a) Total intracluster repulsion energy $\beta\Delta F^{\mathrm{LR}}$ scaled by maximum repulsion barrier $\beta A_{\mathrm{MAX}} = Z^2(\lambda_{\mathrm{B}}/d)/[1.0+0.5/(\kappa^{-1}/d)]^2$ and ϕ-dependent prefactor α for the radius of gyration (see Fig. 7.2), plotted versus cluster size N^* for $Z = 3.0$, 4.0, 6.0, 8.0, and 10.0 (top to bottom) and $\kappa^{-1}/d = 4.0$ (effectively $\kappa^{-1}/d \to \infty$). Blue, yellow, and orange symbols correspond to measurements from simulations at $\phi = 0.015$, 0.030, and 0.060, respectively. (b) Same but for $\kappa^{-1}/d = 4.0$, 3.0, 2.0, and 1.0 at all correspondingly tested Z values (see Table 6.1). For (a) and (b), thick black line corresponds to the expression $\beta\Delta F^{\mathrm{LR}}/[\beta A_{\mathrm{MAX}}/(2\alpha)] = N^{*5/3}$ and dark (light) purple shadings correspond to 10% (20%) deviation from this scaling. Symbol types in (a) and (b) correspond to constant charge Z as listed in Table 6.1 (note that we test various screening lengths κ^{-1}/d at each Z).

that readily leads to the empirically-observed scaling in Fig. 7.3 is one where the surface-energy penalty, rather than scaling as $N^{2/3}$, instead effectively scales with a lesser exponent:

$$\beta\Delta F(N) = -N\beta\Delta\mu_0^{\mathrm{SA}} + \nu_1\beta\varepsilon N^{1/3} + \frac{\beta A_{\mathrm{MAX}} N^{5/3}}{2\alpha} \tag{7.17}$$

Here, ν_1 is some (as yet undetermined) dimensionless prefactor distinct from the ν_0 above. In turn, it is easily shown that solving Eqn. 7.17 for $\beta\Delta f(N^*) \equiv \min_N[\beta\Delta f(N)]$ results in the generalized scaling $N^* \propto \{\beta\varepsilon/[\beta A_{\mathrm{MAX}}]\}^{3/4}$ or, in the unscreened limit, $N^*_\infty \propto \{\beta\varepsilon/[Z^2(\lambda_{\mathrm{B}}/d)]\}^{3/4}$.

During the remainder of this section, our ultimate goal is to demonstrate that this reduced exponent for the surface energy term naturally emerges for our clustered systems because the effective energy penalty is dependent on cluster size N^* in the range $6 \leq N^* \leq 60$. Conceptually, this size-dependence for the surface energy echoes the long-established notion that the generalized surface-tension of a liquid droplet with high curvature $\gamma(R)$ will depart from the reference surface tension γ^∞ of a planar liquid-vapor interface (or very large droplet with low curvature). Indeed, starting with pioneering work by Tolman [210], a vast number of studies have been dedicated to measuring first- and/or second-order corrections for $\gamma(R)/\gamma^\infty$ (the classic first order correction depends on the "Tolman length") to better model, e.g., homogeneous nucleation, but this topic continues to be active and challenging area of research even for model systems like the LJ fluid [104, 139, 154, 207, 211, 213, 223]. Compared to these studies, which are especially difficult

given their general focus on *critically-unstable* droplet formation (usually droplets with radius $R \approx 4d$ at the smallest), the following analysis is notable because we consider *stable* droplets with effective surface tensions dominated by *short-range* attractive bonds (much shorter than, e.g., LJ attraction range) and radii of less than three particle diameters.

Specifically, to capture this size-dependent surface energy, one ought to account for an N-dependent number of missing coordination bonds $z_{\mathrm{c,m}}(N)$ for the surface particles relative to the reference bulk (interior) coordination number $z_{\mathrm{c},0}$. The surface energy penalty in Eqn. 7.17 can then be written

$$\nu_1 \beta\varepsilon N^{1/3} \propto z_{\mathrm{c,m}}(N) \beta\varepsilon N^{2/3} \tag{7.18}$$

with the (to be demonstrated) scaling

$$z_{\mathrm{c,m}}(N) \propto N^{-1/3} \tag{7.19}$$

where we still assume that the number of surface particles at least roughly scales as $N^{2/3}$, i.e., proportional to the squared cluster radius $(R_{\mathrm{G}}/d)^2 = \alpha^2 N^{2/3}$, though making a formal distinction between interior and surface particles is difficult for small N (as discussed later). To demonstrate that the scaling in Eqn. 7.19 is reasonable, we show in Figs. 7.5-7.6 that this size-dependence for $z_{\mathrm{c,m}}(N) = z_{\mathrm{c},0} - z_{\mathrm{c}}(N)$ originates based on the coordination number of (surface) particles $z_{\mathrm{c}}(N)$ measured from MD configurations, which we calculate from the extensive number of intracluster bonds $n_{\mathrm{B}}(N)$. Given our measurement of $n_{\mathrm{B}}(N)$ is at the root of

much of this analysis, we consider its behavior first and proceed backwards to the scaling of Eqn. 7.19.

Looking towards estimating $z_{\mathrm{c,m}}(N)$, consider in Fig. 7.5(a) the extensive number of intracluster bonds $n_{\mathrm{B}}(N)$ measured from MD simulations, where we observe a previously undiscovered (to our knowledge) superlinear growth rate over the range of cluster sizes that we generate. Interestingly, this superlinear behavior contrasts with known small- and large-cluster limits, which are linear in N. Here, $n_{\mathrm{B}}(N)$ is nicely captured at each packing fraction for $6 \leq N^* \leq 60$ by the empirical expression:

$$n_{\mathrm{B}}(N) = (k/2)N\ln(N) \tag{7.20}$$

where k is a ϕ-specific $O(1)$ prefactor, and we include a division by 2 for aesthetic alignment with the next results. (Note that the prefactor k modestly decreases as ϕ increases: this occurs because, as discussed earlier, the cluster radius modestly increases with ϕ for fixed N^*; thus, clusters become less dense and exhibit correspondingly fewer bonds.) This superlinear regime contrasts with the small cluster regime ($3 \leq N \leq 9$), where it is known [7,140] that colloidal clusters dominated by SA bonds maximize their extensive bonding number according to the expression $n_{\mathrm{B}}(N) = 3N-6$. Likewise, in the limit of large droplets, the number of bonds must scale increasingly like in the corresponding bulk fluid, i.e., $n_{\mathrm{B}}(N) \to (z_{\mathrm{bulk}}/2)N$ where z_{bulk} is the coordination number of the reference fluid (or crystal) phase.

To quickly understand why $n_{\mathrm{B}}(N)$ growth should be superlinear over this

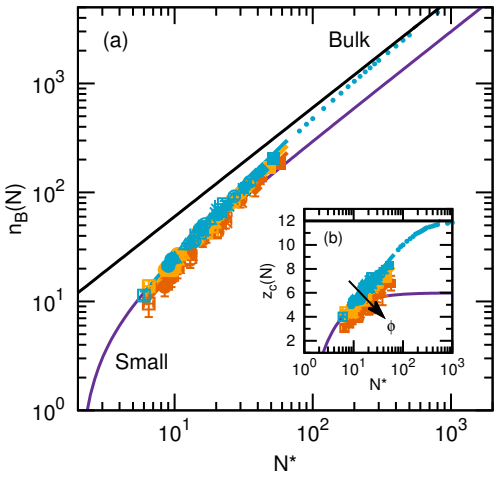

Figure 7.5: (a) Extensive number of intracluster bonds $n_{\rm B}(N)$ versus cluster size N^*. Blue, yellow, and orange symbols correspond to measurements from simulations at $\phi = 0.015$, 0.030, and 0.060, respectively. Symbol types correspond to constant charge Z as listed in Table 6.1 (note that we test various screening lengths κ^{-1}/d at each Z). Blue, yellow, and orange solid lines are of the empirical form $n_{\rm B}(N) = (k/2)N\ln(N)$ found to apply between $6 \leq N^* \leq 60$, where $k = 2.20$, 1.95, and 1.70 with respect to ϕ. Purple line corresponds to small cluster limit [7, 140] $n_{\rm B}(N) = 3N - 6$, which is accurate for $3 \leq N \leq 9$. Black line corresponds to large droplet (bulk) limit $n_{\rm B}(N) = (z_{\rm bulk}/2)N$ where we choose $z_{\rm bulk} = 12$ (see text); this limit becomes near-quantitative for dense droplets of $N \approx O(1000)$. Dashed blue curve is a schematic extension to the solid blue line between $60 \leq N^* \leq 500$. (b) Average coordination number $z_{\rm c}(N)$ versus cluster size N^*. Symbols and lines have same meaning as in (a), where the latter are calculated via the formula $z_{\rm c}(N) = 2n_{\rm B}(N)/N$.

size range, we show in Fig 5(a) extensions of the small- and large-cluster linear regimes (to large and small N where they should respectively fail) to demonstrate that the function $n_{\mathrm{B}}(N) = (k/2)N\ln(N)$ connects these otherwise disparate limits while quantitatively overlapping with the upper reaches of the small cluster trend at $N \approx 10$. To wit, notice that the characteristic slope of the small-N regime is $m = 3$ differs meaningfully from the typical slope in the large-N regime of a very dense bulk fluid or crystal, which we estimate as $m = z_{\mathrm{bulk}}/2 = 6$ with $z_{\mathrm{bulk}} = 12$ because it is the sphere kissing number in three dimensions [163] (this is justified later). Thus, provided z_{bulk} is decidedly larger than 3, a superlinear regime allows for a smooth continuous growth in $n_{\mathrm{B}}(N)$ with respect to N.

This connectivity between very small and large cluster sizes is clearly echoed by the next necessary quantity we must calculate: the average coordination number $z_{\mathrm{c}}(N) = 2n_{\mathrm{B}}(N)/N = k\ln(N)$, which we show in Fig. 7.5(b) for all of our clustered states. Here, we plot $z_{\mathrm{c}}(N)$ values calculated from MD configurations, which begin to bridge the gap (up to the highest cluster sizes we observe) between the highly bond-restricted regime at small N and the bulk regime at large N where the coordination number approaches $z_{\mathrm{c}}(N) \to z_{\mathrm{bulk}}$. Notably, $z_{\mathrm{c}}(N)$ varies by approximately a *factor of 2* over the size range of interest $6 \leq N^* \leq 60$, which underlines that the conventional practice (for larger droplets) of assuming that surface effects are size-independent is problematic for these smaller aggregates.

Interestingly, the relation between coordination number and cluster size that we observe, $z_{\mathrm{c}}(N) = k\ln(N)$ (with $k \approx 2$), has a much stronger scaling than that of a similar relation reported by Godfrin et. al. [63], which was given as

$z_{\mathrm{c}}(N) = 1.5[\ln(N)]^{1/2}$ (here written in our choice of notation). We would simply note that the latter reaches an *asymptotic* coordination number of approximately 4 at very large droplet sizes, which would point to extremely elongated non-compact clusters (even Bernal spiral motifs [32] exhibit $z_{\mathrm{c}} \approx 5$). In contrast, our expression, which is based on data from compact spherical aggregates at the onset of clustering, grows with cluster size and tends to approach the bulk coordination number $z_{\mathrm{bulk}} = 12$ of a dense attractive fluid in the large N limit, as in Fig. 7.5(b).

With $z_{\mathrm{c}}(N)$ in hand, we can proceed to calculate the average number of missing bonds per particle $z_{\mathrm{c,m}}(N)$, which indeed collapses onto a master curve scaling as $N^{-1/3}$ (shown in Fig. 7.6) when the magnitude of the reference (fitting) coordination parameter $z_{\mathrm{c},0}$ is set–in line with measurements of cluster interiors–at values appropriate for highly-packed bulk fluids. To do this, we use the expression

$$z_{\mathrm{c,m}}(N) = z_{\mathrm{c},0} - z_{\mathrm{c}}(N) \tag{7.21}$$

where the only as-yet undetermined value is $z_{\mathrm{c},0}$, which is the coordination number of the reference bulk SA fluid that represents the idealized cluster interior; for our immediate purposes, we treat this parameter as tunable and verify our choices as reasonable below. As shown in Fig. 7.6(a), our data approximately collapse onto a master curve with characteristic $N^{-1/3}$ dependence when $z_{\mathrm{c},0} = 12.0$, 11.5, and 10.5 for $\phi = 0.015$, 0.030, and 0.060, respectively. All of these values–especially for the lowest-density case–are reflective of bulk fluids dominated by short-range attractions, especially here given that energetic gains from bonding occur within attractive wells beyond surface contact that are approximately $0.1d$ in width.

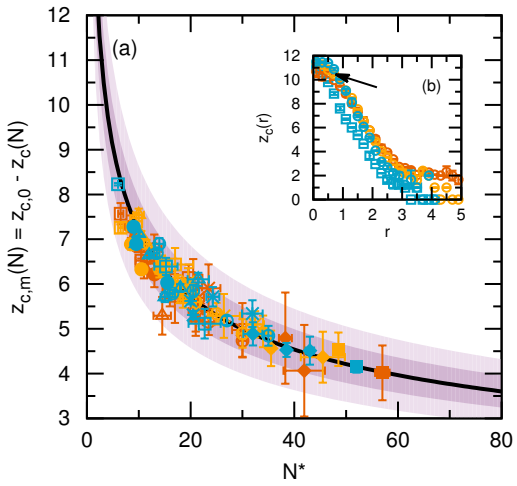

Figure 7.6: (a) Average number of missing bonds per particle $z_{c,m}(N) = z_{c,0} - z_c(N)$ versus cluster size N^*. Blue, yellow, and orange symbols correspond to measurements from simulations at $\phi = 0.015$, 0.030, and 0.060, respectively. Fitting parameter $z_{c,0}$ is the coordination number of the reference bulk dense fluid, found to be $z_{c,0} = 12.0$, 11.5, and 10.5 with respect to ϕ. Thick black line is a scaling guideline with the form $z_{c,m}(N) = 15.5N^{-1/3}$ and dark (light) purple shadings correspond to 10% (20%) deviation from this scaling. Symbol types correspond to constant charge Z as listed in Table 6.1 (note that we test various screening lengths κ^{-1}/d at each Z). (b) Locally-averaged intracluster coordination number $z_c(r)$ measured at radial positions r relative to cluster center of mass for four selected cluster phases. Blue, yellow, and orange circles are for $Z = 3.0$ and $\kappa^{-1}/d = 4.0$ at $\phi = 0.015$, 0.030, and 0.060, respectively, where $50 < N^* < 60$. Blue squares are for $Z = 6.0$ and $\kappa^{-1}/d = 4.0$ at $\phi = 0.015$, where $N^* \approx 20$. Arrow points to inner regions of clusters, highlighting $z_c(r \to 0) \approx 12$.

In Fig. 7.6(b), we demonstrate that these $z_{c,0}$ values are appropriate based on direct measurements of the locally-averaged coordination number $z_c(r)$ as a function of radial position within clusters (relative to cluster center-of-mass). Here, we specifically show results from some of the largest clusters observed ($50 < N^* < 60$), which are most likely to possess bulk-like interiors as $r \to 0$; indeed, it is evident that $z_c(r \to 0) \approx 12$ for these larger clusters, though the limiting value (as above) slightly decreases as ϕ increases, presumably due to the previously-discussed trend in intracluster density. We also observe in Fig. 7.6(b) that the $z_c(r \to 0)$ limit is similar even for smaller clusters, e.g., $N^* \approx 20$, where central particles can still be surrounded by a packed shell of intracluster neighbors.

Taken altogether, the results of Figs. 7.5-7.6 nicely justify the choice to quantify the surface energy penalty of cluster formation from the perspective of a size-dependence in the relative number of missing bonds $z_{c,m}(N)$. Before moving on to consider the impact of the scaling relationships in Eqns. 7.18 and 7.19 for predicting cluster size, we pause to note that in the analysis above, we approximate $z_{c,m}(N)$ for surface particles based on an average measurement of $n_B(N)$ for *all* cluster constituents. Thus, in our approximate treatment, we suspect that *at small* N, we are simultaneously: (1) underestimating the relative fraction of surface particles, which means the number of "surface" particles actually scales as N^m with $m < 2/3$ over the whole intermediate size range; and (2) overestimating the coordination number $z_c(N)$ of surface particles (underestimating $z_{c,m}(N)$), which means that the number of missing surface bonds actually scales as $z_{c,m}(N) \propto N^m$ with $m > -1/3$. Because these errors in the exponents tend to cancel each other,

we expect that the net effective $N^{1/3}$ scaling of the surface term in Eqn. 7.18 holds even given greater precision in the configurational analysis. We take this somewhat imprecise approach because it draws upon relatively unambiguous measurable quantities and bypasses the fraught process of definitively distinguishing between surface and interior particles (consider, e.g., Fig. 7.6(b)). Our approximation is sufficient for the proof-of-concept analysis here, but we imagine a more exacting analysis in this vein would be a worthwhile future endeavor.

7.3.5 Revised free energy model for predicting size

Based on the new scaling for the free energy surface penalty justified in Section 7.3.4 and the generalized free energy term for repulsive contributions in Section 7.3.3, we can return to the extensive free energy model of Eqn. 7.17 and readily derive a new master equation for predicting cluster size N^* based on experimentally-tunable parameters:

$$N^* = \left[\frac{\alpha\nu_2\beta\varepsilon}{\beta A_{\mathrm{MAX}}}\right]^{3/4} = \left[\frac{\alpha\nu_2\beta\varepsilon\{1.0 + 0.5/(\kappa^{-1}/d)\}^2}{Z^2(\lambda_{\mathrm{B}}/d)}\right]^{3/4} \tag{7.22}$$

where, as before, α is the known ϕ-dependent prefactor relating cluster radius and number size and ν_2 is a constant similar to those above that scales the surface energy penalty, which we treat as an empirical tuning parameter. Eqn. 7.22 is the central result of Chapter 7.

As demonstrated in Fig. 7.7, Eqn. 7.22 successfully predicts characteristic cluster sizes for the vast majority of our ≈100 cases over various Z-κ^{-1}/d combi-

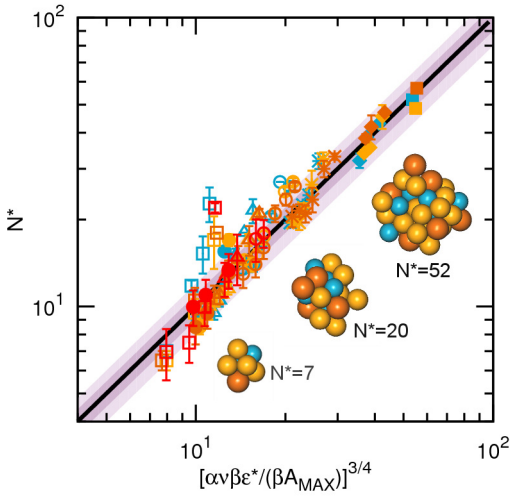

Figure 7.7: Measured cluster size N^* versus predicted cluster size from Eqn. 7.22, where the latter formula is a function of ϕ-dependent radius of gyration coefficient α (see Fig. 7.2); critical attraction strength $\beta\varepsilon^*$; and maximum repulsive barrier height $\beta A_{\mathrm{MAX}} = Z^2(\lambda_{\mathrm{B}}/d)/[1.0+0.5/(\kappa^{-1}/d)]^2$. The constant prefactor $\nu_2 \simeq \sqrt{2}\pi$ scales the surface energy penalty associated with aggregation (see text). Thick black line corresponds to the Eqn. 7.22 relation and dark (light) purple shadings correspond to 10% (20%) deviation from this scaling. Blue, yellow, orange, and red symbols correspond to results from simulations at $\phi = 0.015$, 0.030, 0.060, and 0.120, respectively. Symbol types correspond to constant charge Z as listed in Table 6.1 (note that we test various screening lengths κ^{-1}/d at each Z). The three illustrated clusters are instantaneous configurations observed in MD simulations, with blue, yellow, and orange spheres corresponding to small, medium, and large particles, respectively.

nations and near order-of-magnitude ranges in both size $6 \leq N^* \leq 60$ and bulk monomer packing fraction $0.015 \leq \phi \leq 0.120$. This wide applicability is notable as the underlying free energy framework remains very simple: to wit, intercluster effects can evidently be neglected even as conditions become less dilute (e.g., $\phi \approx 0.120$), though the current model cannot predict more subtle trends known for the SALR model [92] like the growing polydispersity of aggregates with increasing ϕ. Meanwhile, the biggest deviations between measured and predicted N^* (larger than 20%) occur for states combining large charge (e.g., $Z = 15.0$) and small screening length (e.g., $\kappa^{-1}/d = 0.70$), which result in rather non-idealized repulsions that are both strong relative to $k_{\mathrm{B}}T$ and far from the Coulombic limit. Finally, note that the value for prefactor ν_2 that shifts the (already collapsed) predictions into the correct range is $\nu_2 \approx \sqrt{2}\pi$, which we expect should apply rather generally for compact colloidal clusters as it simply converts between measurements of the cluster surface-size based on population and radius.

7.4 Conclusions

We have validated a new and readily applied formula (Eqn. 7.22) that can predict characteristic cluster size N^* for idealized SALR suspensions as a function of the variables controlling monomer-monomer interactions (including attraction strength $\beta\varepsilon$, surface charge Z, and screening length κ^{-1}/d). Eqn. 7.22 and its underlying free energy model represent a semi-empirical adaptation and extension of the canonical free energy model due to Groenewold and Kegel [68,69,231], where we found the latter exhibits a spurious scaling of N^* away from the large-droplet

limit with respect to the ratio of attractive and repulsive interaction strengths driving aggregation. We subsequently find that Eqn. 7.22 performs excellently based on direct comparisons of predicted cluster sizes and measurements of N^* from MD simulations of approximately 100 different systems for very wide ranges in ϕ, Z, and κ^{-1}/d, where we examine states at the onset of clustering that exhibit compact spherical aggregates in the size range $6 \leq N^* \leq 60$.

The predictive quality of Eqn. 7.22 demonstrates that a simple free energy model, which treats SALR systems as reference SA fluids (via classical nucleation theory) with additive repulsive perturbations due to electrostatic effects, can be applied down to *extremely small* cluster sizes ($N^* < 10$) provided one properly corrects for surface effects at small N^*. Conceptually, this is in the spirit of long-standing investigations regarding size-dependent surface tensions in small droplets [104, 139, 154, 207, 210, 211, 213, 223], and practically, we find that one can treat the energy penalty of "interface" formation as a function of an N-dependent number of missing coordination bonds $z_{\mathrm{c,m}}(N)$ for surface particles (referenced against the coordination number in the bulk fluid). Here, this picture is validated in part by configurational analysis of the number of extensive intracluster bonds $n_{\mathrm{B}}(N)$, which revealed a previous undiscovered (to our knowledge) *superlinear* scaling regime for $n_{\mathrm{B}}(N)$ over the size range $6 \leq N^* \leq 60$. Meanwhile, based on the form of the free energy model, we confirm that intercluster effects can be neglected even for rather non-dilute conditions (e.g., $\phi = 0.120$), which is reflected by our observation that cluster size N^* exhibits little variability with respect to ϕ given otherwise fixed conditions.

We look forward to testing the predictive capability of Eqn. 7.22 for real colloidal suspensions that exhibit equilibrium cluster phases, which could help bolster whether SALR pair potentials are a sufficient (if idealized) description of experimental systems. For instance, there has been recent discussion [153, 161, 204] in the literature as to whether accounting for charge renormalization during aggregation is necessary for describing cluster behavior; likewise, Groenewold and Kegel initially postulated that non-trivial charge effects [1, 59, 138, 169] could affect the free energy picture in certain limits. Of course, these effects are not captured by the canonical SALR pair potential examined here, but we now possess a free energy model (Eqn. 7.17) known to describe this simpler system. Thus, ascertaining whether cluster size N^* scales in experiments similarly to the empirical scaling of Eqn. 7.22 would help clarify the degree to which phenomenology and interpretive guidelines derived from the pairwise model are appropriate for real systems. Similarly, it is fascinating to consider how accounting for size-dependent surface effects, here so crucial for producing quantitative predictions, might change for less compact (e.g., elongated) aggregates than those considered here.

Chapter 8

Publications

J.A. Bollinger, J. Carmer, A. Jain, T.M. Truskett, "Impact of solvent granularity and layering on tracer hydrodynamics in confinement." Accepted at *Soft Matter*.

J.A. Bollinger and T.M. Truskett, "Fluids with competing interactions: I. Decoding the structure factor to detect and characterize self-limited clustering." *J. Chem. Phys.*, 2016, 145 (6), p. 064902 (DOI: 10.1063/1.4960338)

J.A. Bollinger and T.M. Truskett, "Fluids with competing interactions: II. Validating a free energy model for equilibrium cluster size." *J. Chem. Phys.*, 2016, 145 (6), p. 064903 (DOI: 10.1063/1.4960339)

R.B. Jadrich, B.A. Lindquist, **J.A. Bollinger**, T.M. Truskett, "Consequences of minimizing pair correlations in fluids for dynamics, thermodynamics, and structure." *Mol. Phys.*, 2016, 114 (16-17), pp. 2411–2423 (DOI: 10.1080/00268976.2016.1159742)

R.B. Jadrich, **J.A. Bollinger**, B.A. Lindquist, T.M. Truskett, "Equilibrium cluster fluids: pair interactions via inverse design." *Soft Matter*, 2015, 11 (48), pp. 9342–9354 (DOI: 10.1039/C5SM01832C)

J.A. Bollinger, A. Jain, T.M. Truskett, "How local and average particle diffusivities of inhomogeneous fluids depend on microscopic dynamics." *J. Phys. Chem. B*, 2015, 119 (29), pp. 9103–9113 (DOI: 10.1021/jp508887r)

J.A. Bollinger, A. Jain, J. Carmer, T.M. Truskett, "Local structure-mobility relationships of confined fluids reverse upon supercooling." *J. Chem. Phys.*, 2015, 142 (16), p.

161102 (DOI: 10.1063/1.4919688)

R.B. Jadrich, **J.A. Bollinger (co-1st author)**, K.P. Johnston, T.M. Truskett, "Origin and detection of microstructural clustering in fluids with spatial-range competitive interactions." *Phys. Rev. E*, 2015, 91 (4), p. 042312 (DOI: 10.1103/PhysRevE.91.042312)

J. Carmer, A. Jain, **J.A. Bollinger**, F. van Swol, T.M. Truskett, "Tuning structure and mobility of solvation shells surrounding tracer additives." *J. Chem. Phys.*, 2015, 142 (12), p. 124501 (DOI: 10.1063/1.4916053)

A. Jain, **J.A. Bollinger**, T.M. Truskett, "Perspective: Inverse methods for material design." *AIChE Journal*, 2014, 60 (8), pp. 2732–2740 (DOI: 10.1002/aic.14491)

L.M. Foster, A.J. Worthen, E. Foster, J. Dong, C. Roach, A. Metaxas, C. Hardy, E. Larsen, **J.A. Bollinger**, T.M. Truskett, C.W. Bielawski, and K.P. Johnston, "High Interfacial Activity of Polymers 'Grafted Through' Functionalized Iron Oxide Nanoparticle Clusters." *Langmuir*, 2014, 30 (34), pp. 10188–10196 (DOI: 10.1021/la501445f)

J.A. Bollinger, A. Jain, T.M. Truskett, "Structure, thermodynamics, and position-dependent diffusivity in fluids with sinusoidal density variations." *Langmuir*, 2014, 30 (28), pp. 8247–8252 (DOI: 10.1021/la5017005z)

A.J. Worthen, L.M. Foster, J. Dong, **J.A. Bollinger**, A.H. Peterman, L.E. Pastora, S.L. Bryant, T.M. Truskett, C.W. Bielawski, and K.P. Johnston, "Synergistic formation and stabilization of oil-in-water emulsions by a weakly-interacting mixture of zwitterionic surfactant and silica nanoparticles." *Langmuir*, 2014, 30 (4), pp. 984–994 (DOI: 10.1021/la404132p)

Bibliography

[1] S. Alexander, P. M. Chaikin, P. Grant, G. J. Morales, P. Pincus, and D. Hone. Charge renormalization, osmotic pressure, and bulk modulus of colloidal crystals: Theory. *J. Chem. Phys.*, 80(11):5776–5781, 1984.

[2] M. P. Allen and D. J. Tildesley. *Computer Simulation of Liquids*. Clarendon Press, New York, NY, USA, 1989.

[3] H. C. Andersen, D. Chandler, and J. D. Weeks. Roles of repulsive and attractive forces in liquids: The optimized random phase approximation. *J. Chem. Phys.*, 56(8):3812–3823, 1972.

[4] V. Anderson and H. N. W. Lekkerkerker. Insights into phase transition kinetics from colloid science. *Nature*, 416:811–815, 2002.

[5] A. J. Archer. Dynamical density functional theory for dense atomic liquids. *J. Phys.: Condens. Matter*, 18(24):5617, 2006.

[6] A. J. Archer and N. B. Wilding. Phase behavior of a fluid with competing attractive and repulsive interactions. *Phys. Rev. E*, 76:031501, Sep 2007.

[7] N. Arkus, V. N. Manoharan, and M. P. Brenner. Minimal energy clusters of hard spheres with short range attractions. *Phys. Rev. Lett.*, 103:118303, Sep 2009.

[8] S. Auer and D. Frenkel. Prediction of absolute crystal-nucleation rate in hard-sphere colloids. *Nature*, 409:1020–1023, 2000.

[9] P. Bahukudumbi and M. A. Bevan. Imaging energy landscapes with concentrated diffusing colloidal probes. *J. Chem. Phys.*, 126(24):244702, 2007.

[10] A. Baranyai and D. J. Evans. Direct entropy calculation from computer simulation of liquids. *Phys. Rev. A*, 40:3817–3822, Oct 1989.

[11] C. M. Bates, T. Seshimo, M. J. Maher, W. J. Durand, J. D. Cushen, L. M. Dean, G. Blachut, C. J. Ellison, and C. G. Willson. Polarity-switching top coats enable

orientation of sub–10-nm block copolymer domains. *Science*, 338(6108):775–779, 2012.

[12] T. Becker, K. Nelissen, B. Cleuren, B. Partoens, and C. Van den Broeck. Diffusion of interacting particles in discrete geometries. *Phys. Rev. Lett.*, 111:110601, Sep 2013.

[13] J. Bergenholtz, N. J. Wagner, and B. D'Aguanno. Thermodynamic self-consistency criterion in the mixed integral equation theory of liquid structure. *Phys. Rev. E*, 53:2968–2971, Mar 1996.

[14] L. Berthier, G. Biroli, J.-P. Bouchaud, W. Kob, K. Miyazaki, and D. R. Reichman. Spontaneous and induced dynamic correlations in glass formers. ii. model calculations and comparison to numerical simulations. *J. Chem. Phys.*, 126(18):184504, 2007.

[15] L. Berthier, G. Biroli, J.-P. Bouchaud, W. Kob, K. Miyazaki, and D. R. Reichman. Spontaneous and induced dynamic fluctuations in glass formers. i. general results and dependence on ensemble and dynamics. *J. Chem. Phys.*, 126(18):184503, 2007.

[16] L. Berthier and W. Kob. The monte carlo dynamics of a binary lennard-jones glass-forming mixture. *J. Phys.: Condens. Matter*, 19(20):205130, 2007.

[17] L. Berthier, A. J. Moreno, and G. Szamel. Increasing the density melts ultrasoft colloidal glasses. *Phys. Rev. E*, 82:060501, Dec 2010.

[18] S. Bhattacharya and J. Bawzdziewicz. Image system for stokes-flow singularity between two parallel planar walls. *J. Math. Phys.*, 43(11):5720–5731, 2002.

[19] T. Biben, J. Hansen, and J. Barrat. Density profiles of concentrated colloidal suspensions in sedimentation equilibrium. *J. Chem. Phys.*, 98(9):7330–7344, 1993.

[20] G. Biroli, J.-P. Bouchaud, K. Miyazaki, and D. R. Reichman. Inhomogeneous mode-coupling theory and growing dynamic length in supercooled liquids. *Phys. Rev. Lett.*, 97:195701, Nov 2006.

[21] I. Bitsanis, J. J. Magda, M. Tirrell, and H. T. Davis. Molecular dynamics of flow in micropores. *J. Chem. Phys.*, 87(3):1733–1750, 1987.

[22] I. Bitsanis, T. K. Vanderlick, M. Tirrell, and H. T. Davis. A tractable molecular theory of flow in strongly inhomogeneous fluids. *J. Chem. Phys.*, 89(5):3152–3162, 1988.

[23] L. Bocquet and J.-L. Barrat. Flow boundary conditions from nano- to micro-scales. *Soft Matter*, 3:685–693, 2007.

[24] J. A. Bollinger, A. Jain, J. Carmer, and T. M. Truskett. Communication: Local structure-mobility relationships of confined fluids reverse upon supercooling. *J. Chem. Phys*, 142(16):161102, 2015.

[25] J. A. Bollinger, A. Jain, and T. M. Truskett. Structure, thermodynamics, and position-dependent diffusivity in fluids with sinusoidal density variations. *Langmuir*, 30(28):8247–8252, 2014.

[26] J. A. Bollinger, A. Jain, and T. M. Truskett. How local and average particle diffusivities of inhomogeneous fluids depend on microscopic dynamics. *J. Phys. Chem. B*, 119(29):9103–9113, 2015. PMID: 25350488.

[27] J.-M. Bomont, J.-L. Bretonnet, and D. Costa. Temperature study of cluster formation in two-yukawa fluids. *J. Chem. Phys.*, 132(18):184508, 2010.

[28] J.-M. Bomont, J.-L. Bretonnet, D. Costa, and J.-P. Hansen. Communication: Thermodynamic signatures of cluster formation in fluids with competing interactions. *J. Chem. Phys.*, 137(1):011101, 2012.

[29] B. J. Borah, P. K. Maiti, C. Chakravarty, and S. Yashonath. Transport in nanoporous zeolites: Relationships between sorbate size, entropy, and diffusivity. *J. Chem. Phys.*, 136(17):174510, 2012.

[30] J. F. Brady and G. Bossis. Stokesian dynamics. *Annu. Rev. Fluid Mech.*, 20(1):111–157, 1988.

[31] M. Broccio, D. Costa, Y. Liu, and S.-H. Chen. The structural properties of a two-yukawa fluid: Simulation and analytical results. *J. Chem. Phys.*, 124(8):084501, 2006.

[32] A. I. Campbell, V. J. Anderson, J. S. van Duijneveldt, and P. Bartlett. Dynamical arrest in attractive colloids: The effect of long-range repulsion. *Phys. Rev. Lett.*, 94:208301, May 2005.

[33] J. Carmer, G. Goel, M. J. Pond, J. R. Errington, and T. M. Truskett. Enhancing tracer diffusivity by tuning interparticle interactions and coordination shell structure. *Soft Matter*, 8:4083–4089, 2012.

[34] J. Carmer, A. Jain, J. A. Bollinger, F. van Swol, and T. M. Truskett. Tuning structure and mobility of solvation shells surrounding tracer additives. *J. Chem. Phys.*, 142(12):124501, 2015.

[35] J. Carmer, F. van Swol, and T. M. Truskett. Position-dependent and pair diffusivity profiles from steady-state solutions of color reaction-counterdiffusion problems. *J. Chem. Phys.*, 141(4):046101, 2014.

[36] A. C. Chan and P. J. Carter. Therapeutic antibodies for autoimmunity and inflammation. *Nat. Rev. Immunol.*, 10(5):301–16, 2010.

[37] D. Chandler, J. D. Weeks, and H. C. Andersen. Van der waals picture of liquids, solids, and phase transformations. *Science*, 220(4599):787–794, 1983.

[38] R. Chopra, T. M. Truskett, and J. R. Errington. Excess-entropy scaling of dynamics for a confined fluid of dumbbell-shaped particles. *Phys. Rev. E*, 82:041201, Oct 2010.

[39] R. Chopra, T. M. Truskett, and J. R. Errington. On the use of excess entropy scaling to describe the dynamic properties of water. *J. Phys. Chem. B*, 114(32):10558–10566, 2010.

[40] G. Cigala, D. Costa, J.-M. Bomont, and C. Caccamo. Aggregate formation in a model fluid with microscopic piecewise-continuous competing interactions. *Molecular Physics*, 113(17-18):2583–2592, 2015.

[41] J. C. Crocker and D. G. Grier. Methods of digital video microscopy for colloidal studies. *J. Colloid Interface Sci.*, 179(1):298–310, 1996.

[42] M. Cynthia Goh, W. Goldburg, and C. Knobler. Phase separation of a binary liquid mixture in a porous medium. *Phys. Rev. Lett.*, 58:1008–1011, Mar 1987.

[43] B. A. Dalton, K. S. Glavatskiy, P. J. Daivis, B. D. Todd, and I. K. Snook. Linear and nonlinear density response functions for a simple atomic fluid. *J. Chem. Phys.*, 139(4):044510, 2013.

[44] H. T. Davis. *Statistical Mechanics of Phases, Interfaces, and Thin Films.* Wiley-VCH, New York, NY, USA, 1996.

[45] P. G. Debenedetti. *Metastable Liquids: Concepts and Principles.* Princeton University Press, Princeton, NJ, USA, 1997.

[46] B. V. Derjaguin and L. Landau. Theory of the stability of strongly charged lyophobic sols and of the adhesion of strongly charged particles in solution of electrolytes. *Acta Physicochim. URSS*, 14:633–662, 1941.

[47] E. R. Dufresne, D. Altman, and D. G. Grier. Brownian dynamics of a sphere between parallel walls. *Europhys. Lett.*, 53(2):264, 2001.

[48] L. Durlofsky, J. F. Brady, and G. Bossis. Dynamic simulation of hydrodynamically interacting particles. *J. Fluid Mech.*, 180:21–49, 7 1987.

[49] J. C. Dyre. Hidden scale invariance in condensed matter. *J. Phys. Chem. B*, 118(34):10007–10024, 2014.

[50] M. Dzugutov. A universal scaling law for atomic diffusion in condensed matter. *Nature*, 381(6578):137–139, 1996.

[51] K. V. Edmond, C. R. Nugent, and E. R. Weeks. Influence of confinement on dynamical heterogeneities in dense colloidal samples. *Phys. Rev. E*, 85:041401, Apr 2012.

[52] D. L. Ermak and J. A. McCammon. Brownian dynamics with hydrodynamic interactions. *J. Chem. Phys.*, 69(4):1352–1360, 1978.

[53] J. R. Errington, T. M. Truskett, and J. Mittal. Excess-entropy-based anomalies for a waterlike fluid. *J. Chem. Phys.*, 125(24):244502, 2006.

[54] L. P. Faucheux and A. J. Libchaber. Confined brownian motion. *Phys. Rev. E*, 49:5158–5163, Jun 1994.

[55] W. Feller. *An Introduction to Probability Theory and Its Applications, Vol. 2.* John Wiley & Sons, Inc., New York, NY, USA, 2nd edition, 1971.

[56] M. E. Ferraro, R. T. Bonnecaze, and T. M. Truskett. Graphoepitaxy for pattern multiplication of nanoparticle monolayers. *Phys. Rev. Lett.*, 113:085503, Aug 2014.

[57] G. Foffi, K. A. Dawson, S. V. Buldyrev, F. Sciortino, E. Zaccarelli, and P. Tartaglia. Evidence for an unusual dynamical-arrest scenario in short-ranged colloidal systems. *Phys. Rev. E*, 65:050802, May 2002.

[58] P. Ganatos, S. Weinbaum, and R. Pfeffer. A strong interaction theory for the creeping motion of a sphere between plane parallel boundaries. part 1. perpendicular motion. *J. Fluid Mech.*, 99:739–753, 8 1980.

[59] D. A. J. Gillespie, J. E. Hallett, O. Elujoba, A. F. Che Hamzah, R. M. Richardson, and P. Bartlett. Counterion condensation on spheres in the salt-free limit. *Soft Matter*, 10:566–577, 2014.

[60] T. Gleim, W. Kob, and K. Binder. How does the relaxation of a supercooled liquid depend on its microscopic dynamics? *Phys. Rev. Lett.*, 81:4404–4407, Nov 1998.

[61] N. Gnan, T. B. Schrøder, U. R. Pedersen, N. P. Bailey, and J. C. Dyre. Pressure-energy correlations in liquids. iv. isomorphs in liquid phase diagrams. *J. Chem. Phys.*, 131(23):234504, 2009.

[62] P. D. Godfrin, R. Castaeda-Priego, Y. Liu, and N. J. Wagner. Intermediate range order and structure in colloidal dispersions with competing interactions. *J. Chem. Phys.*, 139(15):154904, 2013.

[63] P. D. Godfrin, N. E. Valadez-Perez, R. Castañeda-Priego, N. J. Wagner, and Y. Liu. Generalized phase behavior of cluster formation in colloidal dispersions with competing interactions. *Soft Matter*, 10:5061–5071, 2014.

[64] P. D. Godfrin, I. E. Zarraga, J. Zarzar, L. Porcar, P. Falus, N. J. Wagner, and Y. Liu. Effect of hierarchical cluster formation on the viscosity of concentrated monoclonal antibody formulations studied by neutron scattering. *J. Phys. Chem. B*, 120(2):278–291, 2016. PMID: 26707135.

[65] G. Goel, W. P. Krekelberg, J. R. Errington, and T. M. Truskett. Tuning density profiles and mobility of inhomogeneous fluids. *Phys. Rev. Lett.*, 100:106001, Mar 2008.

[66] G. Goel, W. P. Krekelberg, M. J. Pond, J. Mittal, V. K. Shen, J. R. Errington, and T. M. Truskett. Available states and available space: Static properties that predict

self-diffusivity of confined fluids. *J. Stat. Mech.: Theory Exp.*, 2009(04):P04006, 2009.

[67] D. G. Grier. A revolution in optical manipulation. *Nature*, 424:810–816, 2003.

[68] J. Groenewold and W. K. Kegel. Anomalously large equilibrium clusters of colloids. *J. Phys. Chem. B*, 105(47):11702–11709, 2001.

[69] J. Groenewold and W. K. Kegel. Colloidal cluster phases, gelation and nuclear matter. *J. Phys.: Cond. Matt.*, 16(42):S4877, 2004.

[70] J. Guan, B. Wang, and S. Granick. Even hard-sphere colloidal suspensions display fickian yet non-gaussian diffusion. *ACS Nano*, 8(4):3331–3336, 2014. PMID: 24646449.

[71] S. H. and D. M. Heyes. Transport coefficients of hard sphere fluids. *Mol. Phys.*, 101(3):469–482, 2003.

[72] I. W. Hamley. *Introduction to Block Copolymers*, pages 1–29. John Wiley & Sons, Ltd, 2004.

[73] J.-P. Hansen and I. R. McDonald. *Theory of Simple Liquids*. Academic Press, New York, NY, USA, third edition, 2006.

[74] J. P. Hansen and L. Verlet. Phase transitions of the Lennard-Jones system. *Phys. Rev.*, 184(1):151–161, 1969.

[75] J. Happel and H. Brenner. *Low Reynolds Number Hydrodynamics*. Martinus Nijhoff Publishers, Boston, MA, USA, 2nd edition, 1973.

[76] H. He and M. F. Thorpe. Elastic properties of glasses. *Phys. Rev. Lett.*, 54:2107–2110, May 1985.

[77] E. Helfand. Block copolymers, polymer-polymer interfaces, and the theory of inhomogeneous polymers. *Acc. Chem. Res.*, 8(9):295–299, 1975.

[78] D. J. Herr. Directed block copolymer self-assembly for nanoelectronics fabrication. *J. Mater. Res.*, 26:122–139, 2011.

[79] B. Hess, C. Kutzner, D. van der Spoel, and E. Lindahl. Gromacs 4: Algorithms for highly efficient, load-balanced, and scalable molecular simulation. *J. Chem. Theory Comput.*, 4(3):435–447, 2008.

[80] D. M. Heyes and A. C. Braka. The influence of potential softness on the transport coefficients of simple fluids. *J. Chem. Phys.*, 122(23):234504, 2005.

[81] M. Hinczewski, Y. von Hansen, J. Dzubiella, and R. R. Netz. How the diffusivity profile reduces the arbitrariness of protein folding free energies. *J. Chem. Phys.*, 132(24):245103, 2010.

[82] B. P. Ho and L. G. Leal. Inertial migration of rigid spheres in two-dimensional unidirectional flows. *J. Fluid Mech.*, 65:365–400, 8 1974.

[83] H. Hoang and G. Galliero. Shear viscosity of inhomogeneous fluids. *J. Chem. Phys.*, 136(12):124902, 2012.

[84] H. Hoang and G. Galliero. Local shear viscosity of strongly inhomogeneous dense fluids: From the hard-sphere to the lennard-jones fluids. *J. Phys.: Condens. Matter*, 25(48):485001, 2013.

[85] J. J. Hoyt, M. Asta, and B. Sadigh. Test of the universal scaling law for the diffusion coefficient in liquid metals. *Phys. Rev. Lett.*, 85:594–597, Jul 2000.

[86] G. Hummer. Position-dependent diffusion coefficients and free energies from bayesian analysis of equilibrium and replica molecular dynamics simulations. *New J. Phys.*, 7(1):34, 2005.

[87] W. Humphrey, A. Dalke, and K. Schulten. VMD – Visual Molecular Dynamics. *J. Molec. Graphics*, 14:33–38, 1996.

[88] T. S. Ingebrigtsen, J. R. Errington, T. M. Truskett, and J. C. Dyre. Predicting how nanoconfinement changes the relaxation time of a supercooled liquid. *Phys. Rev. Lett.*, 111:235901, Dec 2013.

[89] T. S. Ingebrigtsen, T. B. Schrøder, and J. C. Dyre. What is a simple liquid? *Phys. Rev. X*, 2:011011, Mar 2012.

[90] J. N. Israelachvili. *Intermolecular and Surface Forces*. Academic Press, New York, NY, USA, 2011.

[91] R. B. Jadrich, J. A. Bollinger, K. P. Johnston, and T. M. Truskett. Origin and detection of microstructural clustering in fluids with spatial-range competitive interactions. *Phys. Rev. E*, 91:042312, Apr 2015.

[92] R. B. Jadrich, J. A. Bollinger, B. A. Lindquist, and T. M. Truskett. Equilibrium cluster fluids: pair interactions via inverse design. *Soft Matter*, 11:9342–9354, 2015.

[93] R. B. Jadrich and K. S. Schweizer. Directing colloidal assembly and a metal-insulator transition using a quench-disordered porous rod template. *Phys. Rev. Lett.*, 113:208302, Nov 2014.

[94] A. Jain, J. A. Bollinger, and T. M. Truskett. Inverse methods for material design. *AIChE J.*, 60(8):2732–2740, 2014.

[95] E. A. G. Jamie, H. H. Wensink, and D. G. A. L. Aarts. Probing the critical behavior of colloidal interfaces by gravity. *Soft Matter*, 6:250–255, 2010.

[96] T. Jiang and J. Wu. Cluster formation and bulk phase behavior of colloidal dispersions. *Phys. Rev. E*, 80:021401, Aug 2009.

[97] K. P. Johnston, J. A. Maynard, T. M. Truskett, A. U. Borwankar, M. A. Miller, B. K. Wilson, A. K. Dinin, T. A. Khan, and K. J. Kaczorowski. Concentrated dispersions of equilibrium protein nanoclusters that reversibly dissociate into active monomers. *ACS Nano*, 6(2):1357–1369, 2012.

[98] J. J. Juárez and M. A. Bevan. Interactions and microstructures in electric field mediated colloidal assembly. *J. Chem. Phys.*, 131(13):134704, 2009.

[99] S. A. Khrapak, O. S. Vaulina, and G. E. Morfill. Self-diffusion in strongly coupled yukawa systems (complex plasmas). *Phys. Plasmas*, 19(3):034503, 2012.

[100] J. M. Kim, R. Castañeda-Priego, Y. Liu, and N. J. Wagner. On the importance of thermodynamic self-consistency for calculating clusterlike pair correlations in hard-core double yukawa fluids. *J. Chem. Phys.*, 134(6):064904, 2011.

[101] R. Kjellander and S. Sarman. Pair correlations of non-uniform hard-sphere fluids in narrow slits and the mechanism of oscillatory solvation forces. *J. Chem. Soc., Faraday Trans.*, 87:1869–1881, 1991.

[102] C. L. Klix, C. P. Royall, and H. Tanaka. Structural and dynamical features of multiple metastable glassy states in a colloidal system with competing interactions. *Phys. Rev. Lett.*, 104:165702, Apr 2010.

[103] W. Kob, S. Roldán-Vargas, and L. Berthier. Non-monotonic temperature evolution of dynamic correlations in glass-forming liquids. *Nat. Phys.*, 8(2):164–167, 2012.

[104] K. Koga, X. C. Zeng, and A. K. Shchekin. Validity of Tolman's equation: How large should a droplet be? *J. Chem. Phys.*, 109(10):4063–4070, 1998.

[105] V. Krakoviack. Liquid–glass transition of confined fluids: Insights from a mode-coupling theory. *J. Phys.: Condens. Matter*, 17(45):S3565, 2005.

[106] V. Krakoviack. Mode-coupling theory for the slow collective dynamics of fluids adsorbed in disordered porous media. *Phys. Rev. E*, 75:031503, Mar 2007.

[107] W. P. Krekelberg, J. Mittal, V. Ganesan, and T. M. Truskett. How short-range attractions impact the structural order, self-diffusivity, and viscosity of a fluid. *J. Chem. Phys.*, 127(4):044502, 2007.

[108] W. P. Krekelberg, M. J. Pond, G. Goel, V. K. Shen, J. R. Errington, and T. M. Truskett. Generalized rosenfeld scalings for tracer diffusivities in not-so-simple fluids: Mixtures and soft particles. *Phys. Rev. E*, 80:061205, Dec 2009.

[109] P. Lançon, G. Batrouni, L. Lobry, and N. Ostrowsky. Brownian walker in a confined geometry leading to a space-dependent diffusion coefficient. *Phys. A*, 304(12):65–76, 2002.

[110] S. Lang, V. Boţan, M. Oettel, D. Hajnal, T. Franosch, and R. Schilling. Glass transition in confined geometry. *Phys. Rev. Lett.*, 105:125701, Sep 2010.

[111] S. Lang and T. Franosch. Tagged-particle motion in a dense confined liquid. *Phys. Rev. E*, 89:062122, Jun 2014.

[112] S. Lang, R. Schilling, V. Krakoviack, and T. Franosch. Mode-coupling theory of the glass transition for confined fluids. *Phys. Rev. E*, 86:021502, Aug 2012.

[113] E. Lange, J. B. Caballero, A. M. Puertas, and M. Fuchs. Comparison of structure and transport properties of concentrated hard and soft sphere fluids. *J. Chem. Phys.*, 130(17):174903, 2009.

[114] D. Langevin. Microemulsions. *Acc. Chem. Res.*, 21(7):255–260, 1988.

[115] C. T. Lee, J. Comer, C. Herndon, N. Leung, A. Pavlova, R. V. Swift, C. Tung, C. N. Rowley, R. E. Amaro, C. Chipot, Y. Wang, and J. C. Gumbart. Simulation-based approaches for determining membrane permeability of small compounds. *J. Chem. Inf. Model.*, 56(4):721–733, 2016. PMID: 27043429.

[116] G. X. Li, C. S. Liu, and Z. G. Zhu. Scaling law for diffusion coefficients in simple melts. *Phys. Rev. B*, 71:094209, Mar 2005.

[117] L. Li, S. Kumar, P. M. Buck, C. Burns, J. Lavoie, S. K. Singh, N. W. Warne, P. Nichols, N. Luksha, and D. Boardman. Concentration dependent viscosity of monoclonal antibody solutions: Explaining experimental behavior in terms of molecular properties. *Pharm. Res.*, 31(11):3161–78, 2014.

[118] W. G. Lilyestrom, S. Yadav, S. J. Shire, and T. M. Scherer. Monoclonal antibody self-association, cluster formation, and rheology at high concentrations. *J. Phys. Chem. B*, 117(21):6373–84, 2013.

[119] B. Lin, J. Yu, and S. A. Rice. Direct measurements of constrained brownian motion of an isolated sphere between two walls. *Phys. Rev. E*, 62:3909–3919, Sep 2000.

[120] K. Lin, J. C. Crocker, V. Prasad, A. Schofield, D. A. Weitz, T. C. Lubensky, and A. G. Yodh. Entropically driven colloidal crystallization on patterned surfaces. *Phys. Rev. Lett.*, 85:1770–1773, Aug 2000.

[121] M. Y. Lin, H. M. Lindsay, W. D. A., R. C. Ball, R. Klein, and P. Meakin. Universality in colloid aggregation. *Nature*, 339:360–362, 1989.

[122] R. A. Lionberger and W. B. Russel. A smoluchowski theory with simple approximations for hydrodynamic interactions in concentrated dispersions. *J. Rheol.*, 41(2):399–425, 1997.

[123] N. Liron and S. Mochon. Stokes flow for a stokeslet between two parallel flat plates. *J. Eng. Math.*, 10(4):287–303, 1976.

[124] P. Liu, E. Harder, and B. J. Berne. On the calculation of diffusion coefficients in confined fluids and interfaces with an application to the liquid–vapor interface of water. *J. Phys. Chem. B*, 108(21):6595–6602, 2004.

[125] Y. Liu, W.-R. Chen, and S.-H. Chen. Cluster formation in two-yukawa fluids. *J. Chem. Phys.*, 122(4):044507, 2005.

[126] Y. Liu, J. Fu, and J. Wu. Excess-entropy scaling for gas diffusivity in nanoporous materials. *Langmuir*, 29(42):12997–13002, 2013.

[127] Y. Liu, L. Porcar, J. Chen, W.-R. Chen, P. Falus, A. Faraone, E. Fratini, K. Hong, and P. Baglioni. Lysozyme protein solution with an intermediate range order structure. *J. Phys. Chem. B*, 115(22):7238–7247, 2011.

[128] L. Lobry and N. Ostrowsky. Diffusion of brownian particles trapped between two walls: Theory and dynamic-light-scattering measurements. *Phys. Rev. B*, 53:12050–12056, May 1996.

[129] L. López-Flores, P. Mendoza-Méndez, L. E. Sánchez-Díaz, L. L. Yeomans-Reyna, A. Vizcarra-Rendón, G. Pérez-Ángel, M. Chávez-Páez, and M. Medina-Noyola. Dynamic equivalence between atomic and colloidal liquids. *Europhys. Lett.*, 99(4):46001, 2012.

[130] L. López-Flores, H. Ruíz-Estrada, M. Chávez-Páez, and M. Medina-Noyola. Dynamic equivalences in the hard-sphere dynamic universality class. *Phys. Rev. E*, 88:042301, Oct 2013.

[131] S. Lotfizadeh, H. Aljama, D. Reilly, and T. Matsoukas. Formation of reversible clusters with controlled degree of aggregation. *Langmuir*, 32(19):4862–4867, 2016. PMID: 27124089.

[132] H. Löwen, J.-P. Hansen, and J.-N. Roux. Brownian dynamics and kinetic glass transition in colloidal suspensions. *Phys. Rev. A*, 44:1169–1181, Jul 1991.

[133] B. D. Lubachevsky and F. H. Stillinger. Geometric properties of random disk packings. *J. Stat. Phys.*, 60(5-6):561–583, 1990.

[134] X. Ma, W. Chen, Z. Wang, Y. Peng, Y. Han, and P. Tong. Test of the universal scaling law of diffusion in colloidal monolayers. *Phys. Rev. Lett.*, 110:078302, Feb 2013.

[135] S. Mallidi, T. Larson, J. Tam, P. P. Joshi, A. Karpiouk, K. Sokolov, and S. Emelianov. Multiwavelength photoacoustic imaging and plasmon resonance coupling of gold

nanoparticles for selective detection of cancer. *Nano Lett.*, 9(8):2825–2831, 2009. PMID: 19572747.

[136] E. Mani, W. Lechner, W. K. Kegel, and P. G. Bolhuis. Equilibrium and non-equilibrium cluster phases in colloids with competing interactions. *Soft Matter*, 10:4479–4486, 2014.

[137] E. Mani and H. Löwen. Effect of self-propulsion on equilibrium clustering. *Phys. Rev. E*, 92:032301, Sep 2015.

[138] G. S. Manning. Counterion binding in polyelectrolyte theory. *Acc. Chem. Res.*, 12(12):443–449, 1979.

[139] R. McGraw and A. Laaksonen. Scaling properties of the critical nucleus in classical and molecular-based theories of vapor-liquid nucleation. *Phys. Rev. Lett.*, 76:2754–2757, Apr 1996.

[140] G. Meng, N. Arkus, M. P. Brenner, and V. N. Manoharan. The free-energy landscape of clusters of attractive hard spheres. *Science*, 327(5965):560–563, 2010.

[141] V. N. Michailidou, G. Petekidis, J. W. Swan, and J. F. Brady. Dynamics of concentrated hard-sphere colloids near a wall. *Phys. Rev. Lett.*, 102:068302, Feb 2009.

[142] V. N. Michailidou, J. W. Swan, J. F. Brady, and G. Petekidis. Anisotropic diffusion of concentrated hard-sphere colloids near a hard wall studied by evanescent wave dynamic light scattering. *J. Chem. Phys.*, 139(16):164905, 2013.

[143] J. Mittal, J. R. Errington, and T. M. Truskett. Quantitative link between single-particle dynamics and static structure of supercooled liquids. *J. Phys. Chem. B*, 110(37):18147–18150, 2006.

[144] J. Mittal, J. R. Errington, and T. M. Truskett. Relationship between thermodynamics and dynamics of supercooled liquids. *J. Chem. Phys.*, 125(7):076102, 2006.

[145] J. Mittal, J. R. Errington, and T. M. Truskett. Thermodynamics predicts how confinement modifies the dynamics of the equilibrium hard-sphere fluid. *Phys. Rev. Lett.*, 96:177804, May 2006.

[146] J. Mittal, J. R. Errington, and T. M. Truskett. Relationships between self-diffusivity, packing fraction, and excess entropy in simple bulk and confined fluids. *J. Phys. Chem. B*, 111(34):10054–10063, 2007.

[147] J. Mittal and G. Hummer. Pair diffusion, hydrodynamic interactions, and available volume in dense fluids. *J. Chem. Phys.*, 137(3):034110, 2012.

[148] J. Mittal, V. K. Shen, J. R. Errington, and T. M. Truskett. Confinement, entropy, and single-particle dynamics of equilibrium hard-sphere mixtures. *J. Chem. Phys.*, 127(15):154513, 2007.

[149] J. Mittal, T. M. Truskett, J. R. Errington, and G. Hummer. Layering and position-dependent diffusive dynamics of confined fluids. *Phys. Rev. Lett.*, 100:145901, Apr 2008.

[150] A. J. Moreno and C. N. Likos. Diffusion and relaxation dynamics in cluster crystals. *Phys. Rev. Lett.*, 99:107801, Sep 2007.

[151] D. Nayar and C. Chakravarty. Water and water-like liquids: Relationships between structure, entropy and mobility. *Phys. Chem. Chem. Phys.*, 15:14162–14177, 2013.

[152] A. Nelson, D. Wang, K. Koynov, and L. Isa. A multiscale approach to the adsorption of core-shell nanoparticles at fluid interfaces. *Soft Matter*, 11:118–129, 2015.

[153] T. D. Nguyen, B. A. Schultz, N. A. Kotov, and S. C. Glotzer. Generic, phenomenological, on-the-fly renormalized repulsion model for self-limited organization of terminal supraparticle assemblies. *Proc. Natl. Acad. Sci. U. S. A.*, 112(25):E3161–E3168, 2015.

[154] M. J. P. Nijmeijer, C. Bruin, A. B. van Woerkom, A. F. Bakker, and J. M. J. van Leeuwen. Molecular dynamics of the surface tension of a drop. *J. Chem. Phys.*, 96(1):565–576, 1992.

[155] C. R. Nugent, K. V. Edmond, H. N. Patel, and E. R. Weeks. Colloidal glass transition observed in confinement. *Phys. Rev. Lett.*, 99:025702, Jul 2007.

[156] K. Nygård, R. Kjellander, S. Sarman, S. Chodankar, E. Perret, J. Buitenhuis, and J. F. van der Veen. Anisotropic pair correlations and structure factors of confined hard-sphere fluids: An experimental and theoretical study. *Phys. Rev. Lett.*, 108:037802, Jan 2012.

[157] W. Olivares-Rivas, P. J. Colmenares, and F. López. Direct evaluation of the position dependent diffusion coefficient and persistence time from the equilibrium density profile in anisotropic fluids. *J. Chem. Phys.*, 139(7):074103, 2013.

[158] M. Paloncýová, R. H. DeVane, B. P. Murch, K. Berka, and M. Otyepka. Rationalization of reduced penetration of drugs through ceramide gel phase membrane. *Langmuir*, 30(46):13942–13948, 2014. PMID: 25354090.

[159] G. Pandav, V. Pryamitsyn, J. Errington, and V. Ganesan. Multibody interactions, phase behavior, and clustering in nanoparticlepolyelectrolyte mixtures. *J. Phys. Chem. B*, 119(45):14536–14550, 2015. PMID: 26473468.

[160] G. Pandav, V. Pryamitsyn, and V. Ganesan. Interactions and aggregation of charged nanoparticles in uncharged polymer solutions. *Langmuir*, 31(45):12328–12338, 2015. PMID: 26535914.

[161] J. I. Park, T. D. Nguyen, G. de Queirós Silveira, J. H. Bahng, S. Srivastava, G. Zhao, K. Sun, P. Zhang, S. C. Glotzer, and N. A. Kotov. Terminal supraparticle assemblies from similarly charged protein molecules and nanoparticles. *Nat. Commun.*, 5, 2014.

[162] J. Perrin. Brownian motion and molecules. *J. Phys.*, 9(1):5–39, 1910.

[163] F. Pfender and G. M. Ziegler. Kissing numbers, sphere packings and some unexpected proofs. *Notices Amer. Math. Soc*, 51:873–883, 2004.

[164] D. Pini, G. Jialin, A. Parola, and L. Reatto. Enhanced density fluctuations in fluid systems with competing interactions. *Chem. Phys. Lett.*, 327(34):209 – 215, 2000.

[165] S. Plimpton. Fast parallel algorithms for short-range molecular dynamics. *J. Comput. Phys.*, 117(1):1–19, 1995.

[166] M. J. Pond, J. R. Errington, and T. M. Truskett. Communication: Generalizing rosenfeld's excess-entropy scaling to predict long-time diffusivity in dense fluids of brownian particles: From hard to ultrasoft interactions. *J. Chem. Phys.*, 134(8):081101, 2011.

[167] M. J. Pond, J. R. Errington, and T. M. Truskett. Mapping between long-time molecular and brownian dynamics. *Soft Matter*, 7:9859–9862, 2011.

[168] L. Porcar, P. Falus, W.-R. Chen, A. Faraone, E. Fratini, K. Hong, P. Baglioni, and Y. Liu. Formation of the dynamic clusters in concentrated lysozyme protein solutions. *J. Phys. Chem. Lett.*, 1(1):126–129, 2010.

[169] G. V. Ramanathan. Counterion condensation in micellar and colloidal solutions. *J. Chem. Phys.*, 88(6):3887–3892, 1988.

[170] Y. Rosenfeld. Relation between the transport coefficients and the internal entropy of simple systems. *Phys. Rev. A*, 15:2545–2549, Jun 1977.

[171] Y. Rosenfeld. A quasi-universal scaling law for atomic transport in simple fluids. *J. Phys.: Condens. Matter*, 11(28):5415, 1999.

[172] R. Roth. Fundamental measure theory for hard-sphere mixtures: A review. *J. Phys.: Condens. Matter*, 22(6):063102, 2010.

[173] R. Roth, R. Evans, A. Lang, and G. Kahl. Fundamental measure theory for hard-sphere mixtures revisited: The white bear version. *J. Phys.: Condens. Matter*, 14(46):12063, 2002.

[174] R. Roth, K. Mecke, and M. Oettel. Communication: Fundamental measure theory for hard disks: Fluid and solid. *J. Chem. Phys.*, 136(8):081101, 2012.

[175] C. P. Royall, R. van Roij, and A. van Blaaderen. Extended sedimentation profiles in charged colloids: The gravitational length, entropy, and electrostatics. *J. Phys.: Condens. Matter*, 17(15):2315–2326, 2005.

[176] S. Sastry, T. M. Truskett, P. G. Debenedetti, S. Torquato, and F. H. Stillinger. Free volume in the hard sphere liquid. *Mol. Phys.*, 95(2):289–297, 1998.

[177] P. Scheidler, W. Kob, , and K. Binder. The relaxation dynamics of a supercooled liquid confined by rough walls. *J. Phys. Chem. B*, 108(21):6673–6686, 2004.

[178] P. Scheidler, W. Kob, and K. Binder. The relaxation dynamics of a simple glass former confined in a pore. *Europhys. Lett.*, 52(3):277, 2000.

[179] S. Schemmel, D. Akcakayiran, G. Rother, A. Brulet, B. Farago, T. Hellweg, and G. H. Findenegg. Phase separation of a binary liquid system in controlled-pore glass. *MRS Proceedings*, 790(7):1–6, 2003.

[180] M. J. Schnitzer. Theory of continuum random walks and application to chemotaxis. *Phys. Rev. E*, 48:2553–2568, Oct 1993.

[181] T. B. Schrøder, U. R. Pedersen, N. P. Bailey, S. Toxvaerd, and J. C. Dyre. Hidden scale invariance in molecular van der waals liquids: A simulation study. *Phys. Rev. E*, 80:041502, Oct 2009.

[182] F. Sciortino, S. Mossa, E. Zaccarelli, and P. Tartaglia. Equilibrium cluster phases and low-density arrested disordered states: The role of short-range attraction and long-range repulsion. *Phys. Rev. Lett.*, 93:055701, Jul 2004.

[183] R. P. Sear. Classical nucleation theory for the nucleation of the solid phase of spherical particles with a short-ranged attraction. *J. Chem. Phys.*, 111(5):2001–2007, 1999.

[184] R. P. Sear. Low-temperature interface between the gas and solid phases of hard spheres with a short-ranged attraction. *Phys. Rev. E*, 59:6838–6841, Jun 1999.

[185] R. P. Sear. Nucleation: theory and applications to protein solutions and colloidal suspensions. *J. Phys.: Cond. Matt.*, 19(3):033101, 2007.

[186] R. P. Sear and W. M. Gelbart. Microphase separation versus the vapor-liquid transition in systems of spherical particles. *J. Chem. Phys.*, 110(9):4582–4588, 1999.

[187] F. Sedlmeier, Y. Hansen, L. Mengyu, D. Horinek, and R. Netz. Water dynamics at interfaces and solutes: Disentangling free energy and diffusivity contributions. *J. Stat. Phys.*, 145(2):240–252, 2011.

[188] T. Sentjabrskaja, E. Zaccarelli, C. De Michele, F. Sciortino, P. Tartaglia, T. Voigtmann, S. U. Egelhaaf, and M. Laurati. Anomalous dynamics of intruders in a crowded environment of mobile obstacles. *Nat. Comm.*, 7:11133, 2016.

[189] M. Seul and D. Andelman. Domain shapes and patterns: The phenomenology of modulated phases. *Science*, 267(5197):476–483, 1995.

[190] R. Sharma, S. N. Chakraborty, and C. Chakravarty. Entropy, diffusivity, and structural order in liquids with waterlike anomalies. *J. Chem. Phys.*, 125(20):204501, 2006.

[191] V. K. Shen and J. R. Errington. Determination of fluid-phase behavior using transition-matrix monte carlo: Binary lennard-jones mixtures. *J. Chem. Phys.*, 122(6):–, 2005.

[192] S. J. Shire. Formulation and manufacturability of biologics. *Curr. Opin. Biotechnol.*, 20(6):708–14, 2009.

[193] A. Shukla, E. Mylonas, E. Di Cola, S. Finet, P. Timmins, T. Narayanan, and D. I. Svergun. Absence of equilibrium cluster phase in concentrated lysozyme solutions. *Proc. Natl. Acad. Sci. U. S. A.*, 105(13):5075–5080, 2008.

[194] A. Sierou and J. F. Brady. Accelerated stokesian dynamics simulations. *J. Fluid Mech.*, 448:115–146, 12 2001.

[195] C. A. Silvera Batista, R. G. Larson, and N. A. Kotov. Nonadditivity of nanoparticle interactions. *Science*, 350(6257), 2015.

[196] M. V. Smoluchowski. Drei vorträge über diffusion, brownsche bewegung und koagulation von kolloidteilchen. *Physik Z.*, 17:557–585, 1916.

[197] R. O. Sokolovskii, M. Thachuk, and G. N. Patey. Tracer diffusion in hard sphere fluids from molecular to hydrodynamic regimes. *J. Chem. Phys.*, 125(20):204502, 2006.

[198] T. M. Squires and S. R. Quake. Microfluidics: Fluid physics at the nanoliter scale. *Rev. Mod. Phys.*, 77:977–1026, Oct 2005.

[199] M. E. Staben, A. Z. Zinchenko, and R. H. Davis. Motion of a particle between two parallel plane walls in low-reynolds-number poiseuille flow. *Phys. Fluids*, 15(6):1711–1733, 2003.

[200] A. Stradner, F. Cardinaux, S. U. Egelhaaf, and P. Schurtenberger. Do equilibrium clusters exist in concentrated lysozyme solutions? *Proc. Natl. Acad. Sci. U. S. A.*, 105(44):E75, 2008.

[201] A. Stradner, H. Sedgwick, F. Cardinaux, W. C. K. Poon, S. U. Egelhaaf, and P. Schurtenberger. Equilibrium cluster formation in concentrated protein solutions and colloids. *Nature*, 432:492–495, 2004.

[202] M. T. Sullivan, K. Zhao, A. D. Hollingsworth, R. H. Austin, W. B. Russel, and P. M. Chaikin. An electric bottle for colloids. *Phys. Rev. Lett.*, 96:015703, Jan 2006.

[203] J. W. Swan and J. F. Brady. Particle motion between parallel walls: Hydrodynamics and simulation. *Phys. Fluids*, 22(10):103301, 2010.

[204] M. B. Sweatman, R. Fartaria, and L. Lue. Cluster formation in fluids with competing short-range and long-range interactions. *J. Chem. Phys.*, 140(12):124508, 2014.

[205] A. Szabo, K. Schulten, and Z. Schulten. First passage time approach to diffusion controlled reactions. *J. Chem. Phys.*, 72:4350–4357, 1980.

[206] G. Szamel and E. Flenner. Independence of the relaxation of a supercooled fluid from its microscopic dynamics: Need for yet another extension of the mode-coupling theory. *Europhys. Lett.*, 67(5):779, 2004.

[207] P. R. ten Wolde and D. Frenkel. Computer simulation study of gas-liquid nucleation in a Lennard-Jones system. *J. Chem. Phys.*, 109(22):9901–9918, 1998.

[208] D. N. Theodorou and U. W. Suter. Shape of unperturbed linear polymers: polypropylene. *Macromolecules*, 18(6):1206–1214, 1985.

[209] J. C. F. Toledano, F. Sciortino, and E. Zaccarelli. Colloidal systems with competing interactions: from an arrested repulsive cluster phase to a gel. *Soft Matter*, 5:2390–2398, 2009.

[210] R. C. Tolman. The effect of droplet size on surface tension. *J. Chem. Phys.*, 17(3):333–337, 1949.

[211] A. Tröster, M. Oettel, B. Block, P. Virnau, and K. Binder. Numerical approaches to determine the interface tension of curved interfaces from free energy calculations. *J. Chem. Phys.*, 136(6):064709, 2012.

[212] A. van Blaaderen, R. Ruel, and P. Wiltzius. Template-directed colloidal crystallization. *Nature*, 385:321–324, 1997.

[213] A. E. van Giessen and E. M. Blokhuis. Direct determination of the Tolman length from the bulk pressures of liquid drops via molecular dynamics simulations. *J. Chem. Phys.*, 131(16):164705, 2009.

[214] E. J. Verwey and J. T. G. Overbeek. *Theory of the Stability Lyophobic Colloids*. Elsevier, New York, NY, USA, 1948.

[215] Y. von Hansen, S. Gekle, and R. R. Netz. Anomalous anisotropic diffusion dynamics of hydration water at lipid membranes. *Phys. Rev. Lett.*, 111:118103, Sep 2013.

[216] G. M. Wang, R. Prabhakar, and E. M. Sevick. Hydrodynamic mobility of an optically trapped colloidal particle near fluid-fluid interfaces. *Phys. Rev. Lett.*, 103:248303, Dec 2009.

[217] K. Watanabe, T. Kawasaki, and H. Tanaka. Structural origin of enhanced slow dynamics near a wall in glass-forming systems. *Nat. Mater.*, 10(7):512–520, 2011.

[218] E. R. Weeks, J. C. Crocker, A. C. Levitt, A. Schofield, and D. A. Weitz. Three-dimensional direct imaging of structural relaxation near the colloidal glass transition. *Science*, 287(5453):627–631, 2000.

[219] E. R. Weeks and D. A. Weitz. Properties of cage rearrangements observed near the colloidal glass transition. *Phys. Rev. Lett.*, 89:095704, Aug 2002.

[220] G. H. Weiss. *First Passage Time Problems in Chemical Physics*, pages 1–18. John Wiley & Sons, Inc., 2007.

[221] W. Wen, X. Huang, S. Yang, K. Lu, and P. Sheng. The giant electrorheological effect in suspensions of nanoparticles. *Nat. Mater.*, 2(11):727–730, 2003.

[222] B. Widom. Some topics in the theory of fluids. *J. Chem. Phys.*, 39(11):2808–2812, 1963.

[223] Ø. Wilhelmsen, D. Bedeaux, and D. Reguera. Tolman length and rigidity constants of the Lennard-Jones fluid. *J. Chem. Phys.*, 142(6):064706, 2015.

[224] I. Williams, E. C. Oğuz, P. Bartlett, H. Löwen, and C. P. Royall. Direct measurement of osmotic pressure via adaptive confinement of quasi hard disc colloids. *Nat. Commun.*, 4(2555):1–6, 2013.

[225] I. Williams, E. C. Oğuz, T. Speck, P. Bartlett, H. Löwen, and C. P. Royall. Transmission of torque at the nanoscale. *Nat. Phys.*, 12(1):98–103, 2016.

[226] J. Wu and Z. Li. Density-functional theory for complex fluids. *Annu. Rev. Phys. Chem.*, 58(1):85–112, 2007.

[227] J. Wu, Y. Liu, W.-R. Chen, J. Cao, and S.-H. Chen. Structural arrest transitions in fluids described by two yukawa potentials. *Phys. Rev. E*, 70:050401, Nov 2004.

[228] Y. Xia, T. D. Nguyen, M. Yang, B. Lee, A. Santos, P. Podsiadlo, Z. Tang, S. C. Glotzer, and N. A. Kotov. Self-assembly of self-limiting monodisperse supraparticles from polydisperse nanoparticles. *Nat. Nanotechnol.*, 7(7):479–479, 2012.

[229] E. J. Yearley, P. D. Godfrin, T. Perevozchikova, H. Zhang, P. Falus, L. Porcar, M. Nagao, J. E. Curtis, P. Gawande, R. Taing, I. E. Zarraga, N. J. Wagner, and Y. Liu. Observation of small cluster formation in concentrated monoclonal antibody solutions and its implications to solution viscosity. *Biophys. J.*, 106(8):1763 – 1770, 2014.

[230] A. Yethiraj and A. van Blaaderen. A colloidal model system with an interaction tunable from hard sphere to soft and dipolar. *Nature*, 421:513–517, 2003.

[231] T. H. Zhang, J. Klok, R. Hans Tromp, J. Groenewold, and W. K. Kegel. Non-equilibrium cluster states in colloids with competing interactions. *Soft Matter*, 8:667–672, 2012.

[232] X. Zhang, H. Sun, and S. Yang. Self-limiting assembly of two-dimensional domains from graphene oxide at the air/water interface. *J. Phys. Chem. C*, 116(35):19018–19024, 2012.

[233] Y. Zhuang and P. Charbonneau. Recent advances in the theory and simulation of model colloidal microphase formers. *J. Phys. Chem. B*, 120(32):7775–7782, 2016. PMID: 27466702.

Vita

Jonathan (Jon) Allen Bollinger is from York, Pennsylvania. He received his Bachelor of Science degree in Chemical Engineering, *magna cum laude*, from the University of Maryland, Baltimore County in 2010. He subsequently received a Master of Science degree in Chemical and Biochemical Engineering from the same in 2011, completing a thesis under the supervision of Mariajosé Castellanos that was focused on computational metabolic modeling of the alga *C. reinhardtii* for bioengineering applications. He entered the McKetta Department of Chemical Engineering at the University of Texas at Austin in the fall of 2011 and joined the research group of Thomas M. Truskett. After graduating, he will join the Center for Integrated Nanotechnologies at Sandia National Labs in Albuquerque, NM.

Permanent address: jonathanabollinger@gmail.com

This dissertation was typeset with LaTeX by the author.